Modelling time-varying gravity fields from Level-1B GRACE data using mascons

Stuart Bruce Andrews

Thesis submitted for the degree of

Doctor of Philosophy

School of Civil Engineering and Geosciences

Newcastle University

August 2015

Abstract

As an alternative to spherical harmonics, mass concentration (mascon) parameters have been successfully applied to the recovery of time-varying gravity (TVG) fields from the GRACE satellite mission. However, before meaningful mass anomalies can be estimated, the noise and errors inherent in the solutions needs to be quantified and appropriate procedures adopted for mitigation. The uniqueness of the mascon methodology is the capability to mitigate noise and errors using spatial and temporal constraints, which can be adapted and tailored to any geophysical signal of interest. Therefore, in the first instance, this work was motivated by the need to improve the accuracy of GRACE TVG fields by understanding the effect of noise and errors. This study then aims to validate mascons for recovery of basin scale inter-annual mass variability at a 10 day temporal resolution.

Newcastle University's orbit determination software, *Faust*, was modified to allow for estimation of mascon parameters including: modelling of accelerometer bias values; mascon parameterisation; and processing based on short-arc gravity field recovery and KBRR data. Accuracy assessments were undertaken using simulations in the presence of realistic noise facilitating the comparison of mascons and spherical harmonic coefficients, including an assessment of potential limitations associated with each technique.

Comparisons with time-series derived from CSR RL05 Level-2 data validated the mascon TVG field recovery, before estimation of the mass change of Antarctica, Greenland and Alaska. Several hydrological basins, including the Amazon and Indus were also assessed before the GRACE trends resulting from the Sumatra earthquake of 2004 were investigated. While only provided for validation, these comparisons provide confidence in the mascon mass estimates. Between January 2003 and December 2013 a mass change of -83 ± 12 Gt/year and -242 ± 7 Gt/year were estimated for Antarctica and Greenland respectively by linear regression using mascons with a 10 day temporal resolution.

Overall, the work undertaken in this thesis provides evidence of the improved accuracy achievable when using mascon parameters to estimating TVG fields from Level-1B GRACE data.

As part of this work a processing methodology to estimate mascon parameters from Level-1B GRACE data using Newcastle University's orbit determination software *Faust* has been established and documented. This leaves the University well placed to continue processing mascon solutions from Level-1B GRACE data and to estimate mascon solutions from the GRACE-FO mission.

Through simulations, mascon parameters were found to offer advantages over spherical harmonics for the mitigation of noise and for improving the temporal and spatial recovery of the TVG field from GRACE. The mascon constraint matrix allowed more signal to be preserved up to degree ~35. Using basin constraints, simulation revealed that the constraint matric can be tuned to recovery the gravity changes resulting from any geophysical phenomena of interest. Basin constraints were found to optimise the signal recovery of GLDAS and a known mass change signal over Antarctica and Greenland. A novel way to create realistic noise and errors in the KBRR measurement was also documented.

Generating monthly and 10 day mascon solutions using real data revealed that the noise and errors in mascon solutions is comparably lower than in CRS RL05 solution while also validating the mascon methodology established here. Comparison to published mass trends to those estimated using mascon parameters showed that the estimation of mascon parameters has application in the study of mass change in the cryosphere, hydrological applications and for the study of the co-seismic mass changes resulting from earthquakes.

Acknowledgements

Firstly, I am indebted to Professor Philip Moore for the advice, guidance, support and encouragement he has provided whilst I undertook this work. As my main supervisor he bore the brunt of my questioning, especially about *Faust.* His knowledge has been invaluable. I also wish to thank Professor Matt King. Although leaving Newcastle University early in my studies he still remained involved with this work by answering questions, providing advice and proofreading. Thanks must also be given to my colleagues in the Geodesy Group and my colleagues in the School of Civil Engineering and Geosciences. During my 10 years at the Newcastle University many of you have become good friends and made studying at Newcastle an enjoyable experience.

I owe a special thank you to my parents and family. You have always believed in me and offered your love, support and encouragement. You've made following my dreams easier. I would like to dedicate this thesis in memory of my Grandad, Ronnie. Not only was he a good friend and role model but he encouraged me to ask questions. I miss him daily.

Thank you to my friends for keeping me sane and allowing me to enjoy life away from the computer. You never fail to make me laugh.

Finally, I wish to thank my wife Lizzy for her continual love, support and encouragement. Without her, undertaking this work would not have been possible.

This research was funded by NERC. The data in this thesis was provided by NASA, DLR and GFZ. Thanks to all involved with the GRACE project.

Table of contents

List of Figures

List of Tables

List of Abbreviations

ACC1B	Accelerometer Level-1B data product
AIS	Antarctic Ice Sheet
AOD1B	Atmosphere and Ocean De-aliasing Level-1B product
APC	Antenna Phase Centre
CNES	Centre National d'Eudes Spatiales / French Space Agency
COM	Centre of Mass
CSR	Centre for Space Research
DLR	Deutsches Zentrum für Luft und Raumfahrt / German Aerospace Centre
EA	East Antarctica
EWH	Equivalent Water Height
GFZ	GeoForschungsZentrum / German Research Centre
GIA	Glacial Isostatic Adjustment
GIF48	GRACE Intermediate Field – mean gravity field used in thesis
GIS	Greenland Ice Sheet
GLDAS	Global Land Data Assimilation System
GNV1B	GPS Navigation Level-1B data product
GOA	Gulf of Alaska
GPS	Global Positioning System
GRACE	Gravity Recovery and Climate Experiment
GRGS	Space Geodesy Research Group
GSFC	Goddard Space Flight Centre
JPL	Jet Propulsion Laboratory
KBR1B	KBR(R) Level-1B ranging data
KBRR	K-band Range Rate measurement
NASA	National Aeronautics and Space Administration
OBP	Ocean Bottom Pressure
RL01-RL05	Release 1 to 5 of data series
RMS	Root Mean Square
SCA1B	Star Camera Level-1B data product
TVG	Time-Varying Gravity
VKB1B	Vector product that describes the KBR APC and COM offset
WA	West Antarctica

Chapter 1. Introduction

1.1 *Research background*

The ability to accurately recover the Earth's time-varying gravity (TVG) field every ~30 days to a few hundred kilometres resolution provides a means to assess and improve geophysical models. Observing changes between successive monthly solutions also allows geophysical processes that are of fundamental importance to be studied. One example is the monitoring of the Greenland and Antarctic ice sheets. Greenland contains enough ice to cause global sea level to rise by between 6.5 m and 7.4 m (, with a potential contribution from Antarctica of 58 m (Fretwell et al., 2013). While this is the 'worst case' scenario, it does highlight that having an accurate estimate of the current mass change of these ice sheets, along with realistic uncertainties, is of fundamental interest (Zwally et al., 2005). TVG solutions have also identified important issues such as ground water depletion (e.g. Castle et al., 2014). If not correctly addressed, ground water depletion could result in water scarcity. A United Nations report identified that water scarcity already effects 1.2 billion people and is set to be one of the main issues effecting society in the 21st century (Watkins, 2006).

Since the launch of the Gravity Recovery and Climate Experiment (GRACE) twin satellite mission in 2002, GRACE TVG solutions have been successfully used for estimating ice mass trends (e.g. King et al., 2012, Luthcke et al., 2013, Shepherd et al., 2012), hydrological change (e.g. Awange et al., 2011, Han et al., 2009, Ramillien et al., 2011), ocean mass variability (e.g. Chambers and Bonin, 2012, Chambers et al., 2010), Glacial Isostatic Adjustment (GIA) (e.g. Riva et al., 2009) and studying Earthquake co-seismic and post-seismic deformation (e.g. Han et al., 2008). The spatial and temporal resolution of GRACE will allow the separation of the signals from many of these geophysical phenomena (Swenson and Wahr, 2002). Without GRACE, this would not have been possible.

To generate GRACE TVG solutions, a number of different processing methodologies have been applied to GRACE data. The most common methodology used to estimate the temporal variations of mass anomalies from Level-1B GRACE data is the recovery of spherical harmonic (Stokes') coefficients (Tapley et al., 2004b, Wahr et al., 2004). While some groups are able to generate their own spherical harmonics solutions, most users of GRACE data are heavily reliant on pre-processed Level-2 gravity field

solutions which are provided by the main GRACE processing centres, namely: Centre for Space Research (CSR); Jet Propulsion Laboratory (JPL); and GeoForschungsZentrum (GFZ). More recently mass concentration (mascon) parameters have been used to estimate TVG solutions from Level-1B GRACE data. Mascon parameters allow the Earth's TVG to be modelled at a spatial and temporal resolution unachievable using conventional spherical harmonics (Rowlands et al., 2010). Spatial and temporal constraints, applied during solution generation, can be adapted to any geophysical phenomena of interest, offering the potential to improve the monitoring of geophysical processes. This is the uniqueness of the mascon methodology.

The use of spherical harmonic coefficients and mascon parameters result in solutions that differ in more than their spatial and temporal resolutions. Random noise and systematic errors in the GRACE solutions need to be appropriately treated and mitigated before any meaningful mass anomalies can be estimated. Level-2 spherical harmonic products, which are widely used by researchers who undertake studies of mass flux analysis, rely on post-processing strategies that have been proposed to mitigate the random noise and systematic errors in spherical harmonic coefficients. These include the use of Gaussian smoothing (e.g. Tapley et al., 2004a, Wahr et al., 1998, Wahr et al., 2004), filtering using empirical orthogonal functions (EOF) (e.g. Wouters and Schrama, 2007), destriping (e.g. Swenson and Wahr, 2006) and forward modelling (e.g. Schrama and Wouters, 2011, Wouters et al., 2008). Gaussian smoothing is probably the most common processing strategy (Rowlands et al., 2010). Although, access to solution normal matrices allows users to constrain the higher degrees of their TVG fields to the mean field (e.g. Bruinsma et al., 2010, Save et al., 2012), these are not typically provided as part of the Level-2 solutions and are only available to users generating solutions from Level-1B data.

In contrast the mascon methodology benefits from constraint equations applied during the Least Squares inversion which removes the requirement of post processing, making possible solutions with a 10 day temporal resolution and a spatial sampling of 4° or 2° (Rowlands et al., 2010) with the most recent published mascon solutions using a 1° spatial sampling (Luthcke et al., 2013). At the equator, 1° is ~110 km. The mascon constraint matrix is anisotropic in nature as it can be applied to constrain distinct geographical regions while also taking into account the full noise covariance matrix (Luthcke et al., 2013). The use of mascon parameters has allowed basin scale inter-annual variability to be extracted from the GRACE time series (Rowlands et al., 2010).

Mascon TVG estimates, unlike spherical harmonic coefficients, can also be either local or global in extent as the GRACE K-band range rate (KBRR) data associated with the mascon is dominated by mass flux below the satellite (Luthcke et al., 2008).

1.2 *Motivations, Aims and Objectivises*

Compared with TVG recovery using spherical harmonic coefficients, the 10 day temporal resolution and basin scale inter-annual variability of the mascon methodology has the potential to further improve geophysical models and aid the understanding of geophysical processes. In addition, users of the GRACE TVG solutions, especially those that use the pre-processed Level-2 gravity field solutions, need to understand the limitations of the mascon methodology used to calculate TVG solutions, allowing them to directly compare any subsequent mass flux analysis. Bonin and Chambers (2013) note that no accuracy assessment of the mascons ability to recover a known input signal has been published. Although, the spatial and temporal resolution of the mascon methodology look promising, with studies by Rowlands et al. (2010) and Watkins et al. (2015) finding, when compared to in-situ data, that the mascon constraint equation offer advantages over the post-processing of spherical harmonics solutions, a simulated comparison of the two methodologies, using a known input signal, is still required.

Therefore, the work in this thesis is motivated by the need to improve the accuracy of TVG fields computed from the GRACE data; while aiding users of GRACE solutions to understand the associated limitations of the mascon methodology. One of the key issues to address is how random and systematic errors, present in the instrument data and background models, are handled as they can dominate the solutions (Klees et al., 2008a). If not correctly dealt with, measurement and processing errors and un-modelled mass variations in the GRACE solution could be interpreted as real mass change (Wahr et al., 2006). Systematic errors in geophysical models can also alias into the solutions (Seo et al., 2008a).

This study aims to validate the use of the mascon methodology for the recovery of basin scale inter-annual variability at a 10 day temporal resolution by undertaking an accuracy assessment using simulations. In particular, this will include how random and systematic errors are handled, while identifying the limitations of the mascon methodology. The final results will include an estimate of the current mass trend of Antarctica, Greenland and Alaska and the hydrological changes over the Amazon, Indus, Mississippi and Ganges river basins. The mass redistribution caused by the

Sumatra-Andaman Earthquake will also be investigated. To achieve this aim the following objectives will be pursued:

1. Newcastle University's orbit and gravity field determination software, *Faust*, will be modified to allow for the estimation of mascon parameters.

2. The correct parameterisation to use during the processing steps required to compute gravity field solutions from Level-1B GRACE data will be identified and validated.

3. A simulated comparison of solutions generated through the estimation of mascon parameters and spherical harmonic coefficients will be undertaken.

4. Monthly and 10 day mascon solutions will be generated, from real GRACE data, for the period January 2003 to December 2013 and compared to time-series solutions calculated from CSR release 5 (RL05) Level-2 products.

5. The mass trend of Antarctica, Greenland and Alaska, complete with uncertainties, will be computed. The mass redistribution caused by the Sumatra-Andaman Earthquakes will also be investigated, along with hydrological changes over the Amazon, Indus, Mississippi and Ganges river basins.

The use of simulations will allow the relative accuracy of the mascon and spherical harmonic methodologies to be assessed, along with their ability to resolve basin-level mass changes at a variety of spatial scales. Simulations will also provide an insight into how random noise and systematic errors inherent at higher degree and orders are handled, while allowing the parameterisation of the mascon methodology to be tuned. Actual random noise and systematic errors, obtained during GRACE Level-1B data processing, will be used to create simulated stripes for use during the simulations. The simulations will be used to recover realistic mass change signals. While the simulations will only recovery a single solution, the assessment of the mascon methodology will provide an understanding of the associated limitations, as correctly recovering individual solutions is imperative when using these solutions for deriving longer term trends. The simulations will compare a mascon and spherical harmonic solution using a standard Gaussian smoothing filter for the post processing of the spherical harmonic solution and a spatial constraint matrix applied to the mascon solution. For consistency

with the spherical harmonic approach the simulations will only calculate monthly mascon solutions.

Mascon time-series solutions, generated from real GRACE data, will then be compared with time-series solutions calculated from CSR RL05 Level-2 products, allows the signal recovered at a number of locations to be assessed. The removal of a constant, linear trend and annual and semi-annual signal from the time-series will allow the relative random noise and systematic errors in the solutions to be determined. First the monthly mascon solutions will be compared to the CSR RL05 solutions. On validating the monthly mascon solutions, they will then be compared to the 10 day mascon solutions. Comparing the solutions will reveal any differences in the mascon solutions.

1.3 *Thesis outline*

The outline of the thesis will be as follows. Chapter 2 will describe modelling the Earth's static and temporal gravity field from space, with special attention paid to the development of dedicated satellites missions such as the GRACE. An overview of the scientific instruments on-board GRACE and the GRACE data products will also be provided. In Chapter 3 the causes of the random noise and systematic errors in the GRACE data will be discussed. The different processing methodologies used to estimate TVG solutions will be documented, along with how random noise and systematic errors are mitigated. Finally, methods used to derive mass flux trends will be outlined.

The theory behind the formation of the mascon parameters will be described in Chapter 4. Building on this, in Chapter 5 the processing strategy used to calculate TVG solutions from Level-1B GRACE data will be documented. This will include an explanation and validation of the choice of parameters used during the processing. Using these parameters, a number of simulated comparisons of TVG field recovery using the mascon parameters and spherical harmonic coefficients will be undertaken in Chapter 6. This will validate the use of the mascon methodology to recover basin scale mass change. An assessment of the random noise and systematic errors in the two solutions will also be undertaken.

In Chapter 7, monthly and 10 day mascon solutions will be generated from Level-1B GRACE for the period January 2003 to December 2013. A comparison of time-series will be made between the monthly mascon solutions and the CSR RL05 Level-2 products, allowing for validation and analysis at the noise level. This is followed by a

comparison between the monthly and 10 day mascon solutions. The mass trend of Antarctica, Greenland and Alaska and the hydrological changes over the Amazon, Indus, Mississippi and Ganges river basins will also be presented, along with the post-seismic mass redistribution caused by the Sumatra-Andaman Earthquake. The conclusions are in Chapter 8.

Chapter 2. Gravity Recovery and Climate Experiment (GRACE)

This chapter will provide a brief introduction to the history of observing the Earth's gravity field from space. Following this the concept of satellite to satellite tracking will be introduced before an overview of the dedicated gravity mission GRACE is given with an introduction to the scientific instrumentation and data levels available from the GRACE data centres. Chapter 3 will discuss how GRACE data is used to compute estimates of the Earth's gravity field.

2.1 *Observing the Earth's gravity field from space*

Satellite geodesy started with the launch of Sputnik-1 on October 4, 1957, which was the first artificial satellite to orbit the Earth. However, the tracking of satellites is not a new phenomenon and it has been going on for centuries. One example is the tracking of the moon by Laplace (Seeber, 2003). Artificial satellites can be tracked from the Earth, using methods such as Satellite Laser Ranging (SLR) and Doppler Positioning. The tracking of artificial satellites has allowed scientists to solve scientific problems such as determining the flattening of the Earth. One 'indirect effect' of the tracking of artificial satellites is the creation of gravity fields from analysis of satellite orbits (Rowlands et al., 2002) as gravity signals can be inferred from the perturbed orbits of satellites (Wolff, 1969). This has led to the development of global gravity field models (Seeber, 2003).

The early gravity field models were limited to long wavelength, low degree information. For example, the first gravity field model issued by the National Aeronautics and Space Administration (NASA) Goddard Space Flight Centre (GSFC) was the Goddard Earth Model 1 (GEM-1) (Lerch et al., 1972). GEM-1 was derived from the tracking of 25 satellites over 300 weekly orbits, but was limited to spherical harmonic degree and order 12.

2.1.1 *Advances in gravity field modelling*

Since 1972, there have been improvements in satellite tracking techniques and also an increase in the number of artificial satellites orbiting the Earth, allowing shorter wavelength, higher degree gravity field information to be obtained. The Earth Gravitational Model 1996 (EGM96) (Lemoine et al., 1998) describes the Earth's gravity field up to degree and order 360. Compared to GEM-1, EGM96 offered a fundamental improvement in the spatial resolution of the model. EGM96 utilises gravity data from different sources (e.g. terrestrial gravity surveys and altimetry). However, in EGM96,

satellite tracking is used to provide the spherical harmonics coefficients up to degree and order 70 as part of a composite solution where different techniques are used to computer different spectral bands of the model (Pavlis et al., 2012). The satellite contribution is derived from EGM96S solution, where the 'S' denotes satellite only. EGM96S is based on the analysis of tracking data from 40 satellites. Many gravity field models are available as satellite only solutions (suffix of 'S') or as combined solutions (suffix of 'C'), that use additional gravity information (e.g. terrestrial gravity surveys).

2.1.2 *Dedicated Gravity Satellite missions*

The most recent developments in modelling the Earth's gravity field have been through the launch of dedicated gravity field satellite missions; previously satellite missions mainly had other objectives. Missions such as Challenging Mini-Satellite Payload (CHAMP), launched on July 15th 2000, GRACE, launched on 17th March 2002, and Gravity Field and Steady-State Ocean Circulation Explorer (GOCE), launched on 17th March 2009 have led to further improvement in gravity field models.

Dedicated gravity field missions were required because satellite missions not designed for gravity recovery (non-dedicated satellites) cannot be tracked continuously in their orbit. They can only be tracked from the Earth at short intervals (Rummel et al., 2002). The orbital heights of non-dedicated satellites also caused a problem. Dedicated gravity satellites require a low orbit to capture information at higher spherical harmonics degrees; non-dedicated satellites are generally not in low orbits. However, the orbital height of a satellite is a trade-off between the required resolution of the resulting gravity field and the technical effort of maintaining orbital height (Seeber, 2003). Satellites in lower orbits are subject to significant non-conservative forces, such as atmospheric drag and solar radiation pressure, in addition to gravity field forces.

The benefits that dedicated satellite missions have had to gravity field models can be seen through comparisons to pre-launch fields, such as EGM96S. One of the first gravity fields derived using CHAMP data was the European Improved Gravity Field Model of the Earth by New Techniques (EIGEN-1) (Reigber et al., 2003). EIGEN-1 was the first model to be created from tracking only one satellite and was based on 88 days of CHAMP data from 2000. Compared to EGM96S, EIGEN-1 was able to offer an improved spatial resolution, while offering a factor of two improvement at longer wavelengths. This improvement was a factor of 4 over the oceans (Reigber et al., 2003) as EGM96S contains long wavelength systematic oceanic errors (Pavlis et al., 2012).

One of the first GRACE only gravity field models was GRACE Gravity Model 01 (GGM01) (Tapley et al., 2003). GGM01 was based on 111 days of GRACE obtained during the commissioning phase, and is described to spherical harmonic degree and order 120. GGM01 offered a dramatic improvement over older geoid models (Tapley et al., 2003). The second version of this model, GGM02 (Tapley et al., 2005), based on 14 months of GRACE data, offered a further factor of two improvement over GGM01,with a cumulative error of less than 1 cm geoid height to spherical harmonic degree and order 70. This allowed GRACE to meet the minimum mission goals (Tapley et al., 2005). The GRACE mission can also be used to map time-variations in the Earth's gravity field.

The aim of the GOCE mission was to determine the Earth's mean gravity field to unprecedented accuracy (Bouman et al., 2014b). This is possible as GOCE offered the highest resolution capabilities of mapping the Earth's gravity field from space (Bouman et al., 2014a). While GOCE only gravity fields have been released, Bouman et al. (2014a) found that combing GOCE observations and GRACE data resulted in improvements in gravity field recovery. Bouman et al. (2014a) also showed that GOCE can be used to determine the mass change of Antarctic outlet glaciers. However, due to the short life of the GOCE mission (March 2009 to November 2013), GOCE data is not used in this project.

2.1.3 *Time variable gravity fields*

The gravity field models EGM96, EIGEN-1, GGM02 and later models are all static gravity field models that represent the mean gravity field of the Earth. However, the primary goal of the GRACE mission is to map time-variations in the Earth's gravity field at monthly intervals. This is possible due to the unique orbital configuration of GRACE. Time varying gravity fields allow the difference from the static gravity field to be calculated over short periods (e.g. monthly) and can be used to estimate, among other thing, ice mass trends (e.g. King et al., 2012, Luthcke et al., 2013, Shepherd et al., 2012, Velicogna and Wahr, 2006b), changes in water storage (e.g. Longuevergne et al., 2013) and GIA (e.g. Tregoning et al., 2009).

2.2 *Introduction to GRACE*

GRACE twin satellite mission (Tapley et al., 2004b) was launched in 2002 with the aim of mapping the Earth's time varying gravity field every ~30 days (Wahr et al., 2004) at spatial scales of hundreds of kilometres. GRACE is a joint satellite mission between

NASA and Deutsches Zentrum für Luft und Raumfahrt (DLR). The mission was launched on 17th March 2002 from Plestck, Russia and had an estimated lifespan of 5 years. The mission is still in operation at the time of writing. The GRACE project is under overall direction of the CSR at the University of Texas with the NASA JPL responsible for the development of the science instruments and DLR German Space Operation Centre (GSOC) responsible for the operation of the satellites.

GRACE consists of two satellites separated along-track by ~220 km. The satellites are in nearly identical orbits (Kim and Tapley, 2002) and are near circular at ~500 km altitude and have an inclination of 89.5°. The low height of the orbits, results in a unique sensitivity to the Earth's gravity field, but it also means that the orbits decay naturally by ~30 m/day, resulting in a ground track that does not have a fixed repeat pattern (Tapley et al., 2004b).

Although the GRACE system consists of two satellites, the satellites are independent, and are both subjected to different gravitational accelerations. However, the orbital configuration of GRACE, with one satellite following the other, results in the trailing satellite arriving at the same location as the lead satellite ~27 seconds later (Frommknecht and Schlicht, 2010). Figure 1 shows an artist's impression of the GRACE satellites in orbit.

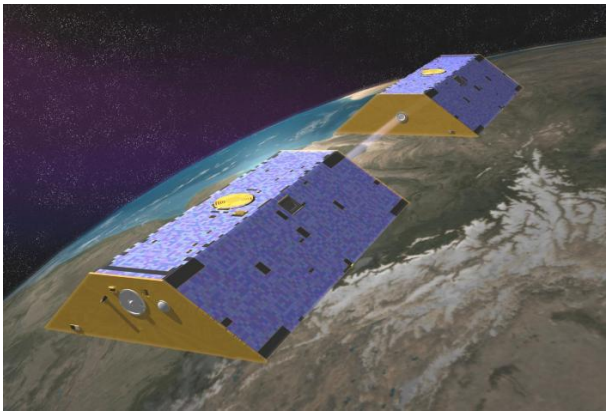

Figure 1. Artist impression of GRACE in orbit (NASA/JPL, 2002).

By measuring the changing separation of the satellites, GRACE allows us to monitor the spatial and temporal geophysical mass variations in the gravity field. To do this the GRACE satellites are equipped with a number of scientific instruments that allowed, shortly after launch, the detection of changes in mass corresponding to 1.4 cm of equivalent water height (EWH) over a radius of 750 km every 30 days (Wahr et al., 2004). Advances in the background models and processing strategies applied to the

GRACE data have since driven this uncertainty/radius downward. The success of GRACE is the result of the orbital configuration which utilises the concept of satellite to satellite tracking and the scientific instrumentation on-board the satellite.

2.3 *Satellite to Satellite Tracking*

The GRACE mission relies on satellite to satellite tracking, a concept that has been around since the 1960's. Satellite to satellite tracking involves the tracking of one satellite using other satellites. In traditional tracking methods, such as SLR and Doppler Positioning, gravity field information is inferred from the monitoring of satellite orbits. Satellite to satellite tracking allows the gravity field information to be modelled from analysis of tracking observations rather than requiring the analysis of accumulated orbital perturbations.

The concept of satellite to satellite tracking was realised in the launch of the TOPEX/Poseidon (T/P) mission in 1992 which saw, for the first time, a satellite being tracked in a high-to-low satellite configuration (Global Positioning System (GPS)-T/P) for a geodetic application (Schwintzer et al., 1995). However, it was only with the launch of the GRACE mission that the low-to-low satellite tracking, first proposed by Wolff (1969), was realised. GRACE uses both high-to-low and low-to-low satellite tracking.

2.3.1 *High-to-low satellite tracking*

High-to-low satellite tracking involves tracking a satellite in a low orbit using a satellite in a high orbit. The high-to-low configuration allows the orbital trajectory of the low satellite, which is affected by the higher frequency components of the gravity field, to be observed using a satellite in a high orbit (Seeber, 2003). GRACE utilises high-to-low satellite tracking as the GRACE satellite orbit are tracked using GPS. This multi-dimensional and continuous tracking of the GRACE satellites using GPS (Kang et al., 2003) allows the position of the satellites to be continuously and accurately determined and allows the gravity field estimates to be correctly registered to a terrestrial reference frame (Kim and Tapley, 2002). Kang et al. (2006b) were able to position the GRACE satellites with a precision of 1 cm in position, using GPS tracking data only. While offering an improvement over traditional methods, tracking a satellite to model the gravity field using GPS is limited to around 1 cm, with a better insight obtained by low-to-low satellite tracking (Frommknecht and Schlicht, 2010).

2.3.2 *Low-to-low satellite tracking*

Low-to-low satellite tracking satellites involves tracking a satellite in a low orbit using another satellite in a low orbit. In GRACE the concept of low-to-low satellite tracking utilises K-band range (KBR) measurements between the two satellites. The idea of measuring the Earth's gravity field using two satellites in identical orbits, separated by 200 km was proposed by Wolff (1969). That paper suggested that the concept of low-to-low satellite tracking was different to that of measuring the long term integrated effects on satellite orbits, as it measures the gradient of the potential field. Rowlands et al. (2002) suggested that it should be possible to estimate the gravity field from short satellite arcs, e.g. 15 minutes of data, with little difference from a gravity field estimated using longer arcs. Although the GRACE mission consists of two separate satellites, in reality the two satellites can be considered to be one instrument, due to the low-to-low satellite tracking between the two satellites.

2.4 *Scientific Instruments*

To recover the Earth's static and time-varying gravity fields the GRACE satellites are equipped with a number of on-board scientific instruments including: a K-band Ranging system; GPS receivers; accelerometers and star cameras. Figure 2 shows the internal layout of a GRACE satellite, including the locations of the different sensors. Both satellites are identical in design. Data from these instruments are available to the scientific community.

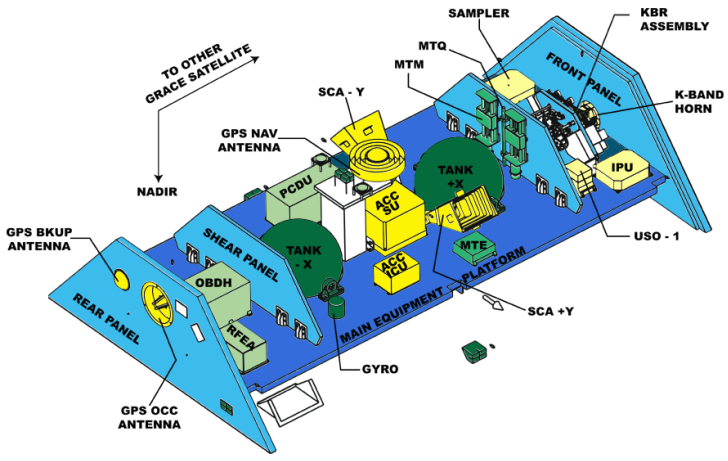

Figure 2. A view inside one of the GRACE satellites showing the different sensors and their relative locations (GFZ-Potsdam, 2001).

2.4.1 *KBR/KBRR*

In orbit the GRACE satellites experience small accelerations as they pass across contours in the gravity field, resulting from the changing strength of the field below the

satellites. These accelerations are applied to the first satellite then the second, continuously changing the distance between them (Dunn et al., 2003) with the perturbations experienced by the different satellites being out of phase. Monitoring this changing distance, through low-to-low satellite tracking, provides a unique insight into the accelerations experienced by a low Earth orbiting satellite (Rowlands et al., 2005), which in turn allows the static and time variable nature of the Earth's gravity field to be mapped.

On-board GRACE the changing distance between the two satellites is measured using the K-band range (KBR) instrument, which is the main observable of the GRACE mission. The range between the satellites K-band antenna phase centre (APC) is measured using a dual frequency K-band instrument which has an accuracy of a few microns (Dunn et al., 2003). The first time-derivative provides a K-band range rate (KBRR) measurement, which is generally used during GRACE data processing and has a precision of 0.1 μm/s (Luthcke et al., 2006b). KBRR measurements are usually provided every 5 seconds.

North-South variations in the gravity field are better sensed by GRACE than East-West variations, due to the 89.5° orbital inclination. The KBR(R) measurement mainly determines the north-south component of the Earth's gravity field. Any gravity signal that only has an east-west component could theoretically be added to the gravity field without affecting the north-south gradient and therefore not be sensed in the range rate. However, in practice this is not the case as the Earth's rotation adds the east-west component (Ditmar et al., 2011). The KBR(R) measurement, along with the GRACE laser retro reflectors and GPS receivers, can be used in the evaluation of the GRACE orbits, through measuring relative orbital accuracies. The KBR(R) Level-1B ranging data are provided in the KBR1B data product.

2.4.2 *GPS*

Global Positing System (GPS) on-board the GRACE satellites is used for positioning. Each GRACE satellite is equipped with a dual frequency, codeless, BlackJack GPS geodetic receiver that is capable of tracking up to 14 GPS satellites (Dunn et al., 2003). The receivers were developed by JPL (Kang et al., 2006a) and have a data quality that is comparable to the precision of geodetic ground receivers. Using GPS has allowed orbital accuracies to be obtained to better than 2 cm in each coordinate (Dunn et al., 2003). The positional accuracy achievable using GPS was validated by Kang et al.

(2008) whose determined the positions of the GRACE satellites to an accuracy of ~1 cm in the radial direction and better than 2.5 cm in the along-track and across-track directions using GPS data. GPS on-board the GRACE satellites will have the advantage of being unaffected by tropospheric delays (Jekeli, 1999).

GPS allows each GRACE satellite to be continuously and accurately determined in terms of position, while allowing gravity field estimates to be correctly registered to a terrestrial reference frame (Kim and Tapley, 2002, Luthcke et al., 2006a). Without the use of GPS for tracking, an extensive ground tracking network would be required to measure the velocity of GRACE. Although GPS can be used to position the GRACE satellites, obtaining the satellite velocity vectors, which are required to recover the gravitational potential, is currently beyond the capability demonstrated by GPS (Jekeli, 1999). The GRACE satellite velocity vectors are recovered using the KBR instrument. In this study the GPS observations are not used directly. Instead the satellite positions are provided in the GPS Navigation Level-1B data product (GNV1B). The GNV1B navigation solution provides the location of the satellites in their orbit.

2.4.3 *Accelerometers*

The ability to obtain highly accurate KBRR measurement depends on accurate information on the inter-satellite alignment (Helsen et al., 2008), which is affected by gravitational and the non-gravitational (non-conservative) accelerations experienced by the satellites (Kim and Tapley, 2002). Each satellite experiences different non-gravitational accelerations. To monitor these changing accelerations the GRACE satellites use three-axes accelerometers, which have accuracies of up to 10^{-10} m/s^2 (Dunn et al., 2003, Flury et al., 2008). These SuperStar accelerometers, manufactured by ONERA, measure the non-gravitational accelerations and surface forces, such as atmospheric drag and solar radiation pressure, which act on the satellites (Kim and Tapley, 2002, Riva et al., 2009). The use of accelerometers is fundamental as the surface forces that act on low Earth orbiting satellites are not currently modelled precisely enough (Van Helleputte et al., 2009) and can be highly variable (Kang et al., 2006a).

The accelerometers work by measuring the changes in the electrostatic forces that are required to keep a proof mass in the centre of a cage. The proof mass and the satellite both experience the same gravitational force but the non-gravitational forces only act on

the satellite allowing the gravitational and non-gravitational forces that effect the satellite to be separated (Van Helleputte and Visser, 2008).

Each GRACE satellite has its own accelerometer and the data is collected in the along-track, across-track and radial directions. The axes in the along-track and radial-direction is an order of magnitude more sensitive than the axis in the cross-track direction (Bezděk, 2010). The data collected by the GRACE accelerometers still needs calibration by applying a bias and a scale factor in each axis (Kang et al., 2006a). The bias is an offset and the scale factor relates to the amplitude of the measurement (Van Helleputte and Visser, 2008). The scale and bias cannot be calibrated before launch, due to the Earth's gravity field being larger than the non-gravitational measurements (Bezděk, 2010). They are therefore calculated in orbit.

Work by Kang et al. (2006a) validated the use of accelerometer data in GRACE processing. The data from the GRACE accelerometers can also be used for atmospheric density modelling and studying solar and geomagnetic storms (Bruinsma et al., 2006, Bruinsma and Forbes, 2010). Studying the atmospheric density improves models of how atmospheric drag effects satellite orbit while offering improvements in re-entry prediction and collision avoidance (Van den IJssel and Visser, 2010). The Level-1B accelerometer data is provided in the accelerometer data product (ACC1B).

2.4.4 *Star cameras*

The star cameras on-board the GRACE satellites are used to orientate the satellites in space. The star cameras have a precision of 25 arc-seconds and allow the translation of the accelerometer data from the spacecraft reference frame to the inertial reference frame (Kim and Tapley, 2002). The data provided from the star camera are available as quaternions. When no quaternions are available the data from the GRACE accelerometers cannot be used (Van Helleputte and Visser, 2008) as this will affect the KBRR measurements as the pointing direction of the KBRR system cannot be determined (Dunn et al., 2003). The Level-1B star camera data is provided in the star camera data product (SCA1B).

2.5 *GRACE data levels*

Data from the GRACE satellites are released at different levels, where each level relates to the amount of processing that has been performed on the raw satellite data. Level-0 is the first level, with each subsequent level having undergone a greater amount of processing. The choice of data level will depend on the requirements of the user.

2.5.1 *Level-0*

Level-0 data is the data that is downloaded directly from the satellite to the mission ground station raw data centre located at DLR in Neustrelitz, Germany (Bettadpur, 2012a). Level-0 data is made up of the raw satellite observations collected by the satellites scientific payload and the satellite housekeeping information. Data is downloaded on each satellite pass, with separate data provided by the two satellites. The raw satellite data goes into a rolling archive stored at JPL and GFZ (Bettadpur, 2012a).

2.5.2 *Level-1A*

Level-1A data is created by applying non-destructive, reversible, processing to Level-0 data (Watkins et al., 2000). This processing involves sensor calibration and time tagging the data with respect to the satellites receiver clock (Bettadpur, 2012a). Editing and quality control flags are also added and the data is reformatted for future processing. Level-1A data is only held by the processing centres JPL and GFZ and is not available to be general scientific community (Kim and Lee, 2009).

2.5.3 *Level-1B*

Level-1B data is created by applying irreversible processing to the Level-1A data. The processing involves applying a low pass filter and a time correction (Kim and Lee, 2009) while the sampling frequency of the scientific data is reduced from 10.034 Hz to 1 Hz (Flury et al., 2008). Level-1B data includes the ancillary data products generated during the processing and the additional data required for future processing. This is the first data level that is available to the wider scientific community. The processing from Level-0 to create Level-1B data is collectively known as Level-1 processing. Level-1B data is the data used in this thesis.

2.5.4 *Level 2*

The processing of Level-1B and the related ancillary data into Level-2 data is known as Level-2 processing. Level-2 processing is carried out at CSR, GFZ and JPL for validation (Watkins et al., 2000). The final Level-2 products released by these processing centres are monthly estimates of the Earth's gravity field, with corrections applied during processing (Flechtner, 2007). Level-2 data is available to the scientific community.

2.5.5 *Releases of GRACE data*

Several different versions of GRACE Level-1B and Level-2 data have been released to the scientific community since first becoming available. Each different release offers

improvements over the previous release. The differences between the first Level-2 data from CSR (CSR RL01) and release 4 (CSR RL04) is due to advances in the background models and processing strategies (Gunter et al., 2009) with CSR RL05 offering a further reduction in noise (Chambers and Bonin, 2012). We are currently on RL02 of the Level-1B data and RL05 of the Level-2 data.

2.6 *GRACE follow-on mission*

The success of the GRACE mission has motivated researchers into proposing a GRACE follow-on (GRACE-FO) mission. Work has been undertaken into possible satellite configurations of any such mission (eg.Wiese et al., 2009), where attempts were made to overcome limitations of the satellite configuration of the current GRACE mission. In the end it was decided that a GRACE-FO mission should be similar to GRACE, but with new technologies included alongside those utilised in GRACE as a test for future missions. The GRACE-FO mission is expected to be launched in August 2017, with the primary mission aim of providing continuity of the GRACE dataset.

With the GRACE-FO not due for launch until 2017, researchers have been investigating possible ways to bridge a gap between GRACE and the GRACE-FO on mission to try and insure the continuity of data. Weigelt et al. (2013) identified that using high-to-low satellite tracking could provide very long-wavelength gravity features at spatial scales of approximately 2000 km.

2.7 *Summary*

Since the launch of Sputnik-1 in 1957, tracking of artificial satellites from the Earth has allowed scientists to solve scientific problems, with an ‘indirect effect’ being the creation of gravity field models. The first gravity field models required the tracking of 25 satellites over 300 weekly orbits, but were limited to spherical harmonic degree and order 12. Subsequent improvements in satellite tracking allowed higher degree gravity field information to be obtained, but it was only with the launch of dedicated gravity field satellite missions that the Earth’s gravity field has been mapped to high spatial resolutions with unprecedented levels of accuracy. More recently, the launch of GRACE twin satellite mission in 2002 has allowed the Earth’s TVG field to be modelled every ~30 days over a 13 year time-period. GRACE provides a means to assess and improve geophysical models while allowing geophysical processes that are of fundamental importance to be studied.

The success of the GRACE mission is based on the unique high-to-low and low-to-low satellite tracking used during the mission. These concepts were discussed in this chapter, along with the main scientific instruments on-board the GRACE satellites, which include: a K-band Ranging system; GPS receivers; accelerometers and star cameras. An overview of these instruments was provided along with an introduction to the data products used in this thesis. Finally, the levels and release of the GRACE data were discussed. The level of data used depends on the requirements of the user, while each subsequent release of GRACE data offers improvements over the previous release. Improvements result from advances in the background models and processing strategies. Differences resulting from the level and release of GRACE data used will be discussed further in subsequent chapters of this thesis.

Chapter 3. Time-Varying Gravity

Chapter 2 provided an overview of GRACE and the associated data products. This chapter will look at the processing methodologies applied to the GRACE data to estimate time varying gravity field solutions. A detailed overview of the random noise and systematic errors inherent in the GRACE solutions will be provided, along with the methods used to mitigate for these. Different methods used to estimate mass flux trends from TVG solutions will also be discussed.

3.1 *Level-1B data to Level-2 solutions*

All GRACE time-varying gravity solutions are estimated from Level-1B data. Level-1B data are the first level of data that are available to the scientific community and includes all the data products, along with any additional data required for processing. The solutions obtained from processing Level-1B data are known as Level-2 products. Level-2 products are monthly or 10 day estimates of the TVG field on which mass flux analysis is then undertaken.

Research groups can process Level-1B data; using the resulting solutions to undertake mass flux analysis. However, due to the complex nature and computational requirement of Level-1B data processing, most researchers are reliant on pre-computed Level-2 products. These pre-computed Level-2 products are provided by the GRACE data processing centres, CSR, JPL and GFZ, although some research groups generate their own Level-2 products and make them publically available, including Centre National d'Etudes Spatiales/Space Geodesy Research Group (CNES/GRGS) (Bruinsma et al., 2010); GSFC (Luthcke et al., 2013); TU Delft (Liu et al., 2010); and TU Bonn (Kurtenbach et al., 2012).

Generating TVG solutions direct from Level-1B data has advantages over using pre-computed Level-2 products. Firstly, the group processing the Level-1B data has control over every step of the processing strategy and the choice of parameters used. Secondly, generating solutions direct from Level-1B data allows access to solution normal matrices, allowing greater control over the mitigation of random noise and systematic errors in the solution (e.g. Bruinsma et al., 2010, Save et al., 2012). Access to the variance-covariance matrix is also available. The mitigation of the random noise and systematic errors in the solution can have a significant impact on any subsequent mass flux analysis. Solution normal matrices are not typically provided as part of the Level-2 products. Random noise and systematic errors will now be discussed.

3.2 *Random noise and systematic errors in the GRACE solutions*

Random noise and systematic errors, hereafter noise, are inherent in GRACE Level-2 products. If not correctly dealt with, noise can be interpreted as real mass change (Wahr et al., 2006). In particular, noise maps into long north-south linear features (Swenson and Wahr, 2006) and need to be appropriately mitigated before any meaningful mass anomalies can be estimated. Figure 3 and Figure 4 show the spherical harmonic TVG solution for June 2006, expressed as cm of Equivalent Water Height (EWH), computed from the CSR RL05 Level-2 product. It is clear that the solution is dominated by these north-south features known as 'stripes'. In Figure 3 and Figure 4 GRACE Intermediate Field (GIF48) (Ries et al., 2011) is the mean background field (Bettadpur, 2012b).

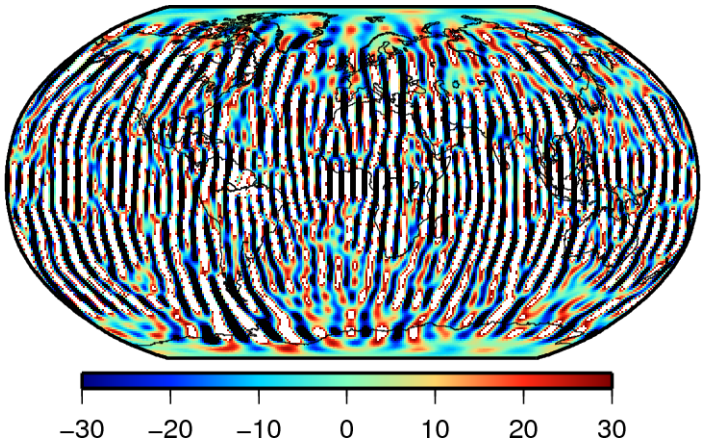

Figure 3. Plot showing the effect that noise has on a monthly GRACE solution. The solution is the CSR RL05 spherical harmonic solution for June 2006 with no mitigation for noise applied. Units cm EWH.

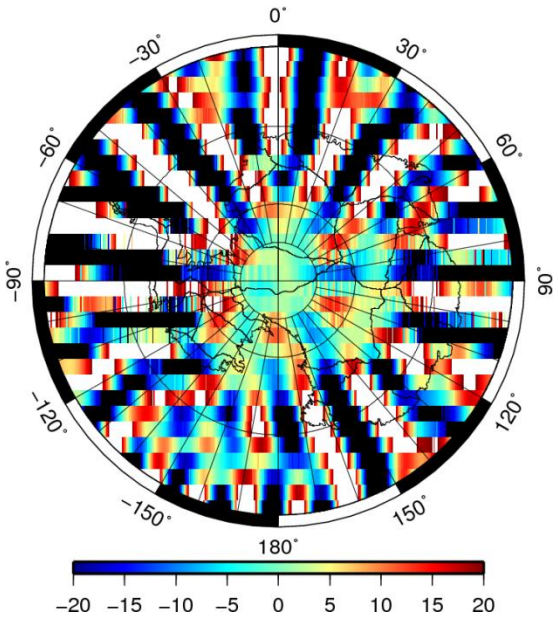

Figure 4. Plot showing the effect that noise has on a monthly GRACE solution over Antarctica. The solution is the CSR RL05 spherical harmonic solution for June 2006 with no mitigation for noise applied. Units cm EWH.

3.2.1 *Stripes*

The noise from GRACE is not white on the sphere and therefore appears as stripes in TVG solutions (Kusche et al., 2009).Stripes suggest a high degree of correlation in the GRACE noise (Swenson and Wahr, 2006). The presence of stripes in the GRACE solutions results from the orbital configuration and limited longitudinal sampling of GRACE (Klees et al., 2008a). KBRR data are only collected along the line of the orbit, meaning GRACE is more sensitive to north-south gravity variances than east-west (Ditmar et al., 2011). Noise is reduced near the poles, as seen in Figure 4, due to the high density of measurements and better sampling of the east-west component of the gravity field (Ditmar et al., 2011). Stripes are not unique to GRACE having previously been identified in altimetry data (e.g. McAdoo and Marks, 1992).

3.2.2 *Noise in the background models*

In addition to stripes, there is also noise in the TVG solutions that result from noise present in the Level-1B data and background models. Visser and Schrama (2005) identified that there were differences between the background models using during solution generation and GRACE observations. These can dominate the TVG solutions at short wavelengths (Klees et al., 2008a) with noise in geophysical models aliasing into the TVG solutions (Seo et al., 2008a). In the CSR RL04 Level-2 products, Bonin et al. (2012) found that real signal could not be separated from noise unless the signal had an

amplitude of over 5 cm. This highlights the need to appropriately treat and mitigate the noise in TVG solutions.

3.2.3 *Noise from the mean background field*

Time-varying gravity field solutions are often represented as anomalies to a mean gravity field model. During the calculation of GRACE TVG solutions, knowledge of the mean gravity field model is required to a high spatial resolution, to minimise the aliasing of noise in the TVG solution solutions (Ries et al., 2011).

There are a number of mean gravity field models available, all of which are provided in the form of spherical harmonics coefficients. One gravity field model used during the calculation of TVG solutions is GIF48. GIF48 represents the Earth's mean gravity field to spherical harmonic degree and order 360 and was released as an improved field to be used during the reprocessing of Level-1B data to create the most recent release of the CSR Level-2 products, RL05 (Bettadpur, 2012b). GIF48 combines a selection of 66 monthly CSR RL04 solutions from between 2003 and 2011 (Bettadpur, 2012b) with terrestrial gravity data from Denmark University Technical (Andersen, 2010). The inclusion of terrestrial data is required as GRACE cannot fully resolve the mean gravity field to a high spatial resolution (Ries et al., 2011). The spatial resolution of GIF48 is an improvement over pre-launch mean fields (e.g. EGM96) and early GRACE derived mean fields (e.g. EIGEN-1), with the inclusion of terrestrial data further improving the spatial resolution (Ries et al., 2011).

In addition to being used for the CSR RL05 solutions, GIF48 is used as the mean field in the JPL RL05 solutions (Watkins, 2012) and, more recently, the JPL mascon solution (Watkins et al., 2015), although limited to degree and order 180. GFZ use their own mean field, EIGEN-6C (Förste et al., 2011), up to degree and order 200 for GFZ RL05 solutions (Dahle et al., 2013). The Level-2 products generated by CNES/GRGS, which are comparable to the RL05 solutions from the official processing centres, use EIGEN-GL04C (Förste et al., 2008) as the mean field. Like GIF48, EIGEN-GL04C and EIGEN-6C both use satellite and terrestrial data and are high resolution mean gravity fields.

A comparison of the time-varying gravity solutions generated by these four groups, using different mean fields, was undertaken by Sakumura et al. (2014). Sakumura et al. (2014) found that all the solutions were able to capture similar signals, with the differences between the solutions mainly resulting from processing strategies applied by

the different groups and how noise in the data were treated. The four solutions were all highly correlated in their identification of seasonal signals, with the EWH variations of all the solutions agreeing within the GRACE error bounds. This suggests that differences in the high resolution gravity fields models used during the calculation of Level-2 products have had limited impact on signal recovery. An agreement between the CSR, JPL and GFZ RL05 solutions was also found by Chambers and Bonin (2012), who compared the solutions over the ocean. All oceanic solutions had a standard error of ~1 cm at low to mid latitudes and between 1.5 to 2 cm in polar and sub polar oceans, with more consistency and less variance than the previous RL04 solution.

Chambers and Bonin (2012) examined the difference between the RL04 and RL05 products from the three official GRACE data processing centres CSR, JPL and GFZ through comparison to an ocean model and found a reduction of between 50-60% in the residuals between RL04 and RL05 solutions. One of the reasons suggested from this reduction is the improvements in the mean gravity field used between the RL04 and RL05 products. Other improvements include advances in processing strategies. Dahle et al. (2014) also found that changes within the background models between GFZ RL04 and RL05 helped improve the time-series recovered, while reducing the noise in the solutions. The improvement between RL04 and RL05 of the Level-2 products has shown that using a high resolution mean gravity field model, such as GIF48, helps minimise the aliasing of the noise into the TVG field solutions. However, some noise will still be present. GIF48 is the mean field used in this thesis.

3.2.4 *Noise from the tidal models*

The mis-modeling of ocean tides can also alias into TVG solutions (Moore and King, 2008). Schrama et al. (2007) identified that tidal errors in CSR RL04 solutions were significantly larger than expected. Ray and Luthcke (2006) found that the amplitude of the tidal errors could be roughly around 1 cm EWH, with larger, more localised, errors over polar regions. Ray et al. (2009) compared four commonly employed global tidal models, analysing the effects that errors in the models had on GRACE solutions. They concluded that all the models had flaws in different regions, with all models requiring improvement around the poles. Tidal models have errors around the poles due to a lack of in situ observations (Schrama and Visser, 2007). Overall, in the study by Ray et al. (2009), Finite Element Solution tidal model (FES2004) (Lyard et al., 2006) performed best around the coast of Antarctica. Although the relevant solution exhibited a large error in the S2 tide off North-West Australia, an error not seen in other models (Ray et

al., 2009). More recently, Stammer et al. (2014) compared updated versions of the four commonly employed global tidal models compared by Ray et al. (2009). Stammer et al. (2014) found, like Ray et al. (2009), that all models had errors around Antarctica, with no model outperforming another, especially at higher latitudes. A comparison with GRACE data revealed that all models were imperfect at basin and sub-basin scale, although new satellite data is expected to provide a valuable addition in helping to improve tidal models in polar regions (Stammer et al., 2014). However, the quality of TVG solutions will not be significantly affected by the choice of background ocean tide model, although the flaws in the different models can become evident during mass flux analysis (Dahle et al., 2014).

3.2.5 *Noise from the AOD1B product*

Another model used during the calculation of TVG solutions is the Atmosphere and Ocean De-aliasing Level-1B (AOD1B) product (Flechtner, 2014). The AOD1B product is used as a background model during Level-1B data processing to reduce the aliasing of short term atmospheric and ocean mass variations into the TVG field solutions. Any noise in the AOD1B product could therefore alias into the TVG solutions. The AOD1B model is produced by GFZ, using an atmosphere and ocean models as input data. Bonin and Chambers (2011) found that although it removed the majority of the signal that could have otherwise aliased into the TVG solutions, RL04 of the AOD1B product did not adequately represent true sub-monthly variations in the atmosphere and oceans. This was due to noise introduced from the input models. Subsequent improvements in the background models used in the latest release of the AOD1B product, RL05, have reduced the noise that is aliased into the TVG solutions (Dahle et al., 2014).

3.2.6 *Noise in the Level-1B GRACE data*

Noise present in the sensors on-board GRACE will cause biases in the Level-1B datasets. This has potential consequences for gravity field recovery as the Level-1B data are used to calculate Level-2 TVG solutions. The GRACE sensors are all interlinked, with the data from one sensor often reliant on data collected by other sensors, along with accurate sensor offset information. In the case of the KBR(R) observation, which is the main observation of the GRACE mission, attitude data from the star camera is required to calculate the KBR APC and to rotate the accelerometer data into the inertial reference frame from the sensor reference frame (Bandikova and Flury, 2014). The star camera is one of the sensors in the GRACE attitude control system (Bandikova et al., 2012). Noise in this sensor will bias the KBR(R) observation in the Level-1B data.

Horwath et al. (2011) identified systematic errors in Level-1B KBR measurement data, induced by biases in the star camera quaternion product (SCA1B) and/or a bias in the vector product (VKB1B) that describes the KBR APC and satellite centre of mass (COM) offset. These products are required to align the two satellites KBR(R) observation as they do not normally have perfect line of sight (Case et al., 2010). Any improvement in the star camera data will improve knowledge of the satellite attitude, reducing the systematic errors in the KBR(R) observations. Horwath et al. (2011) found that, by re-calibrating the APC vector, the noise in the shorter wavelengths of the TVG solutions was reduced. Due to the noise in the official Level-1B KBR(R) data product, the KBRR observations using in the CNES/GRGS Level-2 products were derived in-house (Bruinsma et al., 2010) using the re-calibrated APC vector (Horwath et al., 2011).

Other scientific equipment are effected by noise. Flury et al. (2008) found that the accelerometers were effected by very frequent spikes, caused by the activation of the heaters on-board the GRACE satellites and the resulting current changes. However, they acknowledged that these spikes have very little effect on the gravity field solutions. Kang et al. (2006b) examined errors in the GPS receivers on-board GRACE by analysing how well the GRACE satellites could be positioned in their orbits using only the GPS. Although the accuracy of the orbits was about 1 cm in the radial direction and less than 2.5 cm in the along-track and across-track direction, Kang et al. (2006b) suggested that errors in the positioning of GRACE satellites could be reduced through improvements in the GPS orbits and background models and through better understanding of the GPS antenna offset.

During 2012, a new version of Level-1B data (RL02) was made available to the scientific community by JPL. RL02 of the Level-1B data had improvements in: GPS orbits and clock solutions; alignments and vectors; and KBR antenna phase centre offsets (Kruizinga et al., 2012). This has led to improvements in alignment between the star camera, accelerometer, and K-band ranging system (Chambers and Bonin, 2012), correcting some of the systematic errors identified by Horwath et al. (2011). RL02 of Level-1B data has improved the accuracy of the gravity field recovery (Bandikova and Flury, 2014). RL02 of the Level-1B data, along with changes in the background models, have reduced noise in the GFZ RL05 compared to GFZ RL04 solutions (Dahle et al., 2014). RL02 Level-1B data are also used in RL03 of the CNES/GRGS solution where no re-calibration for the KBR(R) observations has been required, unlike in RL02 of the CNES/GRGS solution.

However, despite these improvements noise in the Level-1B data products will still exist. Bandikova and Flury (2014) look at the improvements in the SCA1B data product between RL01 and RL02 of Level-1B data. Bandikova and Flury (2014) found the SCA1B product still contains higher noise than expected. They applied two different processing methodologies to the Level-1A star camera data to create their own quaternion product. Comparing these to the JPL product, they found the noise in the JPL product was 3-4 times higher, due to JPL's incomplete implementation of processing algorithms. Further improvements at the sensor data level could help reduce noise in GRACE down to the baseline accuracy (Bandikova and Flury, 2014) with un-calibrated sensor errors and uncertainties in the calibration parameters being two errors that could improve the gravity fields recovered (Bandikova et al., 2012).

3.3 *Processing methodologies*

In the Level-2 products provided by the GRACE data processing centres, the user is required to account for the noise, although care is required as the post processing mitigation of noise can result in signal leakage and a reduction of the spatial resolution of the GRACE solution (Bonin and Chambers, 2013). Level-2 products released by other research groups (e.g. Bruinsma et al., 2010) often account for noise during the generation of the product. Therefore, post processing mitigation of noise is not required. However, regardless of the processing strategy applied to Level-1B data and the method used to mitigate noise, the aim is to maximise the signal recovery and spatial resolution of the GRACE TVG fields while reducing leakage and the impact of noise on the solutions.

3.4 *Spherical Harmonics (Stokes') coefficients*

Level-2 Spherical harmonic fields, generated by the GRACE data processing centres (CSR, JPL and GFZ), are the most common way to represent GRACE TVG solutions. Spherical harmonic fields are normally computed directly from Level-1B KBRR and GPS data. However, it is possible to compute spherical harmonic fields using GRACE KBRR data only (Luthcke et al., 2006a).

Mathematically, the Earth's gravitational field, *V*, can be expanded into an infinite number of spherical harmonics using

$$\mathrm{V}(\phi,\lambda,r)=\frac{GM}{R}\left(\sum_{l=0}^{\infty}\sum_{m=0}^{l}\left(\frac{R}{r}\right)^{l+1}(C_{lm}\cos m\lambda+S_{lm}\sin m\lambda)P_{lm}\left(\cos\phi\right)\right) \quad (1)$$

where: ϕ, λ, r are the spherical coordinates (colatitude, longitude and radial distance); *GM* the product of Newton's gravitational constant, *G*, and the Earth's mass, *M*; R the mean radius of the Earth; P_{lm} the normalised Legendre polynomials; and C_{lm}, S_{lm} the normalised gravity field spherical harmonic coefficients of degree *l* and order *m*. The formula for normalisation are provided in Appendix A. GRACE provides TVG fields, which are the differences to the mean gravity field. The delta TVG field can be expressed by

$$\Delta \mathrm{V}(\phi, \lambda, r) = \frac{GM}{R}\left(\sum_{l=2}^{l_{\max}}\sum_{m=0}^{l}\left(\frac{R}{r}\right)^{l}(\Delta C_{lm}\cos m\lambda + \Delta S_{lm}\sin m\lambda)P_{lm}(\cos\phi)\right) \tag{2}$$

The sum over degree *l* and order *m* in Eq. (2) for GRACE is often truncated to $l_{\max}$ = 60; with the summation beginning at *l* = 2. The summation begins at *l* = 2 as degrees 0 and 1 are indeterminable from GRACE. Degree 0 relates to the total mass of the Earth, which is invariant with time. Degree 1 is excluded as GRACE is insensitive to these harmonics as the satellites orbit around the instantaneous centre of mass (Wahr et al., 1998). The $\Delta C_{2,0}$ term calculated from GRACE is also often replaced with that derived using SLR (Cheng et al., 2013). $C_{2,0}$ relates to the flattening of the Earth and results from large scale mass variations from the pole to the equator and vice versa. Following reprocessing of GRACE Level-2 products, using Level-1B RL02 data and the updated background models, there is good agreement between the $\Delta C_{2,1}$ and $\Delta S_{2,1}$ coefficients estimated from GRACE and those derived using SLR (Cheng et al., 2011) so the $\Delta C_{2,1}$ and $\Delta S_{2,1}$ coefficients estimated from GRACE can be used. There are no issues with the GRACE derived $\Delta C_{2,2}$ and $\Delta S_{2,2}$ coefficients. Wahr et al. (1998) provides the total changes in the surface spherical harmonic coefficients of the gravity potential

$$\begin{Bmatrix}\Delta\tilde{C}_{lm}\\ \Delta\tilde{S}_{lm}\end{Bmatrix} = \frac{1}{4\pi R\rho_w}\int_0^{2\pi} d\lambda \int_0^{\pi}\Delta\sigma(\phi,\lambda)P_{lm}\begin{Bmatrix}\cos m\lambda\\ \sin m\lambda\end{Bmatrix}(\cos\phi)\,d\phi \tag{3}$$

where $\Delta\sigma$ is the change in surface mass density (mass/area). The density of water, ρ_w, (1000 kg m^{-3}) is included hence $\Delta\tilde{C}_{lm}$ and $\Delta\tilde{S}_{lm}$ are dimensionless. The relationship between surface harmonics $\Delta\tilde{C}_{lm}$ and $\Delta\tilde{S}_{lm}$ and the gravity field harmonics ΔC_{lm} and ΔS_{lm} is given by Wahr et al. (1998):

$$\begin{Bmatrix} \Delta C_{lm} \\ \Delta S_{lm} \end{Bmatrix} = \frac{3\rho_w}{\rho_{ave}} \frac{1+k_l}{2l+1} \begin{Bmatrix} \Delta \tilde{C}_{lm} \\ \Delta \tilde{S}_{lm} \end{Bmatrix} \quad (4)$$

where ρ_{ave} is the average density of the Earth (5517 kg m^{-3}) and k_l the load Love number of degree l (Farrell, 1972). The gravity field delta spherical harmonic coefficients ΔC_{lm} and ΔS_{lm} are estimated in a Least Squares process, using the observed KBRR and other GRACE tracking data.

After estimation of the spherical harmonic coefficients, some form of post processing is required to mitigate for noise in the solution to allow a meaningful estimation of the TVG solutions. A number of post-processing strategies have been proposed. A simple way of dealing with noise, which increase rapidly with higher degrees, is to truncate the signal, but this reduces the spatial resolution of the gravity field solutions (Klees et al., 2008a). While the spherical harmonic up to degree ~ 20 contains most of the geophysical signal (Wouters and Schrama, 2007) the information in the higher degrees is required for basin level mass flux analysis.

3.4.1 *Gaussian smoothing*

To account for the noise in the higher spherical harmonic degrees of the solution, Wahr et al. (1998) proposed the use of spatial averaging based on a Gaussian averaging function (Gaussian smoothing). Using this methodology, Wahr et al. (1998), recovered hydrological and oceanographic signals from synthetic GRACE gravity data. This method of mitigation of the noise in the TVG solutions is probably the most common post-processing strategy applied to Level-2 products (Rowlands et al., 2010). To create the Gaussian smoother Wahr et al. (1998) modified Jekeli's Gaussian averaging function, *W*, (Jekeli, 1981) as

$$W_0 = \frac{1}{2\pi} \quad (5)$$

$$W_1 = \frac{1}{2\pi}\left[\frac{1+e^{-2b}}{1-e^{-2b}} - \frac{1}{b}\right] \quad (6)$$

$$W_{l+1} = -\frac{2l+1}{b} W_l + W_{l-1} \quad (7)$$

$$b = \frac{\ln(2)}{\left(1-\cos\left(\frac{r}{R}\right)\right)} \quad (8)$$

where l is the degree and r the averaging radius. Multiplying the original spherical harmonic coefficients of degree l by W_l provides smoothed coefficients.

A Gaussian smoother is degree-dependent and therefore an isotropic filter, applying the same smoothing to all orders within a given degree (Han et al., 2005). Increasing (decreasing) the smoothing radius reduces (increases) the noise in the solution (Swenson and Wahr, 2006). However, a larger smoothing radius, while decreasing noise, would also reduce the amplitude of geophysical signal of interest while increasing the spatial extent.

While a Gaussian smoother can be useful for an isotropic noise profile (Chen et al., 2006a), noise in the GRACE fields is not isotropic and is not the same at all degree and orders (Swenson and Wahr, 2006). Therefore, a Gaussian smoother will result in signal loss and leakage of the gravity field signal, as a larger smoothing radius is required to reduce the stripes (Wouters and Schrama, 2007). Signal can leak both in and out of an area of interest (Horwath and Dietrich, 2009). However, one advantage of a Gaussian smoother is that it can be applied to any monthly solution without modification (Klees et al., 2008a). Through a comparison with a global network of 63 GPS sites King et al. (2006) identified that the optimal smoothing radius for the Gaussian smoother, when applied to RL04 CSR Level-2 products, was 500 km. However, improvements in the monthly CSR RL05 products mean that this value is only a benchmark for future studies, with the smoothing radius expected to be lower.

3.4.2 *Non-isotropic filtering*

To address the degree-dependency of the Gaussian smoothing Swenson and Wahr (2006) proposed a method for the mitigation of noise, in the form of stripes, through analysing the spectral signal of the stripes. As estimated spherical harmonic coefficients are dependent on degree and order, degree and order smoothing is required for Level-2 products (Han et al., 2005). The presence of stripes in monthly GRACE solutions indicates that there is a high degree of spatial correlation (Swenson and Wahr, 2006) with correlations identified between degrees and orders.

Han et al. (2005) were able to mitigate for degree and order dependent noise using a non-isotropic filter. The resulting smoothed spherical harmonic coefficients had an improved correlation to geophysical models and data over coefficients filtered using a standard Gaussian smoother. Chen et al. (2006a) proposed two filters based on optimised degree variance, which maximises the variance ratio between land and ocean

boundaries and confines the signal based on this boundaries. Chen et al. (2006a) found an optimised smoother of 500 km mitigated a similar amount of noise at the higher degrees as a 1000 km Gaussian smoother. However, one problem with the Han et al. (2005) and Chen et al. (2006a) filters is that while they act spatially, they do not account for spectral correlation of the noise.

Swenson and Wahr (2006) identified that correlations exited between coefficients of certain degrees and orders, which cause the stripes in the GRACE TVG solutions. These correlations were used to create a 'de-striping' filter. The filter was able to almost half the average error (41.9 mm to 22.0 mm) compared to using a 500 km Gaussian smoother only. For a Gaussian smoother with a resolution of 500 km, ¾ of the variance of the GRACE errors was found to result from spatially correlated noise. The de-striping filter was found to be effective at mitigating north-south stripes.

Although applying de-striping, combined with the Gaussian smoother, performs well, it fails to take into account the statistical information of the spherical harmonic solution, often removing more signal than required (Klees et al., 2008a). Kusche (2007), proposed a filter using a synthetic error covariance matrix, generated from GRACE orbits, and signal covariance matrix. This filter is based on data available to all users of GRACE Level-2 products. The filter behaves close to a Gaussian smoother, while taking into account the variable data at the poles and the anisotropic noise structure. The approximate decorrelation and non-isotropic filter was able to reduce the stripes in the solution compared to a Gaussian smoother, while retaining the amplitude of the signal. However, no comparison was undertaken with the Swenson and Wahr (2006) Gaussian smoother with de-striping. In addition, it is also difficult to directly compare this filter with a Gaussian smoother due to the required tuning parameters used. One of the problems with this filter is that it builds a fully populated matrix, where all coefficients filter the other coefficients, compared to Swenson and Wahr (2006) where the coefficients are filtered based on order and parity (Kusche et al., 2009). This adds complexity to the filter, without any real advantage (Kusche et al., 2009).

Although not available to users of GRACE Level-2 products Kless et al. (2008a) developed an optimal filter that exploited the information in the signal and noise variance-covariance matrices of the GRACE solutions. The anisotropic, non-symmetric filter was found to preform significantly better than the Gaussian smoother and the Gaussian smoother with de-striping; while reducing signal leakage. However, the full

solution variance-covariance matrix is not provided as part of the Level-2 products, meaning most users do not have access to the required statistical information. Excluding the variance-covariance matrices from the solution was found to degrade the filters performance significantly. As the optimal filter relies on the full signal and noise variance-covariance matrices of the GRACE solutions and is therefore only useful to those groups generating their own solutions. Optimal filters also require *a-priori* information or noise models. Because of this many users of GRACE data use a Gaussian smoother with de-striping as a method for mitigation of the noise in the GRACE monthly solutions.

More recently Kusche et al. (2009) modified the filter proposed by Kusche (2007), simplifying to an order only convolution method (no longer a full filter matrix), similar to that of Swenson and Wahr (2006), to facilitate use in the scientific community. Three simplified non-isotropic decorrelation (DDK) filters were analysed, all with different degrees of smoothness. DDK1 has a Gaussian radius equivalent to 1,350 km with DDK2 and DDK3 equivalent to 900 km and 660 km respectively. As expected, the DDK1 was found to mitigate more of the stripes in the GFZ RL04 data, although this was at the expense of reducing the amplitude of real signal. Kusche et al. (2009) concluded, like Swenson and Wahr (2006), that the use of an anisoptric filter retains more signal, while removing more noise, than a Gaussian smoother. For the GFZ RL05 solution, the filters DDK4 and DDK5 have been created.

3.4.3 *Empirical Orthogonal Functions/ Principle component analysis*

To reduce the signal loss and leakage that results from using a Gaussian smoother, Wouters and Schrama (2007) suggested a different approach: decomposing the spherical harmonic coefficients using empirical orthogonal functions (EOF) or principle component analysis (PCA), as it is sometimes known. Rather than the using the spectral signal (e.g. Swenson and Wahr, 2006) or statistical information about the noise (e.g. Klees et al., 2008a, Kusche, 2007), EOF utilises the temporal characteristics of the noise spectrum, which has random behaviour. EOF allows geophysical signal to be isolated, while each mode is tested for noise. Chambers (2006) successfully used EOF analysis to separate the GRACE signal into a spatial pattern and a time series. EOF analysis is able to detect modes with different phases but similar frequencies in addition to modes with different frequencies (Chambers, 2006).

During EOF analysis the total variability in the dataset is split into modes, with the first few modes containing the most power, while the other modes contain noise (Wouters and Schrama, 2007). Chambers (2006) found that when combining GRACE and altimetry data to estimate sea-level variations, the first mode contained up to 76% of the variance. Schrama et al. (2007) used EOF analysis along with a Gaussian smoother to generate grids of EWH from a time-series of GRACE spherical harmonics fields from CSR RL04. Optimising the Gaussian smoother and the number of modes allowed the noise in the solutions to be supressed and 73.5% of the signal variance recovered.

Wouters and Schrama (2007) applied EOF analysis directly to a time-series of unfiltered monthly GRACE spherical harmonics fields from CSR RL04, without using a Gaussian smoother. A comparison of a monthly solution filtered using a Gaussian smoother to the same solution filtered using EOF validated the use of the EOF to mitigate for the stripes from the solutions. During a simulation, more of the signal was retained using EOF than Gaussian smoother. Signal leakage was also reduced compared with Gaussian smoothing. However, there are issues with episodic events such as earthquakes, where the signal is slightly attenuated (Wouters and Schrama, 2007). Such events are often small in amplitude and appear random and can end up being removed from filtered fields. Wouters et al. (2008) has used EOF decomposition to estimate the change mass distribution of Greenland.

3.4.4 ***Regularisation***

The post-processing methods discussed so far are applied to pre-computed GRACE Level-2 products to allow meaningful TVG solutions to be obtained. Regularisation is different. Regularisation allows noise to be mitigated during the gravity field determination, which is the ideal way to handle noise (Swenson and Wahr, 2006).

Groups that generate their own Level-2 spherical harmonic products from Level-1B data can use regularisation (e.g. Bruinsma et al., 2010). The spherical harmonic solution from CNES/GRGS uses a tailored regularisation, where an *a-priori* weight is applied when estimating the spherical harmonic coefficients above degree and order 30. The weight gradually constrains the spherical harmonic coefficients to the mean background gravity field. An individual weight is applied to the coefficients, with some coefficients constrained more than others. The weights are added to the solution normal matrix reducing the north-south streaking associated with noise. Save et al. (2012) also use a regularisation matrix, this time the weight is based on the noise characteristic in CSR

RL04 monthly solutions. A degree and order dependent regularisation matrix was added when solving the normal equations, during the generation of TVG solution. Spherical harmonic coefficients above degree and order 20 were constrained using an L-curve regularisation method. Save et al. (2012) found that regularisation was able to reduce the noise in the GRACE gravity field significantly. A full explanation of regularization can be found in Save et al. (2012).

The benefit of using regularisation is that it leads to more accurate EWH maps than filtering of precomputed solutions (Bruinsma et al., 2010). However, it is limited to those groups who generate their own solutions from Level-1B data (Kusche, 2007). The majority of users of GRACE data are reliant on the Level-2 products released by the processing centres, which still contain noise. While regularisation could be applied by the GRACE processing centres, this would remove the user's ability to apply their own strategy to mitigate noise, limiting the usefulness of the Level-2 products. Access to regularised Level-2 products is only available through groups that use regularisation to mitigate noise and then make their solutions publically available. Regularised solutions do not require further filtering.

3.4.5 *Spatial and temporal resolution of spherical harmonic TVG solutions*

The spatial and temporal resolution of the spherical harmonic TVG solutions recovered using GRACE are limited for a number of reasons (Schrama et al., 2007). Although GRACE is in a relatively low orbit for an Earth observation satellite (about 500 km above the Earth's surface) the higher degree harmonics of the Earth's gravity field (small spatial resolution) attenuate faster with increasing orbital height, resulting in increased noise in these coefficients (Save et al., 2012). For this reason the maximum degree and order of the Level-2 products are limited, which in turn limits the spatial resolution of the TVG solutions. The CSR and JPL Level-2 products are provided to degree and order 60 while the GFZ products are provided to degree and order 90, without any statistical constraints (Dahle et al., 2013).

The GRACE TVG solutions are also reliant on ground coverage. In months when GRACE has been in resonance, resulting in a decrease in ground-track density, the accuracy of the TVG fields was reduced (Klokočník et al., 2013). Periods of 3, 4 and 7 day repeat orbits also modify the noise characteristics of the GRACE solutions (Save et al., 2012). The maximum degree and order of the GFZ products is reduced to 30 during period of resonance (Dahle et al., 2013).

The CNES/GRGS Level-2 products differ from those provided by the three processing centres. The CNES/GRGS products are provided as spherical harmonic solution every 10 days, to degree and order 50. The 10 day temporal resolution is made possible due to the regularisation and the constraining of the solution to the mean background field.

3.5 *Mass concentration (Mascons)*

While the most common way to represent TVG is through spherical harmonic coefficients, mascon parameters have also been applied to the modelling of TVG, primarily at the NASA GSFC (Luthcke et al., 2008, Luthcke et al., 2006b, Rowlands et al., 2005, Rowlands et al., 2010, Sabaka et al., 2010). First applied by Muller and Sjogren (1968) to model lunar gravity variations, mascon parameters are estimated directly from Level-1B data, providing full control over the processing methodology and the mitigation of noise. The estimation of mascon parameters involves calculating a scaling factor for a set of 'delta' spherical harmonic coefficients that represent a uniform layer of surface mass over an area which can be added to the mean background field and used to represent the mass flux at certain time. Rowlands et al. (2010) showed that the only difference between any two mascon areas is these differential coefficients is the shape, size and location of the area.

Like regularisation, the mascon methodology benefits from constraint equations that are applied during the Least Squares inversion, removing the requirement of post processing. The mascon constraint matrix is applied anisotropically, while also taking into account the full noise covariance matrix (Luthcke et al., 2013), resulting in less signal loss (Rowlands et al., 2010). However, unlike regularisation, the constraint matrix can also be applied to constrain distinct geographical regions. This makes possible solutions with a spatial sampling of 4°, 2° or 1° with a 10 day temporal resolution. After deriving the mascon parameters, no further processing is required.

Recovery of local mascon parameters in short arcs from only KBRR data is made possible through the estimation of short arc baseline parameters (Rowlands et al., 2002), although GRACE accelerometer data is required to deal with non-conservative forces and the orbits are required previously to be well determined using GNV1B positioning data. The use of mascon parameters has allowed basin scale inter-annual variability to be extracted from the GRACE time series (Rowlands et al., 2010) due to the increased spatial sampling and temporal resolution of the solutions. The mascon methodology is described in greater detail in Chapter 4.

3.6 *Other Methodologies*

While TVG solutions are mainly estimated as either spherical harmonic coefficients or mascon parameters, other processing methodologies can be utilised. One such method is the use of radial basis functions, which are localised radically symmetric functions. Radial basis functions are useful at calculating a local refinement to the gravity field (Klees et al., 2008b). However, they cannot be used for global gravity field modelling and are therefore not used in this thesis. A full description of radial basis functions is provided in Witter (2009).

Another local gravity field modelling methodology is the use of spherical cap harmonics. Spherical cap harmonics are useful in polar region as, compared to global spherical harmonics, a reduced number of parameters are required to represent gravity in the local area. Again, due to the local nature of spherical cap harmonics, they will not be used in this thesis. A full description of spherical cap harmonics can be found in Ghadi (2013).

3.7 *Deriving mass flux trends*

Having derived TVG solutions from GRACE data, with some methodology applied to mitigate for noise, the solutions need to be analysed to infer estimates of mass flux.

3.7.1 *Spatial averaging kernels*

The use of a spatial averaging kernel as a means to infer mass anomalies from GRACE Level-2 products was proposed by Swenson and Wahr (2002). The method was developed as estimates of TVG from GRACE are not point measurements but a spatial average, due to the spatial resolution of GRACE. To isolate the TVG signal of a region of interest, such as an individual drainage basin, Swenson and Wahr (2002) outlined a method to create a kernel, using spherical harmonics, that described a region of interest. The kernel function then acts like a ‘mask’. By describing the shape of the region as equal to unity inside the region and zero outside the region, the kernel can be used to mask out signal outside the region of interest by consideration of the spherical harmonics of the kernel and TVG.

In addition to isolating the TVG signal, the averaging kernel also mitigates noise in the higher degrees of the GRACE solutions. This is achieved by smoothing the spherical harmonics describing the kernel through truncation. This smoothing is undertaken to improve accuracy at the expense of spatial resolution as a smoothed kernel contains less power at higher degree (Swenson and Wahr, 2002). However, the effect of smoothing

introduces leakage as the kernel function spreads outside the region of interest. This is evident as the boundary of the truncated kernel cannot represent a unit step. The observed 'Gibbs' phenomenon is the result of the truncation of the kernel function. Swenson and Wahr (2002) concluded that the smoothing method best applied to the kernel that maximise signal recovery while minimising noise and leakage was a Lagrange multiplier minimisation method.

The spatial averaging kernel approach was used by Chambers et al. (2004) in one of the first looks at global ocean mass variations from GRACE. Chambers et al. (2004) constructed an averaging kernel over the ocean, isolating the ocean signal, and was able to extract a seasonal variation of global mean water into and out of the oceans. The observed signal agreed with the signal observed using altimetry, within the error bounds of GRACE. Spatial averaging kernels have also been used, for example, by Syed et al. (2008) for the analysis of terrestrial water storage changes from GRACE, by Velicogna (2009) and Pritchard et al. (2010) for the study of ice mass trends, and by Strassberg et al. (2009) for the monitoring of ground water storage.

When studying the ice mass trend of Greenland, Velicogna (2009) used a modified kernel function to reduce measurement noise and signal leakage. Due to omission errors in describing the kernel, the amplitude of the signal was smaller than it should be and there was leakage of signal into the kernel. This was giving results that were low biased. To correct for this a correction scale factor was proposed in Velicogna and Wahr (2006a) and Velicogna and Wahr (2006b) as the averaging kernel was found to not equal unity over most of the region of interest. Using simulations, a scaling factor was calculated by applying 1 cm of mass uniformly over a kernel describing the region of interest. The correct scaling factor was found when the value of the kernel was an average of 1 cm of mass over the region of interest. However, while this returned realistic results, it did not address the problem of signal leakage. In addition, a scaling factor over a large area assumes a uniform mass anomaly. This is imprecise over Greenland, as the mass trend over a basin can be significantly different (Bonin and Chambers, 2013).

3.7.2 *Forward Modelling*

More recently forward modelling, or numerical simulation, has been applied to infer mass anomalies from GRACE Level-2 products. Numerical simulation was first used with GRACE data by Chen et al. (2006b). In a numerical simulation, a region of interest

is given an approximate mass anomaly value which is converted to spherical harmonics and processed the same as the GRACE data (e.g. the same Gaussian smoother is applied). These spherical harmonics are then compared to the spherical harmonics from the monthly GRACE TVG solutions. Based on the difference, a correction to the initial mass anomaly value is calculated. This correction is added to the original mass anomaly value, creating an enhanced value. This new value is then used as the input mass anomaly and the process is repeated, until the difference between the two sets of spherical harmonic parameters is minimised and convergence is reached. Chen et al. (2006b) used this numerical simulation method to calculate the mass trend of the Greenland Ice Sheet.

Wouters et al. (2008) used a more advanced numerical simulation and forward modelling to estimate Greenland's change mass distribution. Rather than estimating the trend for all of Greenland, Wouters et al. (2008) divided Greenland into 16 zones based on drainage basins. A mass anomaly value was assigned to each individual basin. As in Chen et al. (2006b) these mass anomaly values were converted to spherical harmonics and processed the same as the GRACE data, before being compared to the GRACE derived trend map. This process was iterated until an optimal agreement with the GRACE observations was reached. The method used by Wouters et al. (2008) can be seen as the fitting of the global GRACE solutions to regional mascons (Schrama and Wouters, 2011).

Schrama and Wouters (2011) optimised the forward modelling of Wouters et al. (2008) by varying the number of basins using a Least Squares inversion method. They found that merging several of the 16 basins used by Wouters et al. (2008), creating 13 basins, improved the recovery of the mass loss trend. Schrama and Wouters (2011) also found that using too few basins could lead to a reduction of the amplitude of the signal by up to 43%. More recently, the Wouters et al. (2008) forward modelling has been used by King et al. (2012) to estimate the ice mass change of Antarctica. Like Schrama and Wouters (2011), King et al. (2012) used sensitivity tests to validate the basin layout, as well as attempting to correct for leakage using assumptions on the spatial pattern of mass distribution within each basin.

Schrama and Wouters (2011) found that forward modelling reduces leakage compared to a kernel function. Investigating the difference between the trends obtained by Velicogna (2009) and Wouters et al. (2008) over Greenland, Schrama and Wouters

(2011) concluded that the difference was due to signal from outside of Greenland leaking into the Velicogna (2009) solutions. However, forward modelling can also introduce systematic errors into mass trends. Bonin and Chambers (2013) found that the Least Squares inversion method used by Schrama and Wouters (2011) could introduce systematic errors, when calculating the internal mass distribution of Greenland, if process noise is not used during the estimation process. Pre-determined noise is required to stabilise the solution (Bonin and Chambers, 2013). In addition, Bonin and Chambers (2013) investigated the layout of the basins over Greenland. They concluded that the choice of basin layout over Greenland can have significant and systematic effects on the trend recovered.

3.7.3 *Mascons from Level-2 data*

Mascons have also been applied to infer mass anomalies from GRACE Level-2 products by Jacob et al. (2012) and Schrama et al. (2014). However, it is important to point out that these mascons are calculated from Level-2 spherical harmonics products and differ from the mascon parameters estimated from Level-1B data. Jacob et al. (2012) describes mascons as "small, arbitrarily defined regions of the Earth". Schrama et al. (2014) describes mascons as "dishes of approximately the same size that are evenly distributed over the Earth's surface". The Level-2 mascon methodology is very similar to forward modelling.

In Jacob et al. (2012) the Earth is covered in small blocks that are on 0.5° grid. For each glacier area greater than 100 km^2, all the small blocks are joined together to form a mascon. Each mascon is described as a unit mass, uniformly distributed over the area, before being converted to spherical harmonics and filtered using a 150 km Gaussian smoother (the same smoother is applied to the spherical harmonics coefficients of the monthly Level-2 products). The spherical harmonic coefficients describing the mascons are then fit to the monthly Level-2 spherical harmonic coefficients, allowing the monthly variability of each mascon to be found. Computing this for every month creates a time-series for each mascon. All mascons in a region of interest are summed to calculate a total mass trend.

In Schrama et al. (2014) the Level-2 products are converted into EWH differences from the mean field using a Gaussian smoother. These are then used to calculate the scaling parameters that describe the mass at each mascon, where a mascon is a small dish. A number of equal size mascons cover the globe. This process is repeated for each month,

creating a time-series for each mascon. To calculate a time-series for an area of interest all the mascons are summed.

One point of interest is that a Gaussian smoother, rather than a non-isotropic or EOF's filter, is used when undertaking forward modelling or calculating mascons from Level-2 products. This is because a linear post-processing methodology is required so the spherical harmonic coefficients that describe the forward model grid or Level-2 mascon can be fit to the monthly Level-2 spherical harmonic coefficients using linear Least Squares (Bonin and Chambers, 2013). The reliance on a non-isotropic Gaussian smoother is a limitation when forward modelling or estimating mascons from Level-2 spherical harmonic data.

3.7.4 *Mascons from Level-1B data*

Unlike the mascons estimated from Level-2 data, mascons estimated directly from Level-1B data can take advantage of constraint equations that are applied during the Least Squares inversion. Using constraint equations not only removes the requirement of post processing, but it also allows anisotropic constraints to be applied that constrain distinct geographical regions.

Having calculated a scaling factor for each mascon, defined using a set of 'delta' spherical harmonic coefficients that represent a uniform layer of surface mass over an area, the methodology of Schrama et al. (2014) can then be applied to find the total mass of an area, e.g. Greenland. That is, a time-series for an area of interest is obtained through the summation all the mascons in that area. Luthcke et al. (2013) also sum all mascons within a drainage system to calculate the mass change of that system.

3.8 *Summary*

All GRACE TVG solutions are estimated from Level-1B GRACE data, regardless of the gravity field parameters being estimated (spherical harmonic or mascon). While estimating solutions directly from Level-1B data allows the user full control over every step of the processing methodology, including the mitigation of noise, Level-1B processing is computationally expensive and complex. Therefore most users of GRACE data are reliant on pre-computed Level-2 products.

Regardless of the parameter type, noise needs to be appropriately mitigated to allow meaningful mass anomaly estimates to be obtained. Noise results from the orbital configuration and limited longitudinal sampling of GRACE as well as noise in the

background models including: the background gravity field; tidal models; and AOD1B product. Noise is also present in the Level-1B data used to generate the solutions. While there have been recent improvements in the background models and a new release of Level-1B data, which reduced the errors between the RL04 and RL05 solutions from the three official GRACE data processing centres (Chambers and Bonin, 2012), noise will still be inherent in the GRACE solutions.

The strategy for mitigating noise depends on the parameter type being used to estimate the TVG. Spherical harmonic coefficients are the most common parameter type estimated and one of the first strategies proposed to mitigate for the noise was a spatial averaging based on a Gaussian smoother (Wahr et al., 1998). The advantage of a Gaussian smoother is that it can be applied to any solution without modification. However, the noise in GRACE is non-isotropic and a Gaussian smoother is an isotropic filter that is degree dependent. It therefore results in signal loss and leakage of the gravity signal. To address this, Swenson and Wahr (2006) proposed a de-striping filter that uses the spectral signal of the correlations between certain degree and orders to mitigate the stripes. More recently other methods have also been used to mitigate the noise in the GRACE solution, including: a filter based on a synthetic error covariance matrix Kusche (2007); an optimal filter based on the signal and noise variance-covariance (Klees et al., 2008a); an order only decorrelation filter (Kusche et al., 2009); and empirical orthogonal functions (Wouters and Schrama, 2007). However, despite all this a Gaussian smoother is probably the most common post-processing strategy applied to Level-2 products (Rowlands et al., 2010). While regularisation, which applies constraints to the solution normal matrix during the determination of the gravity field, is the is the ideal way to handle noise (Swenson and Wahr, 2006) and results in solutions that do not require post-processing, it is limited to group that generate their own solutions from Level-1B data.

Mascon parameters have also been applied to the estimating of TVG field solutions from Level-1B data. Like regularisation, anisotropic constraints are applied to the solution normal matrix during the determination of the gravity field solution to mitigate for noise. However, unlike regularisation the constraint matrix can be applied to constrain distinct geographical regions, resulting in less signal loss (Rowlands et al., 2010). Although some signal loss will occur through the use of mascon parameters, ~100% of the signal can be accounted for by adding together all the mascons within 600 km of the source mascon (Luthcke et al., 2013). The use of mascons has also allowed

the Earth's TVG to be modelled at a spatial and temporal resolution unachievable using conventional spherical harmonics, with 10 day temporal resolution and up to 1° spatial sampling possible. This has allowed basin scale inter-annual variability to be extracted from the GRACE time series (Rowlands et al., 2010). Therefore, in an attempt to improve the accuracy of TVG fields, they will be estimated using mascon parameters in this thesis.

Not only does the mascon methodology offer a spatial and temporal resolution unachievable using conventional spherical harmonics, having calculated the scaling for each mascon parameter, the mass flux of a drainage system can calculated by the summation of all mascons within that drainage system. This differs from the calculating of a mass flux from GRACE Level-2 products, which is reliant on a spatial averaging kernel function to infer mass anomalies. Spatial averaging kernel function has been found to be subject to leakage and signal loss, requiring a scaling factor to mitigate for. While forward modelling and Level-2 'mascons' have recently been used to estimated mass flux from Level-2 products, as these solutions are estimated using Least Squares they are reliant on a linear Gaussian smoother to mitigate for noise (Bonin and Chambers, 2013). Noise is therefore mitigated using an isotropic, degree dependent filter which is known to result in signal loss and leakage of the gravity signal.

Chapter 4. Formation of the mascon parameters

Chapter 3 provided an overview of recovering TVG solutions from Level-1B data, including the different methodologies used to process the data with a summary of how they deal with noise in the TVG solutions. In this chapter the mascon methodology will be described.

4.1 *Mascon Parameters*

The mascon parameters used in this thesis are based on the NASA GSFC methodology (Lemoine et al., 2007, Luthcke et al., 2006b, Rowlands et al., 2005). This involves calculating a scaling factor for a set of 'delta' spherical harmonic coefficients that represent a uniform layer of surface mass over an area which can be added to the mean background field to represent the mass flux at a certain time. While mascon areas represented using spherical harmonic coefficients are normally regular, they can be any shape. Rowlands et al. (2010) showed that the only difference between the differential spherical harmonic coefficients used to describe a mascon is the shape, size and location of the designated mascon.

Each separate area is formulated as a mascon defined by estimating a scale factor $H(t)$ at time t for a uniform mass, δ^m, of one unit of EWH over the mascon area,

$$\delta^m(\phi,\lambda) = R_e \rho_w \begin{Bmatrix} 1, \text{ over mascon} \\ 0, \text{ elsewhere} \end{Bmatrix} \tag{9}$$

where the mascon is centred on geodetic latitude ϕ, longitude λ; R_e is the radius of the Earth and ρ_w the density of fresh water (1000 kg/m^3). Using Eq. (9) each mascon in the grid can be expanded into spherical harmonics as

$$\delta^m(\phi,\lambda) = R_e \rho_w \sum_{l=0}^{l_{\max}} \sum_{m=0}^{l} (\Delta\tilde{C}_{lm}^{(m)} \cos m\lambda + \Delta\tilde{S}_{lm}^{(m)} \sin m\lambda) \bar{P}_{lm}(\cos\phi) \tag{10}$$

where $\Delta\tilde{C}_{lm}^{(m)}$ and $\Delta\tilde{S}_{lm}^{(m)}$ are dimensionless normalised surface harmonics and $\bar{P}_{lm}$ normalised associated Legendre polynomials. The sum over degree l and order m in Eq. (10) is usually truncated to $l_{\max}$ = 60, due to the reduced signal and increasing noise in the higher degrees (Horwath et al., 2011). A simulation was undertaken to investigate the effect of truncating the summation on signal recovery. A simulated mass was created by loading a 4° block at the equator, described from spherical harmonic degree and order 2 to 60, with 30 cm of EWH. The same block was then loaded with 30 cm of

EWH to degree and order 120, but the degree and orders 2 to 60 were removed. The effect these masses had on the KBRR observations are shown in Figure 5 where t=0 coincides with the satellite at the centre of the block; the boundary of the 4° block is plotted for reference. The block covers ~440 km in diameter in the spatial domain.

Figure 5 shows that in both cases the simulated mass modify the KBRR residuals inside and outside the source area, as also found by Rowlands et al. (2010). The largest KBRR values are observed at the boundary of the source area, with a change from positive to negative as the GRACE satellite pair move over the centre. However, the gravity signal contained in the higher degrees (61 to 120) has substantially less effect on the KBRR residuals than the gravity signal contained in the lower degrees (up to 60). Therefore, GRACE is unable to sense much of the additional signal above degree 60: a similar result was obtained by Rowlands et al. (2010). There is reduced signal in the higher degrees (Horwath et al., 2011).

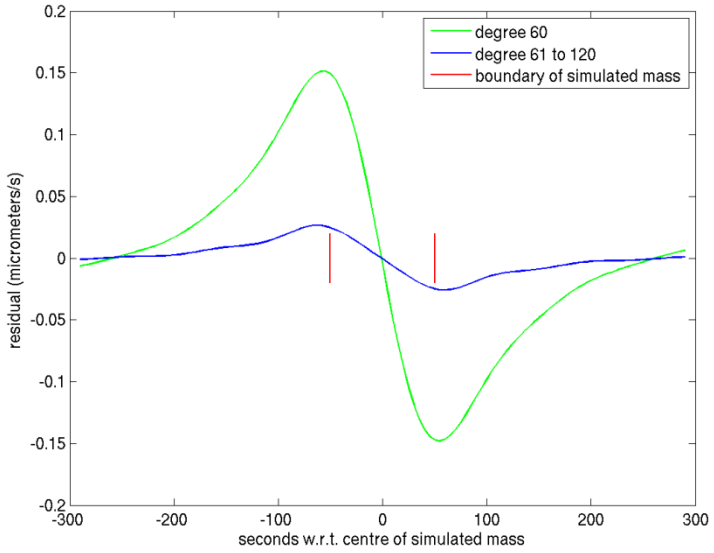

Figure 5. The residuals resulting from the 4° block loaded with 30 cm of EWH described to degree and order 60 (green) and degree and order 120, with degree and order 2 to 60 removed (blue). The boundary of the simulated mass (red) is plotted for reference.

Eq. (10) is used to modify Eq. (11) and Eq. (12) of Wahr et al. (1998) to obtain (delta) spherical harmonic gravitational coefficients, $\Delta C_{lm}^{(m)}$ and $\Delta S_{lm}^{(m)}$, that describe the required mass spread uniformly over a global set of mascons to give

$$\Delta C_{lm}^{(m)} = H(t)\frac{3p_w}{4\pi R_e \rho_{av}}\frac{1+k_l}{2l+1}\Delta\tilde{C}_{lm}^{(m)}$$
$$\Delta S_{lm}^{(m)} = H(t)\frac{3p_w}{4\pi R_e \rho_{av}}\frac{1+k_l}{2l+1}\Delta\tilde{S}_{lm}^{(m)} \qquad (11)$$

In Eq. (11), ρ_{av} is the average density of the Earth (5517kg/m^3) and k_l the load Love number of degree l (Farrell, 1972) to account for the deformation of the load on an elastic Earth. The parameter (H) is a scale factor of the spherical harmonic coefficients used to describe that mascon (Rowlands et al., 2010).

4.2 *Mascon grids*

The masons used in this thesis are global equal area mascons. Each mascon is rectangular in latitude and longitude spanning 2° or 4° in latitude with the longitude span selected to give approximately the same area as a 2° by 2° or 4° by 4° mascon located at the equator. While not strictly 2° by 2° or 4° by 4°, they are referred to as equal area for simplicity. The only exception to the equal area rule is at the poles, where polar caps of 2° in latitude are used. A 2° polar cap is used for both the 2° or 4° mascons. Due to the convergence of longitude at the poles, the number of mascons in a given latitude band will reduce poleward as seen in Figure 6 for a grid of 2° mascons over Antarctica.

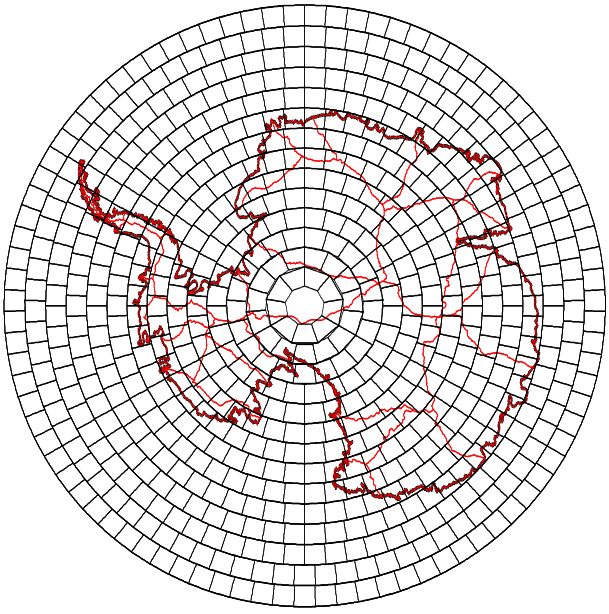

Figure 6. Distribution of 2° equal area mascons around Antarctica. Antarctic drainage basins (Zwally et al., 2012) are also shown (red).

In total there are 2564 4° or 10292 2° equal area mascons covering the globe. Each mascon is described using spherical harmonic coefficients to degree and order 60 using Eq. (10). Figure 7 shows a cross section of a 4° equal area mascon, near the equator, described using different values of $l_{\max}$. The boundary of the mascon (1 inside, zero outside), as defined in Eq. (9), is provided for reference.

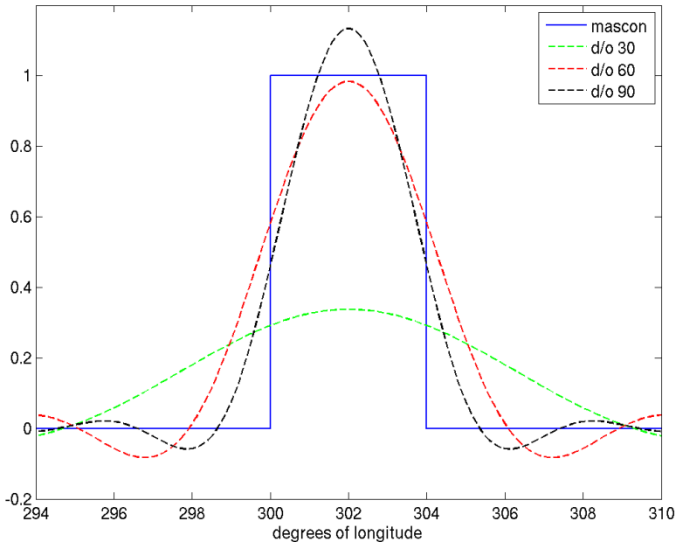

Figure 7. Cross section of the construction of a 4° equal area mascon, near the equator, using spherical harmonics. The outline of the mascon is provided in blue. The mascon is constructed using different values of l_{max} including: 30 (green), 60 (red) and 90 (black).

Figure 7 shows that the mascon shape cannot be defined exactly, using spherical harmonics, for any given value of l_{max}. For l_{max} = 30, a poor representation of the shape of the mascon is obtained. When l_{max} = 60 or 90 the shape of the mascon becomes more evident. For l_{max} = 60 the true amplitude of the mascon is reached, while for l_{max} = 90 the amplitude is greater for the reconstruction. However, for both, the shape of the mascon is not fully recovered, with a blurring of the boundary between inside and outside of the mascon. The problem of defining a mascon area using spherical harmonics is similar to the problem Swenson and Wahr, (2002) experienced when trying to represent the Missouri River Basin as an averaging kernel using spherical harmonics. The summation over degree *l* and order *m* in Eq. (10) can be truncated to l_{max} = 60 as Figure 5 showed that GRACE is unable to sense much of the additional signal above degree 60. In addition, most of the true geophysical signal is restricted to lower degrees, below degree ~20 (Wouters and Schrama, 2007). Using l_{max} = 60, the half wavelength, given in km, of the achievable spatial resolution is given by $D = 20,000 / l_{max}$ (Seeber, 2003). For GRACE, with l_{max} = 60 the half wavelength = 333.333 km.

To visualise, spatially, a mascon described to spherical harmonics degree and order 60, the mascon described in Figure 7 is plotted in Figure 8. In Figure 8, the boundary of the mascon is included for reference.

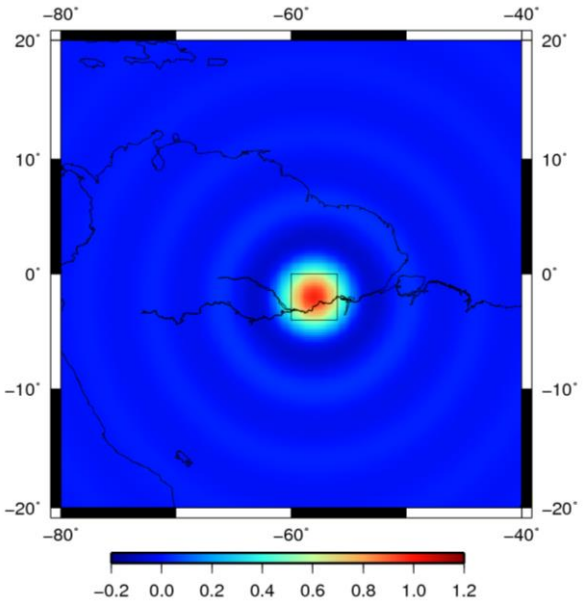

Figure 8. Mascon described to l_{max} = 60. The boundary of the mascon is included for reference. Units of cm EWH.

Figure 8 reveals that the shape of the mascon is not fully described using spherical harmonics to degree and order 60. The problem is the transition at the boundary of the mascon. There is also a rippling in Figure 8, which can also be seen in Figure 7. This is the Gibbs phenomena and is the result of the truncation and the absence of coefficients greater than l_{max} (Swenson and Wahr, 2002). The amplitude of the ripple decreases with increasing distance from the mascon.

The limitations in describing the mascon using spherical harmonics seen in Figure 7 and the resulting rippling seen in Figure 8 raises the question: will the global gravity field be recovered correctly using a set of mascons described to l_{max} = 60? As the spherical harmonics describing each mascon are global, when adding all the coefficients together, will this introduce errors into the recovered gravity field? Will the global gravity field be under/over sampled at certain locations? Ideally, if all the mascon parameters were added together they should equal unity, meaning the gravity field is being sampled correctly. To confirm this, the spherical harmonics that describe all the 4° equal area mascons were loaded with a mass of 1 cm of EWH and added together, with the result plotted up in Figure 9.

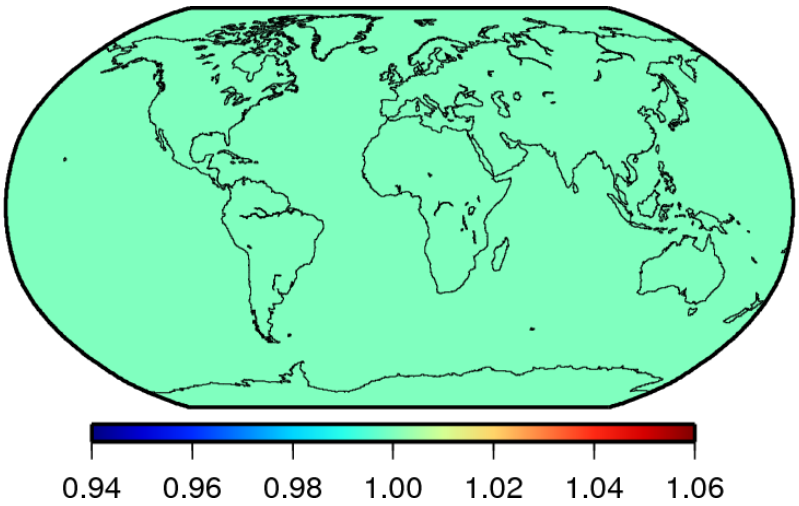

Figure 9. The spherical harmonics that describe all the 4° equal area mascons parameters, loaded with a mass of 1 cm of EWH and added together. Units of cm of EWH.

Figure 9 implies that when added together globally the mascons equal unity, meaning the global gravity field will be correctly recovered. The transition at the boundary of the mascon and the rippling in Figure 8 are not present in Figure 9, although Figure 7 and Figure 8 reveal that there will be some leakage into and out of mascons within a local area. The extent of this leakage was investigated by Luthcke et al. (2013). They found that ~100% of the signal could be accounted for by adding together all the mascons within 600 km of the source mascon. The simulations in Chapter 6 show that the mascon methodology can fully recover an input signal described to degree and order 60, despite the localised leakage at the boundary of the mascon and the rippling seen in Figure 8.

4.3 *Mascon estimation*

Having created a global grid of mascons, the mascon parameter (*H*), can now be estimated. The mascon parameters are estimated in Newcastle University's orbit determination software *Faust* (described in Chapter 5). During the orbital integration and data reduction the spherical harmonic coefficients given in Eq. (11) are used to calculate the mascon scale factor (*H*) by Least Squares, utilising the partial derivatives of the KBRR observation data (c.f. Luthcke et al., 2013), i.e.

$$A_{IJ} = \frac{\partial \Psi_I}{\partial H_J} = \sum_{l=1}^{l_{max}} \sum_{m=0}^{l} \frac{\partial \Psi_I}{\partial \Delta C_{lm}^J} \frac{\partial \Delta C_{lm}^J}{\partial H_J} + \frac{\partial \Psi_I}{\partial \Delta S_{lm}^J} \frac{\partial \Delta S_{lm}^J}{\partial H_J} \tag{12}$$

where A_{IJ} are elements of the design matrix, $\partial\Psi_I / \partial H_J$ the partial derivative of the KBRR observation *i* with respect to the mascon parameter *j*, $\partial\Psi_I / \partial\Delta C^J_{lm}$ and $\partial\Psi_I / \partial\Delta S^J_{lm}$ partial derivatives of the KBRR observations with respect to the delta gravitational coefficients while $\partial\Delta C^J_{lm} / \partial H_J$ and $\partial\Delta S^J_{lm} / \partial H_J$ are partial derivatives of the delta gravitational coefficients with respect to the mascon parameter *j*. Let $\underline{\hat{x}}$ be the Least Squares solution to the KBRR linearized observation equations $A\underline{x} - \underline{b} - \underline{v}_1 = \underline{0}$ with observation Gaussian error $\underline{v}_1$. The solution vector $\underline{\hat{x}}$ includes GRACE orbital parameters and either mascon parameters, H, or corrections ΔH to mascons parameters, H_k, at the k^{th} stage of an iterative procedure (c.f. Sabaka et al., 2010). The vector $\underline{b}$ is formed from the KBRR calculated minus observed residuals. No empirical parameters are estimated, as they could absorb part of the gravity signal, especially when the signal is relatively large (Zhao et al., 2011). A full description of Least Squares and the derivation of the partials is provided in Appendix A.

The mascon parameters are estimated in continuous satellite arcs up to 24 hours in length. However, due to the limited ground coverage of these arcs, one arc is not enough to sample the Earth's TVG. TVG fields are provided with monthly or 10 day temporal resolutions; this requires a number of arcs. Therefore, in this thesis, the normal equations for the individual arcs are combined to create either monthly or 10 day mascon solutions. The choice of arc length used during the estimation of the mascon parameters is examined in Chapter 5.

4.4 *Mascon constraints*

On combining all the normal equations, constraint equations can be applied during the calculation of TVG fields, to reduce the impact of noise in the solutions. Using constraint equations during the Least Squares inversion takes into account the full noise covariance matrix and removes the requirement of post processing (Luthcke et al., 2013). The mascon constraint can therefore be thought of as anisotropic, similar to the optimised filter of Kusche (2007).

Spatial and temporal constraints are imposed on the mascons through pseudo-observations $C\underline{x} - \underline{q} - \underline{v}_2 = \underline{0}$, where $\underline{q}$ is a constant vector incorporating both non-zero constraints and, if the procedure is iterative, the component $-CH_k$. The solution, $\underline{\hat{x}}$ is now obtained from

$$(A^T WA + C^T VC)\underline{\hat{x}} = A^T W\underline{b} + C^T V\underline{q} \quad (13)$$

where *W* is the observation weight matrix (derived from $\underline{v}_1$) and V the pseudo-observations weight matrix. The matrix, *C*, incorporates the mascon spatial and/or temporal constraints. For mascons, J_1, J_2, the pseudo-observations can be written as

$$H_{J_1} - H_{J_2} = 0, \quad (14)$$

where $J_1 \neq J_2;\ J_1, J_2 \in A_k$, the k^{th} mascon region, and zero otherwise. Eq. (14) is equal to zero as mascons close in space and time are expected to be close to each other in value.

The number of spatial constraint equations is related to the number of mascons by the equation $(J^2 - J)/2$, where each mascon is constrained to all the other mascons. There are 3,285,766 spatial constraint equations for the 4° equal area mascon solution. For the 2° equal area mascon solution there are 52,957,486 spatial constraints. An example set of constraint equations for a solution where $J = 5$ is shown in Table 1 for a total of 10 constraint equations.

Constraint No	J_1	J_2	J_3	J_4	J_5	**Mascon Pair**
1	1	-1				$J_1 - J_2$
2	1		-1			$J_1 - J_3$
3	1			-1		$J_1 - J_4$
4	1				-1	$J_2 - J_5$
5		1	-1			$J_2 - J_3$
6		1		-1		$J_2 - J_4$
7		1			-1	$J_2 - J_5$
8			1	-1		$J_3 - J_4$
9			1		-1	$J_3 - J_4$
10				1	-1	$J_4 - J_5$

Table 1. Example constraint equation for a grid of 5 mascons. The central block shows the layout of matrix C in Eq. (13).

The matrix, *C*, in Eq. (13) has the size *n x m*, where *n* is the number of constraint equations and *m* is the number of mascons. The constraint equations are weighted as described in section 4.4.1 or 4.4.2

4.4.1 *10 day weight matrix*

For a 10 day mascon solution the weight matrix, *V*, utilises the following constraints between the mascon parameters,

$$V_{IJ} = S \times e^{(2 - \frac{d_{IJ}}{D} - \frac{t_{IJ}}{T})} \quad (15)$$

where d_{IJ} is the distance in kilometres between the mascons, D the correlation distance, t_{IJ} the time difference in days between the solutions, T the correlation time and S a scale factor. Eq. (15), first described in Rowlands et al. (2005), acts to constrain mascon pairs that are close in both time and space when calculating 10 day mascon solutions. As the distance (in time and space) between the mascons increases, the constraint between the mascons weakens.

In Eq. (15), the scale factor is required to ensure that the constraints are in proportion to the normal matrices. Setting the constraint too small will not substantially reduce the noise in the solution, while adding a large constraint will over-smooth the signal and remove both noise and geophysical signal (Klosko et al., 2009). The value used for S is determined using simulations as described in Chapter 6. A value of $S = 0.001$ was used by Lemoine et al. (2007) and Rowlands et al. (2010). However, the choice of S is dependent on the values chosen for other parameters in Eq. (15) as the weight matrix V is affected by the values assigned to D and T. The same scale factor is used for all constraints in the V matrix.

Rowlands et al. (2005) first showed that it was possible to generate mascon solutions with a 10 day spatial resolution using Eq. (15). As in the mascon solutions of Lemoine et al. (2007), Luthcke et al. (2008), Rowlands et al. (2010) and Luthcke et al. (2013) a correlation time of $T = 10$ days will be used in Eq. (15), where T is in days. However, a '10 day' mascon solution actually contains more than 10 days of data. While the solution is concentrated on a 10 day period, additional days either side are required to increase the spatial sampling of the gravity field. Figure 10 shows how the temporal part of the weight $e^{(1 - \frac{t_{IJ}}{T})}$, from Eq. (15), weights the data that could be included in a 10 day mascon solution.

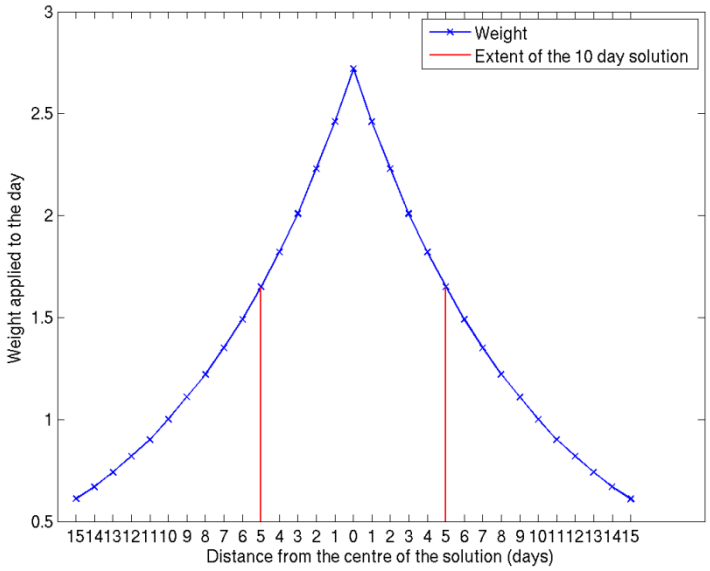

Figure 10. Weight of the temporal constraint as a function of days from the centre of the 10 day solution. The extent of the 10 day solution is provided for reference.

Figure 10 shows the weight of the temporal constraint as a function of days from the centre of the 10 day solution. The extent of the 10 day solution is shown (red line). Figure 10 reveals that the maximum weight is applied at the centre of the 10 day period, with the weight applied to a day decreasing with an increase in time from the centre day. This means that only a finite number of days are required as with an increase in the time constraint, the weight tends to zero. The temporal constraint also applies a greater weight to the days at the centre of the 10 day solutions, than those at the extremes. At 15 days either side of the centre day the weight is ~0.5, compared to ~2.7 at the centre and ~1.6 at the extent of the 10 day period. Using this result, 10 additional days of data will be used either side of the 10 days of the solution period. This will allow for improved spatial sampling of the gravity field. The use of the correlation time, *T*, in the 10 day mascon solutions means that a 10 day solution will be generated from 30 days of data.

4.4.2 *Monthly weight matrix*

No temporal constraint is required for average monthly mascon solutions (Rowlands et al., 2010), leading to a modified version of the weight matrix (Eq. 15), namely

$$V_{IJ} = S \times e^{(1 - \frac{d_{IJ}}{D})} \tag{16}$$

The modified weight matrix now only constrains mascons in space. Unlike 10 day solutions, all the arcs in the monthly solutions are weighted the same. In Eq. (16) the choice of *S* is only dependent on the value of the correlation distance, *D*, with the

weight matrix V affected by S and D. Again, the same scale factor is used for all constraints in the V matrix. Figure 11 is a plot of the spatial part of the weight $e^{(1-\frac{d_{IJ}}{D})}$. Eq. (16), is applied between mascons i and j, depending on the spatial distance between the mascons.

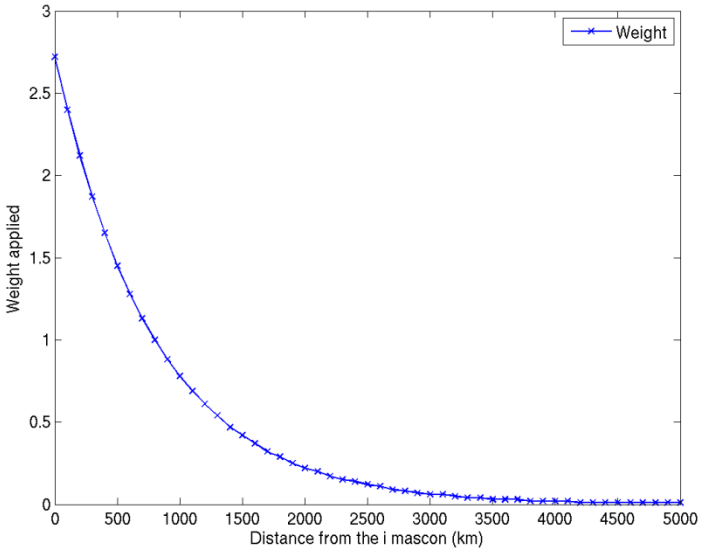

Figure 11. Weight of the spatial constraint as a function of distance from the i^{th} mascon.

Figure 11 shows how the weight decreases and tends to zero with increasing distance. This will constrain mascons together that are close spatially. In Figure 11 a correlation distance of D=800 km is used. The value used for the correlation distance, D, is discussed in Chapter 6.

4.4.3 *Degree 0 and 1 constraints*

In addition to spatial and temporal constraint, pseudo-observations are applied to ensure total mass is conserved (equivalent to a degree 0 term) and that the degree 1 harmonics for surface mass are always equal to zero; GRACE is insensitive to degree 1 harmonics as the satellites orbit around the instantaneous centre of mass. The inclusion of background models during the orbital integration could result in non-zero degree 1 terms as well as mass not being conserved in the solution vector without the use of pseudo-observations. Similarly individual geophysical models do not conserve mass and may give non-zero degree 0 coefficients (Wahr et al., 1998). The degree 0 and 1 pseudo-observations are prescribed a high weight in V to ensure the solution essentially satisfies these conditions. The four constraint equations for degrees l=0, 1 and order m=0,1 are of the form

$$\sum_J H_J \Delta C_{l,m}^{(J)} = \begin{Bmatrix} -\Delta C_{l,m}^{(atmos)} - \Delta C_{l,m}^{(ocean)} \\ 0 \end{Bmatrix} \quad (17)$$

if l,m=0,1 are used in the computations, where the summation is over all mascons and $\Delta C_{l,m}^{(atmos)}$ and $\Delta C_{l,m}^{(ocean)}$ are the harmonics from the GRACE dealiasing product for the ocean and atmosphere. By stipulating Eq. (17), the total contribution due to the mascons for the degree 0 and 1 harmonics will offset the *a priori* mass of the ocean and atmosphere if used in the GRACE computations, giving zero values for these harmonics at all times.

4.4.4 *Constraints between mascon pairs*

The constraint equations in Eq. (15) and Eq. (16) are applied between all pairs of mason parameters, although use of the correlation distance, D, implies that mascons spatially far apart have a constraint of ~zero. The uniqueness of the mascon methodology is that is allows mascons to be constrained based on similar geographical or geophysical properties. For example, a constraint can be applied between a mascon pair when both mascons are over the ocean. Similarly, a constraint can be applied between a land pair. However, when one of the mascon pair is over the ocean and the other over the land the constraint can be set to zero. This decouples what is happening over ocean with that over land.

Similarly, mascons over the land can be further constrained into basins based on geographical properties. An example is hydrology drainage basins. Mascons assigned to a basin can be constrained using either Eq. (15) or Eq. (16). However, if land mascons are in separate basins, the constraint can be set to zero. This decouples, to some extent, mass changes in one basin from its neighbour. However, the spatial constraint in Eq. (15) and Eq. (16) and the temporal constraint in Eq. (16) will act to constrain all mascons in space and time that are within the same basin. The constraint matrix can be easily modified to allow different constraints between pairs of mascon. Simulations using different constraints are included in Chapter 6 to investigate what effect different constraints, and their weights, have on the solutions.

4.5 *Summary*

In this chapter mascon parameters were described, along with how they are estimated during orbital determination. As mascon parameters are truncated to spherical harmonic degree and order 60, due to the reduced signal and increasing noise at higher degrees, the effect of this truncation on signal recovery was investigated using simulations. It was found that GRACE was unable to sense much of the additional signal contained in

higher degrees (61 to 120) and that, although the shape of a mascon cannot be defined exactly to degree and order 60, leakage is spatially limited.

The constraints applied during the 10 day and monthly mascon solutions also were investigated. To mitigate for noise in the mascon solutions, each mascon can be constrained spatially and temporally. These constraints are imposed during the Least Squares inversion. The weight of the temporal constraint, used for the 10 day solution only, was investigated and was found to decrease with an increase in the time from the centre day. This would allow for a 10 day solution to be generated from 30 days of data, with the additional 10 days either side of the 10 day solution period used to improve the sampling of the gravity field. The spatial constraint, used in both solutions, weights mascons based on the spatial distance between them. It was found to decrease with increasing distance, constraining mascons close spatially. The requirement for degree 0 and 1 constraints was also discussed. The inclusion of background models during the orbital integration will result in non-zero degree 0 and 1 terms as individual geophysical models do not conserve mass and will result in non-zero degree 1 terms.

Finally, the use of constraints between mascon pairs was introduced. The uniqueness of the mascon solution over all other GRACE processing methodologies is that mascon pairs can be constrained based on similar geographical and geophysical properties. This allows the mass changes in one mascon to be decoupled, to some extent, from its neighbour. The constraint matrix can be easily modified to allow different constraints between pairs of mascons, allowing the mascon solution to be optimised for signal recovery.

Chapter 5. Data Processing

This chapter will provide a brief overview of Newcastle University's orbit determination software *Faust*, including the background models used. Following this the two processing steps that are required to compute gravity field solutions from Level-1B GRACE data will be described, with an explanation and validation of the choice of parameters used during the processing.

5.1 *Faust*

The GRACE data processing uses Newcastle University's orbit determination software *Faust* (Moore et al., 1999). The name *Faust* is based on Heinrich Faust, the doctor in Goethe's play Faust, who is said to have sold his soul to Satan for eternal youth. The rumour goes that Goethe was wary of analytical science and based his play on the mathematician Gauss, changing the first and the last letters of his name by one letter to arrive at Faust. Naming the software *Faust* is both a tribute to Gauss and that fact that the software evolved from its predecessor SATAN (Sinclair and Appleby, 1986). The initial development of *Faust* is recorded in Boomkamp (1998), which acts as a reference document for users.

Faust uses dynamic orbit determination, which requires precise models of the forces acting on the satellite, solving for parameters of interest using Least Squares. The parametrisation of the mascons was described in Chapter 4. *Faust* has the capability to determine the orbits of multiple satellites simultaneously, making it suitable for the processing of GRACE data. The process of dynamic orbit determination involves the evaluation of force models to calculate the orbit of the GRACE satellites. The numerical integration of the satellite orbits is undertaken using an 8^{th} order Gauss-Jackson algorithm. The on-board GPS provides the observed position of the GRACE satellites, with the K-band range observation providing a measure of the separation of the two satellites. The residual difference between the observed and computed satellite orbits are the result of un-modelled forces acting on the satellites, mis-modelling in the force models and errors in the observations.

Any background model of the Earth's gravitational field can be used in *Faust*. During orbit determination, the omission of time-variability caused by atmospheric and oceanic mass variations, the cryosphere and global hydrology, from the background gravity field models will result in residual observations (difference between the observed and computed orbits of the satellite) that contain the effect of the temporal variability. The

residuals can then be used to model the spatial distribution of the anomalous gravity signal. The force models used in *Faust* are provided in Table 2. As the non-gravitational surfaces forces, such as atmospheric drag and solar radiation pressure, acting on a low orbiting satellite can be highly variable (Kang et al., 2006a) and are not modelled precisely enough (Van Helleputte et al., 2009) the effect of these forces on the GRACE satellite orbits are measured using on-board accelerometers.

Force Models	
Geopotential	GIF48 (Ries et al., 2011) Degree and order: 120 Time dependent coefficients: C_{20}, C_{21}, S_{21} References epoch: 01/01/07
Solid Earth Tides	Solid Earth Tides: IERS Conventions (2010) Solid Earth pole tide: IERS Conventions (2010)
Ocean Tides	FES2004 (Lyard et al., 2006) Degree and order: 80 Ocean pole tide: IERS Conventions (2010)
Third-body attraction	Bodies: Sun, Moon, Venus, Jupiter, Mars, Mercury Ephemeris: JPL DE403 (Standish et al., 1995)
Ocean and Atmosphere De-aliasing	AOD1B (Flechtner, 2014) Degree and order: 100 Time step: 6 h
Numerical integration	
Integrator	Gauss-Jackson 8^{th} order
Step size	5 s

Table 2. The background gravity field model and time variability included in the numerical integration of the satellite orbits in *Faust*. Data and standard for Earth rotation and reference frames as per the International Earth Rotation Service (IERS) Conventions (2010) (Petit and Luzum, 2010).

The main gravity field signals that are not evaluated as part of the force model include, among others, hydrology, GIA and the mass change signal from global ice sheets including Antarctica and Greenland. These signals are excluded as the relevant geophysical models are currently not sufficiently accurate, whilst calculating the temporal variations in these signals is one of the main objectives of the GRACE mission.

During GRACE data processing, the Ocean and Atmosphere De-aliasing product AOD1B (Flechtner, 2014) is added to the mean background field to avoid short term aliasing of ocean and atmospheric mass variations (Dahle et al., 2014). The AOD1B product is generated at GFZ and is provided every 6 hours. The current release of the AOD1B product is RL05. A flow chart showing how Faust is used in this thesis is provided in Appendix B.

5.2 *Accelerometer bias values*

The calculation of gravity field solutions from Level-1B GRACE data in *Faust* is undertaken using a two stage processing strategy. The first stage provides the accelerometer bias values for the short-arc gravity field recovery in the second stage. The choice of arc length used for the gravity recovery will be discussed in section 5.3.3. Regardless of the gravity field parameters being estimated (mascon or spherical harmonic), the underlying processing is the same for the two methodologies to the extent that any differences in the solution will be directly due to the parameterisation (Rowlands et al., 2010) and how noise and errors propagate within the different solutions. Throughout this study the same accelerometer bias values, state vectors and arcs are included in the mascon or spherical harmonic gravity field solutions calculated using *Faust.*

The GRACE accelerometer bias values have to be calculated in-situ, while the satellites are in orbit, as the Earth's gravity field at the surface of the Earth is larger than the non-gravitational forces the accelerometers are measuring, therefore the bias values could not be obtained before launch (Bezděk, 2010). Each GRACE satellite has an accelerometer, each of which has three bias values; namely in the along-track, across-track and radial directions. The bias values, along with accelerometer scale factors, are required to correct the level 1B accelerometer observation using

$$ob_{new} = bias + scale \times ob_{level-1B} \tag{18}$$

with the bias values applying an offset to correct the raw accelerometer observations (Van Helleputte and Visser, 2008).The accelerometer bias values are estimated during simultaneous reduction of KBRR, GNV1B and accelerometer data. Using KBRR and GNV1B data helps isolate the true accelerometer error (Luthcke et al., 2006a).

5.2.1 *A-priori bias values*

Daily *a-priori* values are calculated using

$$bias = c_0 + c_1(T_d - T_0) + c_2 \left(T_d - T_0\right)^2 \tag{19}$$

provided by Bettadpur (2009) in a technical note, released as part of the official GRACE documentation. In Eq. (19), T_d is the modified Julian day at day *d* and T_0 the modified Julian day of the reference epoch. The values c_0, c_1 and c_2 are provided in

Bettadpur (2009) and are a function of the modified Julian date for which the *a-priori* bias value is being calculated. Table 3 and 4 contain the values for c_0, c_1 and c_2 for dates before March 7th 2003 ($T_0 = 52532$) and after March 7th 2003 ($T_0 = 53736$) respectively. Eq. (19) can describe daily variability in the accelerometer bias values to a few percent (Bettadpur, 2009). A separate value for c_0, c_1 and c_2 is provided for each satellite and in the X, Y, Z direction of the GRACE science reference frame (SRF). In the SRF X is the along-track axis that points towards the other satellite, Y is the across-track axis and Z is the radial axis (Case et al., 2010).

Direction (SRF)	**c_0**	**c_1**	**c_2**	**Residual**
Grace-A X	-1.106	2.233E-4	2.5E-7	0.003
Grace-A Y	27.042	4.46E-3	1.1E-6	0.053
Grace-A Z	-0.5486	-1.139E-6	1.7E-7	0.019
Grace-B X	-0.5647	-7.788E-5	2.4E-7	0.002
Grace-B Y	7.5101	7.495E-3	-9.6E-6	0.080
Grace-B Z	-0.8602	1.399E-4	2.5E-7	0.020

Table 3. The values of c_0, c_1 and c_2 for dates before March 7th 2003 ($T_0 = 52532$). Taken from Bettadpur (2009). Units μ / s^2.

Direction (SRF)	**c_0**	**c_1**	**c_2**	**Residual**
Grace-A X	-1.2095	-4.128E-5	9.7E-9	0.002
Grace-A Y	29.3370	6.515E-4	-3.9E-7	0.056
Grace-A Z	-0.5606	-2.352E-6	3.8E-9	0.020
Grace-B X	-0.6049	-1.982E-5	3.5E-9	0.002
Grace-B Y	10.6860	1.159E-3	-4.3E-7	0.076
Grace-B Z	-0.7901	4.783E-5	-6.5E-9	0.020

Table 4. The values of c_0, c_1 and c_2 for dates after March 7th 2003 ($T_0 = 53736$).Taken from Bettadpur (2009). Units μ / s^2.

It is expected that the final accelerometer bias values will differ from the *a-priori* values and this will vary depending on the method of analysis (Bettadpur, 2009).

5.2.2 *Scale factors*

In addition to bias values, Eq. (18) requires scale factors to adjust the amplitudes of the raw accelerometer observations (Van Helleputte and Visser, 2008). Recommended values for these scale factors are also provided in Bettadpur (2009). These values are recommended such that the formula used for estimating the accelerometer *a-priori* biases values (c.f. Eq. (19)) are evaluated using these accelerometer scale factor. There is no reason why the scale factors should be significantly different to 1.0 (Bettadpur,

2009). However, as with the bias values, it is the accuracy of the scale factor, and not the absolute value that is important (Kim, 2000). Bias errors are expected to be smaller for satellites in lower orbits (Visser et al., 2013).The values used for the scale factors are provided in Table 5, along with their uncertainty. The same scale factors are used for every arc within the GRACE time series and held fixed as scale factors for the GRACE accelerometers are approximately constant over time (Bezděk, 2010). Van Helleputte et al. (2009) also found a strong anti-correlation between the scale factors and bias values, aliasing the on-board accelerometer parameterisation if both the bias values and scale factors are estimated simultaneously. The same accelerometer bias and scale values are used regardless of the gravity field parameters being estimated (mascon or spherical harmonic).

Direction (SRF)	**GRACE-A**	**GRACE-B**	**Uncertainty**
X	0.9595	0.9465	±0.002
Y	0.9797	0.9842	±0.02
Z	0.9485	0.9303	±0.02

Table 5. Accelerometer scale factors as provided in Bettadpur (2009).

5.2.3 *Arc length*

The estimation of the accelerometer bias values requires simultaneous reduction of KBRR, GNV1B and accelerometer data in 24 hour arcs, starting at midnight. Arcs of 24 hours are used for several reasons. Firstly, using arcs of 24 hours in length is standard in the literature when estimating the accelerometer bias values (e.g. Bruinsma et al., 2010, Luthcke et al., 2006a, Rowlands et al., 2010) as 24 hour solutions are convenient given that GRACE data is supplied in daily batches. Bettadpur (2009) also states that bias estimates are determined once per day in the orbit determination process (i.e. every 24 hours), while Tapley et al. (2005) estimates the accelerometer bias values daily. Tapley et al. (2005) and Watkins et al. (2015) note that daily accelerometer bias values are able to accommodate the expected bias variability over a month.

However, there are days where 24 hours of GRACE data will not be available to estimate the accelerometer bias values due to missing data. Missing data is generally due to instrument issues and, later in the mission, battery management. Therefore, to accurately determine the daily accelerometer bias values, a minimum amount of data will be required. Although no minimum data requirement is stipulated in the literature or official GRACE documentation, in this study the minimum amount of data required for each 24 hours period was set as 6 hours. If less than 6 hours of data is available over a 24 hour period, no accelerometer bias values will be calculated and that day will be

excluded from the gravity field recovery. A minimum of 6 hours of data was chosen for several reasons. Firstly, this minimum was used by Bruinsma et al. (2010) when undertaking the CNES/GRGS GRACE Level-1B processing. Secondly, during analysis of accelerometer bias values 6 hours of data in *Faust* was found to be sufficient to obtain a daily estimate. The risk of incorrect bias values being calculated and used in gravity field processing is lessened as incorrect bias values are identified in section 5.2.5.

5.2.4 *Empirical parameters*

To allow the accelerometer bias values to be correctly determined, empirical parameters are estimated alongside the bias values and satellite state vector in 24 hour (daily) arcs. These empirical parameters are required to account for small un-modelled forces during the orbit determination (Montenbruck and Gill, 2005), that could otherwise corrupt the calculated accelerometer bias values. Empirical parameters are only estimated during stage 1 of gravity field recovery but not during stage 2 as the empirical parameters would absorb gravity signal.

The choice and combinations of the empirical parameters varies between different processing groups. Some groups use force field empirical parameters, such as once per revolution (OPR) along-track and cross-track accelerations, which apply to the force field, while other groups use cycle per revolution (CPR) parameters, to correct the KBRR measurements. In practice, the combination of empirical parameters that is optimal for each group will relate to the orbital determination software used by that group and how they process the GRACE data. In generating the CNES GRACE solutions Bruinsma et al. (2010) estimate a bias, a bias-rate as well as a 1-, 2-, 3- CPR corrections to the KBRR measurement every orbital revolution of the satellite (~90 minutes). When calculating the Earth gravity model EIGEN-GRACE02S Reigber et al. (2005) estimated a bias and drift (every 90 minutes) and periodic parameters (every 180 minutes) in the KBRR measurement. At NASA GSFC the accelerometer bias, used by Luthcke at al. (2006a) and Rowlands et al. (2010), are calculated using a 1 CPR KBRR measurement parameter every 3 hours, while Tapley et al. (2004a) estimate a KBRR bias and drift (every ~30 minutes) in addition to a 1CPR KBRR measurement parameter (every 90 minutes).

To identify an appropriate set of empirical parameters to use during the calculation of the accelerometer bias values in *Faust*, a number of different sets were tested, with the

correct accelerometer bias expected to result in improvements in residual fit to both the KBRR and GNV1B datasets (Luthcke et al., 2006a). With the accelerometer bias values not expected to exhibit large day-to-day variations (Tapley et al., 2005) and with changes in the bias values occurring relatively slowly on the GRACE accelerometers (Visser et al., 2013) the assumption is made that the time-series that generates the smallest standard deviations will indicate the most appropriate combination of empirical parameters. Table 6 is a list of different sets of empirical parameters that were tested and used to estimate the accelerometer bias values for 5 months of GRACE solutions from May to October 2006.

Test number	**Empirical parameters**
1	OPR every 60 minutes
2	OPR every 30 minutes
3	OPR every 20 minutes
4	OPR every 15 minutes
5	OPR every 10 minutes
6	KBRR -bias, -trend, -1CPR every 90 minutes
7	KBRR -bias, -trend, -1CPR, -2CPR every 90 minutes
8	KBRR -bias, -trend, -1CPR, -2CPR, -3CPR every 90 minutes

Table 6. List of the empirical parameters tested. The accelerometer bias values were calculated for 5 months of GRACE solutions from May to October 2006.

Tests 1 to 5 estimate OPR parameters over different temporal spans. The increase in the frequency of the OPR parameters implies that more OPR parameters are estimated over the 24 hour arc. In test 1, 24 sets of OPR parameters are estimated while Test 5 involved estimating 144 sets of ORP parameters, with each set of OPR parameters comprising the amplitude of the sine and cosine of the orbital argument of latitude. Tests 6 to 8 involve estimating different combinations of CPR parameters bias and trend applied to the KBRR measurements only.

Table 7 and Table 8 contain the mean and standard deviations respectively for the daily accelerometer bias values from May to October 2006, for both GRACE A and B in the along-track (X), cross-track (Y) and radial (Z) accelerometer axis of the SRF. Table 7 reveals that in most cases the mean accelerometer bias value for the same axis and satellite are similar. Only in Test 5 is the mean noticeably different. The standard deviations (Table 8) reveal that Test 5 has the largest standard deviation and hence the largest variability. This suggests that bias values calculated using the OPR parameters in Test 5 are noisy and that unstable accelerometer bias values have been obtained. The standard deviations for Tests 7 and 8 have the lowest standard deviations for all bias values, except in the Z axis of GRACE B, where Test 1 has the lowest. Comparing the

tests which use the OPR parameters (1-5), the lowest standard deviation is provided by either Test 1 or 2. For tests where CPR parameters are applied to the KBRR measurement (6-8), the lowest standard deviation is provided by either Test 7 or 8. The day-to-day variations in the accelerometer bias values were the largest for Test 5.

	GRACE A			GRACE B		
	X	**Y**	**Z**	**X**	**Y**	**Z**
Test 1	-1170.40	28858.00	-539.20	-579.17	10682.00	-736.73
Test 2	-1170.30	28862.00	-537.20	-579.20	10677.00	-736.50
Test 3	-1170.60	28860.00	-539.00	-579.44	10672.00	-738.76
Test 4	-1170.70	28859.00	-539.44	-579.63	10677.00	-739.77
Test 5	-1170.10	29328.00	-498.03	-578.92	10650.00	-695.93
Test 6	-1170.10	28859.00	-535.45	-578.56	10683.00	-740.81
Test 7	-1169.80	28863.00	-531.03	-578.58	10691.00	-740.42
Test 8	-1169.70	28862.00	-534.46	-578.58	10694.00	-740.50

Table 7. Mean value of the accelerometer bias values calculated between May and October 2006 for the 8 tests. Values provided for both GRACE A and B for the along-track (X), cross-track (Y) and radial (Z) SRF axis. Units μ / s^2.

	GRACE A			GRACE B		
	X	**Y**	**Z**	**X**	**Y**	**Z**
Test 1	7.72	65.90	23.75	11.17	154.59	36.69
Test 2	6.94	56.40	53.36	9.85	179.62	61.84
Test 3	9.45	56.50	54.16	12.55	211.56	66.27
Test 4	11.42	82.50	60.34	14.77	171.31	71.74
Test 5	13.84	5574.50	210.83	16.67	626.10	188.77
Test 6	3.22	85.00	75.30	2.05	94.44	65.76
Test 7	1.70	13.30	36.68	1.97	63.85	52.61
Test 8	1.36	12.90	17.38	2.05	74.66	52.32

Table 8. Standard deviation of the accelerometer bias values calculated between May and October 2006 for the 8 tests. Values provided for both GRACE A and B for the along-track (X), cross-track (Y) and radial (Z) SRF axis. Units μ / s^2.

The accelerometer bias value time-series for these 4 tests (1 2, 7 and 8) are plotted in Figure 12 which shows the X, Y and Z bias values time-series for GRACE A and B . The *a-priori* bias values, calculated using Eq. (19), are included for reference. As suggested in Bettadpur (2009) there is an offset between the *a-priori* values and calculated accelerometer bias values. In all 4 tests the time-series for the accelerometer bias values are similar. However, it is possible to see that the times series for Test 1 (red) and Test 2 (green) contain greater variability than Test 7 (blue) and Test 8 (magenta), and certain days where an outlier accelerometer bias values has been calculated. Due to the offset of the *a-priori* values, it is not possible to see all the

variability between the different tests in Figure 12. Figure 13 reproduces the same data as in Figure 12, but the *a-priori* values are excluded.

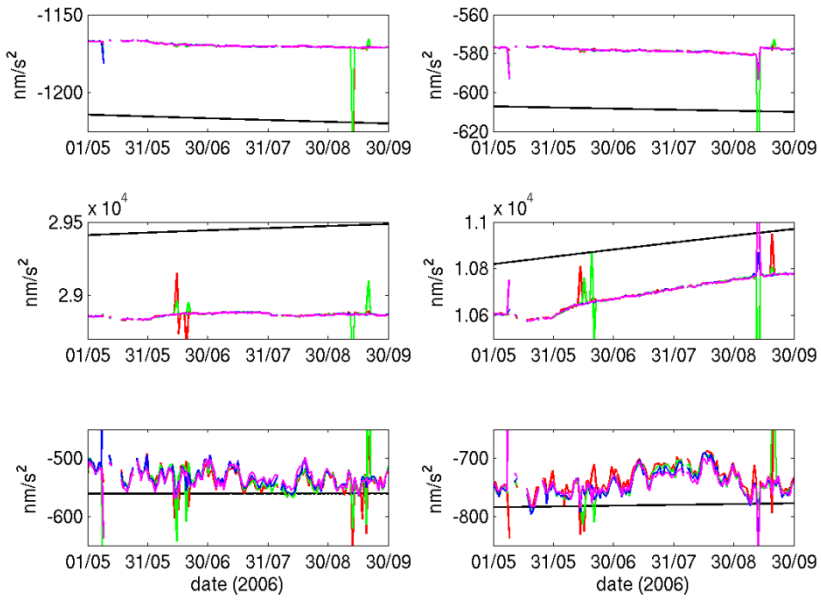

Figure 12. The accelerometer bias values for GRACE-A (left) and GRACE-B (right) in X,Y,Z (SRF) (top to bottom). The *a-priori* value (black) in included along with the values calculated using Test 1 (red), Test 2 (green), Test 7 (blue) and Test 8 (magenta).

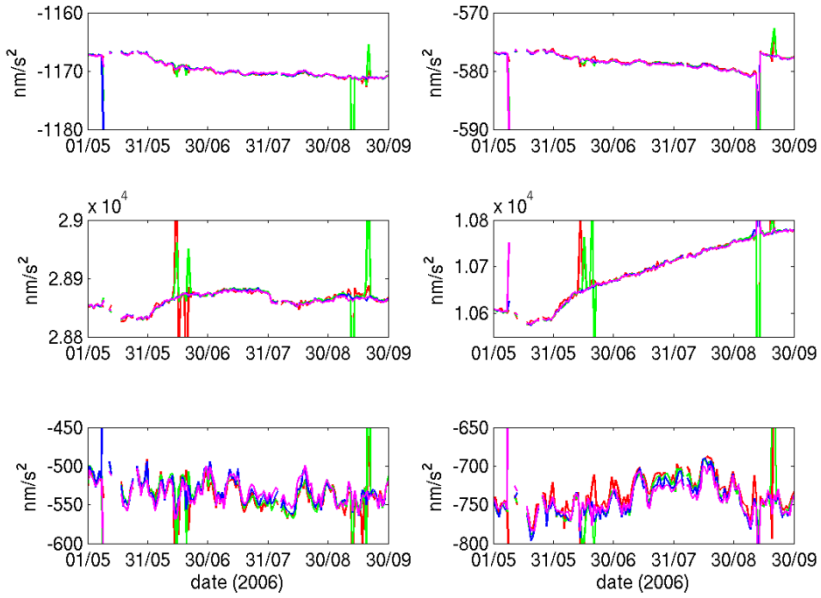

Figure 13. The accelerometer bias values for GRACE-A (left) and GRACE-B (right) in X,Y,Z (SRF) (top to bottom). The bias values calculated using Test 1 (red), Test 2 (green), Test 7 (blue) and Test 8 (magenta) are included. The *a-priori* value is not included.

Figure 13 reveals small day-to-day variations in the accelerometer bias values, with a longer term trend. The small day to day variations were also seen by Van Helleputte et al. (2009) and Bezdek (2010) and were connected to temperature variations that affect

the equipment on-board the GRACE satellites. Flury et al. (2008) found very frequent, sub-minute, spikes in the accelerometer observations that were caused by the activation of the heaters on-board the GRACE satellites. However, these were found to have very little affect on the gravity field solutions. The longer term trend is thought to be caused by the aging of the on-board equipment (Doornbos et al., 2010).

In both Figure 12 and Figure 13 there are daily accelerometer bias values that are outliers in all tests. An incorrect bias value could be due to some 'bad' data included in the solution or as a result of the empirical parameters not correctly absorbing the gravity field mis-modelling. However, what is interesting to note in Figure 13 is that amplitude of these outliers is often reduced when using KBRR measurement CPR parameters (Tests 7 and 8). There are also certain days where no outliers are present estimating KBRR measurement CPR parameters, while outliers occur in the OPR time-series (Test 1 and 2). This suggests that KBRR measurement CPR parameters in Tests 7 and 8 provide more stable estimates of the daily bias values. One final point of interest is the scales of the plots in Figure 13. The scale is much smaller on the plots in the X and Z axis than the Y axis. This is because formal errors in the Y axis were found to be two orders of magnitude greater than that in the X direction (Visser et al., 2013).

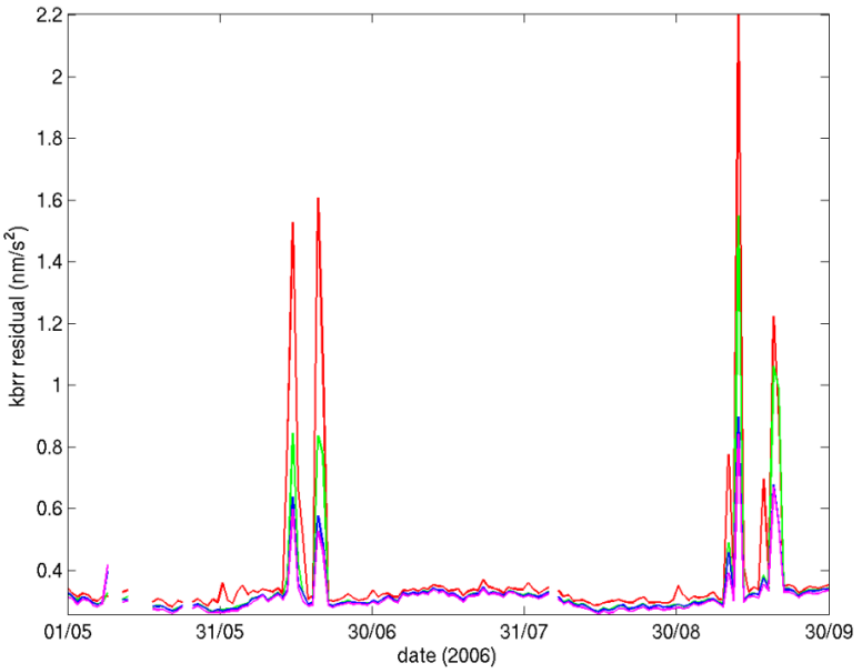

Figure 14. RMS of the daily KBRR residuals for Test 1 (red), Test 2 (green), Test 7 (blue) and Test 8 (magenta).

Figure 14 is a plot of the daily root mean square (RMS) of the KBRR residuals, obtained during the calculation of the accelerometer bias values for Tests 1, 2, 7 and 8,

revealing that the daily KBRR residuals are smaller for Tests 7 and 8. This means that the K-band ranging system empirical parameters used in Tests 7 and 8 improve the residual fit of the KBRR data. This improvement can also be seen in the results presented in Table 7 and Table 8. Therefore, when calculating the accelerometer bias values for use in subsequent processing stages in this thesis, the K-band ranging system empirical parameters described in Test 7 or 8 were adopted. The empirical parameters in Test 7 were chosen as there are only small differences between the results from Test 8 and hence the use of 3 CPR parameters had negligible effect.

5.2.5 *Rejection criteria*

Having determined the empirical parameters to use when calculating the accelerometer bias values, the daily bias values were calculated in 24 hour arcs for each day between 1st Jan 2003 and 31st Dec 2013. Along with the accelerometer bias values for each satellite (6 in total) and the CPR parameters, the satellite state vector was estimated. The solutions are iterated until convergence or the maximum number of iterations (set as 10) was reached. A solution was deemed to have converged once the calculated corrections, for the accelerometer bias values being estimated that iteration, were less than 0.001% of the accelerometer bias values at the start of that iteration.

Next, the bias values were analysed to confirm accuracy. As shown in Figure 12 and Figure 13, the calculated accelerometer bias values often contain outliers. There are also days when no accelerometer bias value have been obtained due to lack of data. Incorrect bias values can result from periods of missing or poor quality data, which cause *Faust* to converge to an incorrect solution. These days need to be identified and then reprocessed in an attempt to produce acceptable accelerometer bias values. Conversely, days with incorrect bias values need to be excluded from the future gravity field processing to mitigate against introduction of errors into the resulting gravity field solutions. The reprocessing is discussed in section 5.2.6.

Missing and incorrect bias values were identified by creating a time series of the accelerometer bias for each of the 3 axis for GRACE A and B and identifying the outliers. The time-series was analysed in 1 year batches. For each year the mean and standard deviation for each accelerometer bias value axis were calculated. Using the mean values a 3 sigma rejection criterion was adopted. As the initial time-series contained gross-outliers the process was undertaken 3 times. All the days rejected were reprocessed to attempt to include these days within gravity field solutions. The rejection

of a day where the ‘correct’ accelerometer bias values had been obtained was not particularly crucial as the identified days were subsequently analysed in further detail and reprocessed if required.

Figure 15, Figure 16 and Figure 17 show the accelerometer bias time-series for GRACE A (left) and GRACE B (right) in the X, Y and Z directions, respectively. The bias values plotted are for 2008. The first row in each figure corresponds to the time-series before any outliers have been removed. The second row shows the time series after the first iteration of the outlier removal procedure. The third and fourth rows show the second and third iteration of the outlier removal procedure respectively. Figure 15-17 reveal that each subsequent iteration, additional outliers were detected.

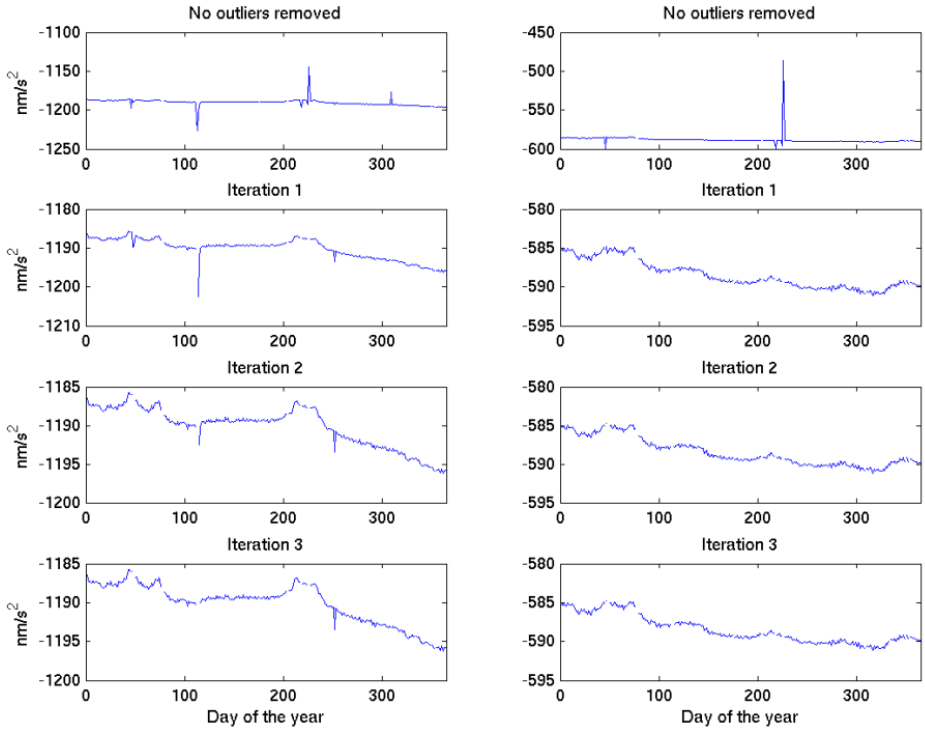

Figure 15. Accelerometer bias values for the X axis of GRACE A (left) and GRACE B (right) for 2008. The top plot shows the bias values before the removal of any outliers. Each subsequent plot represents the results after a further iteration where additional outliers have been removed.

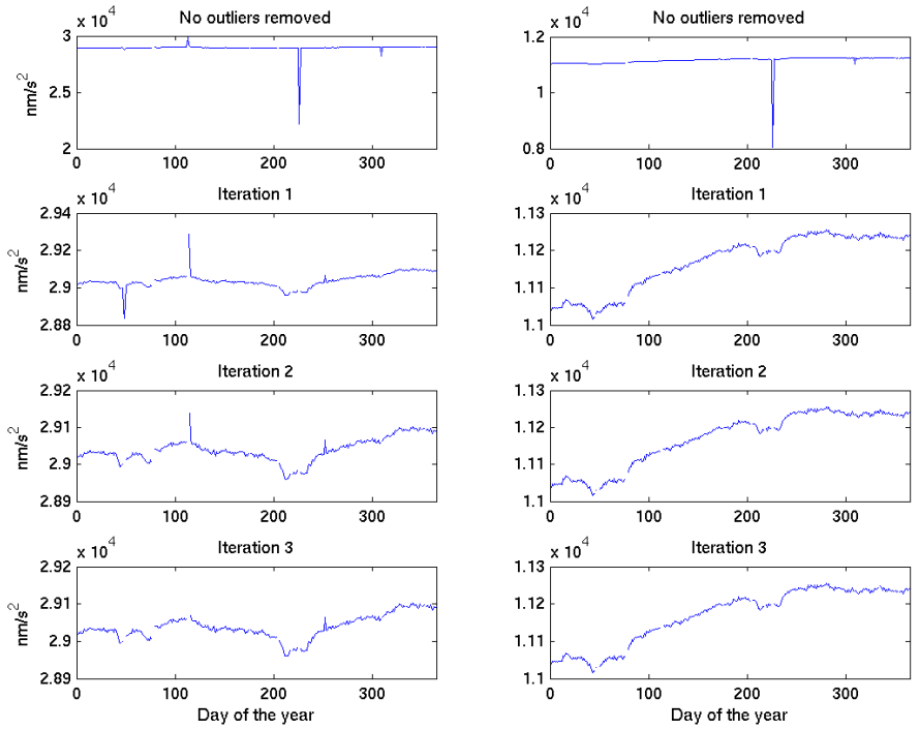

Figure 16. Accelerometer bias values for the Y axis of GRACE A (left) and GRACE B (right) for 2008. The top plot shows the bias values before the removal of any outliers. Each subsequent plot represents the results after a further iteration where additional outliers have been removed.

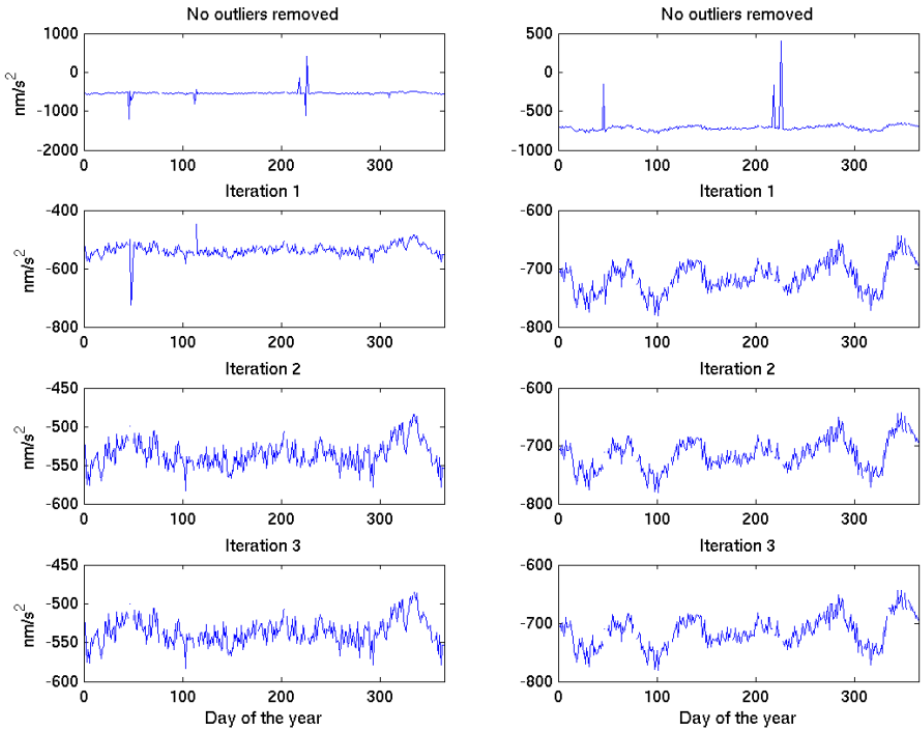

Figure 17. Accelerometer bias values for the Z axis of GRACE A (left) and GRACE B (right) for 2008. The top plot shows the bias values before the removal of any outliers. Each subsequent plot represents the results after a further iteration where additional outliers have been removed.

Table 9 (left) lists the number of days that were identified as outliers that require reprocessing. A total of 762 days were identified from 2003 to 2013.

5.2.6 ***Reprocessing***

To reprocess days where the accelerometer bias values were identified as outliers, each 24 hour arc was broken down into 60 minute arcs. The accelerometer bias values, along with the satellite state vector and the KBRR CPR measurement parameters, were then estimated every 60 minutes: each 60 minute arc solution was iterated until convergence, as described previously. After processing all such arcs within a 24 hour period, a time series of the accelerometer bias values was created for that day with the mean and standard deviation calculated, with outliers over 3 standard deviations from the mean identified and removed. From the remaining arcs a new daily input file was created that could be used to calculate the daily accelerometer bias from the arcs remaining. This new input file had periods of bad data excluded. A minimum of 6 hours of data was required; otherwise no daily accelerometer bias value was calculated. All 762 days were reprocessed with the new daily input files. Outlying and missing accelerometer bias values were again identified. The time-series was again analysed in 1 year batches with any further outliers identified as previously.

Table 9 shows the results of the reprocessing. The number of days that were reprocessed is shown (left) along with the number of days still identified as outliers after reprocessing (middle). For all years there is a reduction in the number of days identified as outliers or where no accelerometer bias values were calculated. However, for some years, there still appears to be a large number of days that have been rejected. For 2011, for example, 109 days were rejected. To investigate this further, each day rejected was compared with a list of days not included in the official GRACE processing centre solutions (available at http://grace.jpl.nasa.gov/data/GraceMonths/). This provides information on the number of days rejected in *Faust,* for which bias values are calculated by the official GRACE processing centres. The number of days rejected using *Faust* where solutions were obtained by the official GRACE processing centres is provided in Table 9 (right). This shows that there are only a handful of days each year where no accelerometer bias values have been calculated using *Faust* over and above those rejected by the GRACE processing centres. The results in Table 9 provide confidence in the rejection criteria. Days where no accelerometer values could be generated or where the bias values are unstable and should not be used have been successfully identified. The increase in days not included in the official GRACE

processing centre solutions from 2011 is due to the equipment on-board the GRACE satellites being turned off for battery management.

Year	Days requiring reprocessing	Days rejected after reprocessing	Not rejected by GRACE processing centres
2003	57	39	5
2004	33	23	2
2005	24	4	2
2006	30	10	6
2007	36	14	4
2008	19	5	2
2009	34	3	1
2010	57	13	5
2011	134	109	14
2012	147	84	3
2013	191	104	2

Table 9. The number of days that required reprocessing (left), the number of days still identified as outliers after reprocessing (middle) and the number of days where solutions were generated by the GRACE processing centres, but where no stable solution has been obtained using *Faust*.

5.3 *Estimation of gravity field parameters*

After stage 1, the estimation of daily accelerometer bias values and days to exclude, stage 2 of the processing strategy involves estimation of the gravity field as spherical harmonic and mascon parameters. The only difference between these is the gravity field parameters being estimated. The underlying processing and the data is the same for the two methodologies. Mathematically the two methodologies are equivalent (Sabaka et al., 2010), although the way in which noise is mitigated can modify this equivalence.

This section describes the fundamental processing behind the estimation of the gravity field parameters. At this processing stage only gravity field parameters and the satellite state vector are estimated. No empirical parameters are estimated as these would absorb gravity field signal.

5.3.1 *KBRR data only*

The gravity field solutions presented here are estimated from KBRR data only, with no GPS/GNV1B data or empirical parameters. The use of KBRR data only removes the computational requirement of processing GPS data which can weaken and corrupt the KBRR measurement if not handled correctly (Luthcke et al., 2006a). It also removes the requirement to correctly assign the relative weight of the different observational data types. Luthcke et al. (2006a) showed that the gravity field can be successfully recovered

from KBRR data using spherical harmonic parameters while estimating the Rowlands et al. (2002) short arc baseline parameters. Mascon parameters are usually estimated using only KBRR data.

5.3.2 *Short baseline parameters*

Traditionally gravity field parameters are estimated in longer arcs; gravity is an 'indirect effect' of traditional satellite tracking (Rowlands et al., 2002). Long satellite arcs (e.g. 1 day or more) were required for the gravity signal to become observable. However, longer arcs increase the effect of unmodelled forces. With the launch of the dedicated gravity field mission, GRACE, and the measuring of the changing distance between the satellites via the K-band ranging system, gravity field parameters can be estimated from short arcs using the short arc baseline parameters (Rowlands et al., 2010) as the KBRR data is dominated by mass below the satellite (Luthcke et al., 2008). This domination is shown in Figure 5.

Short arc baseline parameters were first described in Rowlands et al. (2002), where simulations were undertaken to map the gravity field using a low-to-low satellite configuration, similar to that of GRACE. Traditionally, during gravity field recovery, six components of the satellite vector at solved for at the initial epoch. These components are a Cartesian position and velocity in X, Y and Z. Each of the two GRACE satellites has its own state vector; thus a total of 12 state vector parameters to estimate.

Rowlands et al. (2002) found that use of a restricted set of short arc baseline parameters, instead of traditional Cartesian components of the satellite vector, allowed gravity field solutions to be obtained using the KBRR observations only. The use of short arc baseline parameters allowed the gravity field solutions to be created using KBRR data while benefiting from *a-priori* information inferred from other tracking data types, without the complexity of actually using these data types.

The short-arc approach is based on a reformulation of the 12 position and velocity state vector parameters for the GRACE pair into the equivalent short arc baseline parameters of Table 10.

No.	Description of short arc baseline parameter
P_1	Distance of baseline midpoint from Earth's centre of mass
P_2	Declination of baseline midpoint
P_3	Right ascension of baseline midpoint
P_4	Inertial X component of baseline midpoint velocity
P_5	Inertial Y component of baseline midpoint velocity
P_6	Inertial Z component of baseline midpoint velocity
P_7	Baseline vector length
P_8	Baseline vector pitch
P_9	Baseline vector yaw
P_{10}	Baseline rate-of-change vector magnitude
P_{11}	Baseline rate-of-change vector pitch
P_{12}	Baseline rate-of-change vector yaw

Table 10. Description of the 12 short arc baseline parameters from Rowlands et al. (2002).

The short arc baseline parameters in Table 10 are based on the Cartesian state vector of the baseline (difference vector) between the two satellites and the baseline midpoint, which is the average of the two state vectors of the GRACE satellites (Rowlands et al., 2002). However, the use of short arcs baseline parameters still requires GRACE accelerometer data, in addition to KBRR data, to deal with non-conservative forces. Furthermore, the satellite orbits must have been previously well determined using GNV1B positioning data. *Faust* solves for the short baseline parameters by converting the 12 Cartesian state vector parameters into the short arc baseline parameters, solving for the short arc baseline parameters, converting the short arc parameters back into Cartesian state vector parameters, and then adding the solution to the original 12 Cartesian state vector parameters. Through intensive simulations, Rowlands et al. (2002) found that over short arcs (around 15 minutes) only short arc baseline parameters P_8, P_{10} and P_{11} need to be solved for. Over long arcs (1 day in length) short arc baseline parameter P_1 also needed to be included.

Short arc baseline parameters are only used in stage 2 of the gravity field recovery; the estimate of gravity field parameters. When determining the arc length to use during the estimation of the gravity field parameters in section 5.3.3, only short arc baseline parameters P_8, P_{10} and P_{11} were solved for if the arc length was less than 24 hours. For arcs of 24 hours or more, short arc baseline parameter P_1 was also included. This parametrisation is based on the findings of Rowlands et al. (2002).

5.3.3 *Arc length*

The choice of arc length for gravity field recovery is of fundamental importance. Before the launch of dedicated gravity field satellite missions, such as GRACE, long arcs were

required. Based on extensive simulations Rowlands et al. (2002) showed that when using satellite-to-satellite tracking short arcs (~ 15 minutes) could be used to estimate gravity field parameters. More recently, Mayer-Gurr et al. (2006) estimated gravity field parameters using short arcs with a mean length of 30 minutes. However, while gravity field parameters can be estimated using short arcs of KBRR data and short arc baseline parameters, the correct arc length is still required.

To identify the appropriate arc length to use in *Faust* gravity field recovery was undertaken for May to September of 2006, using real GRACE data. The mascon gravity field solutions were calculated using the accelerometer bias values from stage 1 of the data processing methodology, as described in section 5.2. The solutions were derived using KBRR (and accelerometer) data. No GPS/GNV1B data or empirical parameters were required to stabilise the solutions. Solutions were generated using the arc lengths listed in Table 11.

Arc length	**Mean RMS fit of the KBRR residuals**
30 minutes	0.31 μm/s
60 minutes	0.32 μm/s
90 minutes	0.41 μm/s
24 hour	9.01 μm/s

Table 11. The different arc lengths for which 4 monthly gravity field solutions were generated and the average fit of the KBRR residuals.

Table 11 reveals that the average fit of the KBRR residuals was 0.32 μm/s using 60 minute arcs and 0.31 μm/s and 0.41 μm/s for 30 minute and 90 minute arcs respectively. The fit for the 24 hour arcs was 9.01 μm/s. The results in Table 11 show little difference between arcs of 30 and 60 minutes in length. However, the use of 60 minute arcs is favoured over the 30 minute arcs due to the reduction in storage requirement. With the normal matrices of each solution being ~1.2 GB, 60 minute arcs generate ~864 GB of data for a 30 day solution. The same solution using 30 minutes arcs would generate ~1728 GB of data. Therefore, arc lengths during gravity field processing were chosen to be 60 minutes.

In subsequent analyses the gravity field parameters are estimated for each 60 minute arc with the resulting normal equations combined to create a set of daily normal matrices. These are then combined to create 10 day or monthly mascon solutions.

5.3.4 *Updated state vector values*

Having chosen 60 minute arcs for use in the gravity field recovery, the initial positions and velocity for the satellite state vector were required for each arc. These state vectors were estimated using KBRR and GNV1B data with *a-priori* values for the satellite state vectors taken from the GNV1B data. The solution in *Faust* was iterated until convergence.

The state vector for each arc was then estimated using KBRR data only, while also estimating the short arc baseline parameters. This additional step was undertaken as the use of GNV1B data could have degraded the quality of the state vector and the gravity field parameters will be estimated from KBRR data only. Comparing the state vector values calculated using KBRR and GNV1B data to those calculated using KBRR data reveals that in 97% of arcs very similar state vector values were calculated. The state vector values only begin to differ at the 10^{th} decimal place, when the initial position is in km and the velocity km/s. The RMS values of the KBRR residuals (μm/s) were also identical to four decimal places. Of the 3% of arcs that differed, the RMS of the KBRR residual was lower when the GNV1B data was not included. This suggests that the inclusion of GNV1B data had degraded the quality of state vector.

5.3.5 *KBRR rejection criterion*

The final variable to investigate, prior to gravity field recovery, is the rejection level to be used for the KBRR residuals. During gravity field recovery, erroneous KBRR observations will need to be rejected to avoid bad data corrupting the normal matrices from each 60 minute arc. This in-turn will corrupt the 10 day or monthly solutions, resulting in errors in the solutions. The solutions will also be corrupted if bad arcs are included, which manifest as stripes in the gravity field solution. Therefore, a method for identifying bad arcs needs to be identified. Finally, a complete day should be excluded if a significant number of missing arcs or bad arcs occur that day.

A starting point for the rejection level of the KBRR residuals is Figure 18 which shows the daily RMS for the GRACE KBRR residuals for each day included in the CNES/GRGS 10 day time variable gravity solutions (Bruinsma et al., 2010). Figure 18 reveals that the maximum daily RMS is over 0.6 μm/s, with most solutions around 0.2 and 0.3 μm/s. Rowlands et al. (2005) obtained a daily RMS of 0.3-0.4 μm/s and Lemoine et al. (2007) was able to reduce the RMS to between 0.3-0.36 μm/s with improvements in the background models. These values, along with the values for the

average fit of the KBRR residuals in Table 11, can be used as a basis for testing for an appropriate rejection level to be used during each 60 minute arc to identify outliers in the KBRR data. Figure 18 and Table 11 can also be used as a starting point to find an appropriate value for the average fit of the KBRR residuals for each arc. One interesting point to note from Figure 18 is that daily standard deviation for the GRACE KBRR residuals is not static: it fluctuates over time. This will need to be taken into consideration when deriving the rejection criteria for individual arcs.

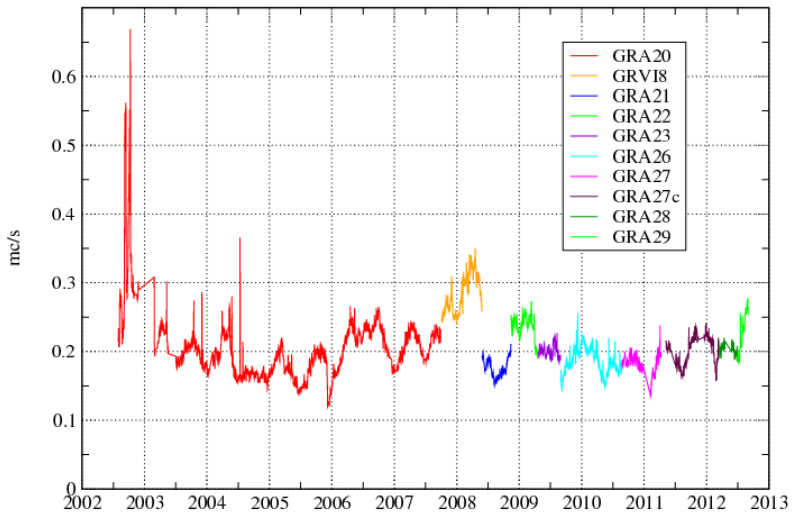

Figure 18. RMS of the GRACE KBRR residuals for each day included in the CNES/GRGS 10 day time variable gravity solutions (Bruinsma et al., 2010).

To test for an appropriate rejection level of the KBRR residuals during the 60 minute arcs, the monthly KBRR residuals were analysed over three test areas:

- The ocean. Using Figure 2 in Chambers and Bonin (2012), which shows the standard deviation of ocean bottom pressure (OBP) from GRACE CSR RL05 products, a quiet area of the ocean was chosen. This area was chosen as there should be little temporal gravity signal, allowing outlying KBRR residuals to be identified. The oceanic approach can also be used to identify and remove bad arcs from the solution.
- The Amazon. This region was chosen as the annual signal over the Amazon is one of the largest seasonal gravitational signals seen in the GRACE data. An investigation of the rejection criterion over the Amazon will help determine if real signal is being rejected.
- Antarctica. Antarctica was chosen as the area around the Pine Island Glacier, is one of the largest mass loss trends observed in the GRACE gravity data. Again,

looking at the rejection criterion over the Antarctica will help to determine if real signal is being rejected.

The boundary of the area analysed for the oceanic area was latitude 5N to 35S and longitude -30W to 10E. The standard deviation of the OBP in Figure 2 of Chambers and Bonin (2012) is between 1 and 2 cm. This is a quiet area of the ocean. The KBRR residuals for every 60 minute arc for June 2006 were analysed. Figure 19 is a plot of all the KBRR residuals. The expectation is that over the ocean the KBR residuals should be small.

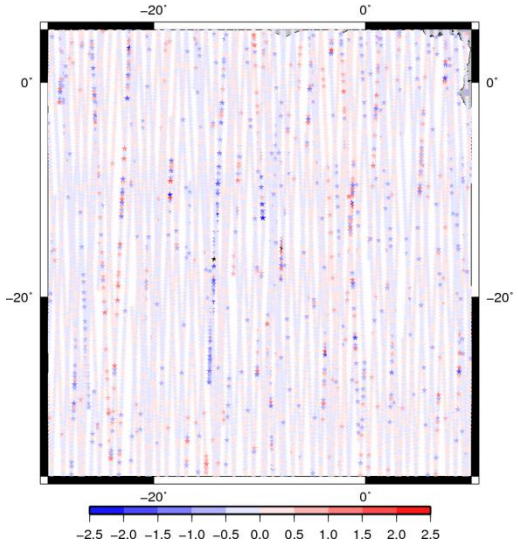

Figure 19. Spatial plot of the KBRR residuals over the ocean test area. Units μm/s.

Figure 19 reveals that most residuals have a value between -0.5 to 0.5 μm/s. However, there are residuals that have absolute values that exceed ±1.5 μm/s. These values are greater than 6 times the daily residuals values suggested in Figure 18 and around 5 times the average daily KBRR residual fit for 60 minutes arcs in Table 11, suggesting that the residuals should be classified as outliers. Often, such residuals values are linear geographically. It is to be noted that each line in Figure 19 represents a satellite pass over the area and represents an individual arc: arcs are of 60 minutes duration and the GRACE satellite orbit period is ~90 minutes.

It is important that outliers are rejected and, when part of a bad arc, that the whole arc is rejected. To identify the correct rejection level to use for the KBRR residual during each 60 minute arc the monthly solution for June 2006 was rerun, with a number of different rejection levels. Table 12 shows the different rejection levels applied to the data, with the number of observations included and rejected from the resulting monthly solution.

The rejection levels were chosen using the data shown in Figure 18 and Table 11. In total there are 12035 KBRR residuals over the test area.

Rejection level (µm/s)	**Included**	**Rejected**
All data included	12035	0
2.0	12028	7
1.8	12026	9
1.6	12017	18
1.4	11999	36
1.2	11959	76
1.0	11903	132

Table 12. Rejection levels applied over the ocean test area with the number of observations included and rejected. Data for June 2006.

However, identifying the correct rejection level is a trade-off between rejecting real signal and including bad data.

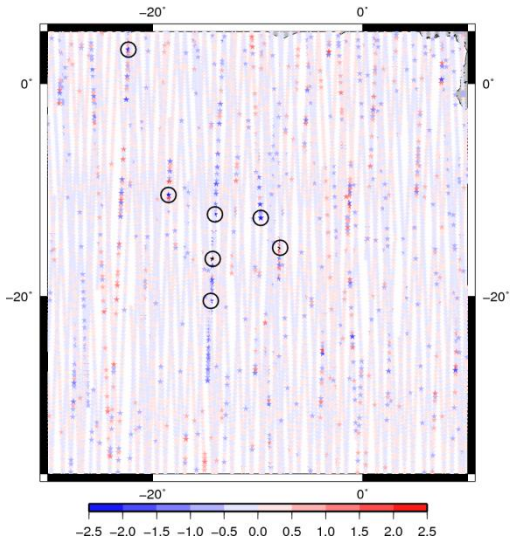

Figure 20. KBRR residuals that exceed ±2.0 µm/s are highlighted for the ocean test. Units µm/s.

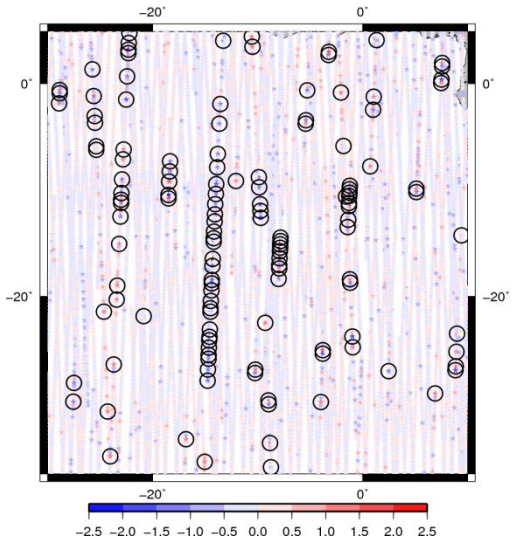

Figure 21. KBRR residuals that exceed ±1.0 μm/s are highlighted for the ocean test. Units μm/s.

In Figure 20 and 21, all observations with residual value exceeding ±2.0 μm/s and ±1.0 μm/s, respectively, are highlighted. Using a rejection criterion of 2.0 μm/s a total of 7 observations have been identified as outliers. However, a large majority of outliers have not been identified. With a rejection criterion of 1.0 μm/s a total of 132 observations have been identified, including the bad arcs. With the average fit of the KBRR residuals in 60 minute arcs 0.32 μm/s in Table 8, a value of 3 standard deviations would be around 1.0 μm/s, suggest that the rejection level should be closer to 1.0 μm/s than 2.0 μm/s.

With this in mind the same rejection levels were applied to the Amazon region. Again, the different rejection levels were applied to the 60 minute arcs in *Faust*. The residuals over the Amazon are for April 2004. April is one of the wettest months over the Amazon and the month when the annual gravity signal peaks. Therefore, April will exhibit some of the largest residuals. No hydrology model is included in the *Faust* analysis and hence the effect of hydrology will be present in the residuals. However, the effect on the residuals relates to the background gravity field models used during orbit determination. Including a hydrological model in *Faust* would reduce the effect of hydrology on the residuals. The area analysed was latitude 20N to 20S and longitude 80W to 40W. Figure 22 shows the residuals for April 2004. In Table 13 the different rejection levels applied to the data are listed along with the number of observations included and rejected from the resulting monthly solution. In total there are 11453 KBRR residuals over the test area. In Figure 22, the horizontal banding results from the

orbital direction of the GRACE satellites (north to south or south to north). The same effect is seen in Figure5.

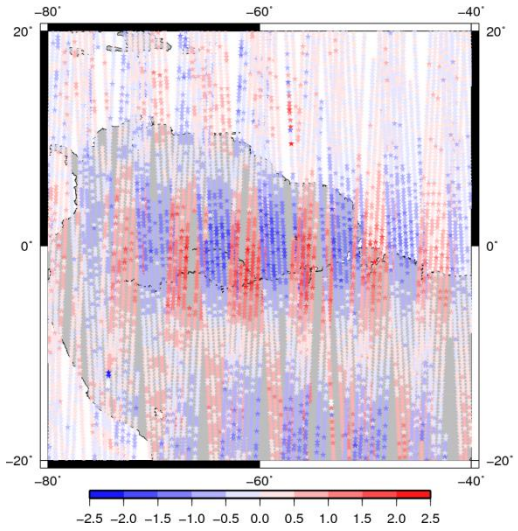

Figure 22. Spatial plot of the KBRR residuals over the Amazon test area. Units are μm/s.

Rejection level (μm/s)	**Included**	**Rejected**
All data included	11453	0
2.0	11436	17
1.8	11392	61
1.6	11309	144
1.4	11106	347
1.2	10689	764
1.0	9991	1462

Table 13. Rejection levels applied over the Amazon test area with the number of observations included and rejected. Data for April 2004.

Table 13 reveals that 17 observations are rejected using a rejection level of 2.0 μm/s, compared with 1462 when using a rejection level of 1.0 μm/s. With a rejection level of 1.0 μm/s over 12% of the observations are rejected over the test area. Figure 23 shows the spatial distribution of the residuals over 1.0 μm/s. Some bad arcs have been identified, although the majority of rejected observations cover the area surrounding the Amazon river. This is the area where large residuals were expected due to the April being the rainy season. This suggests that a rejection level of 1.0 μm/s is too low for a region of high hydrological signal. The rejected observations identified using a rejection levels of 1.4 μm/s and 1.8 μm/s are plotted in Figure 24 and 25, respectively.

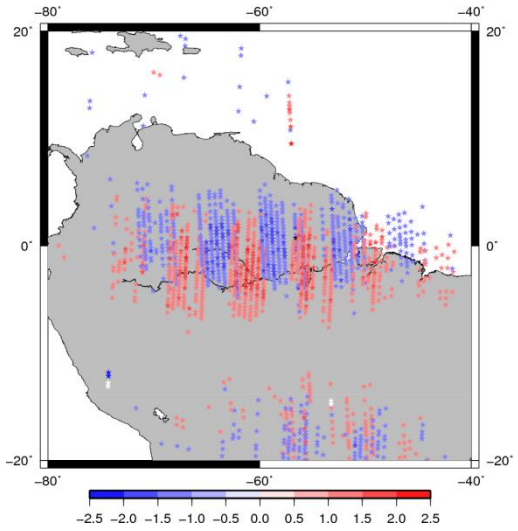

Figure 23. KBRR residuals that exceed ±1.0 μm/s for the Amazon test area. Units μm/s.

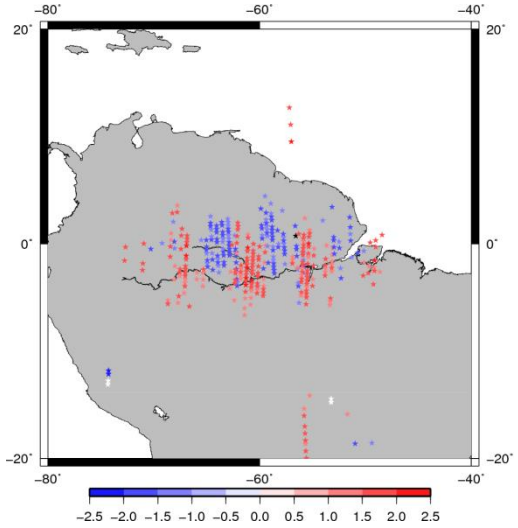

Figure 24. KBRR residuals that exceed ±1.4 μm/s for the Amazon test area. Units μm/s.

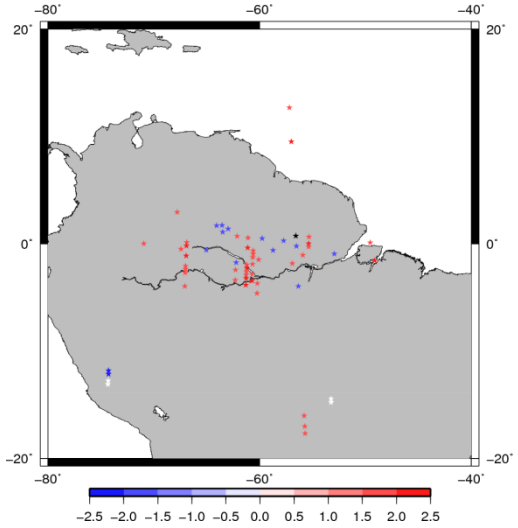

Figure 25. KBRR residuals that exceed ±1.8μm/s for the Amazon test area. Units μm/s.

In Figure 24 around 3% of the data (347 observations) has been rejected, with around 0.5% (61 observations) rejected in Figure 25. Comparing the two figures shows that bad arcs are evident in Figure 24, although at the cost of rejecting what is expected to be real signal. Figure 25 retains most of the observations, but it is harder to identify potential bad arcs in the data. To visualise the difference that using a rejection level of 1.4 μm/s and a rejection level of 1.8 μm/s would have on the solution, the mascon monthly gravity field solutions for these were calculated and then differenced. A map of the difference is shown in Figure 26.

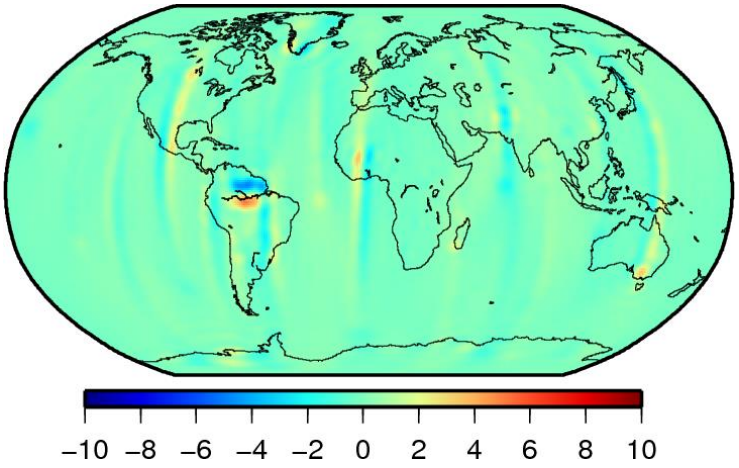

Figure 26. Difference between the 2° monthly mascon solution for April 2004 using the rejection criterion of 1.4 μm/s and the monthly solution calculated using rejection criterion of 1.8 μm/s. Units cm EWH.

Figure 26 reveals that a small amount of the amplitude of the solution over the Amazon (~cm of EWH) is lost for a rejection level of 1.4 μm/s. However, using a rejection level of 1.8 μm/s introduces stripes into the solution. Stripes can be misinterpreted as real signal. The presence of stripes suggests that rejection level of 1.8 μm/s restricts identification of bad arcs and that erroneous KBRR observations are corrupting the normal matrices from each 60 minute arc. Stripes do not appear in the solution when a rejection level of 1.4 μm/s is used.

In consequence the rejection levels between 1.0 μm/s and 1.6 μm/s were tested over Antarctica for January 2003. The results are presented in Table 14. January 2003 was chosen as the reference epoch for the mean gravity field, GIF48, is 1st January 2007. As there is a quasi-linear trend over Antarctica, the residuals become larger with increasing time away from the reference epoch. The KBRR residual should therefore be large for this month. All locations south of 60S considered, a total of 60521 residuals, are plotted in Figure 27.

Rejection level (µm/s)	Included	Rejected
All data included	60521	0
1.6	60211	310
1.5	60182	336
1.4	60135	386
1.3	60068	453
1.2	59952	569
1.1	59785	736
1.0	59523	998

Table 14. Rejection levels applied over the Antarctica test area with the number of observations included and rejected. Data for January 2003.

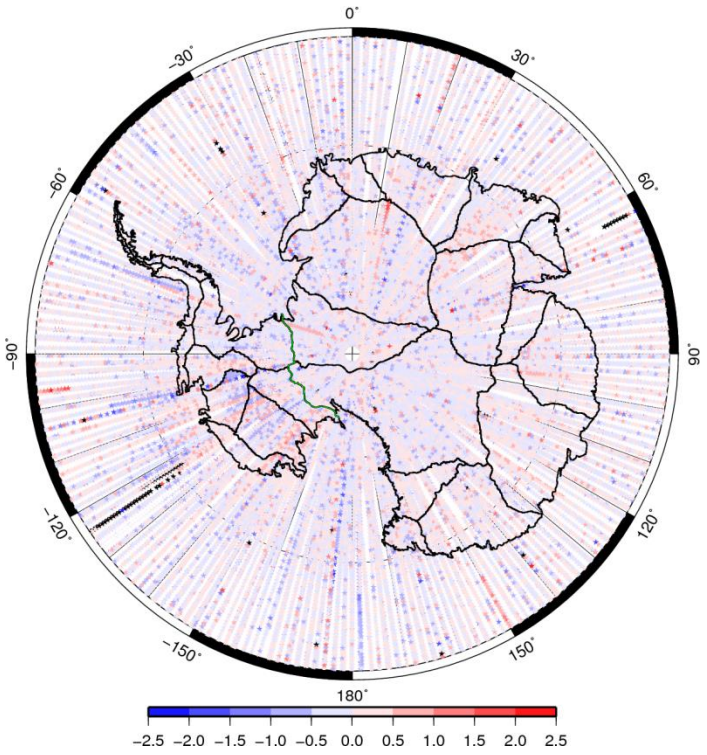

Figure 27. Spatial plot of the KBRR residuals over the Antarctica. Zwally et al. (2012) Antarctica drainage basins as shown for reference. Green divides separates West Antarctica (left) from East Antarctica (right). Units µm/s.

Figure 27 reveals a grouping of larger residuals over West Antarctic (left of green divide), which is where the largest mass loss is occurring. Several bad arcs can also be seen. The Antarctica drainage basins, defined using ICESat data (Zwally et al., 2012), are provided for reference. Table 14 suggests that there is little difference in the number of observations rejected using the different rejection levels. Only 0.5% of the total observations are rejected when a rejection level of 1.6 µm/s is used. Decreasing the rejection level to 1.0 µm/s increases the total number of observations rejected to 1.65%.

Figure 28-30 show the observations that would be rejected using a rejection level of 1.0 µm/s, 1.4 µm/s and 1.6 µm/s respectively. These figures suggest that a rejection level of

1.0 μm/s is too low as it possible that real signal is being rejected over West Antarctica. In Figure 30, some bad arcs are not rejected while Figure 29 represents a balance between including good data and identifying bad arcs.

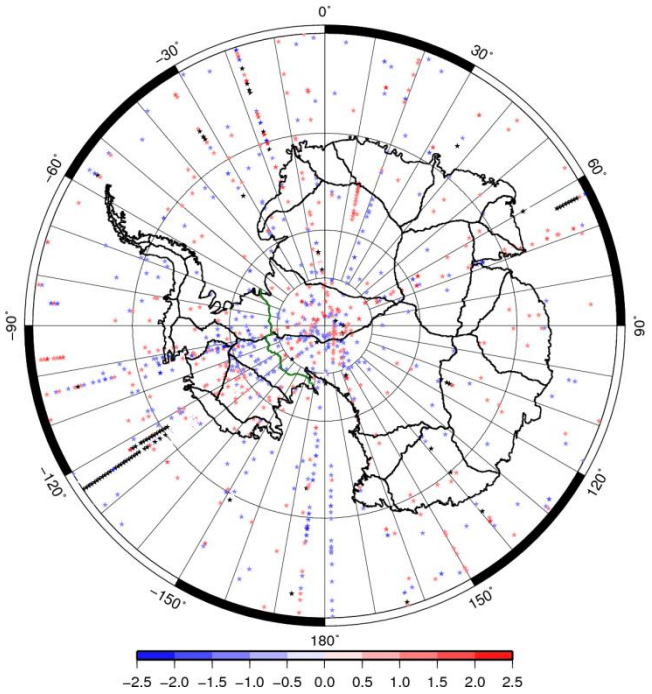

Figure 28. KBRR residuals that exceed ±1.0 μm/s for the Antarctic test area. Zwally et al. (2012) Antarctica drainage basins as shown for reference. Green divides separates West Antarctica (left) from East Antarctica (right). Units μm/s.

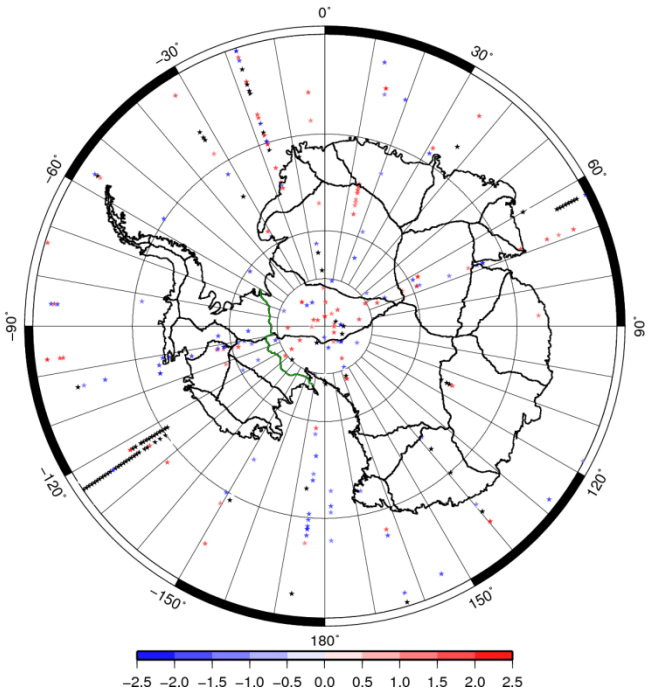

Figure 29. KBRR residuals that exceed ±1.4 μm/s for the Antarctic test area. Zwally et al. (2012) Antarctica drainage basins as shown for reference. Green divides separates West Antarctica (left) from East Antarctica (right). Units μm/s.

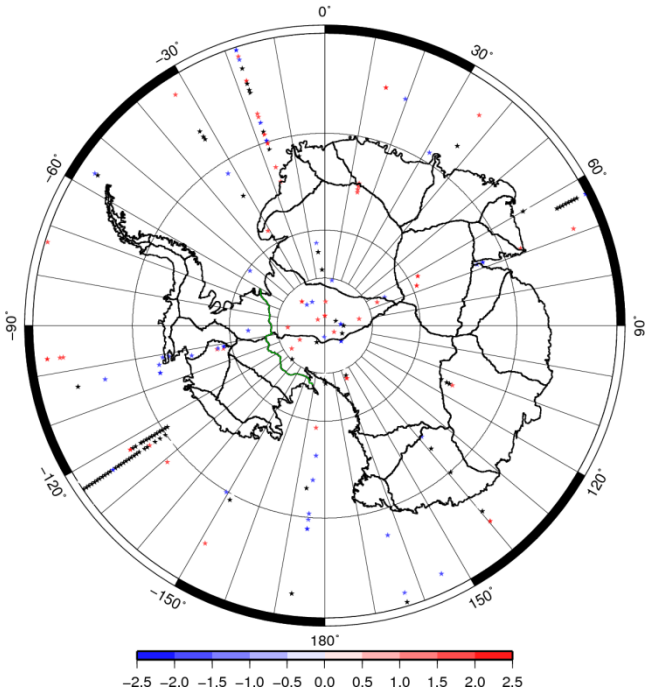

Figure 30. KBRR residuals that exceed ±1.6 μm/s for the Antarctic test area. Zwally et al. (2012) Antarctica drainage basins as shown for reference. Green divides separates West Antarctica (left) from East Antarctica (right). Units μm/s.

All the data presented in the tables and figures suggest that a rejection level of 1.4 μm/s is a reasonable compromise globally, based on the areas tested. However, based on the testing, a value of 1.3 μm/s or 1.5 μm/s could also be used. Using 1.3 μm/s would mean

that more real signal would be rejected with less noise included, while a rejection level of 1.5 μm/s would reject less real signal while allowing more noise into the solution due to the trade-off between signal and noise. A rejection level of 1.4 μm/s was chosen for processing all 60 minute arcs. Any KBRR residual over 1.4 μm/s will be rejected and will not contribute to the solution for that arc. However, any changes in the background gravitational field model will require the rejection level to be revisited. In addition, the tests areas were chosen to represent typical annual and mass loss signals seen in the GRACE data. The processing of additional data and changes in geophysical mass signals will also require the rejection level to be revisited. To validate the rejection criterion, the number of observations over 1.4 μm/s rejected per calendar month from January 2003 to December 2013 are plotted in Figure 31.

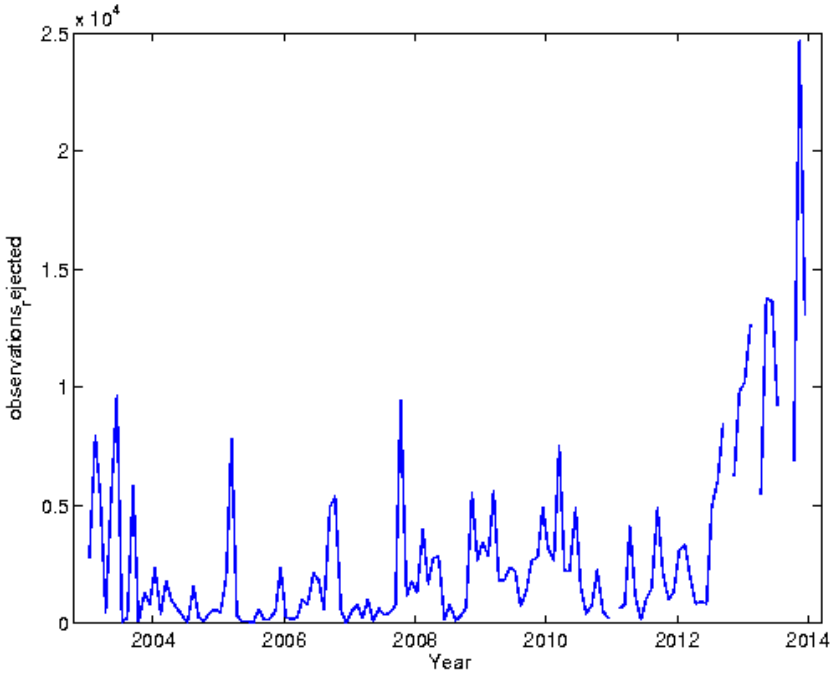

Figure 31. Number of observations rejected for each calendar month during GRACE data processing.

Figure 31 reveals that the number of rejected observations varies throughout the GRACE mission. However, there is a concentration of months with ~5000 observations rejected in early 2003. In addition there are an increasing number of observations rejected from 2012 onwards. To investigate further, the spatial distribution of the rejected data is plotted for three months: February 2003, which has ~8000 observation rejected (Figure 32); October 2007, which has ~9500 observation rejected (Figure 33); and July 2013, which has ~9200 observations rejected (Figure 34). For reference, each month contains ~500,000 KBRR observations.

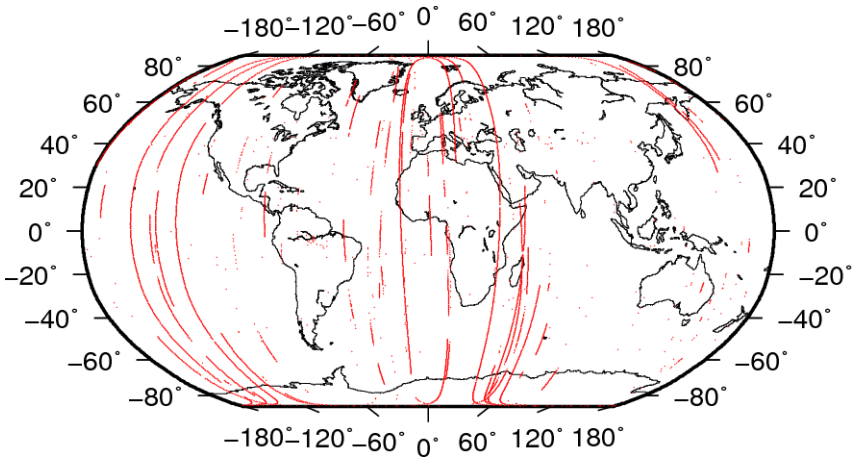

Figure 32. Spatial distribution of the observations rejected over 1.4 μm/s for February 2003.

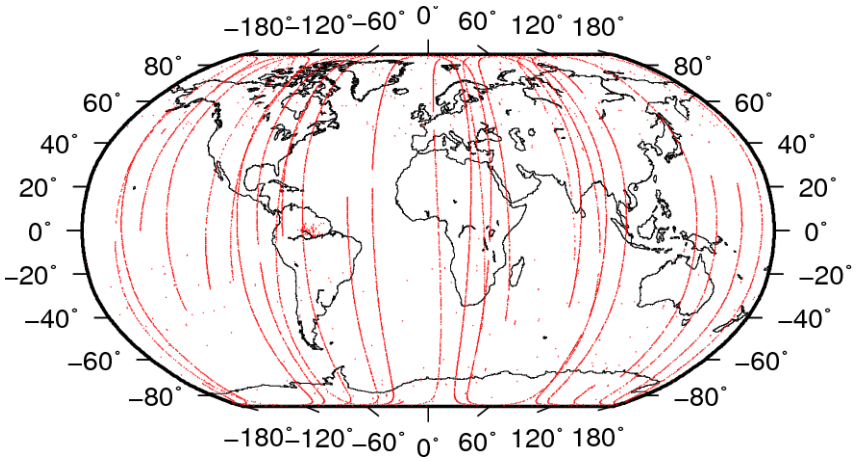

Figure 33. Spatial distribution of the observations rejected over 1.4 μm/s for October 2007.

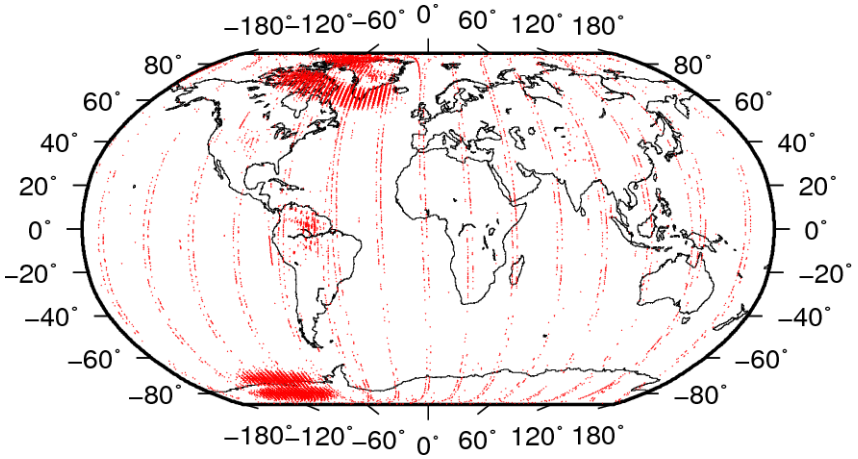

Figure 34. Spatial distribution of the observations rejected over 1.4 μm/s for July 2013.

It is clear from Figure 32 and Figure 33 that the observations rejected do not have a spatial pattern associated with a known mass loss/gain signal in the GRACE data but relate to arcs and therefore can be assumed to be poor data. However, in Figure 34

although some arcs are being rejected, there is a cluster of rejected observations over Greenland and West Antarctica. The spatial distribution of these signals coincides to two areas experiencing the largest mass loss observed by GRACE. Thus, a rejection criterion of 1.4 μm/s is increasingly causing real signal to be rejected in the latter stages of the GRACE mission.

Analysis of the spatial distribution of observations rejected for each month of the GRACE mission reveals that observations start to be rejected over Antarctica and Greenland around August 2010, with an increasing number of observations rejected from 2012 onwards. In addition, as time from the reference epoch (January 2007) of GIF48 increases the value of the residuals over Greenland and Antarctica increase. Therefore, to fully capture the mass loss over Greenland and Antarctica an increased rejection criterion needs to be applied from August 2010 onwards. From August 2010 an updated rejection criterion of 1.6 μm/s will be used. This will be increased to 1.8 μm/s from October 2011 and 2.4 μm/s from August 2012. However, increasing the rejection criterion to allow the mass loss over Greenland and Antarctica to be observed will allow arcs of poor data into the solution elsewhere. This could be interpreted as real signal. The results of the rejection criterion presented here could be used to support the argument that, ideally, there is a need to iterate to remove signal, allowing the rejection criterion to be subsequently lowered after each iteration. However, undertaking iterations of the mascon solution is extremely computationally intensive. Therefore, a rejection criterion of 1.4 μm/s will be used for global analysis, with the modified rejection criterion from August 2010 onwards used for regional analysis over areas of very high signal. The new rejection criterion will only be applied for calculating the mass trend over Greenland and Antarctica. All other trends will be calculated using a rejection criterion of 1.4 μm/s.

Having identified the rejection level to use during the individual 60 minute arcs, bad arcs need to be identified and removed from the 10 day and monthly solutions. With 11 years of data, there are over 95,000 individual arcs to be checked. It is therefore not feasible to manually check all of these. Here, bad arcs are identified in two ways. Firstly, when high numbers of observations are rejected. Secondly, when the RMS of an arc is over 3 times the mean RMS for a certain time period.

Identifying bad arcs based on the number of rejected observations is straight forward. There is normally one KBRR observation every 5 seconds; the majority of 60 minute

arcs will have 720 observations. However, the Gauss Jackson orbital integrator in *Faust* does not process observations at the beginning of each arc during initialising and observations are lost at the end when the integrator reaches the end date. Therefore, most arcs have 692 KBRR observations. Setting the KBRR rejection criterion at ~70 observations is equivalent to rejecting the arc if ~ 10% of the observations are rejected.

In Figure 19, Figure 22 and Figure 27, large KBRR residuals are evident. While some arcs only contain a small number of such residuals, which will be identified using the rejection criterion of 1.4 μm/s during the global data processing, others contain multiple large residuals. This can be clearly seen in Figure 21. It is these bad arcs that need to be identified as, without a rejection level based on the number of residuals rejected, there is a potential that these arcs could be included in a 10 day or monthly solution, when they clearly should not be. Using a rejection value of ~10% seems sensible. This value can be adjusted for arcs with fewer observations.

The second method to reject bad arcs is to utilise the RMS of the KBRR residuals for each 60 minute arc and create a time-series from which the mean and standard deviation are calculated. This was used to identify arcs where the residual value of the observation is over 3 times the mean. The arcs were analysed in batches of 10 days (240 arcs); 10 day batches were used as there should be limited changes in the gravity field over the period. Over the whole dataset (2003 to 2013) the majority of arcs rejected with over 10% of the observation as outliers were also rejected because the RMS of the KBRR residuals in the arc was over 3 times the standard deviation of 10 day mean.

Finally, after considering individual arcs, a complete day can be rejected from the 10 day or monthly solutions if less than 12 arcs exists for that day. Using these rejection criteria, the number of days that were rejected in the gravity field solutions are given in Table 15.

Year	Accelerometer	Bad days	Total	GRACE analysis centres
2003	39	7	46	48
2004	23	5	28	31
2005	4	4	8	12
2006	10	5	15	7
2007	14	7	21	25
2008	5	1	6	3
2009	3	1	4	4
2010	13	2	15	9
2011	109	0	109	104
2012	84	4	88	88
2013	104	8	112	108

Table 15. Number of days not included in the *Faust* solutions. The reason for exclusion (accelerometer or bad day) is given, along with the total number of days not included (Total). The total number of days not included in the official GRACE solutions is given as a comparison in the final column.

Table 15 shows the total number of days excluded for each year (Total), along with the number of days excluded in the official GRACE solutions. The primary reason is due to lack of accelerometer data (accelerometer) or the day rejected containing bad data (Bad Days). Comparing the total number of days rejected with the official GRACE solutions shows a similar level of rejection. This gives confidence that the rejection criteria, during the estimation of the accelerometer basis and the gravity field parameters, are in broad agreement with other analysis centres.

Figure 35 and 36 illustrate the number of days included in the monthly solutions for 2009 and 2013 respectively. The number of days rejected and the reason for rejection are also included. In 2009, only 4 days have been rejected, while in 2013 a total of 112 days were excluded. Figure 36 reveals that a majority of the missing data relates to months where the satellite instruments were turned off to preserve power. For these months no official GRACE solution is available. Plots for each year from 2003 to 2013 are available in Appendix C. The same days are included in both monthly and 10 day solutions.

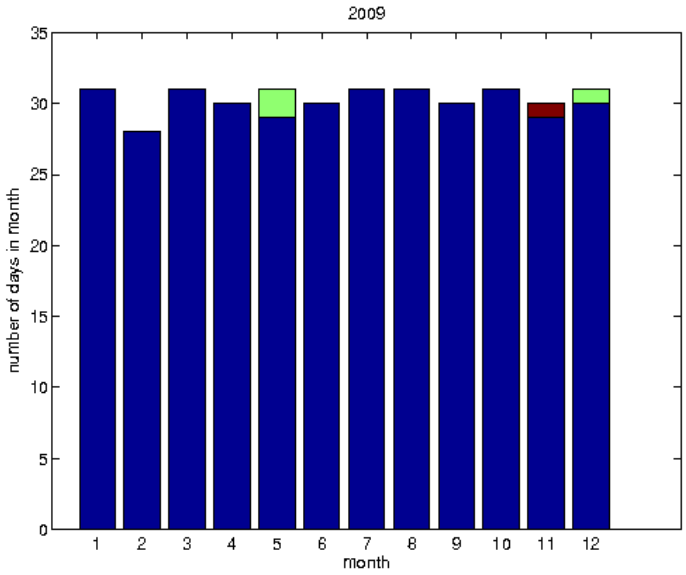

Figure 35. Number of days included in the monthly solution (blue), rejected due to no accelerometer bias value (green) and rejected due to poor data (red) for 2009.

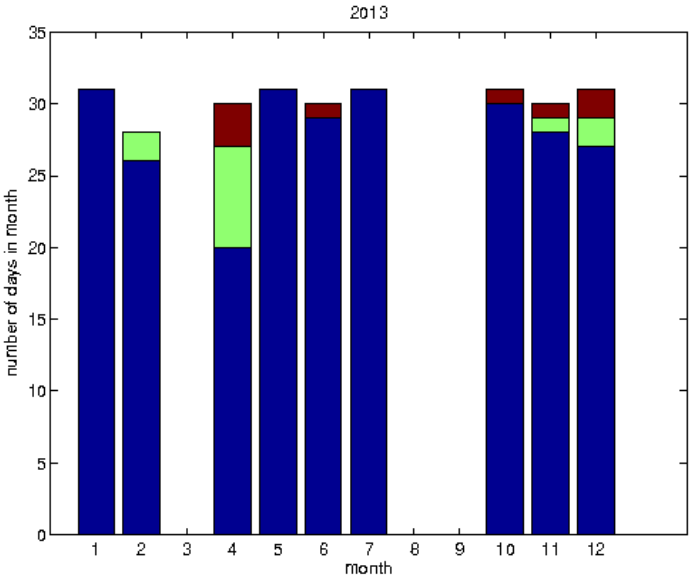

Figure 36. Number of days included in the monthly solution (blue), rejected due to no accelerometer bias value (green) and rejected due to poor data (red) for 2013. The months where no information is available, coincide with months when the satellite measuring equipment was turned off to preserve power. No solutions are available for those months from the official GRACE processing centres.

5.4 ***Summary***

This chapter provided an overview to Newcastle University's orbit determination software *Faust* and the two processing steps required to compute gravity field solutions from Level-1B GRACE data. The first stage provides the accelerometer bias values for the short-arc gravity field recovery in the second stage.

Accelerometer bias values are required to correct the raw accelerometer observations. The estimation of the bias values starts with daily *a-priori* bias values provided by the GRACE mission, with bias values estimated in 24 hour 'daily' arcs starting midnight. Estimating daily accelerometer biases is common among users of GRACE Level-1B data. Alongside bias values, empirical orbital parameters are estimated. Empirical parameters are required to account for small un-modelled forces during the orbit determination (Montenbruck and Gill, 2005). While the choice of empirical parameters varies among users of GRACE Level-1B data, testing revealed that estimating a KBRR 1 CPR and 2 CPR and a KBRR bias and a KBRR trend every 90 minutes alongside the bias values provided the more stable estimates of the daily bias values in *Faust*. While accelerometer scale factors are also used to correct the raw accelerometer observations, they are approximately constant over time (Bezděk, 2010) and there is aliasing of the bias values if estimated simultaneously with scale factors. Therefore the scale factors provided by the GRACE mission were used. In total, bias values were computed for 90% of the days over the period of January 2003 to December 2013. This value was 91% for the official GRACE processing centres.

The second stage in the processing methodology is the gravity field recovery, estimated using short arcs of KBRR data only. Using only KBRR data removes the computational requirement of processing GPS data, which can weaken and corrupt the KBRR measurement if not handled correctly (Luthcke et al., 2006a), while short arcs have been successfully used to recovery the TVG field from GRACE using short arc baseline parameters, first described in Rowlands et al. (2002). Tests revealed that the correct arc length to use in *Faust* was 60 minutes. The use of 60 minute arcs is favoured over the 30 minute arcs due to the reduction in storage requirement, although the 30 minute arcs had a slightly lower average fit of the KBRR residuals. The resulting normal equations from each 60 minute arc, are combined to create a set of daily normal matrices. These are then further combined to create 10 day or monthly mascon solutions.

The final variable investigated was the rejection level to be used for the KBRR residuals. Erroneous KBRR observations need to be rejected to avoid bad data corrupting the normal matrices from each 60 minute arc, and subsequently, the 10 day or monthly solutions. Analysing KBRR residuals over a number of areas revealed that 1.4 μm/s would be a good general global choice for the rejection level. Computing a monthly solution using rejection levels of 1.4 μm/s and 1.8 μm/s found that the rejection level of 1.8 μm/s introduced stripes into the solution. Stripes did not appear in the

solution when a rejection level of 1.4 μm/s was used. This rejection level was also about 3-sigma of the daily RMS obtained by Rowlands et al. (2005) (0.3-0.4 μm/s) and Lemoine et al. (2007) (0.3-0.36 μm/s). However, the choice of a rejection level is a trade-off between reducing noise and rejected signal. Using a rejection level of 1.3 μm/s would reject more real signal although less noise would be included. A rejection level of 1.5 μm/s would reject less real signal while allowing more noise into the solution.

Analysis of the observations rejected each calendar month revealed that from August 2010 onward, a rejection level of 1.4 μm/s eliminated data over West Antarctica and Greenland. These are the two largest mass loss signals in the GRACE time-series, meaning that real data is being rejected. Therefore, from August 2010 an updated rejection criterion of 1.6 μm/s will be used. This will be increased to 1.8 μm/s from October 2011 and 2.4 μm/s from August 2012. However, this increasing rejection criterion will only be applied for calculating the mass trend over Greenland and Antarctica as increasing the rejection criterion will allow arcs of poor data into the solution elsewhere. This could be interpreted as real signal. Therefore, a rejection criterion of 1.4 μm/s will be used for global analysis, with the modified rejection criterion from August 2010 onwards used for regional analysis over areas experiencing large differences from the background gravity field. Alternatively, iterations could be used, allowing the rejection criterion to be subsequently lowered after each iteration. The parametrisation determined in this chapter will be applied to the GRACE processing in Chapter 6 and Chapter 7.

Chapter 6. Simulations

The formation of the mascon parameters has been described in Chapter 4, while Chapter 5 introduced the processing methodology using *Faust* and explained the choice of parameters required while computing the gravity field solutions from Level-1B GRACE data. In this chapter simulations are undertaken to provide an accuracy assessment, and quantify the capability, of the mascon methodology to resolve basin-level mass changes at a variety of spatial scales while understanding how the methodology handles random noise and systematic errors (resulting from inaccuracies in observations or measurements), hereafter noise, inherent at higher degree and orders. To allow for a comparison with the commonly used spherical harmonic coefficients, solutions will be generated through the estimation of both mascon parameters and spherical harmonic coefficients. A standard Gaussian smoothing filter will be applied to the post processing of the spherical harmonic solution while the spatial constraint matrix applied to the mascon solution. Gaussian smoothing is applied to the post processing of the spherical harmonic solution as it is the most common processing strategy (Rowlands et al., 2010).

The majority of the simulations presented in this chapter have been published in Andrews et al. (2014).

6.1 *Simulation Methodology*

The aim of the simulations is to recover a known surface mass distribution from GRACE KBRR data using *Faust*. The effect of the surface mass distribution is computed through a spherical harmonic expansion to a specified degree and order, with the resultant gravitational field added to the mean GIF48 field, from which simulated noise free KBRR tracking data are computed. The normal equations for each 60 minute arc are then combined to create monthly solutions for the two methodologies. Only monthly solutions are calculated using the mascon parameters to allow a direct comparison with the solution calculated using spherical harmonic coefficients. Further, only KBRR data is used as mascon parameters are usually estimated using only KBRR data, as described in section 5.3. In addition Luthcke et al. (2006a) showed that the gravity field can be successfully recovered from KBRR data using spherical harmonic parameters while estimating the Rowlands et al. (2002) short arc baseline parameters. The use of KBRR data only removes the computational requirement of processing the GPS data which can weaken and corrupt the KBRR measurement if not handled correctly (Luthcke et al., 2006a).

Within the simulations, the only difference between the two processing strategies is the gravity field parameters being estimated (spherical harmonic or mascon). The choice of arc length was based on the experimentation in section 5.2.3. During the simulations no GPS/GNV1B data or empirical parameters are required to stabilise the solutions, as is the case during stage 1 of the gravity field solution. The accelerometer bias values used during the simulations are those calculated in section 5.2.

The results presented in section 6.2 for a noise free simulation show that the KBRR tracking data created can be used to describe a simulated mass. Noise is included in the simulation in section 6.5, through creation of simulated stripes, allowing for an examination of how the solutions differ at higher degree and orders using the different methodologies.

6.2 *Simulated recovery of the GLDAS anomaly*

The first simulation was the recovery of a known gravity signal through estimation of spherical harmonic and 2° and 4° mascon parameters to assess the performance of the different methodologies in an ideal case. The introduced signal was the June 2006 Global Land Data Assimilation System (GLDAS) Version 1 (Rodell et al., 2004) anomaly to the 2003-2010 mean derived from monthly averaged data with a 1° spatial resolution. Since hydrology is the largest seasonal contribution to the GRACE signal, this simulation represents the main spatial and temporal variation, with similar characteristics to that contained within real GRACE data. The GLDAS anomaly was scaled upwards so the degree variances contained a similar power as the June 2006 CSR RL05 Level-2 field (Bettadpur, 2012b), as not all geophysical signal is present in the GLDAS anomaly. The 1° gridded GLDAS anomaly was converted to spherical harmonics to degree and order 60 and degree and order 120 with tracking data created from the different harmonic expansions. The two GLDAS anomalies are shown in Figure 37.

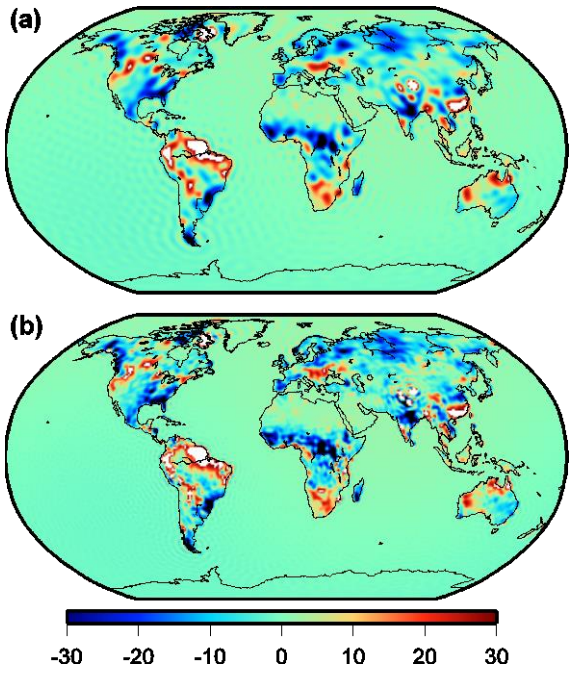

Figure 37. GLDAS mass anomaly for June 2006 as differenced from the 2003 to 2010 mean to degree and order 60 (a); degree and order 120 (b). Note that there is no GLDAS signal in Antarctica or Greenland or over the oceans.

The degree variances of for both GLDAS anomaly models are identical up to degree and order 60. Therefore, a comparison of the recovery of the GLDAS anomaly up to degree and order 60 with the recovery of the GLDAS anomaly up to degree and order 120, allows the effect of omission errors on the parameter estimation to be observed. Gravity field recovery was undertaken, for both GLDAS anomaly models, through spherical harmonic estimation to degree and order 60 (3717 parameters) while the 4° (2°) equal-area mascon solutions involved estimation of 2564 (10292) mascon parameters. The monthly solution was collated from the individual 60 minute arcs. No noise was added to the solution at this stage.

Figure 38 (a) shows the RMS in cm of EWH of the recovered anomaly to the input GLDAS data, described to degree and order 60. This is the ideal case as no noise or omission errors are present. The RMS is provided for various smoothing distances. For spherical harmonic coefficients the distance refers to the Gaussian smoothing radius, while for the mascon solutions the distance is *D* of Eq. (16). As such, the two distances are not directly comparable as they do not equate to the same smoothing radius. The distance 0 km indicates that no Gaussian smoothing has been applied or that the mascon solutions are unconstrained.

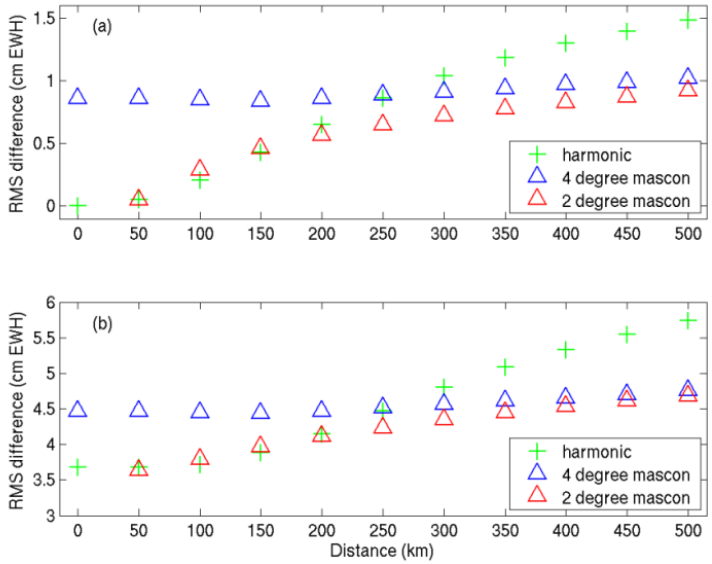

Figure 38. RMS of the differences between the calculated gravity field solutions and the noise free GLDAS anomaly in cm of EWH. GLDAS described to degree and order 60 (a); and degree and order 120 (b). The distance refers to the Gaussian smoothing radius (spherical harmonic coefficient solution) or the correlation distance (mascon solutions). The distance used in the mascons solutions (triangles) is not directly comparable to that used in the harmonic solution (crosses) and do not equate to the same smoothing radius.

Figure 38 (a) reveals that, without Gaussian smoothing (Distance = 0 km) in the noise free case, the spherical harmonic solution is able to exactly recover the reference degree and order 60 GLDAS anomaly using perfect data. Adding Gaussian smoothing dampens the amplitude of the recovered signal. For the 4° mascon solution, the smallest RMS is obtained when a correlation distance of 150 km is used in the constraint matrix, but the solution is not able to fully recover the input GLDAS anomaly. This is to be expected as the GLDAS anomaly was expanded to spherical harmonics degree and order 60 (3717 gravity field parameters) while the 4° mascon solution involves estimation of 2564 mascon parameters. The recovery favours the spherical harmonic solution over the 4° mascon solution with the latter unable to fully recover the gravity field due to the parametrisation. The use of the constraint matrix in the mascon solution does enable a small improvement in the ability to recover this short wavelength signal.

The 2° mascon solution involves estimation of 10292 mascon parameters and consequently nearly a factor 4 more parameters than the spherical harmonic solution. When estimating a mascon solution, Rowlands et al. (2010) found that if no constraint matrix was applied the solution did not invert as it was rank deficient by a large margin. A similar result was obtained here. Adding a constraint matrix with ≥50 km correlation distance was required to stabilise the solution and allow recovery of the GLDAS

anomaly. The resulting RMS to the input GLDAS anomaly is 0.05 cm of EWH, which is the same as the spherical harmonic recovery with 50 km Gaussian smoothing. Increasing the correlation distance in the constraint matrix increases the effect of the constraint matrix and over constrains the mascon solution, reducing high frequency signal.

Figure 38 (b) shows the RMS of the recovered anomaly to the input GLDAS data, described to degree and order 120. This allows the effect of omission errors on the different parameters to be compared. The pattern is similar to the ideal case (GLDAS to degree and order 60), but with an increase in all RMS values. Methodologies that are essentially truncated to degree and order 60 are, of course, unable to fully recover an input signal described to degree and order 120 and hence unable to capture the additional short wavelength (high degree) information. Figure 39 shows the degree unsmoothed/unconstrained variances of the spherical harmonic and mascon solutions to degree 60. The degree variance of the input GLDAS anomaly is included for reference and is shown to degree 120 to show the omitted signal.

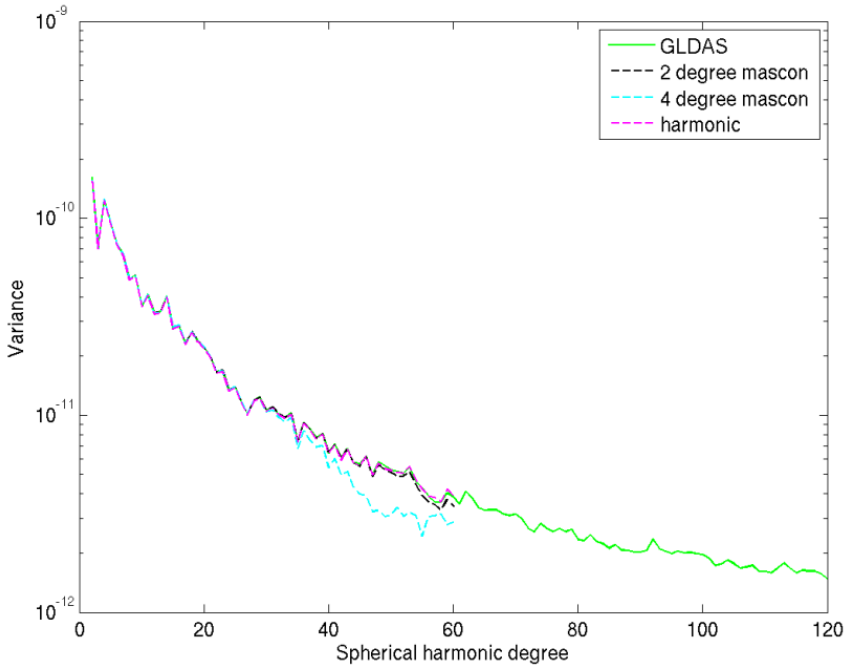

Figure 39. Degree variances of the spherical harmonic and mascon solutions. The degree variances of the noise free input GLDAS anomaly are included for comparative purposes. The degree variance of GLDAS anomaly is shown to degree 120 to show the omitted signal.

In Figure 39 all three solutions match the degree variance of the input GLDAS anomaly to near degree 40 from where the 4° mascon solution loses power. This reduction is the

result of the under sampling of the input signal by the 4° mascon solution. The spherical harmonic coefficient and 2° mascon solutions are able to replicate the degree variances of the GLDAS anomaly. The slight reduction in power at degree ~55 to 60 in the 2° mascon solution is the result of the 50 km correlation distance used in the constraint matrix to stabilise the inversion. The ability of the spherical harmonic and 2° mascon solutions to replicate the degree variances of the GLDAS anomaly up to degree 60 in Figure 39 shows that simulation methodology is valid as a known input signal can be reproduced a from simulated KBRR tracking data. For the remainder of this chapter all processing uses the GLDAS anomaly described to degree and order 120 and hence allows consideration of omission errors.

6.3 *Mascon Centre-to-Centre Distance*

As part of the evaluation of the force model, discussed in section 5.1, the contribution of every mascon to the accelerations of the satellites is calculated. Thus, as for spherical harmonics, mascon solutions presented so far are global in extent with the drawback of added computational expense, at least in the case of the 2° mascon solutions.

Figure 5 revealed that a mass anomaly leaks outside of the source area, and by extension neighbouring mass anomalies will leak into the source area. Figure 5 also showed that this leakage is not global, but spatially limited. The limited spatial extent of a mass anomaly on gravitation experienced at the satellite altitude was noted by Velicogna and Wahr (2006b). This suggests that an adequate approximation of the total contribution of all mascons to the satellite accelerations can be achieved by considering a reduced subset of mascons. This will allow estimation of a local mascon solution and reduce the computational requirement of a global solution.

To investigate this, the simulated recovery of the GLDAS anomaly in section 6.1 was repeated. This time only the contribution to the satellite accelerations of a subset of mascons was estimated. The number of mascons included is based on the distance between the centre of the mascon under consideration to the mascon directly below the leading GRACE satellite. This will be called the centre–to-centre distance and the mascon below the satellite the nadir mascon. Any mascon pair where the centre-to-centre distance is greater than a prescribed value will be excluded from matrix C of Eq. (13) and its effect set to zero. Thus, for each arc only a subset of mascons will be included in the normal equations, reducing the processing time and storage requirement. All the individual arcs will be summed to calculate a monthly solution, as previously.

The solutions are global in extent as each month all mascon parameters are estimated in the monthly solution. 4° and 2° mascon solutions were generated using various centre-to-centre distances. The resulting degree variances are plotted in Figure 40 and Figure 41 respectively and compared to those from the global mascon solutions and input GLDAS anomaly. The 0 km centre-to-centre distance solution refers to the contribution of the nadir mascon only to the acceleration experienced by the GRACE satellites.

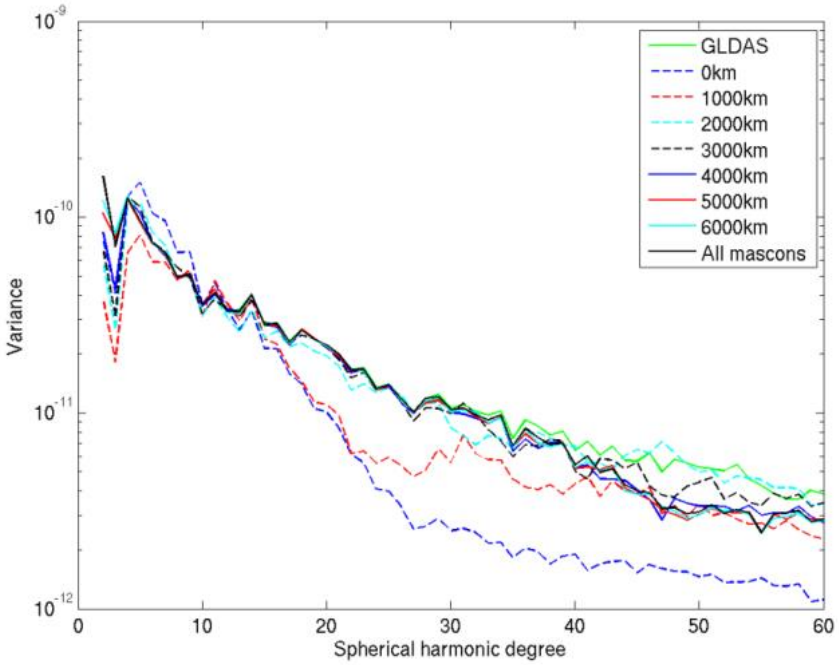

Figure 40. Degree variances of the 4° mascon solutions for a range of centre-to-centre cut-off distances. The degree variances of the input GLDAS anomaly (solid green) and original solution (solid black) are included for reference. All solutions here are noise free.

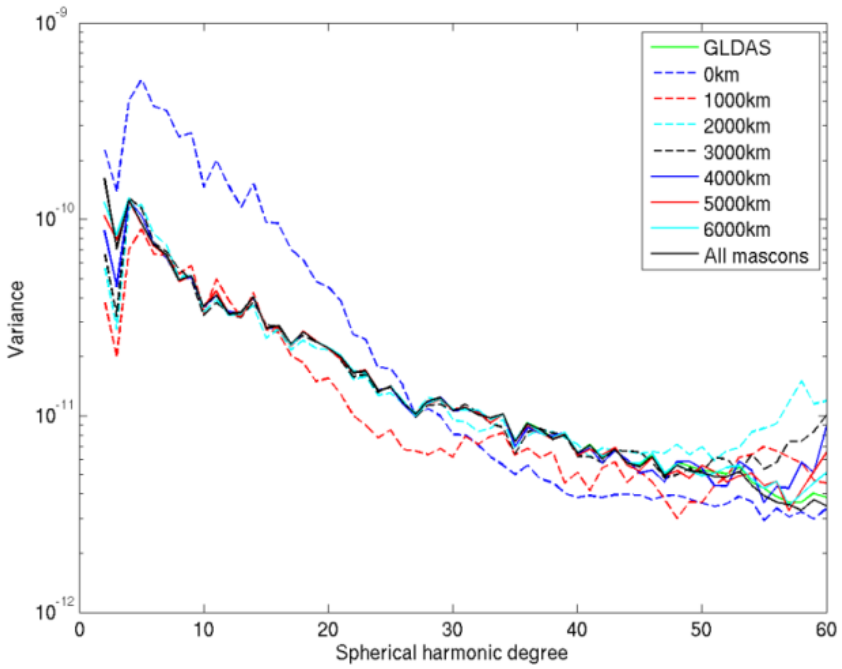

Figure 41. Degree variances of the 2° mascon solutions for a range of centre-to-centre cut-off distances. The degree variances of the input GLDAS anomaly (solid green) and original solution (solid black) are included for reference. All solutions here are noise free.

Figure 40 reveals that for a centre-to-centre cut-off distance of 1000 km or less the degree variances of the original mascon solution are not well recovered as the leakage seen in Figure 5 has not been fully accounted for. All such solutions have reduced power at higher degrees, which dampens short wavelength information in the gravity fields. The 0 km centre-to-centre distance solution in Figure 41 (2° mascon) is anomalous with more power than expected, especially at lower degrees due to the leakage of the spherical harmonics used to define the mascon parameters in Eq. (10). In both Figure 40 and Figure 41, increasing the centre-to-centre distance to 6000 km improves the fit of the degree variances with the original mascon solution, at which point the degree variances for both the 2° and 4° mascon solutions closely resemble the global solution. A centre-to-centre distance of 4000 km or 5000 km could be used, but the solutions have less power at degree 2 and 3 harmonics (longer wavelength).

The contribution to the acceleration experienced by the GRACE satellites at distances from the nadir mascon are plotted in Figure 42, for a nadir mascon located in the Amazon (similar results are observed when the nadir mascon is located elsewhere). The accelerations are given as a percentage of the acceleration of the nadir mascon.

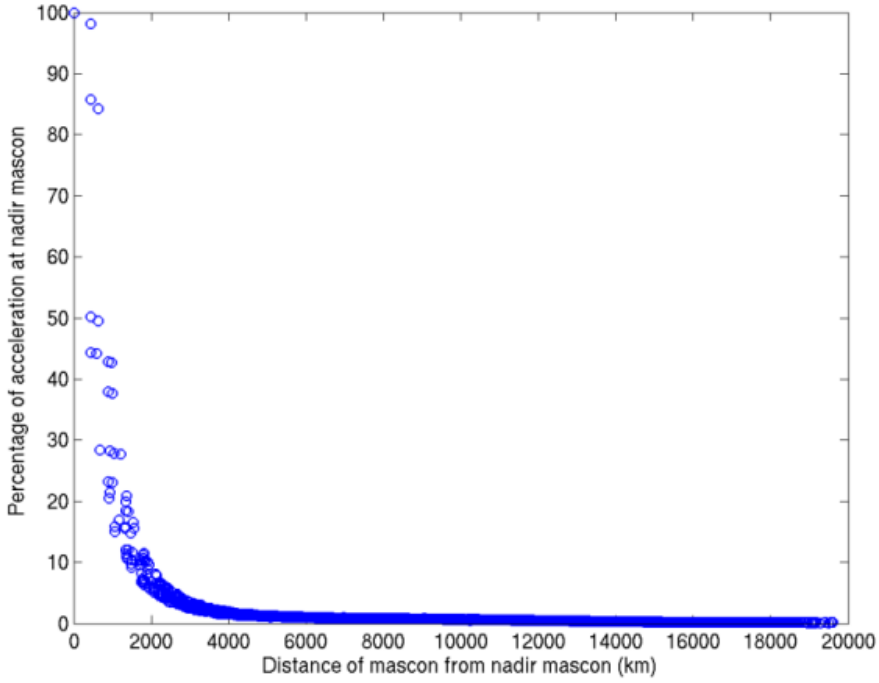

Figure 42. The contribution of mascons to the gravitational acceleration of a satellite over the Amazon as a function of the centre-to-centre distance. Acceleration is given as a percentage of the acceleration of the nadir mascon.

Figure 42 reveals that, as expected, mascons close to the nadir mascon have a larger contribution to the accelerations experienced by the satellites than distant mascons. As the centre-to-centre distance increases, the contribution to the satellite acceleration reduces and approaches zero. Mascons within a centre-to-centre distance of up to 2000 km have the greatest contribution but mascons 2000 km from the nadir mascon still contribute ~10% of the acceleration of the nadir mascon. Mascons with centre-to-centre distances up to 4000 km are still seen to influence the accelerations experienced by the satellites. Above 4000 km the contributions to the accelerations reduce, explaining the relatively small improvements at higher degrees seen in Figure 40 and Figure 41. A centre-to-centre cut-off distance of 6000 km will be used in future processing as the difference between that and a full global solution is minimal.

6.4 *Iteration of the mascons*

In section 6.3 a good approximation to a true mass anomaly (simulated with GLDAS) was obtained by including the contribution of all mascons within a centre-to-centre distance of 6000 km. However, it is also worth investigating if a similar approximation can be achieved by using a smaller centre-to-centre cut-off distance but also iterating the solution. Iteration was shown by Luthcke et al. (2013) to substantially increase

signal recovery. Here, a 4° mascon solution was iterated for the centre-to-centre distances of 0 km, 1000 km and 2000 km. When iterating, the value of the mascon parameters estimated in the previous iteration was used as the starting value in the current iteration. The satellite state vectors were also updated. The RMS of the differences to the known GLDAS anomaly are presented in Table 16. The RMS of the differences for the 3000 km, 4000 km, 5000 km and 6000 km centre-to-centre solutions are also provided (not iterated) for comparison.

Centre-to-centre Distance (km)	Iteration Number	RMS difference to GLDAS anomaly (cm EWH)
0	1	10.5 (6.4)
	2	10.3 (6.1)
	3	9.9 (6.0)
	4	9.8 (5.9)
	5	9.7 (6.0)
	6	9.8 (6.0)
	7	9.8 (6.2)
	8	9.9 (6.3)
1000	1	10.4 (6.2)
	2	10.1 (6.2)
	3	9.9 (6.2)
	4	9.8 (6.2)
	5	9.8 (6.3)
	6	9.8 (6.4)
	7	9.8 (6.5)
	8	9.9 (6.7)
2000	1	9.3 (5.9)
	2	9.1 (5.8)
	3	8.8 (5.6)
	4	8.7 (5.5)
	5	8.6 (5.5)
	6	8.6 (5.5)
	7	8.6 (5.5)
	8	8.6 (5.5)
3000	1	8.3 (5.2)
4000	1	7.7 (4.7)
5000	1	7.6 (4.6)
6000	1	7.5 (4.5)
All mascons	1	7.4 (4.4)

Table 16. RMS of the differences between the iterated 4° mascon solutions and the input GLDAS anomaly in cm of EWH. RMS values are provided over land (and globally). The inclusion of a mascon into the solution depends on the distance between that mascon and the nadir mascon being lower than the centre-to-centre distance.

Table 16 shows that, while iterating will improve the solution, the extent of the improvement is limited. For iterated solutions convergence is normally reached by ~5 steps. The RMS improves with an increase in the centre-to-centre distance of the solution through to 6000 km at which the difference in the RMS is only 0.06 cm of

EWH to the original (all mascon) solution. A similar result is observed for more limited testing of the 2° solution. Iterations improve the solution but are not a substitute for using an appropriate centre-to-centre cut-off distance and the simulations show that iterations were unable to overcome modelling deficiencies associated with an insufficient distribution of mascons when using perfect data. Iterations are therefore not used in the remainder of the simulations. Note that this iterative procedure is not intended as a study of the use of iterating a correctly parameterised solution. Applying iterations to real GRACE observations, as discussed in Luthcke et al. (2013), would be expected to yield improvements due to the separation of signal and noise through enhanced quality control of the residuals. Sabaka et al. (2010) found that forward modelling improved signal recovery while resulting in KBRR residuals that conformed more closely to zero-mean Gaussian distributions.

6.5 *Simulated recovery of the GLDAS anomaly with simulated stripes*

Computations to this point used noise free data. The effect of adding realistic noise to the simulated KBRR observations, generated from observed noise in processing actual GRACE data, can now be tested. In Chapter 5, the two stage processing strategy for GRACE data was discussed. The first stage provides the accelerometer bias values for the short-arc gravity field recovery in the second stage. To generate the KBRR noise the parameterisation of the accelerometer runs, described in section 5.2, was changed. Instead of the KBRR parameterisation, 96 sets of empirical along-track and cross-track once per revolution empirical acceleration parameters were now estimated (as in test 4 in section 5.2.4). The empirical accelerations absorbed the longer wavelength gravity field mis-modelling with the KBRR residuals representing a realistic sample of the noise present in the GRACE data. The empirical acceleration once per rev parameters also lead to slightly different values for the accelerometer biases values and estimated state vectors than the ones obtained in Chapter 5. The small differences in the accelerometer bias values between the runs are assumed to be similar to the differences between the original values and the unknown ‘true’ values. Similarly, the orbit used to calculate the KBRR residuals will be different to the orbits used in the gravity recovery, calculated in section 5.3.4, due to the use of different empirical parameters. The KBRR residuals time series will also contain errors in the orbit introduced from the inclusion of the GNV1B data as well as the KBRR data. GNV1B data is not used in the 60 minutes arcs for gravity recovery as discussed in section 5.3. Furthermore, the KBRR residuals will also contain effects of aliasing of short period signals and errors in the background

models which will affect the real GRACE solution. AOD1B (Atmosphere and Ocean de-aliasing Level-1B) product and the GLDAS anomaly field were used in all computations.

Despite best efforts it is likely that residual geographical correlated terms are present in the KBRR residuals due to the parameterisation failing to absorb all gravity field mis-modelling. To overcome this, the characteristics of the error signatures were preserved but the geographically mass signatures redistributed by applying a Fast Fourier Transform (FFT) to the residual time series. Modified KBRR residuals for each 24 hour were calculated by reconstructing the FFT through keeping the same amplitude of spectral frequency but assigning a random phase. Figure 43 shows the original and modified FFT and KBRR residuals.

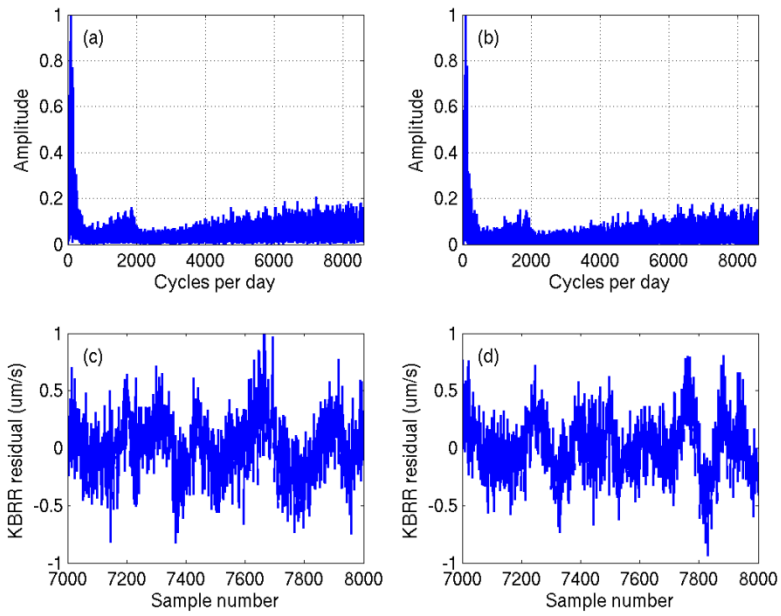

Figure 43. Periodogram of the original KBRR residual time series (a); periodogram created from a FFT of the phase-shifted reconstructed KBRR time series (b); sample of the original KBRR residual time series (c); sample of the phase-shifted reconstructed KBRR residual time series (d).

Figure 43(a) shows the original periodogram, while Figure 43(b) shows the modified spectrum used to generate the required KBRR residuals. Figure 43(c) shows a sample of the original KBRR residuals, while Figure 43(d) shows the modified KBRR residuals. The original and modified KBRR residuals have similar range and noise characteristics. Figure 43(a) shows features that are replicated in Figure 43(b). The low frequencies (i.e. long spatial wavelengths) were investigated and characterised as flicker noise using create and analyse time-series (CATS) (Williams, 2008). Higher frequencies were seen

to be approximately Gaussian with an increase in power between 1800 and 1900 cycles per day. The frequency of this signal with increased power corresponds to about twice the separation distance between the GRACE satellites. Without this artefact it would have been possible to generate the spectrum using a combination of flicker and Gaussian noise. Tests with other days and months showed that the periodogram was representative.

Tracking data, in 60 minute arcs, was created with the modified KBRR residuals and the gravity field solution recovered to degree and order 60. The resulting gravity field is shown in Figure 44.

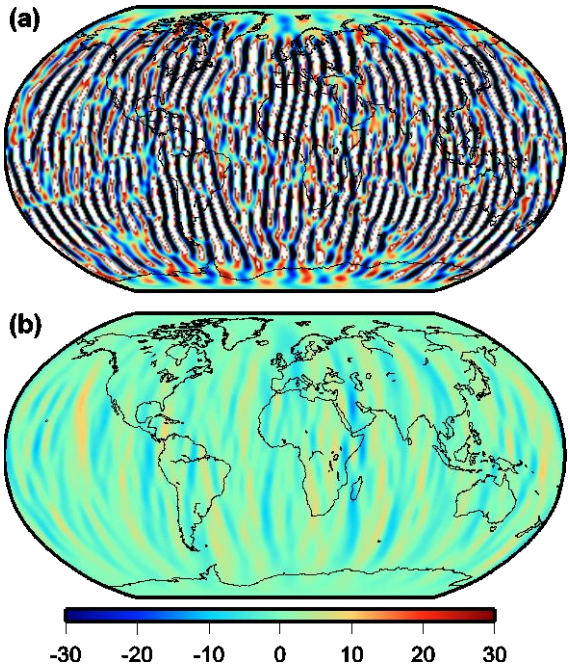

Figure 44. Simulated stripes: unsmoothed (a); with 400 km Gaussian smoothing (b).

Figure 44 reveals that the recovered solution is dominated by short wavelength, high degree, north-south orientated stripes; Figure 44(b) shows the same but with 400 km Gaussian smoothing applied. The stripes are typical of those in the monthly GRACE solutions. Figure 45 is a plot of the degree variance of the simulated stripes.

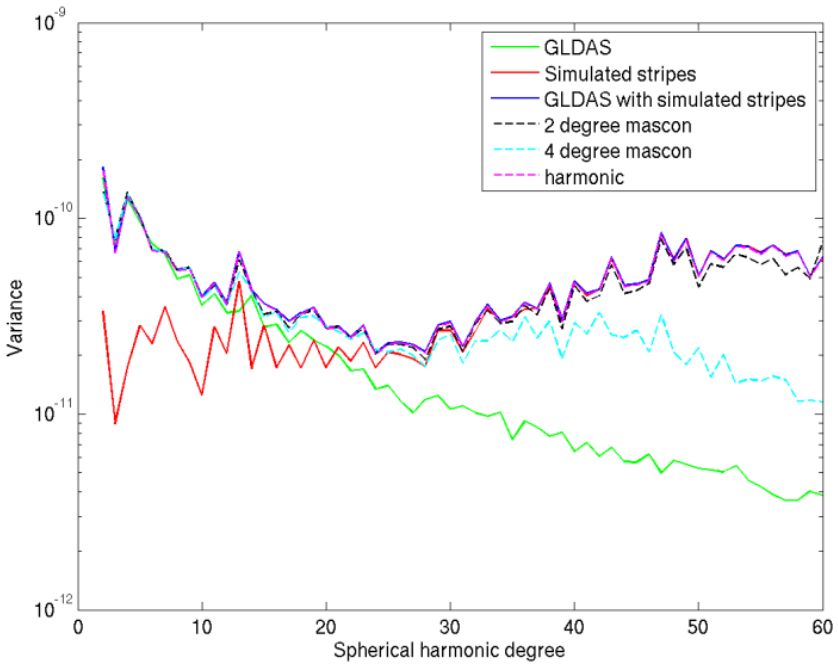

Figure 45. Degree variances of the simulated stripes, GLDAS with simulated stripes added and the unfiltered spherical harmonic and unconstrained mascon solutions. The original GLDAS model is included for comparison.

Figure 45 shows that the simulated stripes begin to dominate the signal between degree 20 and 30. Degree 30 is the degree at which regularisation is normally applied to monthly solutions (Bruinsma et al., 2010, Save et al., 2012) as required to reduce the effect of noise in the high degree coefficients. The power of the degree variances of the simulated stripes above degree 30 was found to be comparable to those of the unsmoothed CSR solution for June 2006. Most of the true geophysical signal is restricted to lower degrees, below degree ~20 (Wouters and Schrama, 2007) but short wavelength signals, as required for hydrological and glaciological basin-level applications, is contained in the higher degrees (Kusche, 2007). This simulation thus allows for an assessment of the ability of the different methodologies to maintain the signal at lower degrees while reducing noise in the higher degrees and maximising recovery at these shorter wavelengths.

The modified KBRR residuals were added to the original tracking data that described the GLDAS anomaly in section 6.2. These residuals emulate the spectrum of real GRACE noise with consequences that mirror the errors in actual monthly GRACE fields. The degree variances of the unconstrained solutions in Figure 45, show that the spherical harmonic and 2° mascon solution are able to reproduce the GLDAS anomaly with simulated stripes. The global values of the 0 km (50 km) solution in Table 17 (spatial constraint mascon solutions) confirm that the simulated stripes are present in the

spherical harmonic and 2° mascon solutions, with RMS values of 38.1 cm and 35.2 cm respectively. The 4° mascon solution is able to reproduce the degree variance of the GLDAS plus simulated stripes to degree ~35, at which point it loses power. This loss of power, a consequence of under sampling of the signal, results in a RMS of 14.7 cm in Table 17 for the 0 km solution. Again, the distance for the spherical harmonic coefficients refers to the Gaussian smoothing radius, while for the mascon solutions the distance is *D* of Eq. (16). As previous, the distances are not directly comparable.

	RMS difference to GLDAS anomaly (cm EWH)				
Distance (km)		**Spatial constraint**		**Basin constraint applied**	
	SH coefficients	4° mascon	2° mascon	4° mascon	2° mascon
0	38.1 (37.1)	14.9 (14.7)	36.4 (35.2)	-	-
50	37.1 (35.9)	14.9 (14.7)	31.4 (30.2)	14.9 (14.7)	31.8 (30.4)
100	31.4 (30.3)	14.1 (13.6)	18.2 (17.3)	14.2 (13.7)	19.3 (17.7)
150	24.3 (23.1)	12.2 (11.1)	13.1 (11.9)	12.6 (11.2)	14.1 (12.3)
200	17.7 (16.4)	10.9 (9.2)	11.1 (9.5)	11.3 (9.3)	11.8 (9.7)
250	13.2 (11.4)	10.1 (8.0)	10.1 (8.1)	10.5 (8.1)	10.7 (8.3)
300	10.9 (8.4)	9.6 (7.3)	9.5 (7.2)	9.9 (7.4)	10.0 (7.4)
350	10.1 (6.9)	9.3 (6.7)	9.1 (6.7)	9.6 (6.8)	9.5 (6.8)
400	10.0 (6.4)	9.1 (6.4)	8.9 (6.3)	9.3 (6.4)	9.2 (6.4)
450	10.1 (6.2)	8.9 (6.1)	8.8 (6.0)	9.2 (6.2)	9.0 (6.1)
500	10.3 (6.2)	8.9 (5.9)	8.7 (5.8)	9.0 (5.9)	8.9 (5.9)
550	10.5 (6.3)	8.8 (5.8)	8.6 (5.6)	8.9 (5.8)	8.8 (5.7)
600	10.7 (6.3)	8.8 (5.7)	8.6 (5.5)	8.9 (5.6)	8.8 (5.5)
650	10.9 (6.4)	8.8 (5.6)	8.6 (5.4)	8.8 (5.5)	8.7 (5.4)
700	11.1 (6.5)	8.8 (5.5)	8.6 (5.4)	8.8 (5.5)	8.7 (5.4)
750	11.3 (6.5)	8.8 (5.5)	8.7 (5.3)	8.8 (5.4)	8.7 (5.3)
800	11.5 (6.6)	8.8 (5.4)	8.7 (5.3)	8.8 (5.3)	8.7 (5.3)
850	11.6 (6.7)	8.8 (5.4)	8.7 (5.3)	8.8 (5.3)	8.7 (5.2)
900	11.8 (6.7)	8.9 (5.4)	8.7 (5.2)	8.8 (5.3)	8.7 (5.2)
950	11.9 (6.8)	8.9 (5.4)	8.8 (5.2)	8.8 (5.3)	8.7 (5.2)
1000	12.0 (6.9)	8.9 (5.3)	8.8 (5.2)	8.8 (5.2)	8.7 (5.2)
1050	12.1 (6.9)	8.9 (5.3)	8.8 (5.2)	8.8 (5.2)	8.7 (5.1)
1100	12.2 (7.0)	9.0 (5.3)	8.9 (5.2)	8.8 (5.2)	8.8 (5.1)

Table 17. RMS (cm of EWH) of the differences between the calculated gravity field solutions and input GLDAS anomalies in the presence of simulated stripes. RMS values are provided over land (globally). The distance refers to the Gaussian smoothing radius (spherical harmonic solution) or the correlation distance (mascon solutions). Mascon solution constrained using spatial (columns 3 and 4) or basin constraints (columns 5 and 6).

Regardless of the strategy used to recover the simulated field, some form of post-processing is required to reduce the effects of noise in the solution. Increasing the Gaussian smoothing distance for the spherical harmonic solution reduces the RMS towards the original GLDAS anomaly, with 400 km Gaussian smoothing producing the lowest RMS to the GLDAS anomaly (Table 17). The global RMS still reduces for 500

km Gaussian smoothing due to smoothing over the oceans, but by 500 km the land signal is over smoothed. Applying a lower smoothing radius allows the simulated stripes to dominate the solution, while a larger smoothing radius reduces the amplitude of geophysical signals and removes short wavelength information.

For both the 4° and 2° mascon solutions, increasing the correlation distance *D* in the constraint matrix reduces the RMS until ~700 km. Over all solutions in Table 17 the 2° mascon solution provides the closest match to the GLDAS anomaly when a correlation distance of ~650 km is used in the constraint matrix. For the 4° mascon solution the effect on the weight matrix *V* of varying the value of *S* in the Eq. (16) was investigated.

The weight matrix *V* is dependent on *S* and *D*. Using $S = 0.001$, the lowest RMS (8.8 cm EWH) was achieved using $D = 700$ km. When $S = 0.01$ (0.0001) were used RMS values of 9.8 (10.3) were obtained. For $S = 0.01$ the lowest RMS was 8.8 cm when $D = 250$ km, while for $S = 0.0001$ an RMS of 9.0 cm was obtained when $D = 1500$ km. Therefore, within the scope of this limited testing, it can be concluded that $S = 0.001$ to be the optimal scale factor for the simulations. This will be used for all further processing. Figure 46 is a plot of the degree variances of GLDAS anomaly (with and without simulated stripes) and the spherical harmonic and mascon solutions.

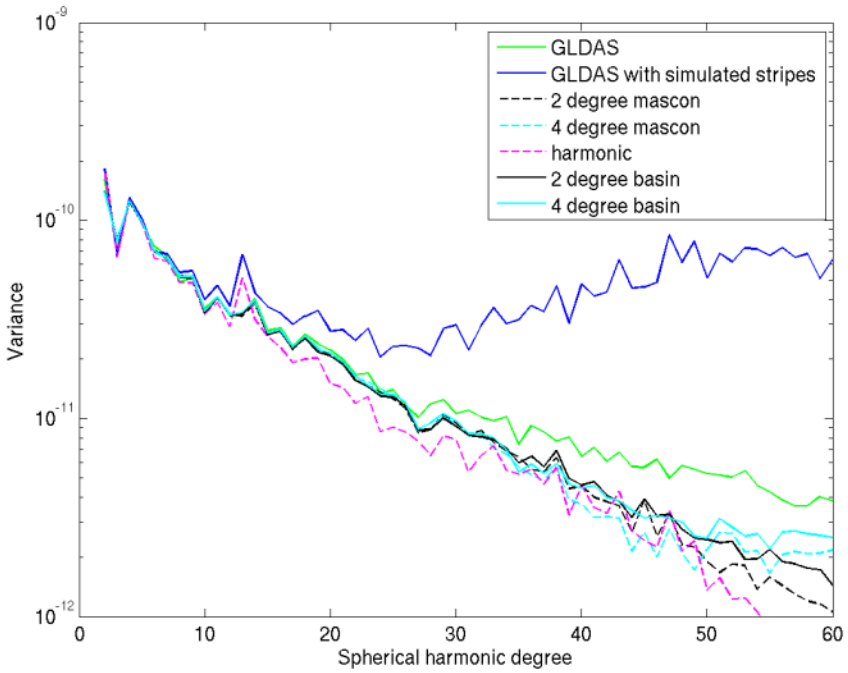

Figure 46. The degree variances of GLDAS (with and without simulated stripes) and the spherical harmonic and mascon solutions. 2° and 4° mascon are the constrained mascon solutions without the basin constraints applied while 2° and 4° basin are the constrained mascon solutions with basin constraints applied. The spherical harmonic solution has 400 km Gaussian smoothing applied; the mascon solutions are constrained using a correlation distance of 700 km in the constraint matrix (without basin constraints) and 900 km (with basin constraint).

Figure 46 shows the degree variances of the spherical harmonic solution with 400 km Gaussian smoothing. It is not possible to directly relate the Gaussian smoothing distance to the mascon correlation distance so the mascon solutions for D = 700 km are shown. This value was chosen as a comparison of the degree variances of the solutions given in Table 17 revealed it removes a comparable amount of noise to the spherical harmonic solution at the higher degrees. It also gives one of the lowest RMS values to the GLDAS anomaly. Figure 46 reveals that all solutions have removed a similar amount of noise above degree 30, and contain less power at these degrees compared to the GLDAS signal. The mascon solutions more closely resemble the power of the GLDAS signal between degree ~15 and 30 than the spherical harmonic solution. The reduced power of the spherical harmonic signal between degree ~15 and 30 could be partly related to the degree dependency of the Gaussian filter which Han et al. (2005) suggested could suppress information over this range. The mascon solution has therefore been able to recover more of the original signal at degrees ~15 to 30 while removing a comparable amount of noise at higher degrees. Due to the 4° mascon solution under-sampling the signal, the 4° mascon solution will not be recovered in any further simulations and not used when calculating mascon solutions from real GRACE data.

6.6 *Basin constraints*

Mascon solutions with spatial constraints are able to remove more noise and retain more signal than spherical harmonics solutions with Gaussian smoothing. However, thus far, the full advantage of the mascon processing strategy has yet to be exploited; namely that the constraint matrix, *C*, in Eq. (13) can be adapted to constrain mascons that share geophysical similarities as in Luthcke et al. (2006b). Thus, in addition to separating mascons into either land or ocean, they are now extended to separate the major hydrological drainage basins defined by the Total Runoff Integrating Pathways (TRIP) dataset (Oki and Sud, 1998). Major Greenland and Antarctic drainage basins are adopted according to Zwally et al. (2012). The result is a constraint matrix where constraints are imposed between all land mascons within the same (hydrological or glaciological) drainage basin, with mascons in different basins uncorrelated. Not all land mascons are within a major hydrological or glaciological basin. Land mascons that are not classified as belonging to a basin were assumed to be correlated, but in most instances d_{IJ} of Eq. (16) reduces the correlation to ~zero. All ocean mascons are correlated as previous.

Table 17 (Basin constraint mascon solutions) summarises the RMS of the differences to the GLDAS plus simulated stripes. For both mascon solutions the use of a basin constraint, while offering a similar or small improvement in the RMS over land, offers an improvement in global RMS values over the solutions without basin constraints. An increase in the correlation distance (800-900 km) is required to obtain these improvements due to the reduced number of constraints based on mascons pairs that share geophysical similarities. The improved global RMS is due to reduction of the simulated stripes over the ocean. As ocean mascons are constrained together, the increased correlation distance allows the effect of the simulated stripes to be further mitigated. The improvement is evident in the degree variances of the mascon solutions (basin) plotted in Figure 46. Comparing mascon solutions with and without basin constraints, the power of the resulting mascon solutions from degrees 30 to 60 more closely matches the input signal when the basin constraint is applied. The constraints have successfully reduced the noise at these degrees while reducing loss of actual signal. Retention of short wavelength signal is of fundamental importance for improving basin-scale hydrological and glaciological recovery and for estimating basin-level mass flux.

The final recovered GLDAS anomalies are shown in Figure 47 for the spherical harmonic solution with 400 km Gaussian smoothing together with the 2° mascon solution using a 800 km correlation distance and basin constraints. The input GLDAS anomaly is provided for reference.

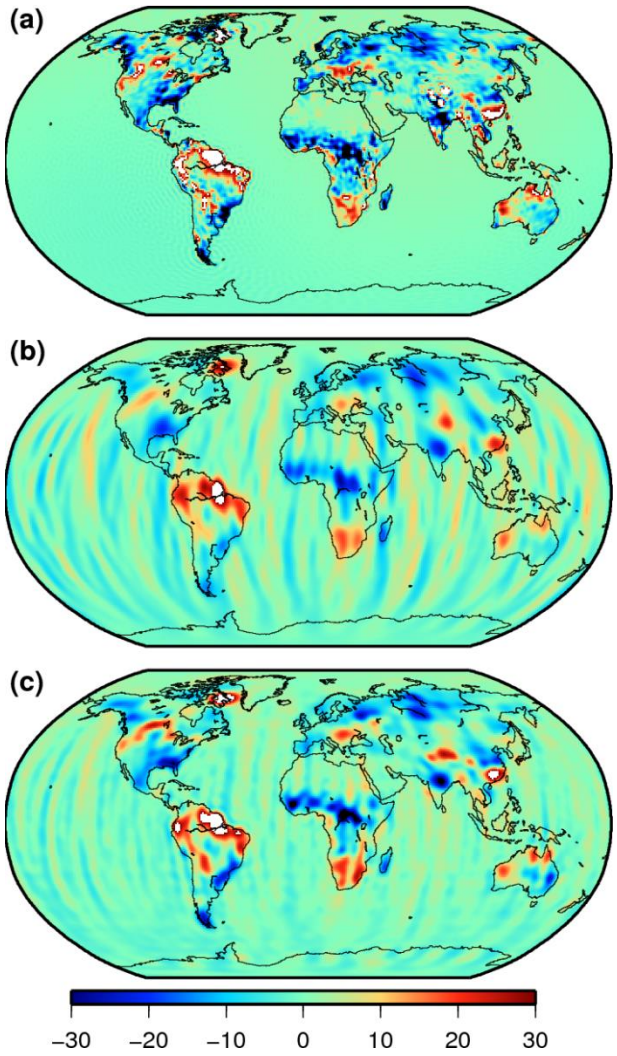

Figure 47. GLDAS anomaly for June 2006 to degree and order 120 (a); Recovered GLDAS anomalies for the spherical harmonic solution with 400 km Gaussian smoothing to degree and order 60 (b); and 2° mascon solution with a basin constraint applied, with 800 km correlation distance (c). Units of cm EWH.

Comparing Figure 47(c) to Figure 47(a) validates the 2° mascon solution. The mascon methodology offers a clear improvement in the recovery of TVG and suppression of simulated stripes compared with a spherical harmonic solution with Gaussian smoothing. The reduction of the simulated stripes over the ocean is particularly evident. Unlike spherical harmonics, mascons allow constraints within areas that share real world geophysical properties. Any number of constraints can be applied with the aim of improving the overall recovery of the time varying gravity field.

6.7 *Simulated recovery of Antarctic mass change signal*

One of the scientific advances provided by the GRACE mission is recovery of continent-wide ice sheet mass change estimates, such as over Antarctica, with temporal resolutions of 30 days or less. So far the simulations have focused on recovery of a GLDAS hydrological anomaly. Given the scientific interest in contribution of ice sheets to sea-level change and the convergence of orbital tracks at the pole we now simulate recovery of a realistic Antarctica mass signal along with the GLDAS anomaly and noise product described in section 6.5. The simulated Antarctica mass signal was derived from the basin mass change rates provided in Table S1 of the supplementary material of King et al. (2012). While King et al. (2012) calculated GRACE solutions to degree and order 60, forward modelling across defined basins resulted in a higher effective resolution. The mass change rates used have been corrected for leakage but still contain the GIA signal that is observable from GRACE. Using the same drainage basins adopted by King et al. (2012), as defined using ICESat data (Zwally et al., 2012), the mass change rates for each basin were converted to a total mass change in cm of EWH using the density of water and the area of each drainage basin. As in King et al. (2012) basins 25 and 26, which cover the northern tip of the Antarctica Peninsula, were merged into a single basin. The resulting mass changes for each basin were then expanded into spherical harmonics to degree and order 60 and added to the mean background field to create the KBRR tracking data. Simulated stripes are included as previous. The simulated Antarctic mass change signal can be seen in Figure 48(a).

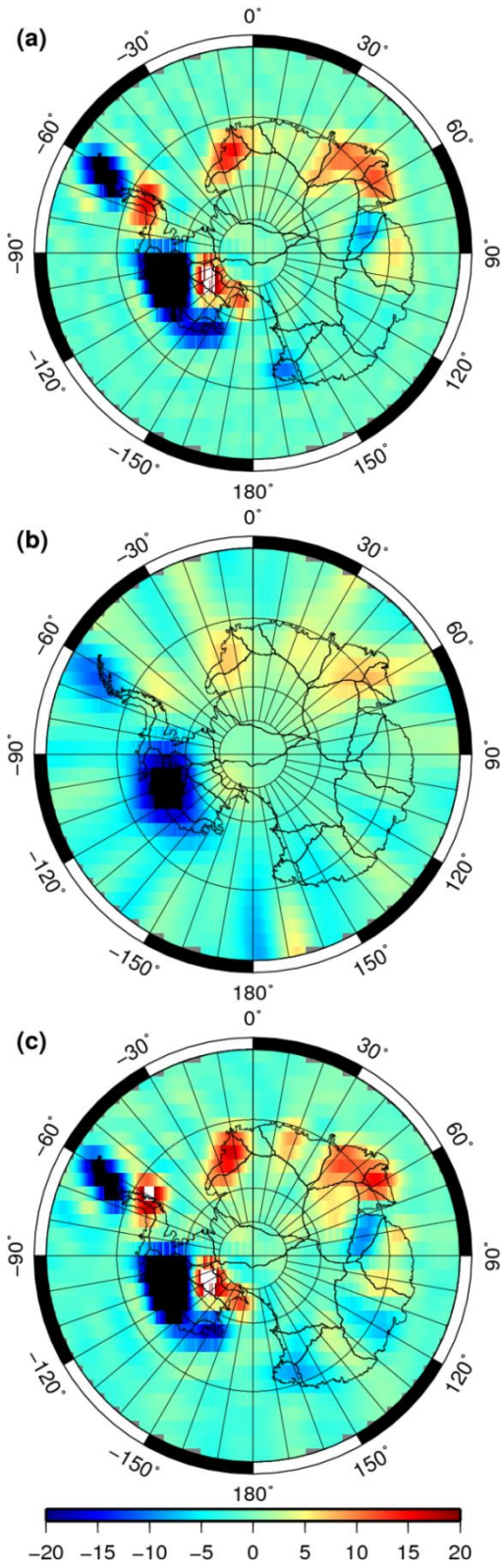

Figure 48. Simulated Antarctic mass change signal (a); spherical harmonic solution filtered with a 350 km Gaussian smoother (b); and 2° mascon solution with basin constraint with correlation distance D = 800 km(c). Units of cm of EWH

Plotting the unfiltered degree variances (Figure 49) reveals that the spherical harmonic and 2° mascon solution were able to reproduce the Antarctica mass signal added to the GLDAS anomaly and simulated stripes. Application of a single value of mass change

per basin is a simplification on the real spatial pattern of change, but this assumption is sufficient for our purposes here.

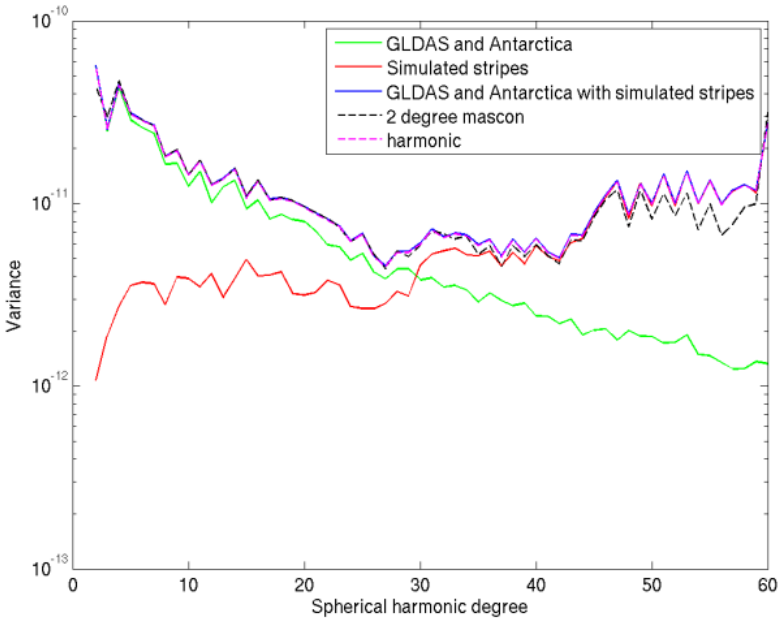

Figure 49. Degree variances of GLDAS and Antarctica, simulated stripes, GLDAS and Antarctica with simulated stripes and the unfiltered spherical harmonic and unconstrained mascon solutions.

	RMS difference to GLDAS anomaly and Antarctic mass change (cm EWH)					
Distance (km)	**Main period**		**Resonance period**		**Reduced thermal control**	
	SH	2° mascon	SH	2° mascon	SH	2° mascon
200	17.7 (16.4)	11.8 (9.8)	20.3 (19.8)	8.1 (5.3)	45.2 (45.5)	13.9 (11.0)
250	13.2 (11.4)	10.7 (8.3)	14.8 (13.8)	8.0 (5.0)	29.9 (29.7)	12.4 (9.3)
300	10.9 (8.4)	10.0 (7.4)	11.6 (9.8)	8.0 (4.9)	20.6 (19.5)	11.7 (8.2)
350	10.1 (7.0)	9.5 (6.8)	10.3 (7.6)	8.0 (4.9)	15.6 (13.7)	11.3 (7.6)
400	10.0 (6.4)	9.2 (6.4)	10.0 (6.6)	8.1 (4.9)	13.2 (10.6)	11.0 (7.2)
450	10.2 (6.3)	9.0 (6.1)	10.1 (6.2)	8.2 (4.9)	12.2 (9.0)	10.9 (7.0)
500	10.4 (6.3)	8.9 (5.9)	10.3 (6.2)	8.3 (4.9)	11.7 (8.1)	10.8 (6.8)
550	10.6 (6.3)	8.8 (5.7)	10.6 (6.2)	8.3 (4.9)	11.6 (7.6)	10.8 (6.6)
600	10.8 (6.4)	8.8 (5.5)	10.8 (6.3)	8.4 (4.9)	11.6 (7.4)	10.8 (6.6)
650	11.0 (6.4)	8.7 (5.4)	11.1 (6.4)	8.5 (5.0)	11.6 (7.2)	10.8 (6.5)
700	11.2 (6.5)	8.7 (5.4)	11.3 (6.5)	8.6 (5.0)	11.7 (7.2)	10.8 (6.5)
750	11.4 (6.6)	8.7 (5.3)	11.5 (6.6)	8.6 (5.0)	11.8 (7.1)	10.9 (6.4)
800	11.6 (6.7)	8.7 (5.3)	11.7 (6.7)	8.7(5.0)	11.9 (7.1)	10.9 (6.4)
850	11.7 (6.7)	8.7 (5.2)	11.8 (6.8)	8.8 (5.1)	12.0 (7.1)	11.0 (6.4)
900	11.9 (6.8)	8.7 (5.2)	12.0 (6.9)	8.8 (5.1)	12.1 (7.1)	11.0 (6.4)
950	12.0 (6.9)	8.7 (5.2)	12.1 (6.9)	8.9 (5.1)	12.2 (7.1)	11.1 (6.4)
1000	12.1 (6.9)	8.7 (5.2)	12.2 (7.0)	9.0 (5.2)	12.3 (7.2)	11.1 (6.4)
1050	12.2 (7.0)	8.7 (5.1)	12.3 (7.0)	9.0 (5.2)	12.3 (7.2)	11.2 (6.5)
1100	12.3 (7.0)	8.8 (5.1)	12.4 (7.1)	9.1 (5.2)	12.4 (7.2)	11.2 (6.5)

Table 18. RMS (cm of EWH) of the differences between the calculated gravity field solutions and the input GLDAS anomaly with Antarctic mass change signal in the presence of different simulated noise products. RMS values are provided over land (and globally). The distance refers to the Gaussian smoothing radius (spherical harmonic coefficient solutions) or the correlation distance (mascon solutions). All mascon solutions utilise basin constraints described in section 4.6. For the thermal mascon solutions the value *S* in Eq. (16) was increased from 0.001 to 0.01.

Solutions were estimated for the spherical harmonics and 2° mascon methodologies with the RMS values shown in Table 18 (main period). The drainage basins used in the mascon solution in Section 6.6 result in mascons within the same Antarctic drainage basin being constrained together, but with mascons in different Antarctic basins uncorrelated. The mascon results are shown in Figure 48(c) revealing this solution has been able to recover most of the input signal (Figure 48(a)) while the spherical harmonic solution filtered with 400 km Gaussian smoothing (Figure 48(b)) has recovered the spatial extent of the signal but with reduced amplitudes. This is important to consider within future GRACE studies of Antarctic ice mass change. The lowest RMS of the differences to the input signal (in EWH) over Antarctica is 8.7 cm for the mascon solution (800 km correlation distance) and 10.0 cm with spherical harmonics

(400 km Gaussian smoothing). As with the global hydrological simulations, more of the signal was recovered using the mascon methodology.

As a final comparison the mascon solution was computed again using only the land/ocean constraints applied in Section 6.5. The RMS of the difference to the input Antarctica signal was 8.8 cm. This highlights the advantage offered by the mascon methodology when real-world geophysical properties are used to define the constraints between the mascons.

6.8 *Simulated recovery of Greenland mass change signal*

The GRACE mission yields continent-wide ice sheet mass change estimates of Greenland. However, over Greenland signals can leak in and out of nearby regions, with the layout of the drainage basins also affecting the results (Bonin and Chambers, 2013). With this in mind, a simulated recovery of a Greenland mass signal will be undertaken in the presence of the simulated stripes, described in section 6.5, only. No other signal will be present. This will help in quantifying the effect the layout of the drainage basins have on the recovered solution while allowing signal leakage to be identified.

The simulated Greenland mass signal was derived from the basin mass change rates provided in Table 2 of Sasgen et al. (2012) which have been corrected from GIA using ICE-5G (Peltier, 2004). Like the simulated Antarctica mass signal in section 6.7, the mass change rates for each basin were converted to a total mass change in cm of EWH using the density of water and the area of each drainage basin. The resulting mass changes for each basin were then expanded into spherical harmonics to degree and order 60 and added to the mean background field to create the KBRR tracking data. Simulated stripes are included as previous. The simulated Greenland mass change signal (without stripes) can be seen in Figure 50 (Greenland only) and Figure 51 (globally). Again, the application of a single value of mass change per basin is a simplification of the real spatial pattern of change, but this assumption is sufficient for the purposes here.

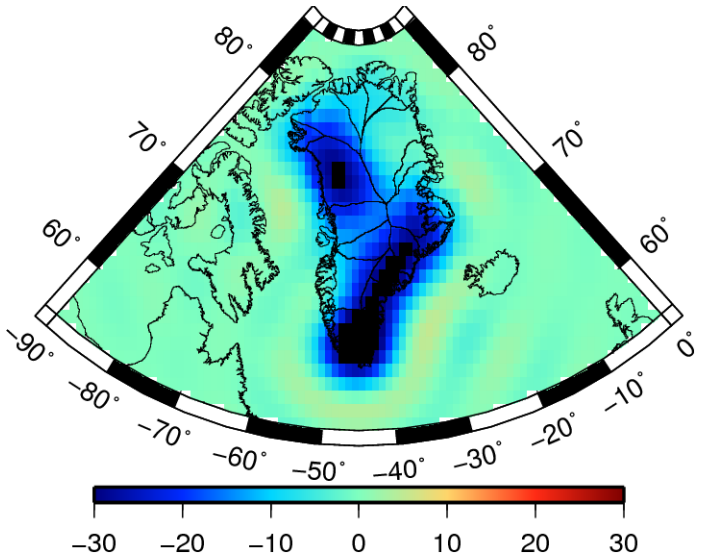

Figure 50. Simulated Greenland input signal. Units are cm of EWH

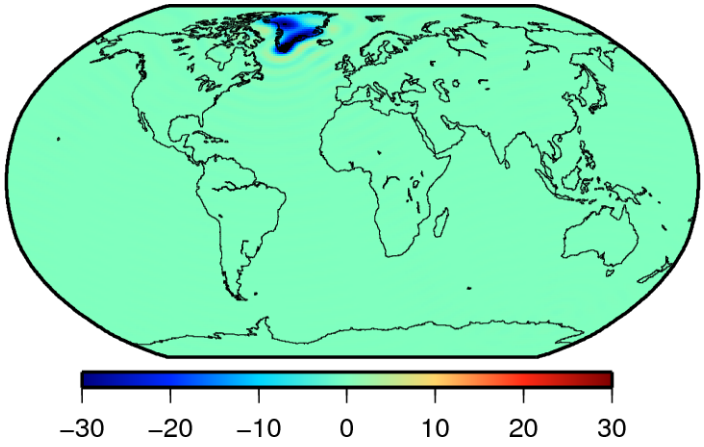

Figure 51. Simulated Greenland input signal plotted globally. Units cm of EWH

As for the simulated recovery of Antarctica, solutions were estimated for the spherical harmonics and 2° mascon methodologies. The results RMS values are shown in Table 19.

Basin layout	**RMS (cm EWH)**
SH	7.46
2° mascon solutions	
Spatial constraint	5.23
Basin constraint – Zwally et al. (2012) basins	2.76
Basin constraint – Greenland major basins	1.76
Basin constraint – Major basins with 1 basin over 2000 m	2.24

Table 19. RMS (cm of EWH) of the differences between the calculated gravity field solutions and the Greenland mass change signal in the presence of the simulated stripes. The RMS is provided for solutions estimated using the spherical harmonics and 2° mascon methodologies. The Gaussian smoothing radius (spherical harmonic coefficient solutions) was 400 km. The 2° mascon solution is provided for four different basin layouts (D=800 km).

To quantify the effects that different drainage basin layouts have on the mascon solution, the 2° mascon methodology was constrained using 4 different drainage basin layouts as shown in Table 19. In all solutions a correlation distance of *D*=800 km was used. A correlation distance of *D*=800 km is required when using basin constraints in the mascon solution (Table 17). The recovery using spherical harmonic parameters is included for reference.

The first basin layout (spatial constraint) is a simple land/ocean constraint, as applied in section 6.5. This results in correlation between all the Greenland mascons, plus a correlation between other nearby land mascons. The second basin layout (Basin constraint – Zwally et al. (2012) basins) uses the Greenland drainage basins as defined using ICESat data (Zwally et al., 2012). These basins were included in the simulated recovery in section 6.6. The layout of the basins over Greenland is shown in Figure 52 with the outlines of the mascons included for reference. The mascons are numbered according to the basin that the mascon has been assigned to. Mascons around Greenland that are not numbered are ocean mascons. The use of drainage basins allows constraints to be imposed between all land mascons within the same glaciological drainage basin, with mascons in different basins uncorrelated.

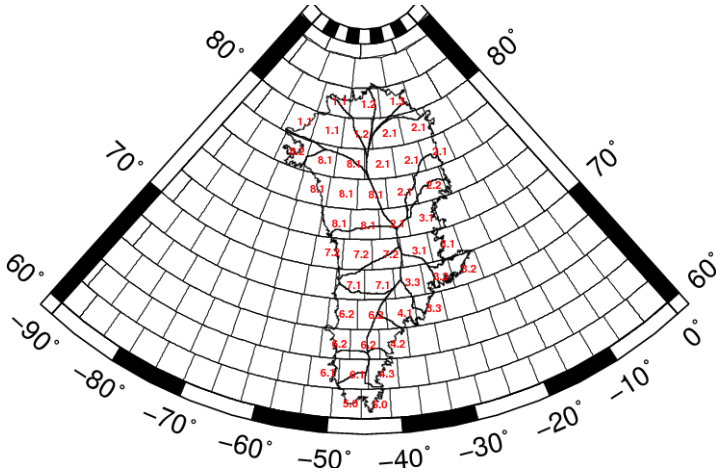

Figure 52. Greenland drainage basins as defined using ICESat data (Zwally et al., 2012) (black). The distribution of 2° equal area mascons around Greenland is shown for reference. Mascons over Greenland are numbered according to the Zwally et al. (2012) basin in which they lie.

In Figure 52 there are different basins that have the same integer number, but are subdivided using a decimal point e.g. 8.1, 8.2, 8.3. For the Zwally et al. (2012) basins, these ‘sub-basins’ are treated as individual basins. There are a total of 19 sub-basins. The third basin layout (Basin constraint – Greenland major basins) combines the sub-

basins within an integer basin to create ‘major-basins’. For example sub-basins 8.1, 8.2, 8.3 are combined to form basin major-basin 8. Combining all the sub-basins within each integer basin creates 8 major-basins. There are now more mascons in each basin.

Luthcke et al. (2006a) estimated a mascon solution over Greenland where the mascons were separated into basins above and below 2000 m and found that the interior of Greenland was experiencing an increase in mass, with the main mass loss signal occurring around the margins. Accordingly, the major-basin layout was modified to create an additional basin for all mascons above 2000 m in elevation (Basin constraint – Major basins with 1 basin over 2000 m). The mascons above 2000m in elevation were identified using the basin layout in Luthcke et al. (2006a) and formed a new basin (basin 9). The mascons included in this new interior basin can be seen in Figure 53.

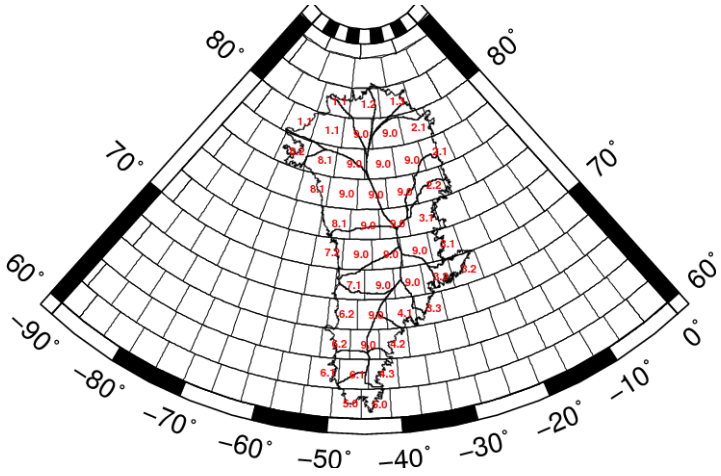

Figure 53. Greenland drainage basins as defined using ICESat data (Zwally et al., 2012) (black). The distribution of 2° equal area mascons around Greenland is shown for reference. Mascons over Greenland are numbered according to the Zwally et al. (2012) basin in which they lie. All mascons identified as being above 2000 m in elevation are numbered 9.0

The results from Table 19 reveal that the RMS of the difference between the calculated gravity field solution and the Greenland mass change signal, in the presence of the simulated noise product, is lowest for the Greenland major basins layout with all the 2° mascon solutions having an RMS value that is lower than for the recovery using spherical harmonic parameters. This again highlights the advantage offered by the mascon methodology when real-world geophysical properties are used to define the constraints between the mascons.

The differences between the calculated gravity field solution and the Greenland mass change signal is plotted in Figure 54 for the Zwally et al. (2012) drainage basins (Figure

54 (a)) and the major basins (Figure 54 (b)). Figure 54 confirms that the layout of the major basins has been able to recover more of the input signal compared with the Zwally et al. (2012) drainage basins. This improvement is the result of more mascons in each basin.

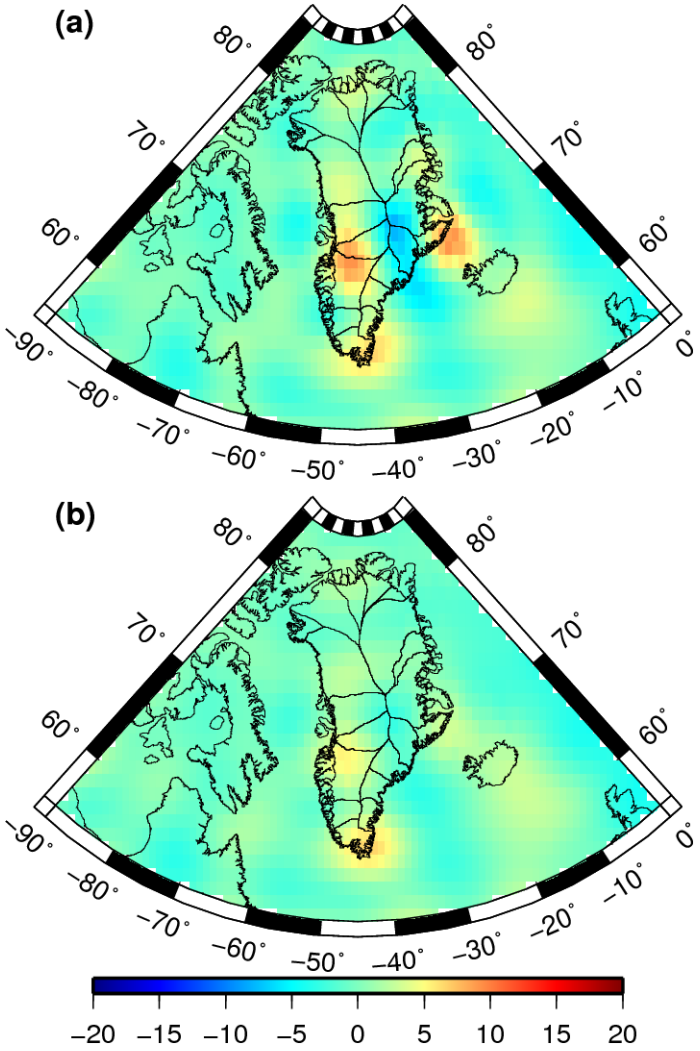

Figure 54. Difference to the input Greenland signal for the Zwally et al. (2012) drainage basins (a) and the major basins (b). Units cm of EWH.

6.8.1 *Leakage of GIA*

Regions surrounding Greenland, such as Hudson Bay, are known to have a strong GIA signal with potential for this signal to leak into Greenland when using the mascon methodology. To investigate this, the GIA signal from ICE-5G around Greenland was recovered using the basin layouts in Table 19 and plotted in Figure 55. The GIA signal was expanded into spherical harmonics to degree and order 60 and added to the mean background field to create the KBRR tracking data. Simulated stripes are included as previous.

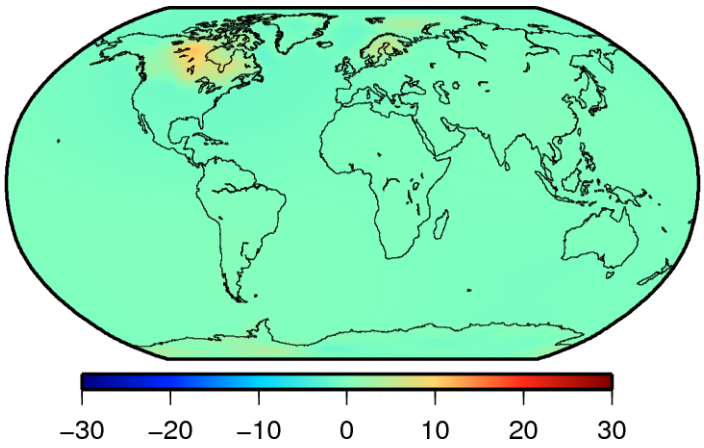

Figure 55. Global distribution of GIA from ICE-5G. The strong signal over Hudson Bay is evident. Units cm of EWH. To aid visualisation, the simulation stripes are not included.

Solutions were estimated for the spherical harmonics and 2° mascon methodologies, with the RMS values shown in Table 20. The 4 different mascon basin layouts described in section 6.8 were again applied to recovered GIA signal.

Basin layout	**RMS** (cm EWH)
SH	1.05
2° mascon solutions	
Spatial constraint	1.00
Basin constraint – Zwally et al. (2012) basins	2.74
Basin constraint – Greenland major basins	1.81
Basin constraint – Major basins with 1 basin over 2000 m	1.91

Table 20. RMS (cm of EWH) of the differences between the calculated gravity field solutions and GIA from ICE-5G with the simulated stripes. The RMS is provided for solutions estimated using the spherical harmonics and 2° mascon methodologies. The Gaussian smoothing radius (spherical harmonic coefficient solutions) was 400 km. The 2° mascon solution is provided for four different basin layouts (D=800 km). The only difference between the mascon solutions is the layout of the drainage basins over Greenland.

The results in Table 20 reveal that 3 out of the 4 basin layouts applied to the mascon methodology have a greater leakage of the GIA signal into Greenland, compared to using spherical harmonic coefficients. The only basin layout that has less leakage is the land/ocean (spatial constraint).

As the solutions in Table 20 contain the simulated stripes, which could be the cause of the apparent leakage, the solutions were calculated again without the simulated stripes. This is therefore a recovery of the GIA signal only. Solutions were estimated for the 2° mascon methodology with the four basin layouts used in Table 20. The RMS values obtained were 0.47 cm for the spatial constraint, 0.67 cm for the Zwally et al. (2012) basins, 0.60 cm for the Greenland major basins and 0.60 cm for the major basins with 1

basin over 2000 m. The RMS of the spherical harmonic solution was 0.58 cm. This reveals that most of the apparent leakage in Table 20 is the result of the simulated stripes not being completely removed in the mascon solutions. In Table 20 it would be expected that the land/ocean spatial constraint layout would contain the least noise as all land mascons are constrained together. Over Greenland the Zwally et al. (2012) basins layout would also be expected to contain the most noise as there are basins that contain only one or two mascons. When considering GIA leakage only, the spatial constraint has the lowest leakage. The leakage of the spherical harmonic and 2° mascon methodology, using the Greenland major basins and Major basins with 1 basin over 2000 m, are not significantly different.

Through recovering more of the Greenland signal than any other basin layout (Table 19) while limiting the leakage of GIA into Greenland, the Greenland major basins layout will be will be used to constrain the mascon solutions over Greenland. The basin constraint used in section 6.7 will be modified over Greenland to include the Greenland major basins.

6.9 *Simulated recovery of Greenland, GIA, GLDAS and Antarctica*

The Greenland component of the basin constraint, used in section 6.7, was modified to incorporate the Greenland major basins. This was then applied to the recovery of GLDAS anomaly (section 6.2), the Antarctica mass change signal (section 6.7), the Greenland mass change signal (section 6.8) and GIA signal (section 6.8.1). The combined signal to be recovered (without stripes) is shown in Figure 56. Figure 56 represents the majority of the signal GRACE would be expected to recover. This signal will be termed the ‘total’ signal. The total signal was expanded into spherical harmonics to degree and order 60 and added to the mean background field to create the KBRR tracking data. During the recovery simulated stripes are included as previous.

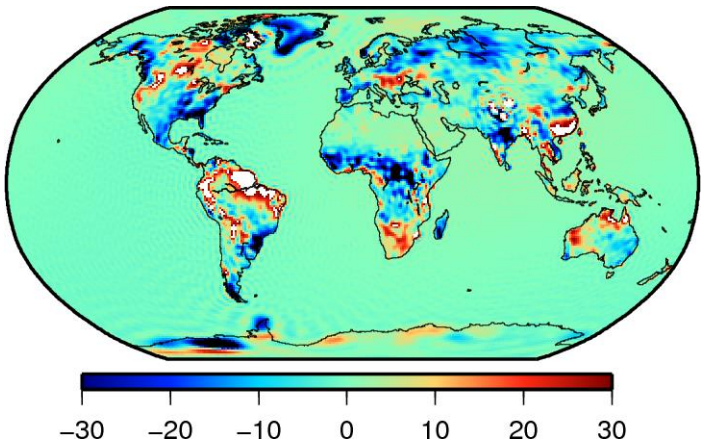

Figure 56. Simulated 'total' input signal. Includes the Greenland, GIA, and Antarctica mass change signals and the GLDAS anomaly. Units cm of EWH

Solutions were estimated for the spherical harmonics and 2° mascon methodologies with the RMS values shown in Table 21. For comparison, over Greenland the basin constraint was updated to contain all the different basin layouts described in section 6.8.

Basin layout	**RMS** (cm EWH)	
	Land	Globally
SH	10.09	6.49
2° mascon solutions		
Spatial constraint	8.79	5.39
Basin constraint – Zwally et al. (2012) basins	8.73	5.31
Basin constraint – Greenland major basins	8.71	5.30
Basin constraint – Major basins with 1 basin over 2000 m	8.73	5.31

Table 21. RMS (cm of EWH) of the differences between the calculated gravity field solutions and the total signal. The RMS is provided for solutions estimated using the spherical harmonics and 2° mascon methodologies. The Gaussian smoothing radius (spherical harmonic coefficient solutions) was 400 km. The 2° mascon solution is provided for four different basin layouts (D=800 km) where the only difference between the mascon solutions is the layout of the drainage basins over Greenland. RMS values are provided over land and globally.

The results in Table 21 highlight the advantage offered by the mascon methodology, over the use of spherical harmonic coefficients, when real-world geophysical properties are used to define the constraints between the mascons. For the mascon solutions, the lowest RMS (8.71) is obtained when using the Greenland major basins, compared to 8.79 for the simple land/ocean spatial constraint and 8.73 for the Zwally et al. (2012) basins and the major basins with 1 basin over 2000 m. This confirms the choice of the Greenland major basins to recover a mass change signal over Greenland.

6.10 *GRACE resonance and thermal control issues*

Periods where the GRACE satellites are in 3, 4 and 7 day repeat orbits modify the noise characteristics of the GRACE solutions (Save et al., 2012), while recent GRACE

solutions are affected by poor satellite thermal control. For replicating the GRACE errors and studying the correlations between the spherical harmonic coefficients in CSR RL05 solutions, covariance matrices are provided by CSR for the three characteristic periods in the GRACE mission: early mission (Feb 2002-May 2005), main part of the mission (Jul 2007- Dec 2010), and recent months (Feb 2011 -) which are affected by poor thermal control. Poor thermal control is the result of changes in accelerometer heating, brought on by decreasing battery performance (Kim and Tapley, 2015). Only three covariance matrices are required as the monthly variations within these periods are sufficiently minor as to be unimportant (John C Rise, personal communication, 2014). An additional covariance matrix is available for months where the satellite is in a repeat orbit (resonance). The effect these different periods have on the noise is investigated through recovery of the GLDAS anomaly and Antarctica mass change signal for two additional sets of simulated noise. The GLDAS anomaly and Antarctica mass change signal are the same as in previous simulations.

The first set of simulated noise relates to September 2004, when the GRACE satellites were in 61:4 resonance (Klokočník et al., 2013). In 61:4 resonance the satellite ground-track repeats every 61 orbital revolutions in the time the Earth revolves 4 times relative to the ascending node. This gives 122 repeating ascending and descending passes every 4 days spaced on average every 3° in longitude. The second set relates to March 2011, which corresponds to a period when the GRACE satellites are affected by poor thermal control. KBRR residuals for Sept 2004 and March 2011 with simulated noise were derived using the method of section 6.5. The modified FFT and KBRR residuals were computed for Sept 2004 and March 2011 (as in Figure 43). For Sept 2004, Figure 57 revealed that the noise in GRACE during resonance is indistinguishable from that of the main part of the mission. The March 2011 residuals are shown in Figure 58.

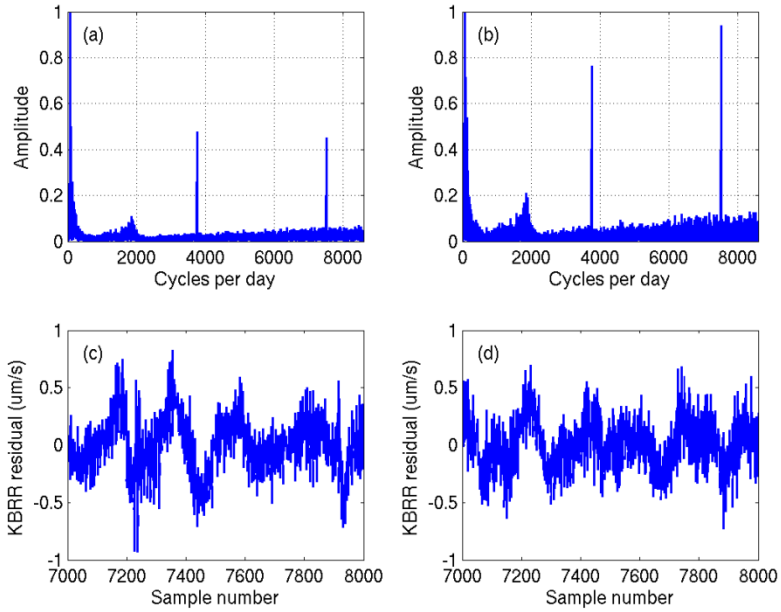

Figure 57. Periodogram of the resonance KBRR residual time series (a); periodogram created from a FFT of the phase-shifted reconstructed KBRR time series (b); sample of the resonance KBRR residual time series (c); sample of the phase-shifted reconstructed KBRR residual time series (d).

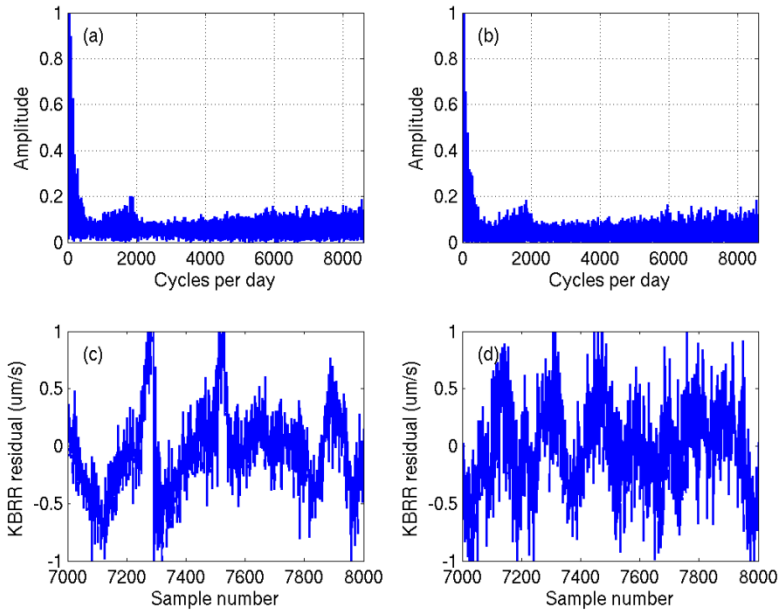

Figure 58. Periodogram of the poor thermal control KBRR residual time series (a); periodogram created from a FFT of the phase-shifted reconstructed KBRR time series (b); sample of the poor thermal control KBRR residual time series (c); sample of the phase-shifted reconstructed KBRR residual time series (d).

Figure 58 reveals an increase in the amplitude of the KBRR residuals; compare Figure 58 (c) and Figure 58 (d) with Figure 43 (c) and Figure 43 (d). This increase in amplitude

is the result of the poor thermal control, which we would expect to increase from 2011 onwards.

Table 18 summarises the RMS of the difference to the GLDAS and Antarctica mass loss signal in the presence of simulated stripes from three periods (main, resonance and thermal control). The simulated stripes for the main period are described in section 6.5. The RMS values are provided for the spherical harmonic and 2° mascon solutions. In the resonance period, increasing the Gaussian smoothing until 400 km reduces the RMS at which point the signal recovered is comparable to the main period; the larger global RMS suggests more of the stripes remain over the oceans. For the mascon solution the lowest RMS obtained is obtained when a correlation distance of 250 km is used, which is a much lower than the distance required for the June 2006 simulation of the main period. The RMS is also much lower, suggesting the mascon methodology is able to deal well with periods of resonance. This spatial resolution is adequate for a spherical harmonic field to degree and order 60. Similarly, a mascon correlation distance of 250 km, equivalent to the distance between centres of 2° equatorial mascons, provides the ties between neighbouring mascons. It would appear that the resonance facilitates separation of spatial and temporal errors in our simulation leading to more accurate surface mass recovery than in non-resonant periods.

In the period of reduced thermal control both the spherical harmonic and mascon solutions are degraded. The lowest RMS (11.6 cm EWH) for the spherical harmonic solution is obtained with 600 km Gaussian smoothing. Even with this smoothing radius, the RMS obtained is larger than for the main and resonance periods. For the mascon solution, the lowest RMS (10.8) is obtained with a correlation distance D=600 km, compared to 8.7 (8.0) for the solutions with the original (resonance) noise. To achieve this RMS the value S in Eq. (16) was increased from 0.001 to 0.01 which increases the effect the constraint matrix has on the solution. For both the mascon and spherical harmonic solutions a larger constraint matrix is required to deal with the noise resulting from the poor thermal control. While the recovery in the presence of the thermal stripes is not as favourable for both methodologies, when compared to the original or resonance periods, the mascon methodology is still able to recover more of the input signal than the spherical harmonic methodology while also reducing the noise over the ocean.

Based on the simulations, a correlation distance of D=800 km will be used during the main mission period. A value of D=800 km will also be used during periods of reduced thermal control, although the scale, S, will be modified to S=0.01, as required in the simulations. The RMS between D=600 km (10.8) and D=800 km (10.9) for the period of reduced thermal control is minimal. For periods when the GRACE satellite are in resonance, a value of D=400 km will be used. Again, the difference between the RMS of D=250 km (8.0) and D=400 km (8.1) is minimal.

6.11 *Summary*

The simulated recovery of a noise and error free GLDAS mass anomaly showed that there is no quantifiable difference between a mass anomaly solution recovered from KBRR data using spherical harmonics and a 2° equal area mascon solution; both recovered the input GLDAS anomaly. A 4° mascon solution does not have the required resolution to recover the gravity field solution to degree and order 60 due to the number of mascon parameters estimated being less than the gravity field parameters required; this causes a loss of higher degree information in the gravity field. Therefore only 2° mascon solutions will be used when calculating mascon solutions from real GRACE data. Recovery of the GLDAS mass anomaly described to degree and order 120 revealed that all methodologies are affected by omission errors, with the additional short wavelength (high degree) information not being captured.

For the mascon solution, the recovery of global mass distributions was found to require contributions to the satellite accelerations of all mascons within approximately 6000 km of the nadir mascon. This has implications when estimating a non-global mascon solution, and is useful in reducing computational effort for high resolution global mascon solutions. The use of iterations cannot compensate for an insufficient distribution of mascons.

The recovery of the GLDAS anomaly with simulated stripes reveals the advantage of the mascon solution over a spherical harmonic solution smoothed with a Gaussian smoother when attempting to reduce high degree and order noise. The use of the mascon spatial constraint matrix allowed more signal to be preserved up to degree ~35, while the addition of constraints between mascon parameters that share geophysical similarities resulted in a further reduction of the lost signal at all degrees. This improvement is further evident in the simulated recovery of the Antarctic mass signal which also confirms the advantage of the mascon solution over the spherical harmonic

recovery validating the use of this methodology in polar regions. Over Greenland, an 8 basin layout was found to optimise signal recovery again highlighting the advantage offered by the mascon methodology when real-world geophysical properties to define constraints between the mascons.

The recovery of the GLDAS anomaly and Antarctica mass change signal with simulated stripes, created during periods when GRACE was in resonance and suffering from poor thermal control, revealed that in both cases the mascon methodology was able to recover more of the input signal than using spherical harmonic methodology. This advantage was especially evident during periods of resonance. The use of the mascon methodology also reduced the effect of stripes over the ocean. However, both the spherical harmonic and mascon solutions were degraded during periods of reduced thermal control. In particular, the reduced thermal control necessitated tighter constraints between the various mascons than during the main part of the mission.

Finally, the values used for scale factor *S* was found to be optimal during the simulations. It is possible that when processing real data, adaptations may be required. This will be investigated in Chapter 7. Furthermore, adaptations to the *S* appear to be necessary as the GRACE mission ages.

Chapter 7. Results

In Chapter 5 the parameters used to compute gravity field solutions from Level-1B GRACE were described, while known mass signals were recovered using simulations in Chapter 6. In this chapter the results obtained from processing Level-1B GRACE data are presented, applying the knowledge gained in Chapter 5 and Chapter 6. Monthly and 10 day mascon solutions are generated and compared to Level-2 CSR RL05 solutions for validation. Once validated, the mascon solutions will be used to estimate the mass trend of Antarctica, Greenland and Alaska. The mass trend of several hydrological basins, including the Amazon and Indus, will also be recovered. Finally, the GRACE trends resulting from the Sumatra earthquake of 2004 will be investigated. The trends are provided for the purpose of validation of the mascon solutions as geophysical interpretation of the mass change is outside the scope of this study.

7.1 *GRACE time-varying gravity solutions*

GRACE time-varying gravity solutions were generated through the estimation of mascon parameters. Solutions were calculated using the processing methodology described in Chapter 5, with the parametrisation identified through simulations in Chapter 6. Monthly and 10 day mascon solutions were calculated for the period January 2003 to December 2013.

The main difference between monthly and 10 day solutions is the days included in the solutions: monthly solutions use data for a calendar month, 10 day solutions use a weighted rolling window of 30 days of data. Both solutions use the same set of daily normal matrices. There is also a difference in the constraint matrix of the solutions, which is discussed in Chapter 4.

7.1.1 *Mascons solutions to spherical harmonic coefficients*

Having generated monthly or 10 day mascon solutions, each individual solution is converted to spherical harmonic coefficients. This is undertaken for two reasons. Firstly, estimating mascon parameters involves calculating a scaling factor for a set of ‘delta’ spherical harmonic coefficients that represent a uniform layer of surface mass over an area which can be added to the mean background field and used to represent the mass flux at a certain time. The spherical harmonic expansion of the mascon area is a global function and, due to the truncation of the expansion to degree and order 60, there will be local leakage into and outside of the area of the mascon (shown in Figure 7). Therefore each mascon cannot be considered in isolation. Secondly, geophysical models

applied as corrections during time-series analysis, e.g. GIA, are provided as a global set of spherical harmonic coefficients. Having both the mascon solutions and the corrections described using spherical harmonic coefficients will aid in applying the required corrections.

To convert the individual mascon parameters into a global set of spherical harmonic coefficients, the calculated mascon parameters estimated for each individual solution epoch, monthly or 10 day, are multiplied by the spherical harmonic coefficients used to describe the mascon. All the individual mascons are then added together, similar to Figure 9, to create the global set of spherical harmonic coefficients. The difference from Figure 9 is that the mascons will not equal 1 cm EWH globally, but will describe the recovered TVG field. This method was used in the simulations in Chapter 6. Figure 48(c) shows that mascon parameters can be correctly converted into spherical harmonic coefficients which can in-turn be plotted to describe a TVG field.

7.1.2 *Corrections*

Although the mascon constraint matrix, applied during the generation of the solution, removes the requirement to apply post-processing to mitigate noise in the solutions, corrections are applied to the mascon solutions to allow estimates of mass flux to be inferred. Firstly, monthly estimates of degree 1 spherical harmonic coefficients are added to the mascon spherical harmonic coefficients. This is required as degree 1 coefficients are not observed by GRACE (Wahr et al., 1998) and a condition of the mascon analysis is that total degree one harmonics are zero. Chen et al. (2005) found that not including degree 1 coefficients in GRACE mass flux analysis impacted on the recovery of basin scale water storage estimates, with polar regions even more sensitive to the exclusion of low degree terms. The use of degree 1 coefficients, derived by Swenson et al. (2008), is standard across the majority of users of GRACE data (e.g. Luthcke et al., 2013, Shepherd et al., 2012, Velicogna, 2009, Wouters et al., 2013).

The signal from GIA also needs removing from GRACE to allow mass variations to be calculated (Barletta et al., 2008). GIA is observed by GRACE and introduces uncertainty into ice mass trend estimates (Velicogna and Wahr, 2002). While GIA appears as a constant trend over the life of the GRACE satellite and will not contaminate the GRACE signal (Velicogna, 2009), differences in GIA models will result in different corrections being applied during mass flux analysis. The GIA signal is large over Antarctica with current errors in GRACE ice mass trend estimates dominated

by GIA uncertainties (Velicogna and Wahr, 2006b). To help quantify the errors introduced through the choice of GIA model over Antarctica, mass flux analysis will be estimated using a selection of three different GIA models; namely, ICE-6G (VM5a) (Argus et al., 2014), IJ05_R2 (Ivins et al., 2013) and W12a (Whitehouse et al., 2012). The latter two models are supplemented by ICE-5G outside of Antarctica. By changing only the GIA model, any differences in mass flux analysis will relate to the GIA model chosen. The resulting mass trends over Antarctica will then be presented as a range. Outside Antarctica only ICE-6G is used as IJ05_R2 and W12a are Antarctica only models.

For solutions where the hydrology signal is not of interest (e.g. polar mass trend estimates), signal leakage can be reduced through the removal of a hydrology model (Sabaka et al., 2010). Here, hydrology is modelled using GLDAS (Rodell et al., 2004). Leakage is reduced as the distribution of leakage is concentrated in regions with high hydrological variability (Seo et al., 2006). However, some glaciated areas in GLDAS contain unrealistically high values for predicted water storage. Similar to Jacob et al. (2012), the values from GLDAS over Alaska and Greenland were set to zero before the hydrology was removed. In addition the modelled values for Antarctica were not used. While Luthcke et al. (2013) opted to removed hydrology during the generation of mascon solutions, here hydrology is removed when undertaking mass flux analysis. As hydrology is of interest to many users of GRACE data, not removing hydrology during solution generation allows the hydrology signal to be studied using the mascon solutions presented here. However, care needs to be taken when removing the hydrology signal. Models that describe individual components of the Earth's surface mass do not conserve mass and will therefore have a C_{00} term that is nonzero (Wahr et al., 1998). To correct for this, a compensatory water layer will be applied uniformly across the oceans when hydrology is removed. This correction was applied by King et al. (2012).

While GRACE is able to recover C_{20}, it is not well determined due to orbital geometry and the short separation between the satellites (Chen et al., 2005). Therefore replacing C_{20} coefficients with those derived using SLR is common in the literature when using spherical harmonic coefficients (e.g. Barletta et al., 2013, King et al., 2012, Schrama et al., 2014, Velicogna and Wahr, 2013). Corrections for C_{20} are provided for CSR RL05 by Chen et al. (2013). However, the mascon methodology does not estimate spherical

harmonic coefficients explicitly, therefore there is no requirement to replace the C_{20} coefficients with those derived using SLR (Shepherd et al., 2012). The NASA GSFC mascons solutions do not apply a correction for C_{20}. In addition, the most recent release of the GFZ Level-2 product (RL05) have C_{20} coefficients that are close to those derived from SLR. Chambers and Bonin (2012) found that replacement of the GRACE derived C_{20} with that from SLR made no significant difference to the GFZ solutions. However, they do note that the mean GFZ field is based on RL04 coefficients, where C_{20} had been replaced with the SLR derived value.

Finally, Dobslaw et al. (2013) advise that the monthly mean of the AOD1B product is restored before estimating mass flux. This is due to an anomalous trend in the background ocean models used in the AOD1B product. This is corrected for by adding the GAD products, which are modelled non-tidal ocean bottom pressure variations averaged over a month (Chambers and Bonin, 2012), to the mascon solutions. A linear trend in the background field is also reinstated. The GIF48 mean gravity model has a reference epoch of 1 January 2007 (Ries et al., 2011). The mascon solutions have been mapped to this epoch. Corrections are applied to each individual mascon solution.

7.1.3 *Mascon solutions to grids of EWH*

Having applied the corrections, each monthly and 10 day mascon solution is evaluated on a 1° by 1° global grid. Evaluating the spherical harmonics coefficients that describe the mascon solutions on a 1° by 1° global grid allows TVG field to be represented as EWH values, which is common in the literature. A number of time-series are shown in section 7.2 and 7.3. Using these time-series, trends are calculated at each point on the global grid. These trends can be used to determine the mass trend of a region of interest, as shown in section 7.4.

To create a grid of EWH values, the global gravity field harmonic coefficients, ΔC_{lm} and ΔS_{lm}, are first converted into global surface harmonics coefficients, $\Delta \tilde{C}_{lm}$ and $\Delta \tilde{S}_{lm}$, using Eq. (13) of Wahr et al. (1998), namely

$$\begin{Bmatrix} \Delta \tilde{C}_{lm} \\ \Delta \tilde{S}_{lm} \end{Bmatrix} = \frac{\rho_{ave}}{3\rho_w} \frac{2l+1}{1+k_l} \begin{Bmatrix} \Delta C_{lm} \\ \Delta S_{lm} \end{Bmatrix} \tag{20}$$

where ρ_w is the density of water (1000 kg m^{-3}), ρ_{ave} is the average density of the Earth (5517 kg m^{-3}) and k_l the load Love number of degree *l* (Farrell, 1972). The surface

harmonics coefficients are then expressed as EWH values at every 1° of colatitude and longitude (ϕ, λ) using

$$\mathrm{EWH}(\phi, \lambda) = R_e \sum_{l=0}^{l\max} \sum_{m=0}^{l} (\tilde{C}_{lm} \cos m\lambda + \tilde{S}_{lm} \sin m\lambda) P_{lm} (\cos \phi) \tag{21}$$

where l is degree and m is order and $\bar{P}_{lm}$ normalised associated Legendre polynomials. The radius of the Earth, R_e is included (in cm) to provide the result in units of cm of EWH. The summation is limited to $l_{\max}$ = 60 due to the truncation of mascon solution to degree and order 60.

7.1.4 *Linear regression*

Having generated the 1° by 1° global grids, a time series was generated at each point. Separate time-series were calculated for the monthly and 10 day mascon solutions. From these time-series, a constant, linear trend and annual and semi-annual signals were estimated using linear regression. The linear trends are used in section 7.4 to derive regional mass trends. One point to note is that the linear regression applied here assumes no correlation between the EWH values in the time-series; that is the data exhibit Gaussian noise and hence consecutive data points are uncorrelated. This assumption is made in the majority of published GRACE trends. However, Williams et al. (2014) found significant autocorrelation in time-series over Antarctica. While this autocorrelation is acknowledged, determining time-series autocorrelation is beyond the scope of this study.

7.1.5 *Error Analysis*

Generating solutions directly from Level-1B data yields the full variance-covariance matrix which can be used to estimate the variance associated with each EWH value at each epoch of the time series for the 1° by 1° global grid. In section D.15 of Appendix D of Bomford (1980), a method to calculate the variance of a solution is described. Therefore, the variance can be calculated for every EWH value on every monthly or 10 day global grid using

$$\sigma^2_{(\phi,\lambda)} = f^T N^{-1} f \tag{22}$$

where N^{-1} is the variance-covariance matrix associated with the monthly or 10 day mascon solution. The variance-covariance matrix contains the effects of the mascon

spatial and/or temporal constraints and has been multiplied by the unit variance, σ_0, given by

$$\sigma_0 = \sqrt{\left\{\frac{[wv^2]}{(s-t)}\right\}} \tag{23}$$

where $[wv^2]$ is the sum of the squares of the weighted residuals over the month or 10 day period with *s* being the total number of observations over the period and *t* the number of unknowns used to calculate the solution vector. The use of σ_0 corrects for scale error in the original weights, *w*. The vector *f* of Eq. (22) is given by

$$f_i = \sum_{l=0}^{l\max} \sum_{m=0}^{l} (\Delta C_{lm}^i \cos m\lambda + \Delta S_{lm}^i \sin m\lambda) P_{lm}(\cos\phi) \tag{24}$$

where ΔC_{lm}^i and ΔS_{lm}^i are the spherical harmonic gravitational coefficients that describe the i^{th} mascon and the summation is to degree and order 60, i.e. $l_{\max}$ = 60. The vector *f* includes the contribution of all mascons.

Figure 59 shows the standard error calculated for the monthly mascon solution of June 2006.

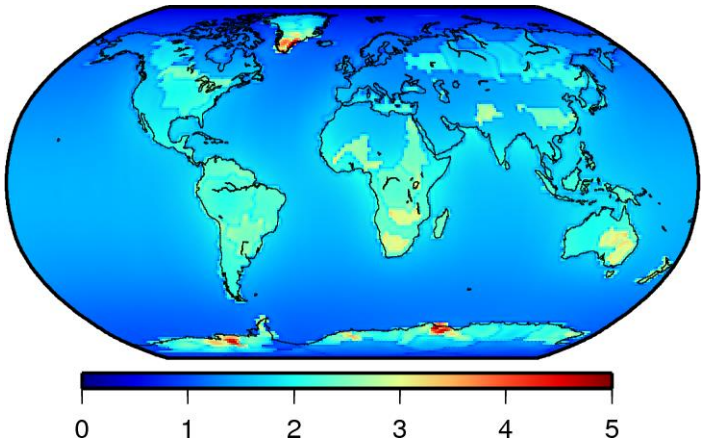

Figure 59. The standard errors for the monthly mascon solution of June 2006. Units cm (EWH).

Figure 59 reveals that over the oceans the standard error is less than 2 cm EWH around the equator, with smaller values obtained towards the poles. The ocean constraint correlates all ocean mascons together. Over land the standard errors varies, with a spatial pattern that correlates to the drainage basins used in the mascon constraint

matrix. It is clear that drainage basins with the larger standard error values are the smaller drainage basins; this is evident in the smaller hydrological drainage basins over southern Africa. This occurs as smaller drainage basins contain fewer mascons, increasing the standard error as the basins are not as well constrained. The areas of the largest standard errors, over South Greenland and Antarctica, relate to drainage basins that contain only 2 or 3 mascons each. The relationship between mascons and drainage basins is shown in Figure 86 for Antarctica and Figure 91 for Greenland. Outside the hydrological, Greenland and Antarctica drainage basins, all other land mascons are constrained together resulting in a lower standard error. Therefore, Figure 59 reveals that the standard error is dominated by the mascon constraint matrix. The spatial pattern of the standard error is similar for all monthly and 10 day solutions, although the standard errors are smaller in the 10 day solutions. Overall, Figure 59 provides confidence in the mascon solutions.

Calculating the variance for every EWH value for each monthly or 10 day mascon solution would allow weights to be assigned when deriving trends from time-series of EWH values. The weight is the reciprocal of the variance. However, the calculation of the weight is very time consuming.

7.2 *Monthly solutions*

To validate the monthly mascon solutions, time-series plots of mass flux were generated and compared to time-series calculated using CSR RL05 Level-2 data for a number of locations. In total, 124 monthly mascon and CSR RL05 solutions are available spanning the period January 2003 to December 2013. There are certain months where no mascon solution was calculated due to poor data (i.e. June 2003) or, as in the later part of the GRACE mission, the equipment on-board the GRACE satellites was turned off to conserve power (i.e. January 2011; June 2011; May 2012; October 2012; March 2013; August 2013; and September 2013). These months are also missing from all the official GRACE solutions. To allow for an accurate comparison, the same corrections are applied to the CSR RL05 and the monthly mascon solutions. For the comparison, hydrology is still included and the GIA signal was removed using ICE-6G. The only difference between the solutions is that the C_{20} coefficient for each monthly CSR RL05 solution was replaced with those provided by Chen et al. (2013). Noise was mitigated from the CSR RL05 solution using a 400 km Gaussian smoothing (Wahr et al., 1998) and a de-striping filter (Swenson and Wahr, 2006).

Comparing the mascon and CSR RL05 time-series plots at a number of "quiet" locations where only a small signal is observed by GRACE will allow an assessment of the mascon solution at the noise level. For example, comparing the solutions in the Sahara desert, where minimal annual rainfall occurs, should reveal that there is little difference between the two solutions. While there may be a small annual signal, noise is expected to dominate the signal. Similar comparisons can be made at quiet points over the oceans. These comparisons, along with the results of the simulations, should provide confidence that any differences in mass flux trends are a representation of reality and not an artefact of noise.

The comparison of the time-series plots was undertaken at 6 points. The spatial distribution of these points is shown in Figure 60. These 6 points (Sahara and Ocean-1, -2, -3, -4 and -5) correspond to locations where there is only a small annual gravity signal. The 5 ocean points were chosen using Figure 2 in Chambers and Bonin (2012), which shows the standard deviation of OBP from GRACE CSR RL05 products. OBP is the sum of the mass of the ocean and atmosphere above the ocean floor. Ocean point 1 has a standard deviation of less than 1 cm, with a standard deviation between 2 and 4 cm for ocean points 2 and 3 and between 2 and 3 cm for ocean point 4 and 5. The point over the Sahara is located where the desert receives the lowest annual rainfall (Kelley, 2014).

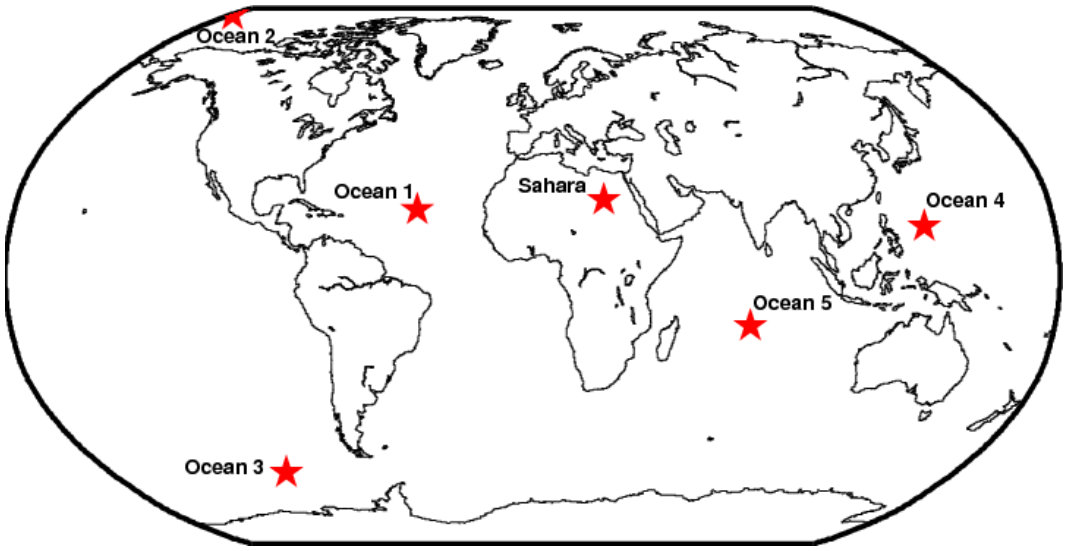

Figure 60. Location of the 6 points used for a comparison between the monthly mascon and the CSR RL05 mass flux analysis time-series.

The latitude and longitude of the points are in Table 22 which also contains the standard deviation of the noise in the individual time-series, allowing the noise in the CSR RL05

and mascon time-series to be compared. The standard deviations were calculated after estimating and removing a constant, linear trend and annual and semi-annual signals from the time-series. This should remove the majority of the signal, leaving mainly noise. To confirm that the majority of the signal had been removed, lag plots were generated. Lag plots offer a visual tool for examining autocorrelation (Stockwell, 2006). In a lag plot autocorrelation is shown as a diagonal signature, a random distribution is plotted as a cloud, and a periodic distribution shown as a circle. To produce the lag plots, the remaining signal in month *n* of the time-series was plotted against the signal in the preceding month *n-1*. The lag is therefore 1. This was undertaken for both the mascon and CSR RL05 time-series and would reveal, visually, if any temporal correlation exists. A correlation coefficient was then calculated, which is also included in Table 22.

Location	**Latitude**	**Longitude**	**Correlation coefficient**		**SD (cm EHW)**	
			CSR RL05	**Mascon**	**CSR RL05**	**Mascon**
Ocean 1	20°	320°	0.16	-0.17	1.7	1.0
Ocean 2	85°	180°	0.33	0.39	1.9	2.2
Ocean 3	60° S	255°	0.32	0.35	2.0	1.5
Ocean 4	15°	135°	0.00	0.27	1.9	1.4
Ocean 5	15° S	75°	-0.08	0.38	2.0	1.3
Sahara	23°	27°	0.09	0.14	1.8	1.1

Table 22. Standard deviation of the noise in the time-series for the 6 points after estimating and removing a constant, linear trend and annual and semi-annual signal. The correlation coefficient is that between the remaining signal in month *n* of the time-series, against the remaining signal in the preceding month *n-1*.

7.2.1 ***Ocean 1***

The time series at ocean point 1 before any signal was removed for noise analysis is plotted in Figure 61. The standard deviation of the OBP in Figure 2 of Chambers and Bonin (2012) is less than 1 cm, allowing noise in the two solutions to be assessed. As the standard deviation is relatively small, the true signal from GRACE is assumed to be small.

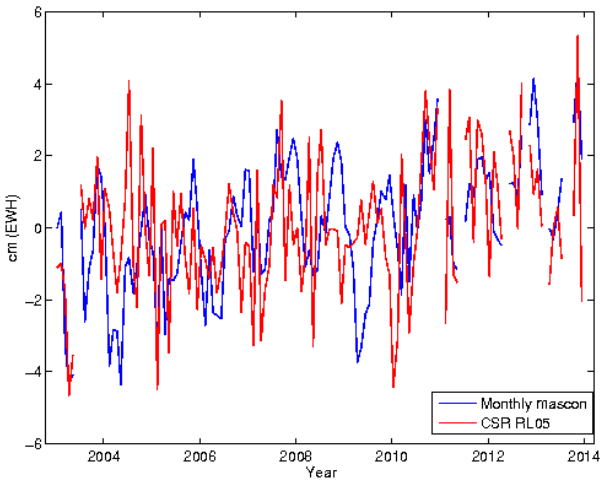

Figure 61. Mass flux time-series at ocean point 1 for the monthly mascon solution (blue) and the CSR RL05 solution (red). Units of cm (EWH).

Figure 61 shows that the scatter and trend in both time-series are similar, with amplitude between ± 4 cm. To analyse the noise in the time-series, a constant, linear trend and annual and semi-annual signals were estimated and removed with the residuals checked for temporal correlations using a lag plot (Figure 62).

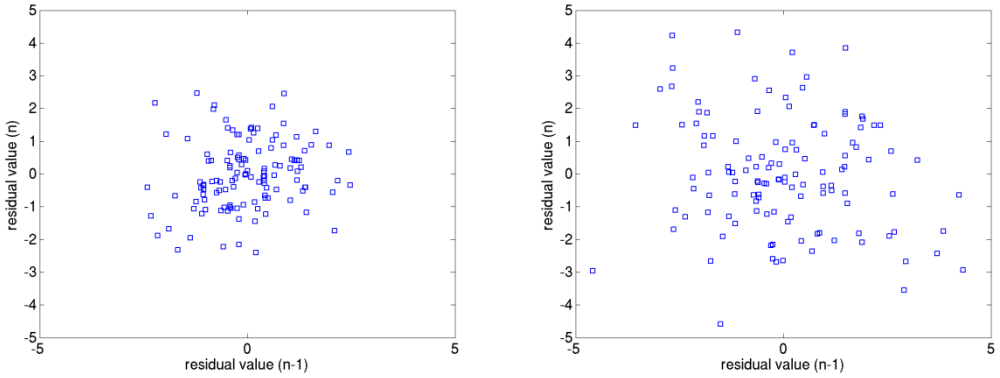

Figure 62. Lag plot of the remaining signal in the mascon solution (left) and CSR RL05 solution (right) after a constant, linear trend and annual and semi-annual signals in the time-series were estimated and removed. Units cm EWH.

Both the lag plots in Figure 62 suggest there is little temporal correlation in the time-series, as the lag plot is a cloud pattern. This is confirmed by the correlation coefficient in Table 22. The standard deviations in Table 22 reveal that at this location there is less noise in the mascon solution compared to the CSR RL05 solution.

While the results presented here use the correlation distance, *D*, determined in the simulations, the value of *S* differs slightly. A scale of S=0.004 was used during the main mission period and when the GRACE satellites were in resonance, while a value of

S=0.04 was used during periods of reduced thermal control. This compares with values of *S*=0.001/ *S*=0.01 used during the simulations in Chapter 6. The reason for this difference is that generating monthly mascon solutions, using real GRACE data, allowed the value used for *S* to be investigated in the presence of real noise. A number of different values of *S* were tested as shown in Table 23. In common with the simulations, the value of *S* used during periods of poor thermal control (i.e. April 2011 onward) is a factor of 10 greater than during the main mission period and months when the satellite was in resonance.

Scale (*S*) Main and Resonance(Thermal)	**Standard deviation of noise** (cm EWH)
0.001(0.01)	1.77
0.002(0.02)	1.32
0.004(0.04)	1.02
0.006(0.06)	0.92
0.008(0.08)	0.86
0.01(0.1)	0.83

Table 23. Table showing the values of S applied in Eq. (16) when calculating the monthly mascon solution. The resulting standard deviations of the noise, after removing a constant, linear trend and annual and semi-annual signals from the time-series, are provided. The standard deviations are calculated for time-series at ocean point 1.

Table 23 reveals that increasing the scale, *S*, reduces the relative standard deviation of noise in the time-series. This is expected as increasing *S* increases the weight of the constraints. The effect of *S* on the time-series in Figure 61 is shown in Figure 63. For clarity the time-series in Figure 61 was generated using *S*=0.004(0.04).

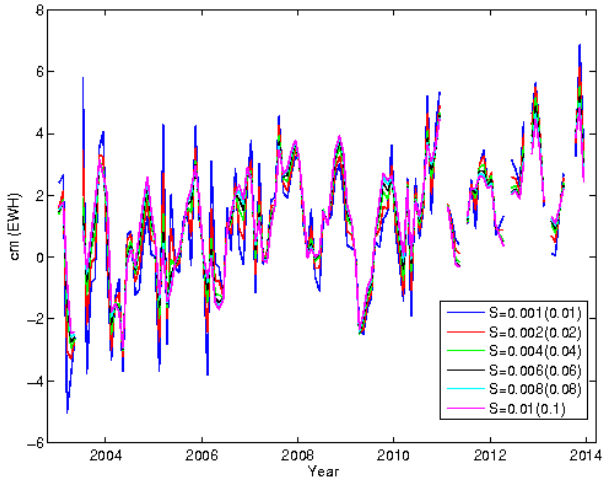

Figure 63. Monthly mascon mass flux time-series at ocean point 1 for different scale factors (*S*) in Table 23. Units cm (EWH).

As suggested by the results of Table 23, Figure 63 reveals that increasing the scale removes some of the variability in the time-series. An increase in the scale from 0.001(0.01) to 0.002(0.02) has the largest impact. However, once the scale is increased above 0.004(0.04), the impact on the time-series is reduced. This reduction was seen in Table 23, where the impact on the relative standard deviation of increasing the scale reduces above 0.004(0.04) becomes less pronounced. These results suggests that the higher variability seen when using a scale of 0.001(0.01) or 0.002(0.02) is the result of noise in the solutions, which is reduced when using a larger scale factor.

While the choice of the scale, *S*, is trade-off between reducing noise and reducing real signal, increasing the scale was found to have a greater impact on noise (Luthcke et al., 2013). The results in Table 23 and Figure 63 suggest that a good choice for the scale factor is 0.004(0.04). Increasing the scale above this has a reduced effect on noise, while potentially affecting the signal. Therefore, a scale factor of 0.004(0.04) was used during all subsequent GRACE processing. The effect of this scaling is further investigated in section 7.4, through a comparison with published mass trend estimates.

7.2.2 ***Ocean 2***

The time-series at ocean point 2 are plotted in Figure 64, where the standard deviation of the OBP is between 2 to 4 cm EWH (Chambers and Bonin, 2012). Again, comparing the two time-series allows the noise in the two solutions to be assessed, although the signal recovered should be larger than at ocean point 1 as the standard deviation of the OBP is larger.

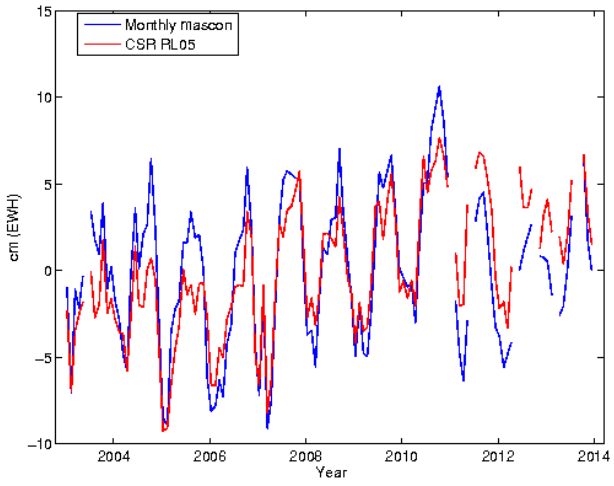

Figure 64. Mass flux time-series at ocean point 2 for the monthly mascon solution (blue) and the CSR RL05 solution (red). Units cm (EWH).

Figure 64 shows that the signal fluctuates between +/- 10 cm of EWH. Both time-series have a similar signal, appearing to be less affected by noise and having a clearer annual signal than at ocean point 1. This is to be expected as noise in the GRACE solution are expected to be around 1 cm of EWH, with localised variations (Ray and Luthcke, 2006).Therefore, as the amplitude of the signal from the GRACE solution increases, the impact of noise on the time-series should decrease. To analyse the noise in the time-series, a constant, linear trend and annual and semi-annual signals were estimated and removed with the remaining signals checked for temporal correlations using a lag plot. The results are plotted in Figure 65.

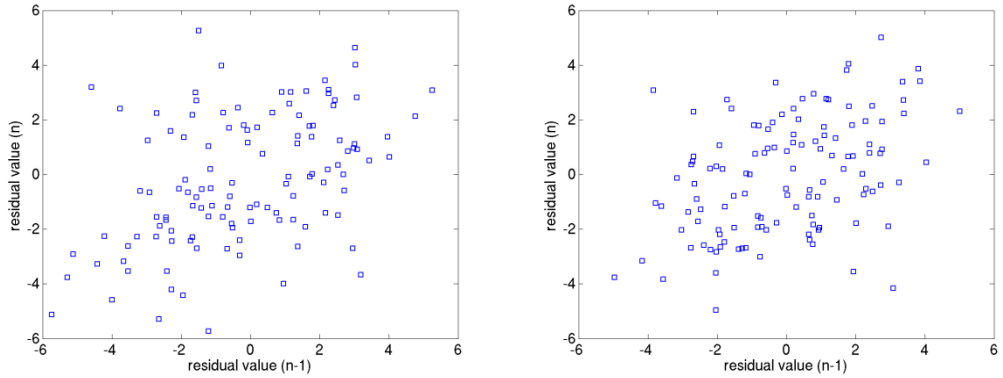

Figure 65. Lag plot of the remaining signal in the mascon solution (left) and CSR RL05 solution (right) after a constant, linear trend and annual and semi-annual signals in the time-series were estimated and removed. Units cm EWH.

Comparing Figure 65 with Figure 62, for both the mascon and the CSR RL05 times-series, confirms that there is a weak positive correlation. This suggests that there could be real signal remaining. Calculating the correlation coefficient confirmed this. A correlation coefficient of 0.52 was obtained for the mascon time-series, with 0.42 obtained for the CSR RL05 time-series. Figure 66 is a plot of the time-series after a constant, linear trend and annual and semi-annual signals were estimated and removed.

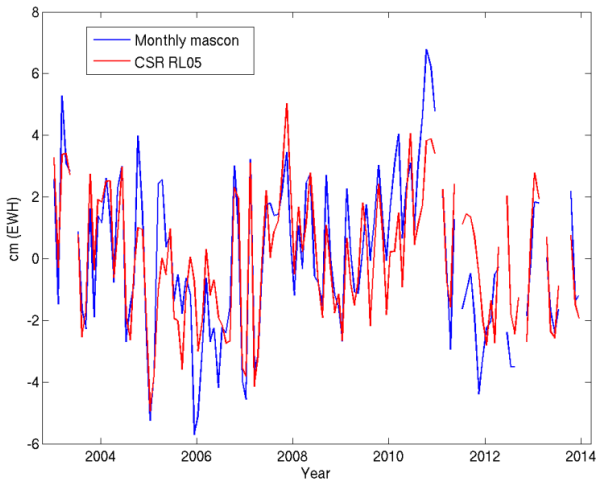

Figure 66. Mass flux time-series at ocean point 2 for the monthly mascon solution (blue) and the CSR RL05 solution (red) after a constant, linear trend and annual and semi-annual signals in the time-series were estimated and removed. Units cm (EWH).

Figure 66 reveals that in both time-series there is a signal which appears to have a period of between 7 and 8 years. This frequency is similar to an aliasing period relating to the K1 tide, which Moore and King (2008) found would alias into the GRACE satellite orbits at the period of 2791.4 days. The aliasing effect of the K1 tide was also found to increase its signature pole-ward. Aliasing by the K1 tide was also found by Ray and Luthcke, (2006). It appears that the K1 tidal signature is aliasing both solutions at this point. This itself is an interesting result and suggests that the background tidal model is not as well defined in the Arctic. In a study of four tidal models, Ray et al. (2009) found that all models required improvement in polar regions. The limitations of tidal models in polar regions was also observed by Stammer et al. (2014).

A signal with a period of 2791.4 days was therefore estimated and removed from both time-series with the correlation coefficients from Table 22 obtained. For both time-series estimating and removing this additional signal reduced the correlation coefficient; from 0.52 to 0.39 for the mascon time-series, and from 0.42 to 0.33 for the CSR RL05 time-series. It is possible that other tidal frequencies are present. The standard deviations calculated at ocean point 2 and presented in Table 22 suggest that there is slightly more noise in the mascon solution at this point. Possible reasons for this are unknown, although the difference could result from the different tidal and background models used during the calculation of the CSR RL05 and mascon solutions.

7.2.3 *Ocean 3*

The two time-series at ocean point 3 are plotted in Figure 67. The standard deviation of the OBP is 2 to 4 cm. However, due to the location off the coast of Antarctica, ocean point 3 can be affected by leakage of signal from the land (Chambers and Bonin, 2012). Therefore comparing the two time-series at this point allows the noise over the ocean to be assessed as well as any leakage from a large nearby land signal.

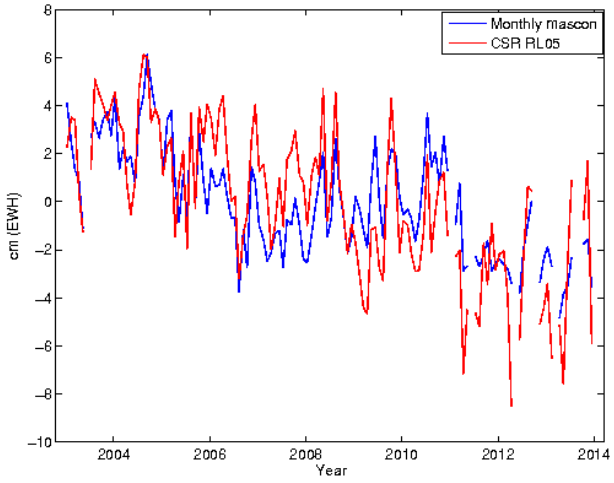

Figure 67. Mass flux time-series at ocean point 3 for the monthly mascon solution (blue) and the CSR RL05 solution (red). Units cm (EWH).

Figure 67 shows that the signals fluctuate between +/- 6 cm of EWH with similar trends. To analyse the noise in the time-series, a constant, linear trend and annual and semi-annual signals were estimated and removed with the remaining signals checked for temporal correlations using a lag plot. The results are plotted in Figure 68.

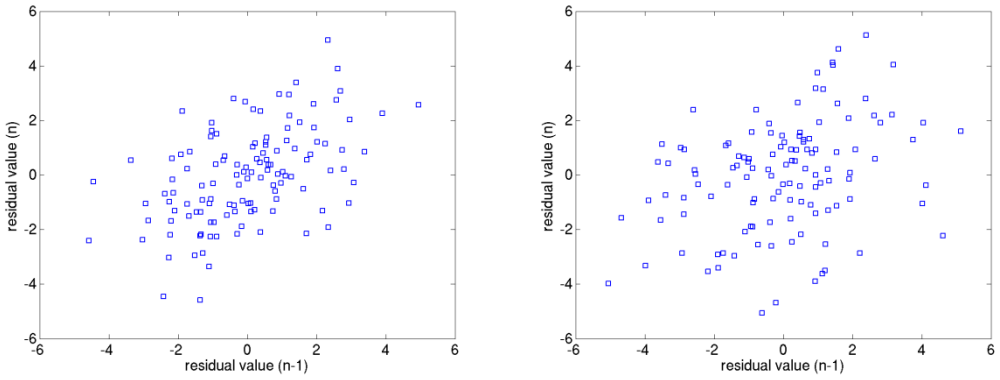

Figure 68. Lag plot of the remaining signal in the mascon solution (left) and CSR RL05 solution (right) after a constant, linear trend and annual and semi-annual signals in the time-series were estimated and removed. Units cm EWH.

As in Figure 65, there again appears to be a weak correlation in Figure 68. A correlation coefficient of 0.5 for the mascon solution and 0.33 for the CSR RL05 solution confirmed this. Figure 69 is a plot of the time-series after the constant, linear trend and annual and semi-annual signals were estimated and removed.

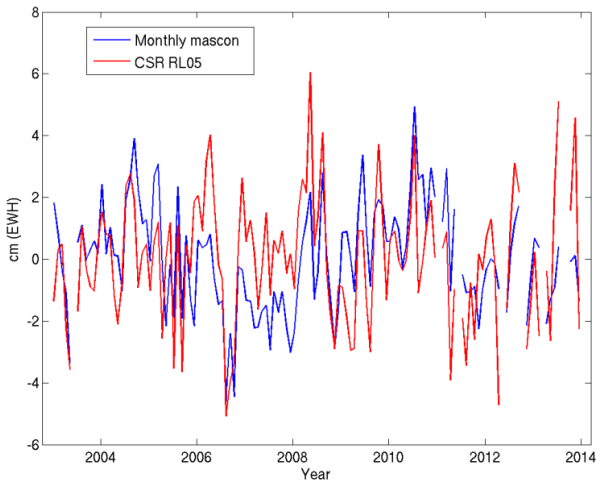

Figure 69 Mass flux time-series at ocean point 3 for the monthly mascon solution (blue) and the CSR RL05 solution (red) a constant, linear trend and annual and semi-annual signals in the time-series were estimated and removed. Units cm (EWH).

As in Figure 66, Figure 69 appears to contain a signal with a period of between 7 and 8 years. Again this could be due to the aliasing of the K1 tide. Ray et al. (2009) found that ocean models need improvement around Antarctica. As before a signal with a period of 2791.4 days was estimated and removed from both time-series with the correlation coefficients of Table 22 obtained. The correlation coefficient for the mascon solution was reduced from 0.5 to 0.35. For the CSR RL05 time-series this was reduced from 0.33 to 0.32. The small reduction in the correlation coefficient of the CSR RL05 solution (0.33 to 0.32) suggests that a signal with a period of 2791.4 days was not present; there was initially less residual signal in the CSR RL05 time-series. This could be the result of the different tidal and background models used during the calculation of the two solutions. However, it is possible that there is another signal with a different period in the time-series. The standard deviations at ocean point 3 in Table 22 suggest there is there is less noise in the mascon solution at this point around the Antarctic. Again, this could be the result of the different tidal and background models used. However, it could also suggest that there is less leakage in the mascon solution.

7.2.4 *Ocean 4*

The two time-series at ocean point 4 are plotted in Figure 70. Ocean 4 should provide a general reflection of the noise over the oceans as, apart from isolated locations, noise in tidal models are lower closer to the equator (Ray et al., 2009).

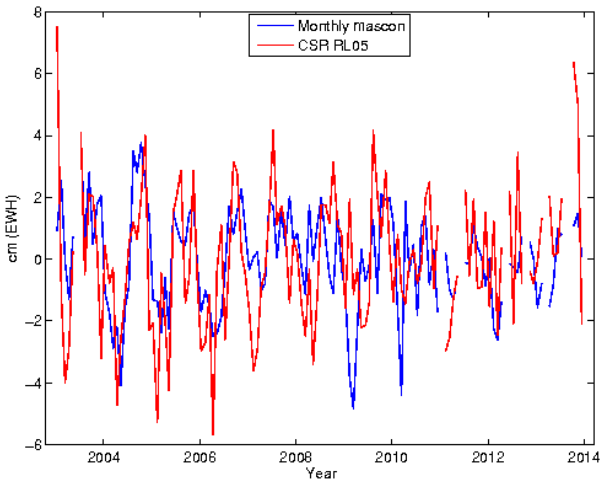

Figure 70. Mass flux time-series at ocean point 4 for the monthly mascon solution (blue) and the CSR RL05 solution (red). Units cm (EWH).

Figure 70 shows that the time-series fluctuate between +/- 4 cm of EWH. To analyse the noise in the time-series, a constant, linear trend and annual and semi-annual signals were estimated and removed with the remaining signals checked for temporal correlations using a lag plot. The results are plotted in Figure 71.

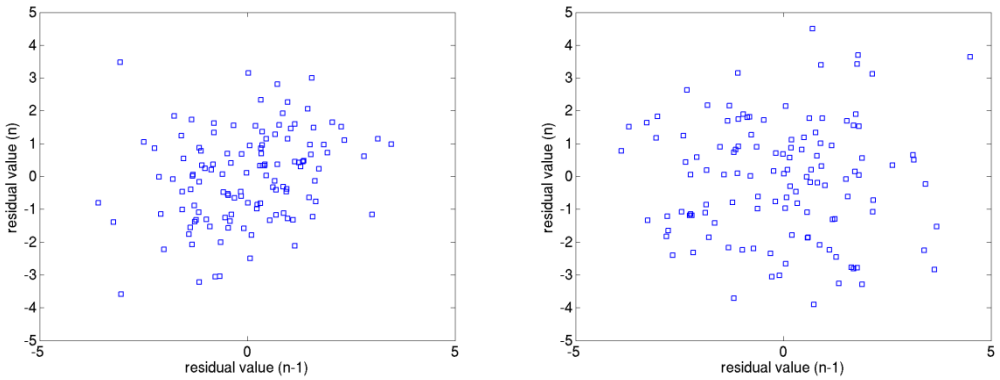

Figure 71. Lag plot of the remaining signal in the mascon solution (left) and CSR RL05 solution (right) after a constant, linear trend and annual and semi-annual signals in the time-series were estimated and removed. Units cm EWH.

Figure 71 suggests that there is little temporal correlation in the two time-series and is confirmed by the correlation coefficients in Table 22. The standard deviations in Table

22 again reveal that there is less noise in the mascon solution at this location, with the noise at the level suggested by Chambers and Bonin (2012).

7.2.5 *Ocean 5*

The two time-series at ocean point 5 are plotted in Figure 72. The standard deviation of the OBP is 2 to 3 cm. Again, comparing the two time-series at this point will allow the general noise over the oceans to be assessed.

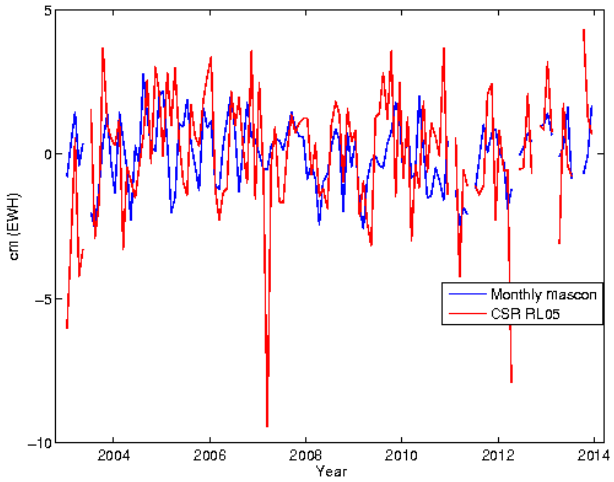

Figure 72. Mass flux time-series at ocean point 5 for the monthly mascon solution (blue) and the CSR RL05 solution (red). Units cm (EWH).

Figure 72 shows that the time-series of mass flux of the two signals fluctuate between +/- 4 cm of EWH, although there are some points in the CSR time-series that appear to be outliers. As previously, to analyse the noise in the time-series, a constant, linear trend and annual and semi-annual signals were estimated and removed with the remaining signals checked for temporal correlations using a lag plot. The results are plotted in Figure 73.

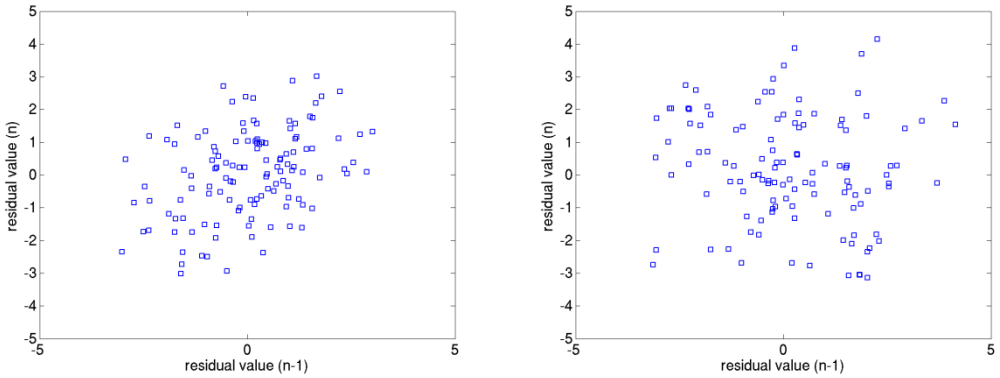

Figure 73. Lag plot of the remaining signal in the mascon solution (left) and CSR RL05 solution (right) after a constant, linear trend and annual and semi-annual signals in the time-series were estimated and removed. Units cm EWH.

Figure 73, suggests that there is little temporal correlation in the time-series, confirming the results in Table 22. The standard deviations in Table 22 show that there is comparably less noise in the mascon solution at this location.

7.2.6 *Sahara desert*

Having compared the solutions over the ocean and found that, at all but one point, the noise in the mascon solution is lower than in the CSR RL05 solution, the solutions were compared over the Sahara desert. The location analysed is one of the driest parts of the Sahara, receiving between 1 to 5 mm of rainfall a year which normally occurs between January and May (Kelley, 2014). Comparing the two time-series at this point allows noise over land to be accessed. The two time-series are plotted in Figure 74.

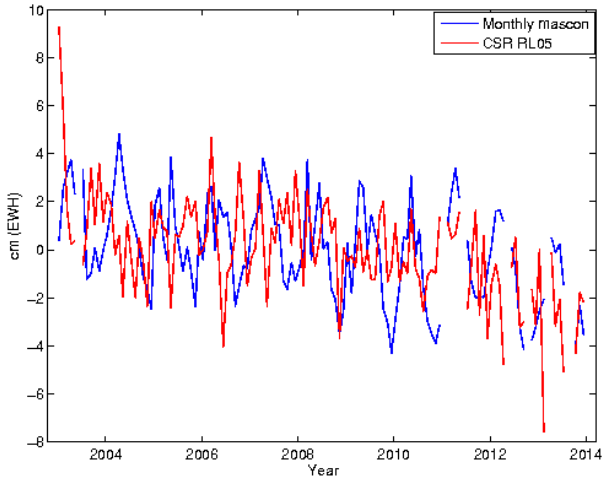

Figure 74. Mass flux time-series for a point in the Sahara desert for the monthly mascon solution (blue) and the CSR RL05 solution (red). Units cm (EWH).

Figure 74 shows that the time-series of the two signals fluctuates between +/- 4 cm of EWH. As over the ocean, to analyse the noise in the time-series a constant, linear trend and annual and semi-annual signals were estimated and removed with the remaining signals checked for temporal correlations using a lag plot (Figure 75).

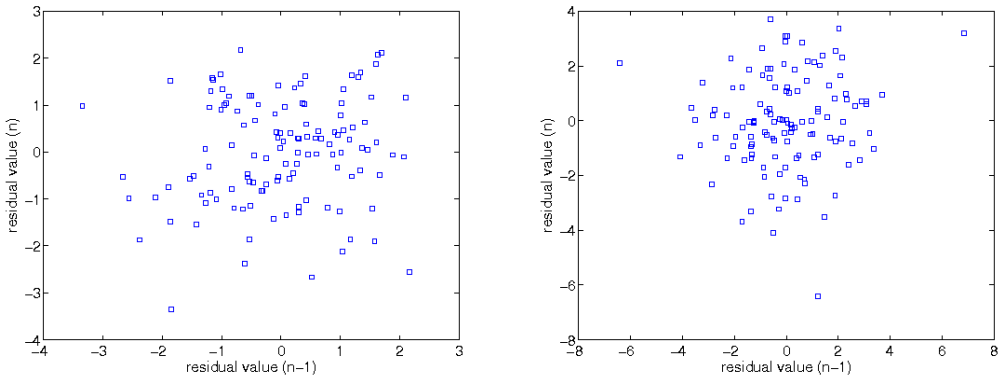

Figure 75. Lag plot of the remaining signal in the mascon solution (left) and CSR RL05 solution (right) after a constant, linear trend and annual and semi-annual signals in the time-series were estimated and removed. Units cm EWH.

Figure 75 suggests that there is little temporal correlation in the solutions, confirmed by the correlation coefficient in Table 22. The standard deviation of the noise in Table 22 reveals, as over ocean, that the noise is lower in the mascon solution at this location.

A point of interest in Figure 74 is that the mascon time-series contains a clear annual signal, which is not evident in the CSR RL05 time-series. The cause of this annual signal will now be investigated as such a signal is not expected at this location. In Figure 76 the mascon and CSR RL05 time-series from Figure 74 are plotted alongside two additional GRACE time-series and a time-series created using the GAC and GLDAS products. All the time-series are calculated at the same location and are offset from each other to aid comparison.

The two additional GRACE time-series were made with www.thegraceplotter.com, courtesy of CNES/GRGS (CNES/GRGS, 2015), with one created using the CNES/GRGS GRACE spherical harmonic solution and the other created using the CSR RL05 Level-2 data, filtered using a DDK5 filter (Kusche et al., 2009). The CSR RL05 DDK5 time-series uses the same CSR RL05 Level-2 data, but with the DDK5 filter to remove noise rather than a 400 km Gaussian smoother with a de-striping filter. The CNES/GRGS time-series is computed from the CNES/GRGS RL03-v1 monthly spherical harmonic solutions which mitigate for noise using regularisation, where all spherical harmonic coefficients above degree and order 30 are constrained to the

background gravity field. While the time-series from the GRACE plotter are not corrected for GIA, this will not introduce an annual signal into the time-series as GIA is a constant trend over the life of the GRACE satellite (Velicogna, 2009). GIA is also small over the Sahara. The GAC time-series is included as it is the monthly average of the AOD1B product (Flechtner, 2014). During the GRACE data processing undertaken here, the AOD1B product was added to the mean background field to avoid short term aliasing of ocean and atmospheric mass variations. A time-series from GLDAS is included to provide a model of the expected water variability at the location, including any possible contributions from soil moisture, total canopy water storage, snow and surface runoff (Rodell et al., 2004).

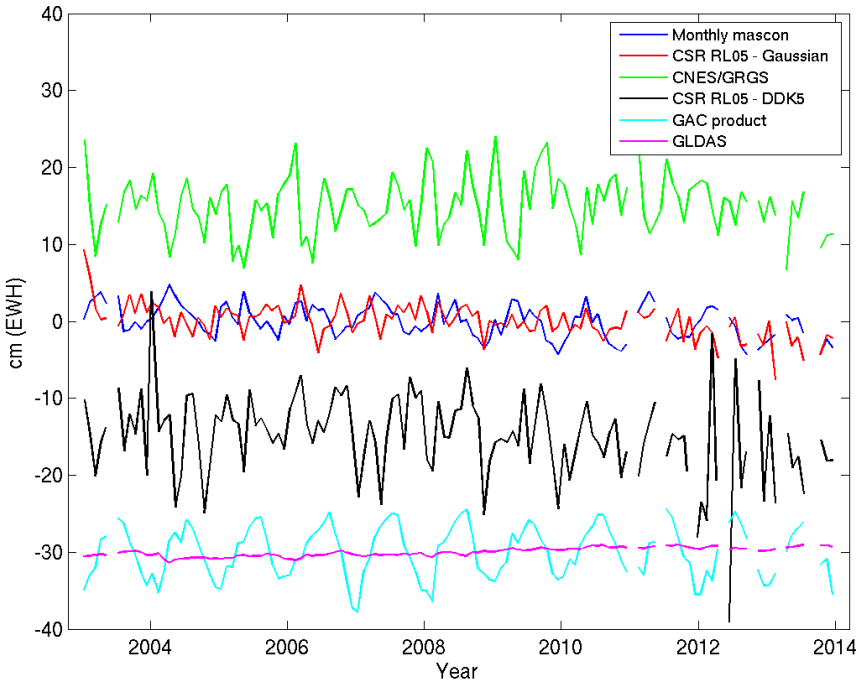

Figure 76. The mascon and CSR RL05 time-series from Figure 74 with time-series from the CNES/GRGS solution, a CSR RL05 time-series filtered using a DDK5 filter (Kusche et al., 2009) and a time-series of the GAC and GLDAS products. The different time-series have been offset by 15 cm EWH to allow for easy comparison. The CNES/GRGS and CSR RL05 - DDK5 time-series were made with www.thegraceplotter.com, courtesy of CNES/GRGS (CNES/GRGS, 2015).

Figure 76 allows for a direct comparison of the 4 GRACE time-series at the same geographical location. Although the time-series have been offset to aid the comparison, it is clear that all time-series are different with different phases and amplitudes. The mascon time-series contains less noise than the CNES/GRGS time-series and CSR RL05 time-series filtered using a DDK5 filter. Although the CNES/GRGS time-series could contain an annual signal, this is not entirely clear due to noise. No seasonal cycle is evident in the CSR RL05 time-series filtered using a DDK5 filter. Figure 76 also

identifies an important point: namely the effect of the filter on time-series, especially at the noise level. The difference between the two CSR RL05 time-series, which use the same data, would be expected to be minimal as the only difference between these time-series is the filter used to remove noise. Another important point highlighted by Figure 76 is the problem of finding a quiet point over land to validate the noise in GRACE solutions.

While it is possible that some, or all, of the GRACE time-series in Figure 76 could contain an annual signal, in most time-series the signals are masked by noise. Therefore, the validity of the annual signal in the mascon solution needs to be confirmed. To investigate any potential geophysical cause of the annual signal in the mascon time-series a comparison was made with the GAC time-series. The GAC product is the monthly average of the AOD1B product. This comparison should highlight if the AOD1B product is aliasing the signal. Comparing the time-series of the GAC product, with the monthly mascon solution, reveals that the GAC product is several months out of phase and is larger in amplitude than the monthly mascon time-series. The next comparison was made to hydrology modelled using GLDAS. Figure 76 reveals that there is no distinguishable signal in the GLDAS time-series, which is expected as this part of the Sahara only receives between 1 to 5 mm of rainfall a year. However, GLDAS does not include ground water or surface water storage.

It is therefore possible that the annual signal seen in the mascon solution could be real signal including any mis-modelling of the atmospheric loading. Another contributing factor, while not necessarily the source of this signal, is that the Nile has been dammed approximate 5° east of the Sahara point. This has created one of the world's largest artificial lakes, lake Nubia/Nasser, which fluctuates in water height between 160 m and 183 m, with an annual variation of about 5 m observed over the GRACE period (El Gammal et al., 2010). The lake is gradually filled from September with the water level reaching a peak in early spring before being discharged for irrigation. The lowest water level is reached in July/August (Muala et al., 2014). Longuevergne et al. (2013) found that the gravity changes resulting from the changing water height of Lake Nasser can be seen in GRACE data over the lake. The Sahara point is also only 2 mascons away from Lake Nasser. While the mascons are in different drainage basins, implying that the two points should be uncorrelated, it is possible that some degree of correlation could exist if the lake is on the boundary of the Nile drainage basin. At a distance of 5° (~550 km)

it is possible that the signal from the lake could contribute to the annual signal in the mascon solution.

To investigate, the gravity signal of Lake Nasser was estimated using the methodology of Moore and Williams (2014). Lake Nasser was described using a kernel function, with the lake height recovered using altimetry. These were combined to estimate the gravity signal of the lake on a monthly basis. The results are shown in Figure 77.

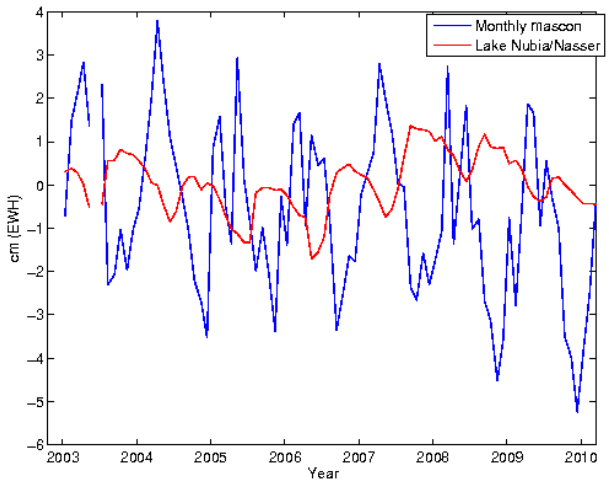

Figure 77. The monthly mascon time-series plotted along with the gravity signal of Lake Nasser, estimated using the methodology of Moore and Williams (2014), at the Sahara desert point.

Figure 77 reveals that the gravity signal of Lake Nasser can be observed at the Sahara point. Although the phase of the Lake Nasser time-series does not match that of the mascon time-series, the results here suggest that it is possible that signals have leaked into the mascon time-series. While commenting directly on the cause of the seasonal variation obtained over the Sahara point is beyond the scope of this work, the results found here do suggest that it is entirely possible that a small seasonal signal could exists at this location. However, it cannot be ruled out that the annual signal seen in the mascon time-series is the result of errors in the background models, particularly atmospheric pressure, used during data processing.

The results presented in this section validate the signal recovery of the monthly mascon solution, suggesting that the constraint matrix applied during the calculation of the monthly mascon solution is able to reduce the noise over both the land and the ocean. The noise is generally lower in the mascon solution, compared with the CSR RL05 solution, confirming the results of the simulations in Chapter 6. Having compared the

standard deviations of the noise at all 6 points, the use of S=0.004(0.04) in the constraint matrix is validated by the reduction of the standard deviation of the noise in the mascon time-series. Table 24 shows the effect of increasing the scale from S=0.001(0.01) to S=0.004(0.04) on the standard deviation of the noise in the time-series at the 6 locations tested. At all locations increasing the scale, reduced the noise. For clarity, all the time-series in section 7.2 were generated using S=0.004(0.04).

Location	**Latitude**	**Longitude**	**Standard deviation of noise** (cm EWH)	
			Scale (*S*) Main and Resonance(Thermal)	
			0.001(0.01)	0.004(0.04)
Ocean 1	20°	320°	1.8	1.0
Ocean 2	85°	180°	2.6	2.2
Ocean 3	60° S	255°	2.3	1.5
Ocean 4	15°	135°	2.4	1.4
Ocean 5	15° S	75°	2.0	1.3
Sahara	23°	27°	2.2	1.1

Table 24. Table showing the effect of increasing the scale in Eq. (16) from S=0.001(0.01) to S=0.004(0.04) in terms of the standard deviation of the noise in the time-series at the 6 locations tested.

7.3 *10 day solutions*

Having validated the monthly mascon solution through a comparison with the CSR RL05 solution, the 10 day mascon solution will now be compared with the monthly mascon solution. The comparison will be undertaken at the points of section 7.2. While there are 124 monthly mascon solutions spanning the period January 2003 to December 2013, there are 359 10 day solutions. Like the monthly solutions, 10 day solutions are not generated for the month of poor data (June 2003) or when the equipment on-board the GRACE satellites was turned off to conserve power (January 2011; June 2011; May 2012; October 2012; March 2013; August 2013; and September 2013). In addition, there are 13 ten day solutions that were not generated due to periods of missing data. The majority of these overlapped with the missing months discussed above. These missing solutions were identified by stipulating that out of the 30 days incorporated into each 10 day solution, a minimum of 15 were required. Further, out of the 10 days that formed the central period, a minimum of 5 days were required.

The monthly and 10 day solutions are generated using the same daily normal matrices and, thus, are expected to recover a similar signal. The only difference between the two solutions is the use of the temporal constraint matrix in Eq. (15) in the 10 day solution and the difference in the days included in the solution. While even daily solutions would not to be able to capture sub-daily mass variations (Sabaka et al., 2010), there are some

mass variations that are sub-monthly (Seo et al., 2008b). These should be sampled using 10 day solutions, but averaged and therefore aliased within the monthly solutions. As in the monthly solution a scale factor of S=0.004/0.04 was used for the 10 day mascon solutions.

The first comparison was at ocean point 1. Figure 78 is a plot of the time-series from the 10 day and monthly mascon solutions.

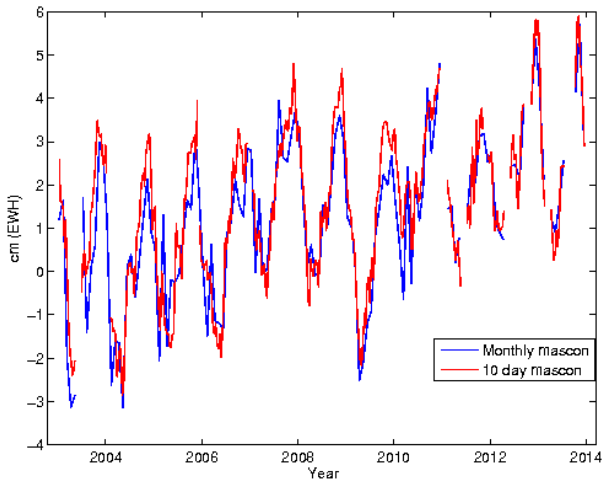

Figure 78. Mass flux time-series at ocean point 1 for the monthly mascon solution (blue) and the 10 day mascon solution (red). Units cm (EWH).

Figure 78 reveals that both mascon solutions capture near-identical signals. To analyse the noise in the signal, as with the comparisons in section 7.2, a constant, linear trend and annual and semi-annual cycles in the two time-series were estimated and removed. A lag plot of the 10 day solutions was created to investigate temporal correlation in the time-series. The result is plotted in Figure 79, which also included the lag plot of the monthly solution from Figure 62 for comparison.

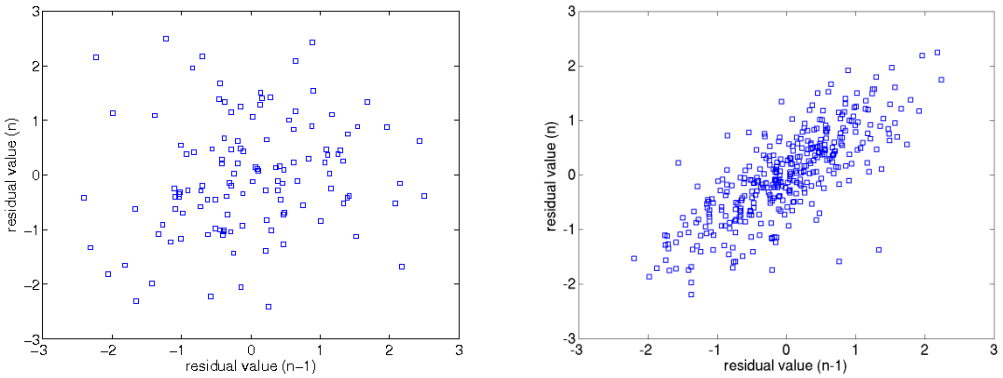

Figure 79. Lag plot of the remaining signal in the mascon solution (left) and the 10 day mascon solution (right) after a constant, linear trend and annual and semi-annual signals in the time-series were estimated and removed. Units cm EWH.

Figure 79 shows that the 10 day solution (right) has a strong temporal correlation, compared to the monthly mascon solution (left). The correlation coefficient for the 10 day solution is 0.78, compared to the monthly solution of 0.16. However, this correlation should be expected as the constraint matrix used during the generation of the 10 day solutions constrains mascon solutions close in time. In addition, each subsequent 10 day solution will be related to the previous 10 day solution due to the overlapping of data. The plot of the 10 day time-series in Figure 79 (right) is similar to the moving average lag plot of Stockwell (2006) which is expected as the 10 day mascon constraint is similar to a moving average. As this high correlation will be present in all 10 day time-series, no further lag plots of the 10 day solutions will be generated. The time-series in Figure 78 suggest that the noise in both the mascon solutions is similar.

The times-series of the 10 day and monthly mascon solutions were generated at ocean point 2 and are shown in Figure 80. Like Figure 78, Figure 80 reveals that the two solutions capture a very similar signal. There are only slight differences between the two solutions; some of the peaks in the monthly mascon time-series have a greater amplitude than the peaks in the 10 day solution. This difference is up to ~3 cm. The converse is true in Figure 78, although the difference there is only ~1 cm.

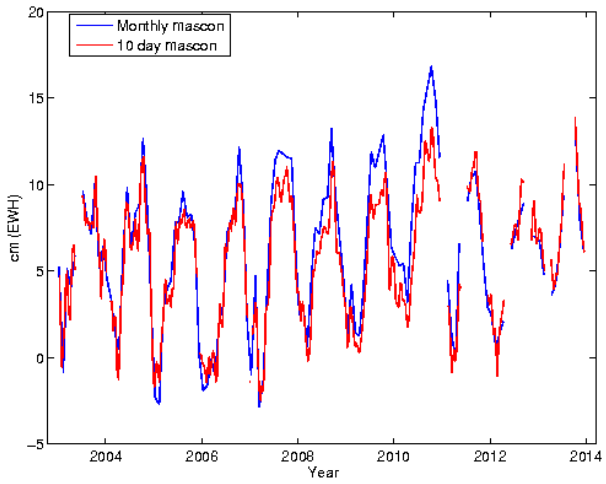

Figure 80. Mass flux time-series at ocean point 2 for the monthly mascon solution (blue) and the 10 day mascon solution (red). Units cm (EWH).

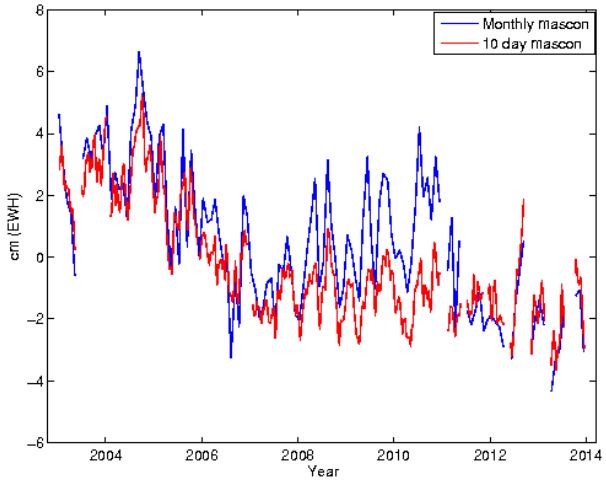

Figure 81. Mass flux time-series at ocean point 3 for the monthly mascon solution (blue) and the 10 day mascon solution (red). Units cm (EWH).

The times-series of the 10 day and monthly mascon solutions were generated at ocean point 3 (Figure 81). Unlike Figure 78 and Figure 80, which show that the two solutions capture a similar signal there are differences in the time-series, mainly between 2007 and 2011. At first glance it appears as if the monthly time-series contains more noise. Similar to Figure 63, the effect of using difference values for the scale, *S*, on the 10 day solution was investigated. The results are shown in Figure 82 where the monthly mascon solution (*S*=0.004(0.04)) was plotted along with the 10 day solution using scales of *S*=0.001(0.01), *S*=0.004(0.04), *S*=0.008(0.08) and *S*=0.01(0.1).

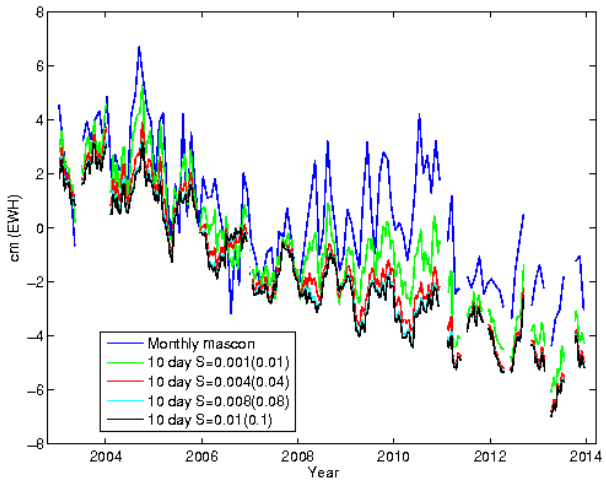

Figure 82. 10 day mascon time-series at ocean point 3 for different scale factors. The monthly mascon solution (*S*=0.004(0.04)) is included for reference. Units of cm (EWH).

Figure 82 reveals that the difference between the monthly and 10 day mascon solutions relates to the value of the scale, *S*. When a scale of *S*=0.001(0.01) is used for the 10 day mascon solution, the resulting time-series is closer to the monthly mascon solution. Reducing the scale in the 10 day mascon solution weakens the constraint. Sabaka et al. (2010) found that using a temporal constraint improved the mascon solutions over ocean areas. The temporal constraint tightens the constraint between mascons, resulting in a stronger constraint in the 10 day mascon solution. Therefore, it is possible that there is aliasing in monthly solution that does not appear in the 10 day solution, scaled using *S*=0.004(0.04), due to the stronger constraint. This aliasing could be the result of errors in the ocean model, which Ray et al. (2009) found needed improvement around Antarctica, or signal leakage from the land (Chambers and Bonin, 2012). However, Watkins et al. (2015) found that there are times when the *a-priori* variance of a time correlated solution needs to be increased to reflect the expected mass change, such as after an earthquake. The *a-priori* variance can be increased by reducing the correlation. The findings of Watkins et al. (2015) suggest that there are some signals that could be masked in the 10 day mascon solution if the solution is over constrained.

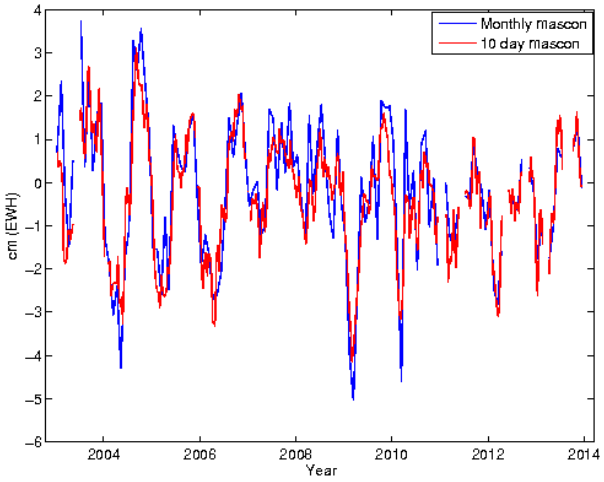

Figure 83. Mass flux time-series at ocean point 4 for the monthly mascon solution (blue) and the 10 day mascon solution (red). Units of cm (EWH).

The times-series of the 10 day and monthly mascon solutions were generated at ocean point 4. Figure 83 reveals that at ocean point 4, both the mascon solutions capture a similar signal. There is very little difference between the two solutions. The times-series of the 10 day and monthly mascon solutions were generated at ocean point 5 and are shown in Figure 84.

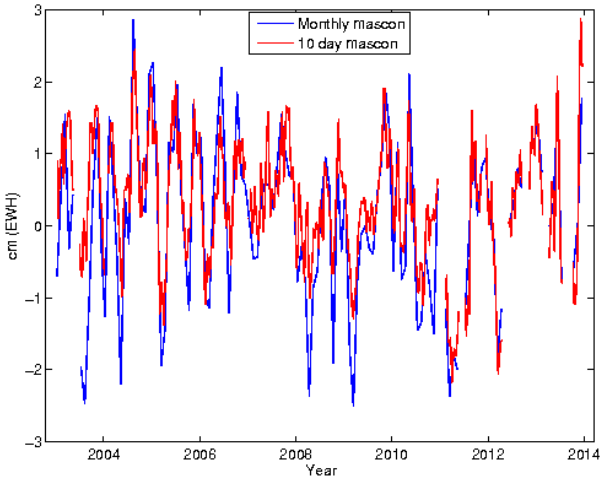

Figure 84. Mass flux time-series at ocean point 5 for the monthly mascon solution (blue) and the 10 day mascon solution (red). Units of cm (EWH).

Again, Figure 84 reveals that both mascon solutions capture a similar signal. As in Figure 80 there is a reduction in the amplitude of the signal in the 10 day time-series of up to ~1 cm. The time-series of the 10 day solution appears to contain less noise than the time-series of the monthly solution. The final comparison of the 10 day and monthly mascon signals is at the point in the Sahara (Figure 85).

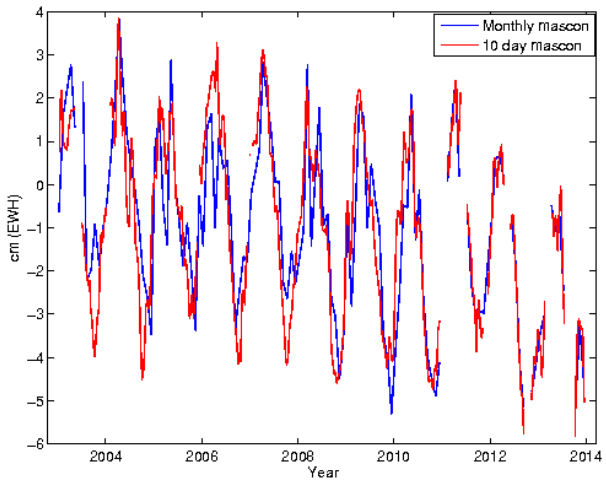

Figure 85. Mass flux time-series for a point in the Sahara desert for the monthly mascon solution (blue) and the 10 day mascon solution (red). Units of cm (EWH).

As at the ocean points, Figure 85 reveals that the two time-series recover similar signals, with the annual signal present in the monthly mascon solution also present in the 10 day solution.

Overall, the comparison of the 10 day and monthly mascon time-series reveals that there is minimal difference between the two mascon solutions. At the majority of locations, a similar signal and amplitude was obtained, with any difference relating to mass variations that are sub-monthly aliasing the monthly solutions (Seo et al., 2008b). The difference in the two mascon time-series at ocean point 3 could be the result of aliasing in the monthly mascon solution. However, the results of Watkins et al. (2015) indicate that care needs to be taken when using the 10 day mascon solutions as signal could be masked if the solution is over constrained.

7.4 *Mass trends*

The 10 day and monthly mascon solutions are now used to calculate mass trend for regions of interest. The results in section 7.3 reveal that the signal recovered using the monthly and 10 day mascon solutions are similar, suggesting that there should be little variation in the mass trend estimated. However, it is expected that the 10 day solution will better capture sub-monthly variations due to less aliasing of the signals (Seo et al., 2008b) and the use of a temporal constraint (Sabaka et al., 2010).

To calculate the mass trend, using the 10 day or monthly mascon methodology, the mass trend of each individual mascon must be determined. Within this study a trend is calculated at each point on the 1° by 1° global grid, as described in section 7.1.3. The

mass trend, expressed as cm of EWH/year at each point is then assigned to the 2° mascon in which the 1° by 1° point lies. This allows the average mass trend of each mascon to be calculated. Multiplying by the area of the mascon and density of fresh water, (1000 kg m^{-3}), the mass trend of each mascon can be expressed as kg/year or Gt/year. The total trend over a drainage basin can be calculated by summation of all mascons within that basin (e.g. Luthcke et al., 2013, Schrama et al., 2014).

For regions that contain multiple drainage basins, such as Antarctica and Greenland, the total trend can be calculated by summation of the mass trend of all drainage basins within that area. Sub-regions, such as East and West Antarctica, are calculated the same way. Mass trends are provided with uncertainties of 1-sigma, where the uncertainty is the formal error from the linear regression. In the case of the 10 day mascon solution, the uncertainties have been multiplied by $\sqrt{3}$ for equivalence with the monthly solutions. This is required as the linear regression is fit through 3 times as many solutions. In addition, Figure 79 revealed a strong temporal correlation in the 10 day mascon solution. This is disregarded during the linear regression. Systematic errors in models are not included in the uncertainties. Within this study, the mass trends are provided for validation of the mascon solutions, while geophysical interpretation is beyond the scope of the study.

7.4.1 *Antarctica*

The mass trend of Antarctica is of major interest, due to its contribution to global sea level. A recent study (King et al., 2012) found that present day mass loss over Antarctica is contributing 0.19±0.05 mm/year to sea level rise. Recovery of Antarctica mass change using the 10 day and monthly mascon solutions will be compared to estimates published in the literature.

When calculating Antarctica mass trend, the corrections described in section 7.1.2, were applied. These include the removal of the GLDAS hydrology model globally. It is worth noting that published studies often disagree about the current mass trend of Antarctica. For example, two recent GRACE derived estimates have Antarctic mass trend ranging from -69±18 Gt/year (King et al., 2012) to -143±73 Gt/year (Velicogna, 2009). Although these studies use the same Level-2 data, the disagreement is the result of the GIA correction applied. GIA is the largest uncertainty over Antarctica. The mascon solutions presented here will have GIA corrected using three GIA models (ICE-6G,

IJ05_R2 and W12a). However, for comparison to published mass trends, where possible, the same GIA correction used by the authors will be applied.

To estimate the mass trend of Antarctica from the 2° mascons, the mascons were assigned to the same Zwally et al. (2012) drainage basins used to constrain the solutions. The relationship between mascons and drainage basins is shown in Figure 86.

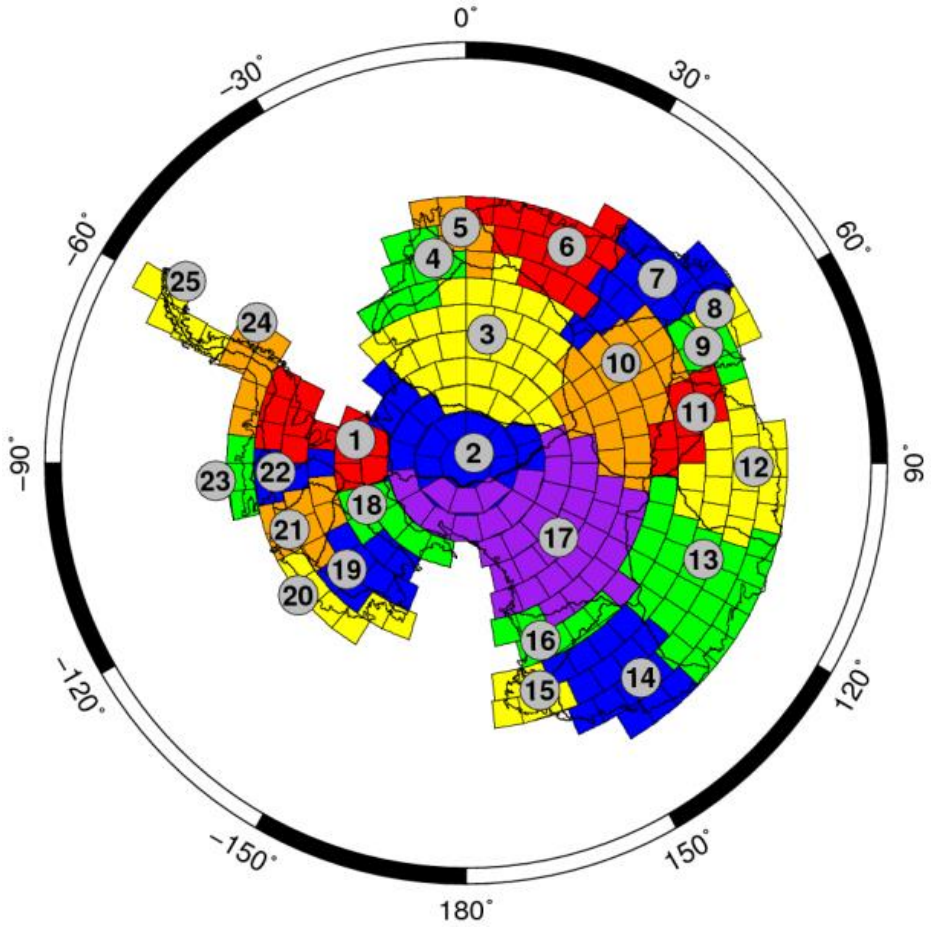

Figure 86. The layout of the 2° mascons over Antarctica. The mascons relate to the Zwally et al. (2012) Antarctica drainage basins. The basin outlines are provided for reference.

Figure 86 shows that the 2° equal area mascons do not fall perfectly within the Zwally et al. (2012) basins. When a mascon straddles the boundary of two or more basins, the mascon is assigned to the drainage basin with the largest proportion. In addition, coastal mascons that cover both land and ocean, are included to fully represent the land mass of Antarctica. These mascons are defined as land mascons and are constrained to other mascons in the same basin during the generation of the solutions. In Figure 86, East Antarctica is comprised of basins 2 to 17, while basins 1 and 18 to 25 are classified as West Antarctica. The mass change of East and West Antarctica are calculated through

summation of the relevant basins. The total mass change is the summation of the mass change of East and West Antarctica.

The mass change (Gt/year) of East and West Antarctica and the Antarctic Ice Sheet (AIS) is summarised in Table 25. The estimates are provided for the 10 day and monthly mascon solutions using the three GIA models for the period January 2003 to December 2013.

Solution		**Mass trend estimate Jan 2003 – Dec 2013**		
		W12a	**IJ05_R2**	**ICE-6G**
Monthly	East Antarctica	55 ± 7	26 ± 7	27 ± 7
	West Antarctica	-144 ± 5	-131 ± 5	-157 ± 5
	AIS	-89 ± 12	-104 ± 12	-130 ± 12
10 day	East Antarctica	56 ± 7	27 ± 7	28 ± 7
	West Antarctica	-139 ± 5	-126 ± 5	-152 ± 5
	AIS	-83 ± 12	-98 ± 12	-124 ± 12

Table 25. Mass change of East and West Antarctica and the AIS for the monthly and 10 day mascon solutions. The estimates are provided for three common GIA models. All values Gt/year.

Table 25 reveals the mass change of Antarctica ranges -89 to -130 Gt/year, for the monthly mascon solution and -83 to -124 Gt/year for the 10 day mascon solution. The range of the solutions is the direct result of the GIA correction applied, as the only difference between the monthly and 10 day estimates is the choice of GIA model. The mass change of the AIS is nearly 50% larger when using ICE-6G compared to W12a. However, regardless of the GIA model applied, East Antarctica is gaining mass while West Antarctica is losing mass. As the mass loss in West Antarctica exceeds the mass gain in East Antarctica, overall Antarctica was found to be losing mass. While Table 25 reveals that the choice of GIA model affects the mass trend estimated, a comparison between the monthly and 10 day solutions, for the same GIA model, reveals no significant differences. Table 26 shows a breakdown of the mass trends estimated in Table 25; the GRACE only mass trend is provided, along with the corrections applied to obtain the mass change.

	GRACE only	GIA correction			Hydrology
Monthly		**W12a**	**IJ05_R2**	**ICE-6G**	
East	64 ± 7	-8	-37	-36	-0.32
West	-100 ± 5	-44	-30	-57	-0.28
AIS	-36 ± 12	-52	-67	-93	-0.60
10 day					
East	65 ± 7	-8	-37	-36	-0.32
West	-95 ± 5	-44	-30	-57	-0.28
AIS	-30 ± 12	-52	-67	-93	-0.60

Table 26. The mass change from GRACE only along with the corrections applied. All values Gt/year.

Table 26 shows that the GIA correction can be over half the size of the mass change estimate derived from the GRACE solution. The GIA models apply different corrections to East and West Antarctica and this highlights the impact of the GIA model on the solution. As the generation and validation of published GIA models is beyond the scope of this work, Table 26 supports the premise of including the Antarctica mass change estimates for a range of GIA models in order to reflect the uncertainty of modelling Antarctic GIA. Finally, Table 26 reveals that the GLDAS hydrology correction applied over Antarctica is small, being less than -1 Gt/year over Antarctica.

The estimates derived using mascons can be compared to mass trends published by other groups, a selection of which is shown in Table 27. The values in Table 27 cover different time periods, levels of GRACE data and GIA corrections. Apart from the 10 day mascon solution of Luthcke et al. (2013), all the studies use monthly CSR RL05 Level-2 products. To aid the comparison, results from the mascon solutions are also included in Table 27 using, where possible, the same period of data and the same GIA correction as the published mass change estimates. Where groups have generated their own GIA model, a comparison will be made to all three GIA models presented in Table 25.

There are several recent studies, such as Jacob et al. (2012), King et al. (2012) and Shepherd et al. (2012) that were not included in Table 27. While these studies have been important to understand the current ice mass change of Antarctica, they use the older CSR RL04 data. The mascon solutions presented here are based on RL02 of the Level-1B data. Level-1B RL02 was also used to create the CSR RL05 products. For the purpose of validation, only studies that use CSR RL05 data were included over Antarctica as Gunter et al. (2014) found an average systematic bias of -34.4 Gt/year of mass trend between estimates derived using CSR RL04 and CSR RL05 solutions. A greater mass loss was observed when estimates were derived from CSR RL05 data. A

similar conclusion was observed by Williams et al. (2014). The studies by Gunter et al. (2014) and Williams et al. (2014) highlight the difficultly in comparing solutions derived using different releases of GRACE data.

Study	Period	Data	GIA model	EA	WA	AIS
Gunter et al. (2014)	02/03 – 10/09	CSR RL05	Own	5 ± 38	-105 ± 22	-100 ± 44
Monthly	02/03 – 10/09	Level-1B	W12a	7 ± 11	-105 ± 5	-98 ± 16
			IJ05_R2	-22 ± 11	-91 ± 5	-113 ± 16
			ICE-6G	-21 ± 11	-118 ± 5	-139 ± 16
10 day	02/03 – 10/09	Level-1B	W12a	11 ± 6	-98 ± 3	-88 ± 16
			IJ05_R2	-18 ± 6	-85 ± 3	-103 ± 16
			ICE-6G	-17 ± 6	-112 ± 3	-130 ± 16
Luthcke et al. (2013)	12/03 – 12/10	Level-1B	IJ05_R2	62 ± 28	-144 ± 30	-81 ± 26
Monthly	12/03 – 12/10	Level-1B	IJ05_R2	-4 ± 10	-118 ± 5	-122 ± 16
10 day	12/03 – 12/10	Level-1B	IJ05_R2	-3 ± 10	-113 ± 5	-115 ± 16
Sasgen et al. (2013)	01/03 – 09/12	CSR RL05	Own	26 ± 13	-140 ± 16	-114 ± 23
Monthly	01/03 – 09/12	Level-1B	W12a	49 ± 8	-135 ± 5	-86 ± 13
			IJ05_R2	20 ± 8	-122 ± 5	-101 ± 13
			ICE-6G	21 ± 8	-148 ± 5	-127 ± 13
10 day	01/03 – 09/12	Level-1B	W12a	51 ± 8	-130 ± 5	-79 ± 13
			IJ05_R2	22 ± 8	-116 ± 5	-94 ± 13
			ICE-6G	23 ± 8	-143 ± 5	-120 ± 13
Schrama et al. (2014)	02/03 – 06/13	CSR RL05	W12a	54 ± 18	-145 ± 6	−91 ± 23
Monthly	02/03 – 06/13	Level-1B	W12a	55 ± 7	-144 ± 5	-89 ± 12
10 day	02/03 – 06/13	Level-1B	W12a	57 ± 7	-135 ± 5	-79 ± 12
Velicogna et al. (2014)	01/03 – 12/13	CSR RL05	ICE-5G			−180 ±10
Monthly	01/03 – 12/13	Level-1B	ICE-5G			-171 ± 12
10 day	01/03 – 12/13	Level-1B	ICE-5G			-165 ± 12
Williams et al. (2014)	03/03 – 07/12	CSR RL05	W12a	97 ± 13	−159 ± 9	−58 ± 16
Monthly	03/03 – 07/12	Level-1B	W12a	47 ± 8	-136 ± 5	-89 ± 13
10 day	03/03 – 07/12	Level-1B	W12a	48 ± 8	-130 ± 5	-81 ± 13

Table 27. Published mass change estimates of Antarctica. The author, period, data and GIA model is provided for reference. The results for East and West Antarctica are given where available. The error bounds of William et al. (2014) excludes the contribution of GIA. All values Gt/year.

Comparing the published AIS mass trend estimates in Table 27 reveals that the values range from −58 ± 16 to −180 ±10 Gt/year. The range reflects the different time periods but, more importantly, the model used to correct for GIA. A comparison of the published AIS mass trends of Table 27 with the mascon derived mass trends in Table 25, reveals that the mascon solutions generally agree within the error bounds of the published studies, although the comparison is not ideal due to the different periods of the studies in Table 27. In addition, the results in Table 27 use GIA models not included in Table 25 while Gunter et al. (2014) and Sasgen et al. (2013) have developed their own GIA models. The impact that GIA has on the mass change has already been identified. Therefore, a comparison will be made between the published studies and mascon solutions in Table 27.

Gunter et al. (2014) estimated a mass trend of -100 ± 44 Gt/year between February 2003 and October 2009. As Gunter et al. (2014) generated their own GIA model, the mascon mass trends were calculated for the same period correcting for GIA using the three models in Table 25. A comparison to the mascon results presented in Table 27 reveals that all the estimated mascon mass trends are within the error bars of the Gunter et al. (2014) study.

Luthcke et al. (2013) estimated a trend of -81 ± 26 Gt/year, correcting GIA using IJ05_R2. A comparison to the mascon results presented in Table 27 reveals that the mascon results are outside these error bounds. Investigating this further, the West Antarctica mass trends obtained from the mascon solutions were found to be within the error bounds of the Luthcke et al. (2013) study. The main different was over East Antarctica, where Luthcke et al. (2013) calculated a mass gain of 62 ± 28 Gt/year compared to a small loss in the mascon solutions. One possible reason for this difference is that although the Luthcke et al. (2013) method estimates mascon parameters from Level-1B, the authors use a 1° equal area solution, with different parametrisation and background models.

However, despite these differences, the solutions would be expected to agree within stated error bounds. Therefore, the difference caused by the GIA correction was investigated. Although Luthcke et al. (2013) corrects GIA using IJ05_R2, Luthcke et al. (2013) modified IJ05_R2 using an ensemble of Earth models with upper- and lower-bounds. This model is not publically available. With this in mind the GIA in the mascon solutions presented here were corrected using W12a. This resulted in an AIS mass

trends of -106 ± 16 (-100 ± 16) Gt/year for the monthly (10 day) mascon solutions. These are within the error bounds of the Luthcke et al. (2013) estimate. This suggests that the difference between the two mascon solutions could be the result of the GIA model used.

In addition, Table 5 of Luthcke et al. (2013) was used to calculate the GRACE only mass trend, by reinstating the GIA trend. A mass trend of -34 ±8 Gt/year for the AIS was obtained. Comparable values of -54 ± 16 (-48 ± 16) Gt/year were obtained for the monthly (10 day) mascon solutions. While this shows that there are differences between the solutions, it reveals that there is a closer agreement between the estimates than when the IJ05_R2 GIA correction was applied.

Sasgen et al. (2013) estimated an AIS trend of -114 ± 23 between January 2003 and September 2012. For comparison, the mascon estimates were calculated for the same period using the three GIA models in Table 25 as Sasgen et al. (2013) developed their own GIA model. In Table 27 the mascon estimates obtained using IJ05_R2 and ICE-6G fall within the error bounds of the estimate calculated by Sasgen et al. (2013), with the W12a estimates just outside. The comparison suggest a good agreement between the mascon solutions presented here and the Sasgen et al. (2013) solution. In Table 27, good agreements were also found to the results of Schrama et al. (2014) and Velicogna et al. (2014).

The final comparison undertaken was to the study of Williams et al. (2014), where a mass trend of −58 ± 16 Gt/year was obtained for AIS between March 2003 and July 2012. GIA was corrected using W12a. The mascon estimates in Table 27 were outside the error bounds of the Williams et al. (2014) study, although the error bounds of the Williams et al. (2014) study do not include the error introduced from GIA. One difference in the study of Williams et al. (2014), compared with the other studies in Table 27 and the results presented here, is that significant autocorrelation was found to be present when calculating mass trends. The other studies do not account for this. This could be the cause of the differences between the solutions. Although investigating this is beyond the scope of the work presented here, this could be an avenue for future work.

Overall the comparisons provide confidence in the mascon mass trends for the AIS. The spatial distribution of the Antarctica mass change is plotted in Figure 87 and Figure 88 for the monthly and 10 day mascon solutions respectively. In both plots GIA was corrected using W12a.

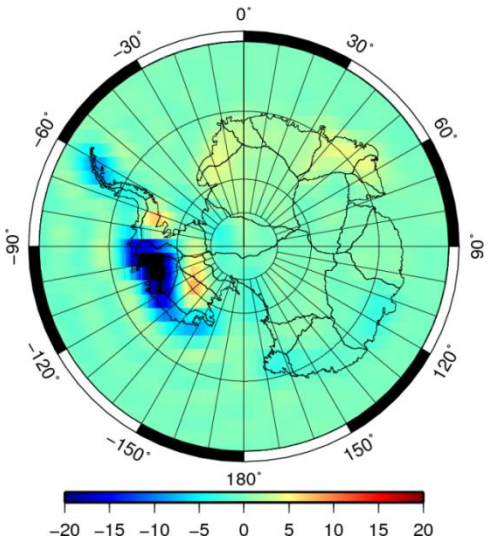

Figure 87. Spatial distribution of the Antarctic mass change from the monthly mascon solution. GIA corrected using W12a. Units cm/year (EWH).

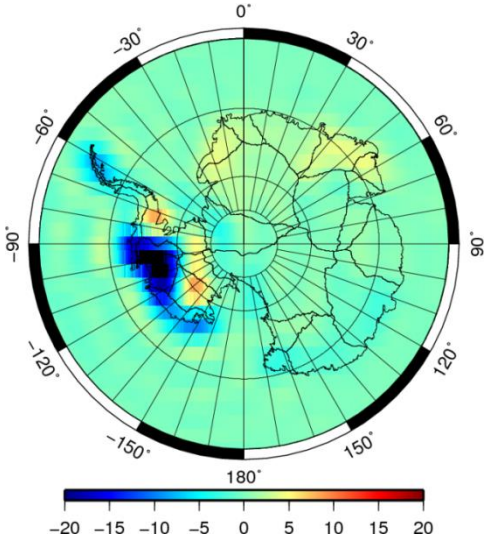

Figure 88. Spatial distribution of the Antarctic mass change from the 10 day mascon solution. GIA corrected using W12a. Units cm/year (EWH).

Figure 87 and Figure 88 exhibit little difference in the spatial distribution of the mass trend. Both show East Antarctica gaining mass, with mass loss in West Antarctica. The mass loss over West Antarctica is dominated by a mass loss in basin 21, which contains the Thwaites Glacier. A similar result was obtained by King et al. (2012). Figure 89 and Figure 90 are time-series plot of mass change over East and West Antarctica and AIS respectively.

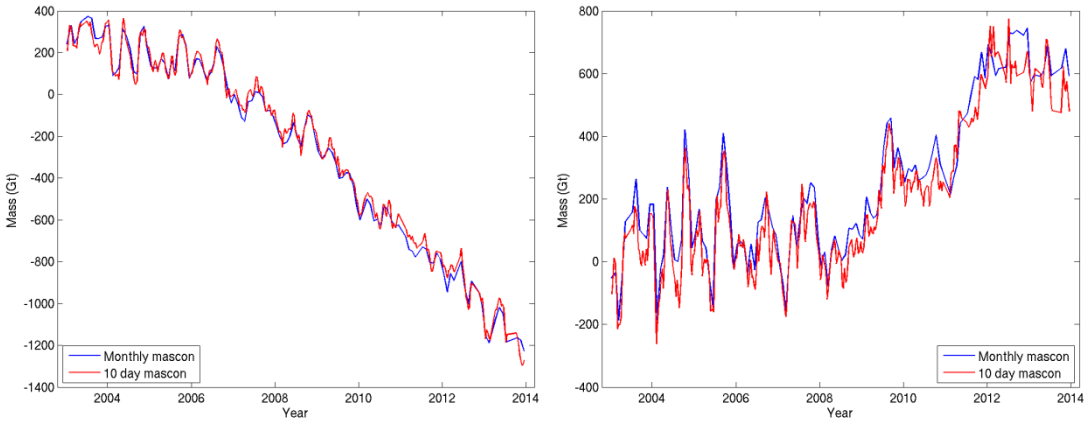

Figure 89. Time series of mass, in Gt, for West Antarctica (left) and East Antarctica (right) from the monthly and 10 day mascon solutions.

Figure 89 shows that the mass of East Antarctica was relatively stable until 2008 after which the area has experienced mass gain until ~2012. Over the time period of the GRACE mission, West Antarctica has always been losing mass, and with acceleration since 2006. Overall, Figure 90 shows the mass loss of Antarctica. The mass trends estimated using the 10 day and monthly mascon solutions are very similar.

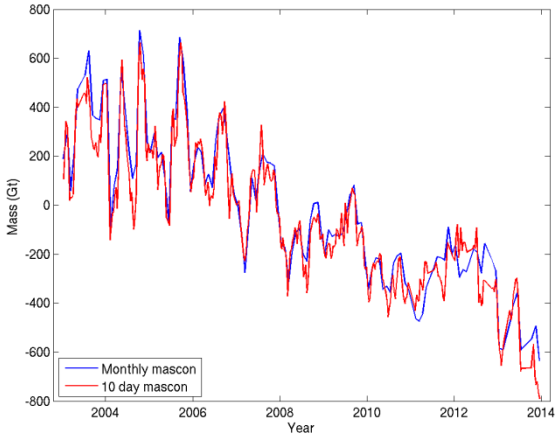

Figure 90. Time series of mass, in Gt, for the Antarctic Ice Sheet from the monthly and 10 day mascon solutions.

7.4.2 *Greenland*

As for Antarctica the mass trend of Greenland is of major interest due to its contribution to sea level rise. Jacob et al. (2012) found that together Antarctica and Greenland contribute 0.41±0.08 mm/year to sea level rise. To determine Greenland's contribution to rising sea level, an accurate estimate of the current mass change is required. Similar to Antarctica, the mass trend using the 10 day and monthly mascon solutions will be compared to estimates published in the literature.

As discussed in Chapter 6, a layout of 8 basins was found to best capture a realistic mass signal over Greenland. The relationship between the mascons and the drainage basins is shown in Figure 91. As over Antarctica, the mascons often straddle two or more basins. As previously, the mascon is assigned to the drainage basin in which the largest proportion lies. In addition, mascons around the coast of Greenland, are included to fully represent the land mass of Greenland.

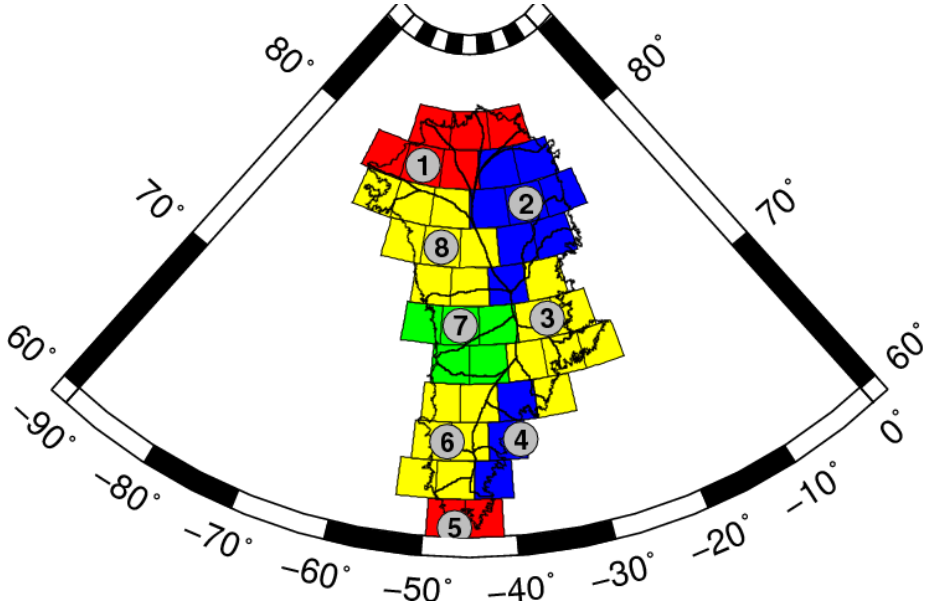

Figure 91. The layout of the 2° mascons over Greenland. The mascons relate to the Zwally et al. (2012) Greenland drainage basins with outlines provided for reference.

Using the basins of Figure 91, mascon mass trends for Greenland were calculated. Table 28 reveals that over Greenland, the 10 day solution produces a larger mass loss than the monthly solution, with a difference of 10 Gt/year between the two solutions. This differs from Antarctica, where the monthly solution has a slightly larger mass loss signal than the 10 day solution. However, the difference in the mascon solutions over Greenland in ~4% of the total monthly trend, compared to ~7% over Antarctica. Alongside the mass trend in Table 28, the GRACE only results are provided along with the GIA and GLDAS hydrology corrections. The GIA correction is small over Greenland while there are a limited number of GIA models, with ICE-5G being the most commonly used. In Table 28, GIA is corrected using ICE-6G, the newest release in the ICE series. Over Greenland, the hydrology correction is also small.

Solution	Mass trend	GRACE only	ICE-6G	Hydrology
Monthly	-232 ± 6	-232 ± 6	-0.41	0.28
10 day	-242 ± 6	-242 ± 6	-0.41	0.28

Table 28. The mass trend for Greenland along with the GRACE only trend and the corrections applied. All values Gt/year.

As for Antarctica, comparisons are made with published results. Again, the same time-periods were compared with GIA corrected using the same GIA models, where possible. The results from the published studies and comparable mascon solutions are shown in Table 29. Studies by Jacob et al. (2012) and Shepherd et al. (2012) are not included as they are based on CSR RL04 data.

Study	Period	Data	GIA model	GIS
Luthcke at al. (2013)	12/03 – 12/10	Level-1B	ICE-5G	-230 ± 12
Monthly	12/03 – 12/10	Level-1B	ICE-5G	-201 ± 6
10 day	12/03 – 12/10	Level-1B	ICE-5G	-226 ± 6
Schrama et al. (2014)	02/03 – 06/13	CSR RL05	Ensemble	-278 ± 19
Monthly	02/03 – 06/13	Level-1B	ICE-5G	-233 ± 6
10 day	02/03 – 06/13	Level-1B	ICE-5G	-244 ± 6
Velicogna et al. (2014)	01/03 – 12/13	CSR RL05	Huy-2	-280 ± 58
Monthly	01/03 – 12/13	Level-1B	ICE-5G	-232 ± 6
10 day	01/03 – 12/13	Level-1B	ICE-5G	-242 ± 6

Table 29. Published mass trend estimates of Greenland. The author, period, data and GIA model used in the study is provided for reference. The Huy-2 model used in Velicogna et al. (2014) is described in Simpson et al. (2009). All values Gt/year.

Luthcke et al. (2013) obtained a mass trend for Greenland of -230 ± 12 Gt/year between December 2003 and December 2010. The comparison with the mascon solutions revealed that, while the monthly solution is outside the error bounds of the Luthcke et al. (2013) study, the 10 day estimate agrees within the error bounds. The study of Luthcke et al. (2013) also uses 10 day mascons.

Schrama et al. (2014) estimated a mass trend of -278 ± 19 Gt/year, between February 2003 and June 2013. This differs from the mascon solutions in Table 29, which are outside the error bounds of the Schrama et al. (2014) study. Although different GIA models were used, the GIA correction is unable to explain the difference between the solutions as Table 28 revealed the GIA correction over Greenland is small. This needs to be investigated further.

Over Greenland, Velicogna, (2009) found that a linear trend was insufficient to represent mass variability, but the mascon results presented in Table 29 were estimated using a linear trend only. As Schrama et al. (2014) use a trend function that accounts for acceleration, the difference to the Schrama et al. (2014) study appears to relate to the acceleration of the mass loss over Greenland, which is evident in Figure 4 of Schrama et

al. (2014). Schrama et al. (2014) estimated an acceleration of -31 ± 3 Gt/year^2 for the period February 2003 and June 2013.

Between February 2003 and June 2013 accelerations of -28 ± 6 (-22 ± 6) Gt/year^2 were calculated for the monthly and 10 day mascon solutions in Table 29. Using a similar trend function to Schrama et al. (2014), namely

$$M(\mathrm{t}) = \mathrm{a}_0 + a_1(t - t_0) + \frac{1}{2}a_2(t - t_0)^2 \tag{25}$$

where a_0 is an offset, a_1 a mass trend and a_2 an acceleration, mass trends of -299 ± 6 and -296 ± 6 Gt/year were obtained for the monthly and 10 day mascon solutions over Greenland for the period February 2003 and June 2013. These trends are within the error bars of the Schrama et al. (2014) study and highlights the effect of including an acceleration has on the estimated mass trend. In Eq. (25), t is the current epoch and $t_0 = \frac{1}{2}(t_2 - t_1)$, where t_1 and t_2 are the minimum and maximum epochs in the time-series.

The final comparison was to the study of Velicogna et al. (2014), where a mass trend of -280 ± 58 Gt/year was obtained between January 2003 and December 2013. Velicogna et al. (2014) corrected for GIA over Greenland using Huy-2 (Simpson et al., 2009), with ICE-5G outside of Greenland. The mascons solutions in Table 29 are outside the error bounds of the Velicogna et al. (2014) study. However, Velicogna et al. (2014) use the method of estimating the mass trends described in Velicogna, (2009), where a quadratic trend is fit to the time-series. The calculated acceleration term from the Velicogna et al. (2014) study was -25.4 ± 1.2 Gt/year^2. Accelerations of -23 ± 6 (-16 ± 6) Gt/year^2 were obtained for the mascon solutions presented here. Using Eq. (25), mass trends of -295 ± 6 (-289 ± 6) Gt/year were obtained for the monthly and 10 day mascon solutions for the period January 2003 and December 2013. By including the acceleration, these mass trends now agree within the error bounds of the Velicogna et al. (2014) study.

Overall the comparisons here provide confidence in the mascon mass trends estimated for the GIS. The linear monthly trend obtained over Greenland is presented in Figure 92. Figure 93 is the linear trend from the 10 day mascon solution. In both plots GIA corrected using ICE-6G.

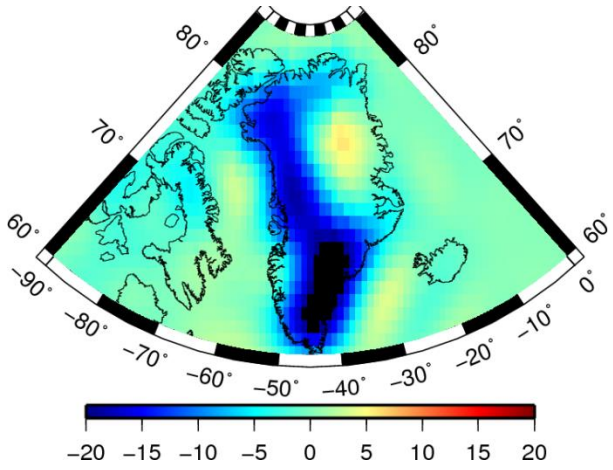

Figure 92. Spatial distribution of the mass trend of Greenland from the monthly mascon solution. GIA corrected using ICE-6G. Units cm/year (EWH).

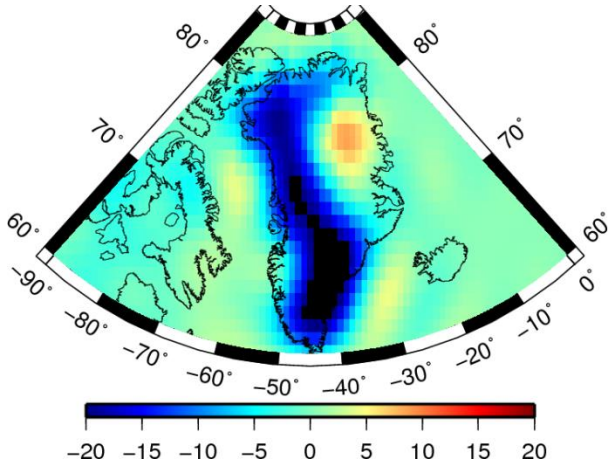

Figure 93. Spatial distribution of the mass trend of Greenland from the 10 day solution. GIA corrected using ICE-6G. Units cm/year (EWH).

Figure 92 and Figure 93 are similar, with little difference in the spatial distribution of the mass trend. Both figures reveal a mass loss that is concentrated in South Greenland, which extends up the West coast. The spatial distribution of mass loss shown is similar to that obtained by Luthcke et al. (2013) and Schrama et al. (2014). The solution of Schrama et al. (2014) also shows a small mass gain in North East Greenland.

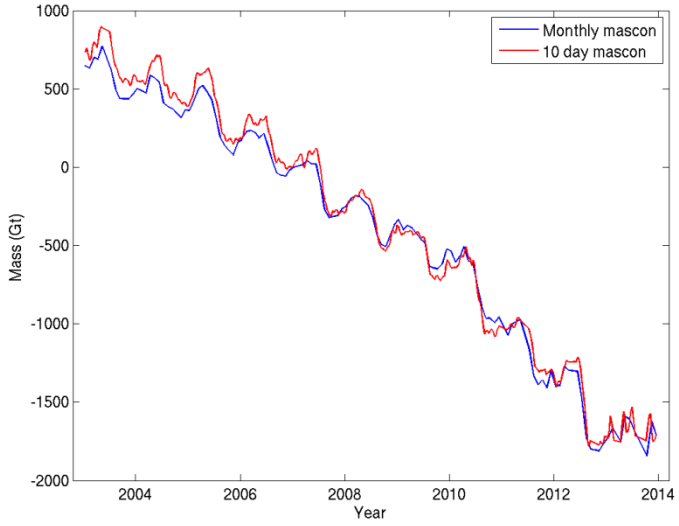

Figure 94. Time series of mass trend, in Gt, for the Greenland Ice Sheet. Mass time-series from the monthly and 10 day mascon solutions.

Figure 94 shows the time-series of the Greenland Ice Sheet from January 2003 to December 2013 used to calculate the linear trend in Table 28. The annual signal over Greenland can be clearly identified, along with the overall mass loss trend. The mass loss in the 10 day mascon solution is larger than that in the monthly mascon solution, explaining the difference in Table 28. This difference is due to the temporal constraint in the 10 day solution. Without the use of a temporal constraint, the solution over Greenland would contain additional noise due to the reduced number of mascons per basin compared with larger basins such as the Amazon (Sabaka et al., 2010). The apparent stabilisation of the mass loss between August 2012 to December 2013 in Figure 94 can also be seen in the results of Velicogna et al. (2014).

Accelerations of -23 ± 6 (-17 ± 6) Gt/year^2 were estimated from the time-series shown in Figure 94. Using Eq. (25) mass trend of -295 ± 6 (-289 ± 6) Gt/year were obtained over Greenland for the monthly and 10 day mascon solutions for the period January 2003 and December 2013. The time-series from Figure 94 are plotted in Figure 95 for the monthly mascon solution (left) and the 10 day mason solution (right). The linear trend and the trend calculated using Eq. (25) are plotted for comparison. Figure 94 highlights the problem of obtaining trends from time-series over Greenland. Although investigating the most appropriate way to estimate the mass trend over Greenland is beyond the scope of the work presented here, this could be an avenue for future work.

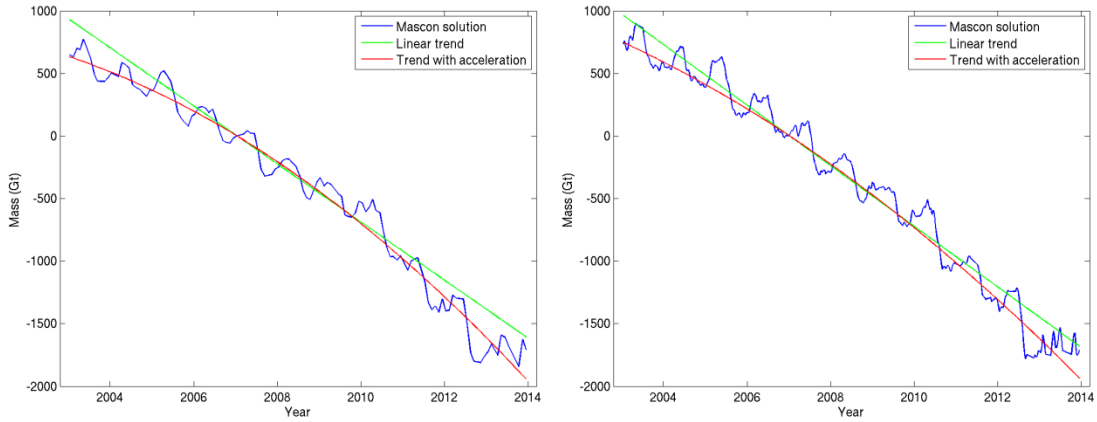

Figure 95. Time series of mass trend, in Gt, for the Greenland Ice Sheet. Mass time-series from the monthly (left) and 10 day (right) mascon solutions. The linear trend and trend calculated using the acceleration are included.

7.4.3 *Alaska*

Recent GRACE estimates have put the mass change of the Gulf of Alaska (GOA) at between -35 ± 3 (Schrama et al., 2014) and -69 ± 11 Gt/year (Luthcke et al., 2013). For a comparison, the mass trend of GOA was calculated using the mascon solutions using the GOA drainage basin shown in Figure 96 where the glaciers (blue) are provided for reference. The glacier locations are taken from the National Snow and Ice Data Centre's World Glacier Inventory (WGMS, 1999). The drainage basin in Figure 96 is similar in spatial distribution to the basin in Luthcke et al. (2013).

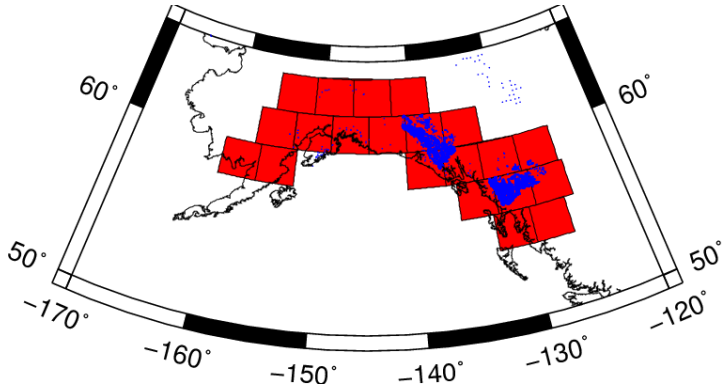

Figure 96. The layout of the 2° mascons over GOA. The locations of the glaciers (blue) are provided for reference.

The mascon mass estimates for the GOA region are provided in Table 30 along with the GRACE only estimate and the GIA and hydrology corrections.

	Mass trend	GRACE only	GIA	Hydrology
Monthly	-43 ± 1	-43 ± 1	-1	1
10 day	-47 ± 1	-47 ± 1	-1	1

Table 30. The mass change for Alaska along with the GRACE only mass change and the corrections. All values Gt/year.

Table 30 shows that the mass trend of GOA was estimated at between -43 ± 1 and -47 ± 1 Gt/year for the monthly and 10 day mascon solutions. This is between the -35 ± 3 Gt/year estimated by Schrama et al. (2014) and the -69 ± 11 Gt/year estimated by Luthcke et al. (2013). A comparison to these published results is shown in Table 31. As for Antarctica and Greenland, the results in Table 31 were compared to a mascon solution covering the same period and using the same GIA corrections.

Study	Period	Data	GIA model	GOA
Luthcke et al. (2013)	12/03 – 12/10	Level-1B	ICE5G + LIA	-69 ± 11
Monthly	12/03 – 12/10	Level-1B	ICE5G + LIA	-60 ± 1
10 day	12/03 – 12/10	Level-1B	ICE5G + LIA	-64 ± 1
Schrama et al. (2014)	02/03 – 06/13	CSR RL05	ICE5G	-35 ± 3
Monthly	02/03 – 06/13	CSR RL05	ICE5G	-43 ± 1
10 day	02/03 – 06/13	CSR RL05	ICE5G	-47 ± 1

Table 31. Published mass change estimates of Alaska. The author, period, data and corrections used in the study are provided for reference. All values Gt/year.

Luthcke et al. (2013) estimated the mass trend of GOA as -69 ± 11 Gt/year, including a -10 Gt/year correction for the Little Ice-Age (LIA). A comparison to the mascon results presented in Table 31 reveals that the mascon results are within the error bounds of the Luthcke et al. (2013) estimate. To aid the comparison the -10 Gt/year LIA correction was added to the mascon solutions. This rate is based on the GIA rebound observed by Larson et al. (2005) using GPS and sea level observations.

Schrama et al. (2014) estimated the mass trend of GOA as -35 ± 3 Gt/year, correcting for GIA using an ICE-5G model ensemble. A comparison to the mascon results presented in Table 31 reveals that the mascon results are just outside the error bounds of the Schrama et al. (2014) estimate. However, as discussed previously, Schrama et al. (2014) smooths the spherical harmonic coefficient with a Gaussian smoother so some differences are expected. In addition, the layout of the Alaska drainage basin is similar in spatial distribution to the basin in Luthcke et al. (2013) and is therefore expected to be closer to the Luthcke et al. (2013) mass trend. The mass change of Alaska is plotted in Figure 97 and Figure 98.

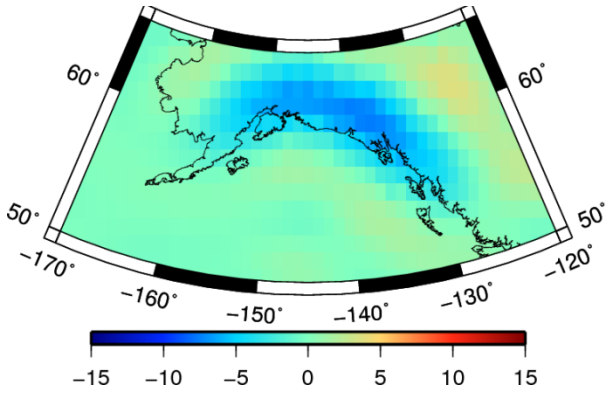

Figure 97. Spatial distribution of the mass change over Alaska from the monthly mascon solution. GIA corrected using ICE-6G. LIA correction has not been included in the plot. Units cm/year (EWH).

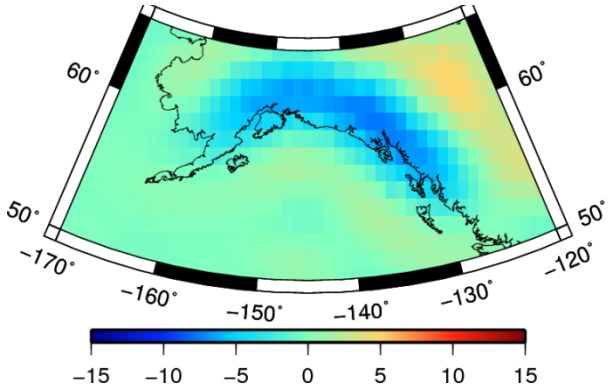

Figure 98. Spatial distribution of the mass change over Alaska from the 10 day mascon solution. GIA corrected using ICE-6G. LIA correction has not been included in the plot. Units cm/year (EWH).

Figure 97 and Figure 98 show that the mass loss over Alaska is concentrated around the eastern part of the Gulf of Alaska. The spatial distribution of the mass loss is similar to the mass loss obtained by Luthcke et al. (2013). Figure 99 is a plot of the mass over the GOA from January 2003 to December 2013. The annual signal can be clearly identified, along with the overall mass loss trend.

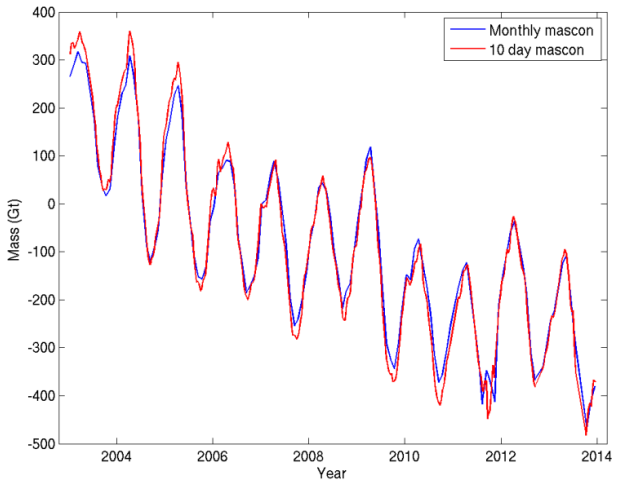

Figure 99. Mass change time-series from the monthly and 10 day mascon solutions over Alaska in Gt.

7.4.4 *Hydrology*

GRACE can also be used to estimate variations in continental water storage. It is the first system capable of measuring an entire drainage basin, including ground water (Klosko et al., 2009). This is important as globally there are areas that are suffering chronic water stress (Watkins, 2006). To validate the mascons for hydrological applications, the mass variation was calculated for four hydrological drainage basins, with the results presented in Table 32. The Amazon and Ganges were chosen due to the large annual variability (Chen et al., 2005); the Mississippi due to its large size, with GRACE able to deliver an accuracy comparable to ground water observation systems (Klosko et al., 2009); and the Indus as this basin is suffering ground water depletion, with water being extracted faster than it is being replenished (Klosko et al., 2009). In Table 32 the mass change of each basin is provided along with the GRACE only and ICE-6G GIA correction. No hydrology model is removed as this is the signal of interest. The GIA correction is small for all basins except the Mississippi, which is known to have a GIA signal (Klosko et al., 2009).

Basin	Solution	Mass trend	GRACE only	GIA
Amazon	**Monthly**	41 ± 7	43 ± 7	-2
	10 day	47 ± 7	49 ± 7	-2
Ganges	**Monthly**	-19 ± 2	-17 ± 2	-2
	10 day	-21 ± 2	-19 ± 2	-2
Indus	**Monthly**	-9 ± 1	-7 ± 1	-2
	10 day	-11 ± 1	-9 ± 1	-2
Mississippi	**Monthly**	-10 ± 3	-29 ± 3	18
	10 day	-17 ± 3	-35 ± 3	18

Table 32. The mass trend of four hydrological drainage basins. All values Gt/year.

As previously, the mascon solutions can be compared to values published by other groups. The results are shown in Table 33. However, as no hydrological estimates have so far been published using RL05 data, the published values use RL04 data. This is not ideal as different releases of the GRACE data have been shown to cause systematic offsets in mass trends estimated. In addition, the studies use data from 2002. The mascon solutions presented here start January 2003. Therefore, some differences are expected.

Basin	Study	Period	Data	GIA model	Mass trend
Amazon	Baur et al. (2013)	05/02 – 04/11	CSR RL04	ICE-5G	43 ± 14
	Monthly	05/02 – 04/11	Level-1B	ICE-5G	38 ± 10
	10 day	05/02 – 04/11	Level-1B	ICE-5G	48 ± 9
	Llovel (2010)	08/02 – 07/09	CSR, JPL and GFZ RL04	ICE-5G	78 ± 13
	Monthly	08/02 – 07/09	Level-1B	ICE-5G	75 ± 13
	10 day	08/02 – 07/09	Level-1B	ICE-5G	88 ± 9
Ganges	Baur et al. (2013)	05/02 – 04/11	CSR RL04	ICE-5G	-25 ± 6
	Monthly	05/02 – 04/11	Level-1B	ICE-5G	-29 ± 2
	10 day	05/02 – 04/11	Level-1B	ICE-5G	-30 ± 2
	Llovel (2010)	08/02 – 07/09	CSR, JPL and GFZ RL04	ICE-5G	-11± 1
	Monthly	08/02 – 07/09	Level-1B	ICE-5G	-26 ± 3
	10 day	08/02 – 07/09	Level-1B	ICE-5G	-21 ± 3
Indus	Llovel (2010)	08/02 – 07/09	CSR, JPL and GFZ RL04	ICE-5G	-7 ± 1
	Monthly	08/02 – 07/09	Level-1B	ICE-5G	-9 ± 2
	10 day	08/02 – 07/09	Level-1B	ICE-5G	-12 ± 2
Mississippi	Llovel (2010)	08/02 – 07/09	CSR, JPL and GFZ RL04	ICE-5G	-14 ± 4
	Monthly	08/02 – 07/09	Level-1B	ICE-5G	-9 ± 5
	10 day	08/02 – 07/09	Level-1B	ICE-5G	-22 ± 5

Table 33. Published mass trend estimates of four hydrological drainage basins. The author, period, data and corrections used in the study are provided for reference. All values Gt/year.

Despite these differences, the results for the Amazon drainage basin in Table 33 are promising, with the mascon solutions within the error bounds of Baur et al. (2013) and Llovel (2010). For the Ganges basin, the mascon estimates agree within the error bounds of Baur et al. (2013), although they are outside the error bounds of the Llovel (2010) study. This difference could be the result of the data period and the release of data used. For the Mississippi and Indus basins the mascon solutions are just outside the error bounds of Llovel (2010). However, due to the differences described above, these differences are not deemed significant.

Figure 100 shows the mass trend over the Amazon, Ganges, Mississippi and Indus for the monthly and 10 day mascon solutions from January 2003 to December 2013. The Amazon basin shows a clear annual signal, with no obvious trend. The amplitude of the 10 day solution is larger than the monthly mascon solution. This is to be expected due to the averaging of sub monthly mass variations within the monthly solutions. For the Ganges, as for the Amazon, the amplitude of the 10 day mascon solution is larger than the monthly mascon solution and no linear trend is obvious.

The trend over the Mississippi basin, again shows that the 10 day mascon solution has a larger amplitude than the monthly mascon solution. However, it is worth nothing that the difference in the mass trends obtained for monthly and 10 day mascon solution in Table 33 is the result of fitting a linear trend through the time-series in Figure 100. This highlights that the amplitude of the time-series can have an effect on the mass trend estimated, especially when the amplitude of the time-series appears to contain a longer period signal. In Figure 100, the Indus is the only drainage basin that has a clear mass loss. Between August 2002 to October 2009, Rodell et al. (2009) estimated a mass loss of -18 ± 5 Gt/year from the lower part of the Indus basin, caused by ground water depletion in three Indian states. Although this estimate is larger than the mascon solutions in Table 33, which are for a similar period, the study of Rodell et al. (2009) does not include the upper drainage basin. In Figure 100, the large amplitude seen over the Indus in 2003 and 2005 was also observed by Rodell et al. (2009).

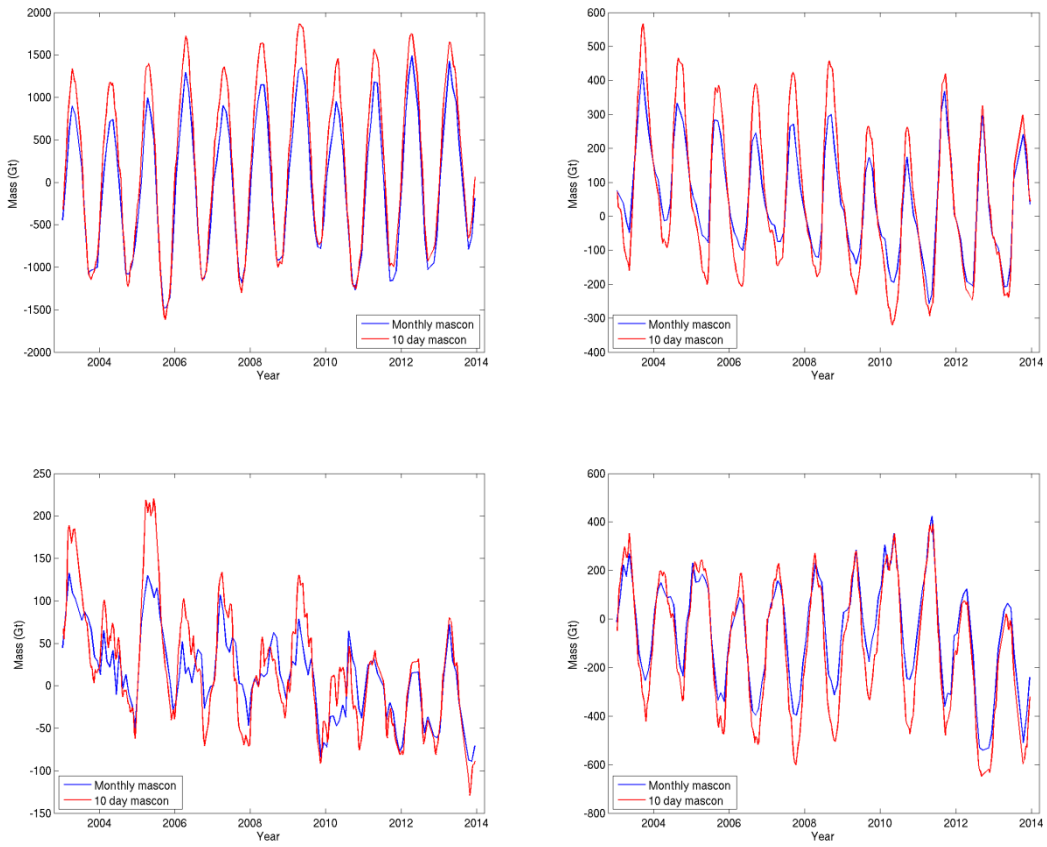

Figure 100. Time series of mass change, in Gt, for the Amazon (top left), Ganges (top right), Indus (bottom left) and Mississippi (bottom right). Mass time-series from the monthly and 10 day mascon solutions.

Overall, the results presented here provide confidence in the ability of the mascon solution to recover hydrological signals. Although some of the mascon estimates are outside the error bounds of the published solutions, there are differences between the releases of GRACE data. In addition, the published studies contain data from 2002. No mascon data is available for 2002. Finally, Figure 100 highlights that linear trends are not always suitable for estimating mass trends.

7.4.5 *Sumatra-Andaman Earthquake*

GRACE has been able to detect changes in the Earth's gravity field resulting from earthquakes. One of the first earthquakes studied using GRACE was the Sumatra-Andaman earthquake (e.g. Han et al., 2006) which occurred on 26th December 2004 and had a seismic moment magnitude (M_w) between 9.1 and 9.3 (Lay et al., 2005). Han et al. (2006) observed the mass distribution caused by the earthquake's co-seismic deformation. As no mascon solutions have been published of mass distributions caused by an earthquake, it is of interest to see if such as solutions can be recovered. A time-series of the monthly mascon solution was generated and compared to a time-series

calculated using CSR RL05 Level-2 data, as in section 7.2. The corrections described in section 7.2 were applied to the solutions and the results are plotted in Figure 101. The location of the time-series is near the epicentre of the earthquake.

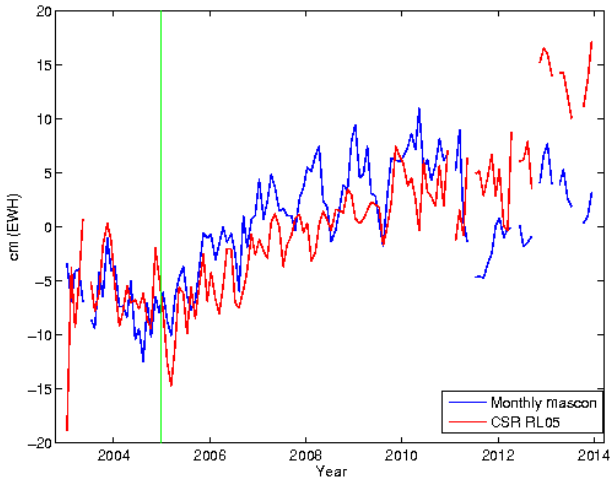

Figure 101. Time-series observed by the CSR RL05 solution and monthly mascon solution at the location of the blue star in Figure 103 and Figure 104. The timing of the Sumatra-Andaman Earthquake is shown by the green vertical line. Units cm EWH.

Figure 101 reveals that the time-series are similar, both before and after the earthquake. After the earthquake, both solutions have a positive trend, although there are some differences in annual variations of the signals. Next, the monthly and 10 day mascon solutions were compared. When comparing the solutions, a number of different scale factors were tested as the results of Watkins et al. (2015) found that care needs to be taken when using the 10 day mascon solutions to extract the mass change relating to events such as earthquakes. Watkins et al. (2015) found full recovery of the mass change signal was only achieved by increasing the *a-priori* variance of the constraints in the region. This is similar to reducing the scale, *S*. The results are shown in Figure 102.

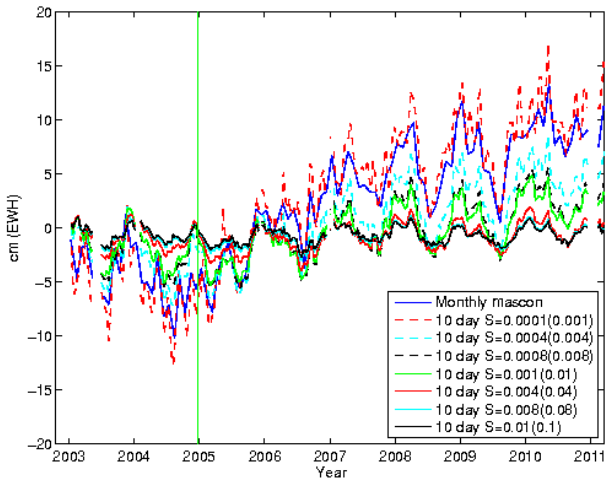

Figure 102. The 10 day mascon time-series at the epic-centre of the Sumatra-Andaman earthquake for different scale factors. The monthly mascon solution (*S*=0.004(0.04)) is included for reference. Units EWH cm.

Figure 102 reveals that the trend seen in the monthly mascon and CSR RL05 time-series is only recovered using the 10 day mascon solution if the scale factor is reduced. The current scale factor used in the 10 day mascon solutions is, in the case of an earthquake, not able to replicate the post-seismic deformation observed. A similar trend is only obtained once the scale factor is reduced to 0.0001(0.001), namely a factor of ten smaller than the constraint applied to the 10 day mascon solution. This confirms the results of Watkins et al. (2015) and highlights that care needs to be taken when using the 10 day mascon solution. The difference between the monthly and 10 day mascon solutions is the temporal constraint applied to the 10 day solution.

The results in Figure 102 also highlight that the 10 day mascon solution is currently not optimised to detect changes resulting from an earthquake. The mascon constraint matrix needs to be optimised for each geophysical problem studied. The optimal layout of the constraint matrix can be determined using the simulated recovery of a known mass signal (e.g. section 6.8). The mass trends from January 2003 to December 2006, two years either side of the earthquake are shown in Figure 103 and Figure 104 for the monthly and 10 day solutions respectively.

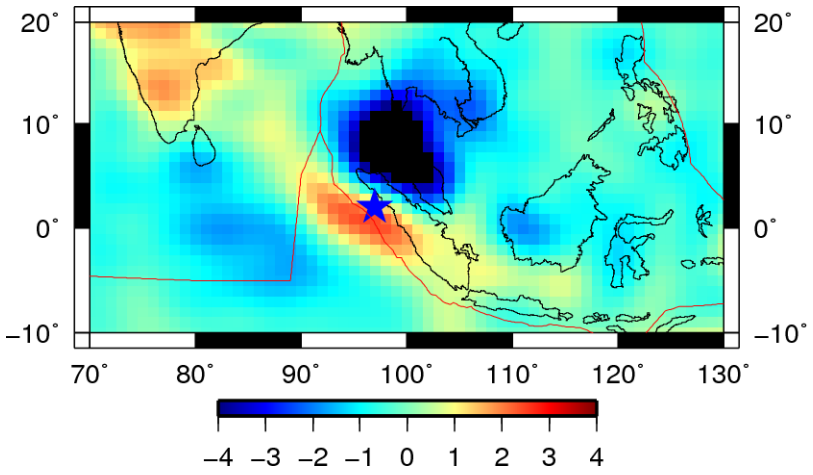

Figure 103. Spatial distribution of the mass trend around Indonesia from the monthly mascon solution. GIA corrected using ICE-6G.Units cm/year (EWH). Trend from January 2003 until December 2006. The blue star, on the fault-line of the Sumatra-Andaman Earthquake, indicates the location of the time-series in Figure 101 and Figure 102.

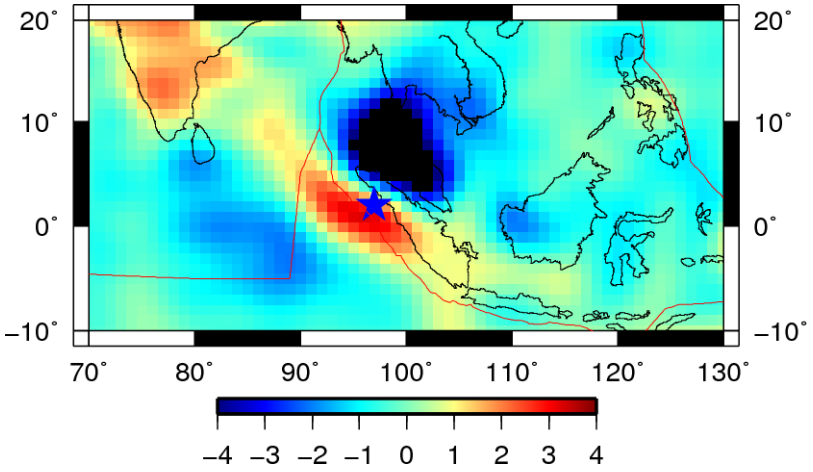

Figure 104. Spatial distribution of the mass trend around Indonesia from the 10 day mascon solution. GIA corrected using ICE-6G.Units cm/year (EWH). Trend from January 2003 until December 2006. The blue star, on the fault-line of the Sumatra-Andaman Earthquake, indicates the location of the time-series in Figure 101 and Figure 102. Scale factor of the constraint applied to the 10 day mascon solution reduced to 0.0001(0.001).

Comparing Figure 103 with Figure 104 reveals similar trends after reducing the scale factor of the constraint applied to the 10 day mascon solution to 0.0001(0.001). The locations of the post-seismic deformation in Figure 103 and Figure 104 match those observed by Han et al. (2006) which, along with Figure 101, shows that mass distributions caused by an earthquake can be recovered using the mascon methodology. The trends are provided for the purpose of validation of the mascon solutions. The causes of the co-seismic are outside the scope of this study

7.5 *Summary*

The results presented in this chapter validate the TVG field recovery using the mascon methodology. The processing methodology described in Chapter 5, along with the parametrisation identified using the simulations in Chapter 6, were successfully applied to calculate monthly and 10 day mascon solutions for the period January 2003 to December 2013 from actual GRACE data.

The validation of the monthly mascon solutions was undertaken through a comparison to solutions calculated using CSR RL05 Level-2 data. Time-series of mass flux were compared at 6 locations where only a small signal is observed by GRACE, with similar trends observed. To analyse the noise in the two solutions, a constant, linear trend and annual and semi-annual signals were estimated and removed from the time-series. At 5 of the 6 locations the standard deviation of the noise was lower in the mascon solution, providing confidence that the observed mass flux is a representation of reality and not contaminated by noise. The comparison over the Sahara desert highlighted the problem of finding a quiet point over land to validate the noise in GRACE solutions, with a small (+/- 4 cm EWH) annual signal observed in the mascon time-series. Investigations revealed that a small seasonal signal could possibly exist at this location, although errors in the background models used during data processing cannot be ruled out. Aliasing through mis-modelling of the K1 tide was also observed in the time-series at ocean points 2 and 3.

In addition to validation, the estimation of the mascon solutions from GRACE allowed an assessment of the scale S used in Eq. (15) and Eq. (16) to be undertaken. The findings revealed that the scale estimated in the simulations needed an increase to reduce the noise in the time-series. Increasing the scale at ocean point 1 was found to reduce the noise in the time-series, while having a minimal effect on the signal. (Luthcke et al., 2013) found that increasing the scale had a significant impact on noise. A scale of S=0.004 was used during the main mission period and when the GRACE satellites were in resonance, while a value of S=0.04 was used during the periods of reduced thermal control.

Comparisons of monthly and 10 day mascon solutions at the same 6 locations revealed that the two solutions are similar. While some differences in the amplitude of the two signals were evident, these were small with the amplitude of both the monthly and 10 day mascon solutions larger in different time-series. Differences were expected as there

are mass variations that are sub-monthly (Seo et al., 2008b). These will alias into the monthly solutions. However, the comparison at ocean point 3 highlighted that care needs to be taken with the scale of the 10 day solution as mass change signals can be masked if over constrained. A similar result was found by Watkins et al. (2015) when analysing the JPL mascon solution.

The mascon solutions were subsequently used to estimate the mass trends of Antarctica, Greenland and Alaska. These trends were provided for the purpose of validation of the mascon solutions, with geophysical interpretation outside the scope of this study. The mascon trends over Antarctica revealed that similar trends were obtained for the two mascon solutions, although the mass loss was slightly larger in the monthly mascon solution. The mascons solutions were then compare to published studies, covering the same period and using the same GIA model. The differences between the mascon solutions and published values generally agreed within the error bounds.

Over Greenland there was 10 Gt/year between difference between the monthly and 10 day mascon solution, with the 10 day mascon solution exhibiting a larger mass loss signal. However, the difference was only ~4% of the total monthly trend, compared to a difference of ~7% over Antarctica. The comparisons to published studies provide confidence in the mascon mass trend estimated for Greenland. While only the 10 day estimate agrees within the error bounds of the study of Luthcke et al. (2013) when a linear trend was estimated, the mascon solutions were within the error bounds of the Schrama et al. (2014) and Velicogna et al. (2014) studies when estimating the trend using Eq. (25) with an acceleration term. This was required as Schrama et al. (2014) and Velicogna et al. (2014) use acceleration terms when calculating the mass trend of Greenland.

Over Alaska the mascon solutions were similar, although the 10 day mascon solution exhibited a larger mass loss signal. Comparisons to two previous studies again provide confidence in the mascon mass trend estimated, with the mascon estimates falling between the published results. The mascon solutions were in closer agreement with the study of Luthcke et al. (2013), which may simply be a consequence of the close similarity between the mascon drainage basins used in both studies.

The mass change of four hydrological basins, including the Amazon and Indus, were also assessed. Again the mascon mass change estimates agreed well with other studies. The majority of the mascon mass trend estimates were within the error bounds of the

published results, despite the comparison being made to CSR RL04 solutions which include data from 2002. The 10 day mascon solution for the Mississippi identified stronger signatures during the flooding of 2003 and 2005, which bias the trend estimated for this basin. This highlights that, despite the simplicity of the results, the use of simple regression is inappropriate in certain situations.

Finally, the GRACE trends resulting from the Sumatra earthquake of 2004 were investigated. A comparison between the CSR RL05 and monthly mascon solution found that both time-series were similar, both before and after the earthquake. Comparing the monthly and 10 day mascon time-series revealed, as identified by Watkins et al. (2015), that the scale factor used in estimating the 10 day mascon solution needed to be reduced to permit full recovery of the mass change signal. Care needs to be taken when using the 10 day mascon solutions to extract mass change particularly for events such as earthquakes. As found in the simulations, the mascon constraint matrix needs to be considered for each geophysical problem studied.

As with all GRACE mass change studies there is some uncertainty whether to include an acceleration term in the regression as the span of the data is relatively short (11 years here) and there is also uncertainty whether some trends are deterministic or stochastic (Moore and Williams, 2014, Williams et al., 2014).

Chapter 8. Conclusion

The work in this thesis was motivated by the need to improve the accuracy of TVG fields computed from the GRACE data, with the aim to validate the use of the mascon methodology for the recovery of basin scale inter-annual variability at a 10 day temporal resolution.

To achieve this aim, work was undertaken in three main work packages:

1. The modification of *Faust* and the development of processing methodology. Newcastle University's orbit determination software, *Faust*, was modified to allow for the estimation of mascons parameters and a two stage processing methodology was developing, along with the associated parameterisation required to compute gravity field solutions from Level-1B GRACE data.

2. Simulations. Accuracy assessments were undertaken using simulations. Simulations allowed a comparison between solutions generated using mascon parameters and spherical harmonic coefficients, in the presence of realistic noise, along with an assessment of potential limitations associated with each technique.

3. Solution generation. Monthly and 10 day mascon solutions were generated, using real GRACE data, for the period January 2003 to December 2013. Comparisons to time-series solutions calculated from CSR RL05 Level-2 products validated the mascon TVG field recovery. The mass trends of Antarctica, Greenland and Alaska were then computed, along with mass redistribution caused by the Sumatra-Andaman Earthquake and the hydrological changes over the Amazon, Indus, Mississippi and Ganges river basins.

This chapter summarises the conclusions for each of these steps before making recommendations for further work.

8.1 *Software modification and processing methodology*

The decision to modify *Faust* to estimate mascon parameters was based on the advantage of the mascon methodology to estimate mass trends at spatial and temporal resolutions unachievable using conventional spherical harmonic solutions. This offered the opportunity to improve GRACE TVG fields. The generation of TVG fields direct from Level-1B GRACE data would also provide access to the covariance matrix, which

can be taken into account during solution generation. The use of spatial and temporal constraints, used during the generation of the mascon solutions, offered the opportunity to adapt the mascon solutions to any geophysical phenomena of interest while offering advantages over spherical harmonic solutions filtered using a Gaussian smoother in mitigation of random noise and systematic errors that are inherit in GRACE solutions. The ability to estimate mascon parameters would also allow for an assessment of the comparable accuracy of the mascon and spherical harmonic methodologies to be undertaken. This is of interested to the scientific community. It would also establish the facility to estimate mascon parameters at Newcastle University.

An overview of the noise and errors in GRACE TVG solutions was provided in Chapter 3. Noise and errors were found to be dominated by north-south stripes, resulting from the GRACE orbital configuration. Noise and errors were also present in background models and Level-1B data used during solution generation. While recent improvements in the background models and the new release of Level-1B data has resulted in a reduction in noise and errors, some noise and errors still remain. The mascon constraint matrix, applied during solution generation, appears best placed to mitigate noise and errors. Applying constraints during solution generation is the ideal way to handle noise (Swenson and Wahr, 2006). The summation of all mascons within a drainage basin to estimate mass flux of that basin also has advantages over other methodologies, such as a spatial averaging kernel function. Spatial averaging can result in signal loss and leakage. While forward modelling and Level-2 ‘mascons’ are an improvement over spatial averaging, using a degree dependent Gaussian smoother to mitigate for noise and errors is a limiting factor.

Faust was modified to estimate mascon parameters, as described in Chapter 4, which are based on NASA’s GSFC methodology. This required updating the Least Squares partials in *Faust,* as in Appendix A. Through simulations in section 4.2, the problem of describing the mascons to degree and order 60 was identified, resulting in local leakage in and out of the individual mascons. However, when estimating all mascons within 6000 km or globally, the global gravity field can be correctly represented using mascons. In addition, a simulation revealed that GRACE is relatively insensitive to gravity signal contained in the higher degree (61-120) harmonics. In section 4.4, the mascon spatial constraint, applied during solution generation, was investigated and found to be a function of the distance between mascon pairs. For 10 day mascon solutions, the temporal constraint decreased with an increase in the time from the centre

day allowing a 10 day mascon solution to be estimated from 30 days of data, due to the weight of the constraint tending to zero. The 10 days of data either side of the 10 day solution period would be used to improve the sampling of the gravity field.

Successful estimation of a GRACE TVG gravity field solution requires the correct parametrisation of *Faust* during the two stages of the gravity field recovery. This parametrisation is described in Chapter 5. TVG fields can be estimated from KBRR data only, using short arc parametrisation. In section 5.3.3, tests revealed that a sensible arc length to use in *Faust* was 60 minutes. Through experimentation (section 5.3.5), 1.4 μm/s was determined to be a good choice for KBRR rejection level used during orbit and gravity field determination. 1.4 μm/s was a found to be a good compromise between reducing noise and rejected signal. The daily GRACE accelerometer bias values were calculated using 24 hour arcs with a KBRR 1CPR and 2CPR and a KBRR bias and a KBRR trend estimated every 90 minutes alongside the bias values. During testing (section 5.2.4), this choice of empirical parameters provided the most stable bias values. Using this parametrisation, bias values were obtained for 90% of the days over the period January 2003 to December 2013, compared to 91% of the days for the official GRACE processing centres.

8.2 *Simulations*

In Chapter 6, comparisons using simulations revealed the advantages of mascon methodology over the use of spherical harmonic coefficients, where noise and errors were mitigated in the spherical harmonic recovery using a Gaussian smoother. The aim of the simulations was to recover a known mass distribution from GRACE KBRR data, allowing an accuracy assessment between the methodologies to be undertaken. While the recovery of a noise and error free GLDAS anomaly, in section 6.2, revealed no quantifiable difference between the two methodologies, with both similarly affected by omission errors, it was during the recovery of the GLDAS anomaly with simulated stripes, section 6.5, that the advantage of the mascon methodology was identified.

Using a mascon constraint matrix to mitigate noise and errors allowed more signal to be preserved up to degree ~35, while removing more noise. However, the full advantage of the mascon methodology is that the constraint matrix can be adapted to any geophysical phenomena of interest. Modifying the constraint matrix to include basin constraints (hydrological and glaciological), described in section 6.6, resulted in a further reduction of signal loss at all degrees. The simulated recovery over Greenland, section 6.8,

showed that the basin layout is important and can be tuned to optimise signal recovery. Over Antarctica the mascon methodology was validated for use in polar-regions in section 6.7. The mascon constraint matrix can be optimised for signal recovery.

In section 6.10, signal recovery was also tested when GRACE was in resonance and suffering from poor thermal control. In both cases, the recovery of the GLDAS anomaly and Antarctica mass change signal revealed that the mascon methodology was able to recover more of the input signal than using spherical harmonics. However, both solutions were degraded during poor thermal control (from April 2011). This required a tighter constraint than during the main part of the mission. The simulations in Chapter 6 revealed that the optimal choice for the correlation distance, used in the spatial constraint matrix during the main mission period and during periods of poor thermal control, was D=800 km. A correlation distance of D=400 km was found to be optimal during periods of resonance. For the scale applied to the constrain matrix, a value of S=0.001 was found to be optimal during the main mission and periods of resonance, increasing to 0.01 during periods of poor thermal control.

The simulations also allowed for an assessment of the mascon methodology, revealing potential limitations in the mascon methodology. A 4° mascon solution does not have the required resolution to recover a known mass distribution, when the mass distribution is described to spherical harmonic degree and order 60, as shown in section 6.2. This has implications for studies that use this resolution. However, the mass distribution can be successfully recovered using a 2° mascon solution. For that reason only 2° mascon solutions were presented in this thesis. In addition, during orbital determination, the contributions to the satellite accelerations of all mascons within 6000 km of the nadir mascon were required to recovery a mass distribution (section 6.3). This has implications for non-global mascon solutions. The use of iterations was also not able to compensate for an insufficient distribution of mascons in section 6.4. However, this does not affect the work in this thesis as all mascon TVG fields are global solutions.

The majority of the simulations presented in this thesis have been published in Andrews et al. (2014). To aid comparison, the mascon and spherical harmonic solutions in the simulations were for monthly solutions only.

8.3 *Solution generation*

Monthly and 10 day 2° mascon TVG solutions were generated between January 2003 and December 2013 in Chapter 7. The solutions were generated from real GRACE data,

using the parameterisation described in Chapter 5 and the results of the simulations in Chapter 6. The solutions were generated for the purpose of validating the mascon methodology developed in this thesis.

Comparison of time-series derived from the monthly mascon solutions with a time-series from Level-2 CSR RL05 solutions, section 7.2, provided confidence in the mascon mass flux. Similar trends and signals were observed in both solutions. The locations were chosen to compare the solutions at the noise level, with only a small signal observed by GRACE. At 5 of the 6 locations compared, the standard deviation of the noise in the time-series was comparably lower in the mascon solution. Time-series comparisons, between the 10 day and monthly mascon solutions, at the same locations (section 7.3), found that the trends signal were again similar at the locations tested. This provided confidence in the 10 day mascon solution. Although Sabaka et al. (2010) found that using a temporal constraint resulted in improvements in mascon solutions over ocean areas, the 10 day and monthly mascon time-series comparisons revealed that care needs to be taken with the scale, *S*, in the 10 day mascon solution as real mass change signals can be masked. At ocean point 3, the scale factor needed to be reduced before the mass flux signal observed in the monthly mascon and CSR RL05 solutions could be recovered. Although this was only seen at one location tested, a similar result was observed during the 10 day and monthly mascon time-series comparison at the epicentre of the 2004 Sumatra-Andaman earthquake, section 7.4.5. To recover the post-seismic mass trend, seen in the monthly mascon solution, in the 10 day mascon solution, the scale factor applied to the 10 day mascon solution needed to be reduced to 0.0001(0.001).

In addition to validation, the time-series comparisons revealed two other interesting issues. Firstly, that it is hard to find quiet locations over land to validate the noise in GRACE solutions. At one of the driest parts of the Sahara a small annual signal was observed in the GRACE solutions (section 7.2.6). It was found that this could be a real signal, although it could also be the result of errors in the background models used during orbit determination. Secondly, background tidal models were found to be aliasing into the GRACE solutions. In polar regions, the K1 tidal signature appeared to be aliasing into both the mascon and CSR RL05 solutions (section 7.2.2).

Generating mascon TVG solutions from real GRACE data also allowed the value of *S*, determined using simulations, to be assessed. In section 7.2, the scale applied to the

mascon constraint matrix needed to be increased from S=0.001(0.01) to 0.004(0.04) to reduce the noise in the mascon solutions. While this was shown to have minimal effect on the signal, it reduced the noise. The generation of TVG solutions from real GRACE data also allowed the KBRR rejection criteria, applied during orbit determination, to be validated. In Chapter 5, section 5.3.5, using the quantity and spatial distribution of rejected observations per calendar month, it was deemed that a rejection criteria of 1.4 μm/s was the correct value to use for the majority of the GRACE mission. Studying plots of the spatial distribution of the rejected observations revealed that the majority of observations rejected coincide with arcs of poor data and outliers with no spatial significance. However, this changes towards the end of the GRACE mission. From August 2010 observations are increasingly rejected over Greenland and West Antarctica. The spatial location of the rejected observations coincides with the two locations of the largest mass loss signal in the GRACE data, with the mass trend becoming increasingly different from the static gravity field. Therefore, from August 2010 an updated rejection criterion of 1.6 μm/s was used. This was increased to 1.8 μm/s from October 2011 and 2.4 μm/s from August 2012. However, increasing the rejection criteria allows arcs of poor data into the solution elsewhere. Therefore, the new rejection criterion was only applied for calculating the mass trend over Greenland and Antarctica in Chapter 7.

The generation of mass trends (section 7.4), allowed for a comparison to published results. The mascon solutions presented here were, generally, within the error bounds of published studies. This provides confidence in the mascon solutions to recover basin scale inter-annual variability at a 10 day temporal resolution. Using linear regression, a mass trend of -89 ± 12 Gt/year for the mascon solution was obtained over Antarctica for the monthly mascon solution, with a trend of -83 ± 12 Gt/year for the 10 day mascon solution. GIA was corrected using W12a. Over Greenland, mass trends of -232 ± 6 Gt/year and -242 ± 6 Gt/year were calculated for the monthly and 10 day mascon solution. Estimating mass trends over Greenland using a linear trend and acceleration resulted in a mass loss of -295 ± 6 Gt/year and -289 ± 6 Gt/year for the monthly and 10 day mascon solutions respectively. However, the difference between these two estimates highlights that care needs to be taken when fitting trends through relatively short time-series, especially when the time-series may contain accelerations. Over the Gulf of Alaska, trends of -43 ± 1 Gt/year and -47 ± 1 Gt/year were obtained using linear regression. In all cases GIA was corrected using ICE-6G. No correction was applied

over Alaska for the Little Ice Age. Despite published solutions only using CSR RL04 data, the mascon mass trends over the hydrological basins compared well. This provided confidence in the ability of the mascon methodology to recover hydrological signals.

Overall, the comparisons and mass trend estimates presented in Chapter 7 validated the mascon methodology and the use of 10 day mascon to recover GRACE TVG solutions. The monthly and 10 day mascon solutions agreed within the uncertainties of 1-sigma, where the uncertainty is from the linear regression. The simulations in Chapter 6 revealed that the mascon methodology was able to preserve more signal at higher degrees, required for the basin scale inter-annual variability. The mascon was found to be able to recover more of the input signal than using spherical harmonics while having the advantage that the constraint matrix, as shown over Greenland, which can be optimised to aid in signal recovery.

8.4 *Summary of main contributions*

A processing methodology to estimate mascon parameters from Level-1B GRACE data using Newcastle University's orbit determination software *Faust* has been established and documented. This leaves the University well placed to continue processing mascon solutions from Level-1B GRACE data and to estimate mascon solutions from the GRACE-FO mission.

Through simulations an accuracy assessment of the mascon parameters was undertaken. Mascon parameters were found to offer advantages over spherical harmonics for the mitigation of noise and for improving the temporal and spatial recovery of the TVG field from GRACE. The mascon constraint matrix allowed more signal to be preserved up to degree ~35. Using basin constraints, simulation revealed that the constraint matric can be tuned to recovery the gravity changes resulting from any geophysical phenomena of interest. Basin constraints were found to optimise the signal recovery of GLDAS and a known mass change signal over Antarctica and Greenland. A novel way to create realistic noise and errors in the KBRR measurement was also documented.

Generating monthly and 10 day mascon solutions using real data revealed that the noise and errors in mascon solutions is comparably lower than in CRS RL05 solution while also validating the mascon methodology established here. Comparison to published mass trends to those estimated using mascon parameters showed that the estimation of mascon parameters has application in the study of mass change in the cryosphere,

hydrological applications and for the study of the co-seismic mass changes resulting from earthquakes. Overall, the work undertaken in this thesis provides evidence of the improved accuracy achievable when using mascon parameters to estimating TVG fields from Level-1B GRACE data.

8.5 *Recommendations for further work*

As the results of the work undertaken in this thesis, the capability of estimating mascon parameters from GRACE Level-1B has been established at Newcastle University. The ability to estimate TVG solutions from GRACE Level-1B data using mascons offers the opportunity to study mass anomalies, with the mascon spatial and temporal constraints adaptable to any geophysical signal of interest. This is the uniqueness of the mascon methodology. Although only presented here for validation, understanding of the mass trends of the world's major ice sheets is of interest due to their contribution to sea level rise. The most appropriate method from estimating a trend over Greenland also needs to be determined, along with an assessment of leakage. In addition, Williams et al. (2014) found significant autocorrelation in time-series over Antarctica and Figure 79 (right) revealed autocorrelation in the 10 day mascon solutions. This needs to be considered when estimating mass trends from mascon solutions.

Recent work by Watkins et al. (2015) used mascons of a circular shape. It is possible to modify *Faust* to estimate mascons that are circular or hexagonal in shape. This would make for an interesting comparison. Another interesting comparison would be the mascon solution presented here to spherical harmonic solutions where noise and errors were mitigated during solution generation using regularisation. Work could also be undertaken to use results from the mascon solutions presented here to improve geophysical models.

During orbit determination, the KBRR rejection criterion in section 5.3.5 needed modification after August 2010 due to mass loss signal over Greenland and West Antarctica increasing in difference from the background gravity field. Future work could be undertaken to allow the mascon solution to be iterated, allowing the rejection criterion to be subsequently lowered after each iteration. Although computationally intensive, this could be a good way to retain real signal while mitigating for noise and errors. Less computationally expensive is to use the previous monthly TVG solution as a background model. A background gravity field with a time-variable component could also be used.

Finally, with the GRACE-FO mission expected to be similar to GRACE, the work undertaken in this thesis leaves Newcastle University in a position to undertaken analysis on the data from this new mission and any further releases of Level-1B GRACE data.

8.6 *Availability of the mascon solutions*

I am happy to make the monthly and 10 day mascon solutions presented in this thesis available to the wider scientific community. The solutions can be provided as global spherical harmonic coefficients or as grids of EWH values for any region of interest. The use of a constraint matrix during solution generation will mean that no additional post processing is required by the user. Therefore, the solutions can be used directly for geophysical interpretation. As required, the mascon constraint matrix can be optimised to each geophysical problem studied.

Appendix A

Formula for normalisation

The Legendre polynomials are normalised using

$$\overline{P}_{nm}(\cos\theta) = \sqrt{k(2n+1)\frac{(n-m)!}{(n+m)!}}P_{nm}(\cos\theta) \tag{A.1}$$

where θ is the colatitude and P_{nm} the un-normalised polynomials for degree *n* and order *m*. The value for *k* is given by

$$k = \begin{Bmatrix} 2, & \mathrm{m} \neq 0 \\ 1, & \mathrm{m} = 0 \end{Bmatrix} \tag{A.2}$$

While normalised Legendre polynomials are denoted by a bar, this is often dropped for simplicity. Normalised spherical harmonic coefficients are obtained using

$$\begin{Bmatrix} \overline{C}_{nm} \\ \overline{S}_{nm} \end{Bmatrix} = \sqrt{\frac{(n+m)!}{k(2n+1)(n-m)!}} \begin{Bmatrix} C_{nm} \\ S_{nm} \end{Bmatrix} \tag{A.3}$$

where C_{nm} and S_{nm} are the un-normalised gravity field spherical harmonic coefficients of degree *n* and order *m.*

Method of Least Squares

During dynamic orbit determination and data reduction, parameters of interest are solved in *Faust* using Least Squares, which is a differential correction procedure that aims to minimise the sum of the squares of the residuals,

$$\sum_{i=1}^{n} w_i (O_i - C_i)^2 \tag{A.4}$$

where O_i is the i^{th} observation and C_i is the corresponding calculated at time *t*; the epoch of observation *i*. w_i is the weight assigned to the observation by,

$$w_i = \frac{1}{\sigma_i^2} \tag{A.5}$$

where σ_i is the standard deviation of the observation *i*. During the Least Squares procedure, corrections to the *a-priori* parameters values are calculated from the observations so that

$$\underline{P} = \underline{P} + \Delta\underline{P} \tag{A.6}$$

where $\underline{P}$ is the vector of parameters of interest sought during the data reduction, $\underline{P}$ is the vector of the *a-priori* values which are the best available approximation and $\Delta\underline{P}$ is the correction estimated. The most accurate correction is estimated when C_i most closely resembles O_i in the Least Squares sense.

In an ideal case the computed values may be represented as $C_i = C_i(\underline{P})$. As $\underline{P}$ is not known a Taylor series expansion of $C_i(\underline{P})$ is required giving

$$C_i(\underline{P}) = C_i(\underline{P} + \Delta\underline{P}) = C_i(\underline{P}) + \frac{\partial C_i(\underline{P})}{\partial \underline{P}} . \Delta\underline{P} \tag{A.7}$$

Substituting (A.7) into (A.4) then the Least Square process involves minimising

$$I = \sum_{i=1}^{n} w_i (O_i - C_i(\underline{P}) + \frac{\partial C_i(\underline{P})}{\partial \underline{P}} . \Delta\underline{P})^2 \tag{A.8}$$

I is minimised with respect to all components of $\Delta\underline{P}$

$$\frac{\partial I}{\partial \Delta \underline{p}_j} = -2\sum_{i=1}^{n} w_i \left(O_i - C_i(\underline{\mathrm{P}}) + \frac{\partial C_i(\underline{P})}{\partial \underline{P}} . \Delta \underline{P}) \right) \frac{\partial C_i(\underline{P})}{\partial \Delta \underline{p}_j} \equiv 0 \tag{A.9}$$

In matrix form (A.9) can be written as

$$N \Delta \underline{P} = \underline{b} \tag{A.10}$$

which is the normal equations consisting of

$$N_{jk} = \sum_i w_i \frac{\partial C_i(\underline{P})}{\partial \underline{p_j}} \frac{\partial C_i(\underline{P})}{\partial \underline{p_k}} \tag{A.11}$$

and

$$b_j = \sum_i w_i (\mathrm{O}_i - C_i(\underline{\mathrm{P}})) \frac{\partial C_i(\underline{P})}{\partial \underline{p_j}} \tag{A.12}$$

The normal equations have a solution provided N is invertible. If there are sufficient observations then N is a symmetric positive definite matrix. Each b_j is the sum of the weighted residuals $\mathrm{O}_i - C_i$, and the partials $\frac{\partial C_i(\underline{P})}{\partial \underline{p_j}}$. The normal equations are evaluated at each observation time t_i using the Gauss-Jackson 8$^{\text{th}}$ order numerical integrator. For consistency with Chapter 4, (A.10) can be written as

$$(A^T W A)\hat{\underline{x}} = A^T W \underline{b} \tag{A.13}$$

or

$$(A^T W A + C^T V C)\hat{\underline{x}} = A^T W \underline{b} + C^T V \underline{q} \tag{A.14}$$

with the mascon constraint matrix included. The design matrix A contains the KBRR observation partials with respect the parameters of interest. Thus, with W=day (w_1 , w_2 ... w_N) when estimating the mascon parameters (H), the correction $\Delta \underline{H}$ is estimated from the GRACE KBRR observation data using Eq. (12) of Chapter 4 i.e.

$$A_{IJ} = \frac{\partial \Psi_I}{\partial H_J} = \sum_{l=1}^{l_{max}} \sum_{m=0}^{l} \frac{\partial \Psi_I}{\partial \Delta C_{lm}^J} \frac{\partial \Delta C_{lm}^J}{\partial H_J} + \frac{\partial \Psi_I}{\partial \Delta S_{lm}^J} \frac{\partial \Delta S_{lm}^J}{\partial H_J}$$

where , $\partial\Psi_I / \partial H_J$ is the partial derivative of the KBRR observation *i* with respect to the mascon parameter *j*. As the each mascon is defined using spherical harmonics, up to degree and order 60, $\partial KBRR_I / \partial H_J$ requires the summation of $\partial\Psi_I / \partial\Delta C_{lm}^J$ and $\partial\Psi_I / \partial\Delta S_{lm}^J$ which are partial derivatives of the KBRR observations with respect to the delta gravitational coefficients, with $\partial\Delta C_{lm}^J / \partial H_J$ and $\partial\Delta S_{lm}^J / \partial H_J$ the partial derivatives of the delta gravitational coefficients with respect to the mascon parameter *j*.

Appendix B

Flow chart of how the mascon parameters are estimated

Faust is Newcastle University's orbit determination software. *Faust* uses dynamic orbit determination, which requires precise models of the forces acting on the satellite, solving for parameters of interest using Least Squares. *Faust* has the capability to determine the orbits of multiple satellites simultaneously, making it suitable for the processing of GRACE data. The process of dynamic orbit determination involves the evaluation of force models to calculate the orbit of the GRACE satellites. The numerical integration of the satellite orbits is undertaken using an 8^{th} order Gauss-Jackson algorithm.

When starting this thesis, *Faust* was already an established piece of orbit determination software and is well documented in the thesis of Boomkamp (1998). The main modification I made to *Faust* was reading in the mascons, as spherical harmonic coefficients, to allow the calculation of the mascon parameters. The mascon parameters are calculated using Eq. (13), in Section 4.4, from geophysical information from satellite tracking data.

In *Faust* the orbits of the GRACE satellites are simulated numerically using mathematical models and observed via the KBRR data. Parameters of interest are estimated using Least Squares (described in Appendix A) by minimise the sum of the squares of the residuals. Below is a brief flow chart of how *Faust* is used to estimate mascon parameters:

Within *Faust*

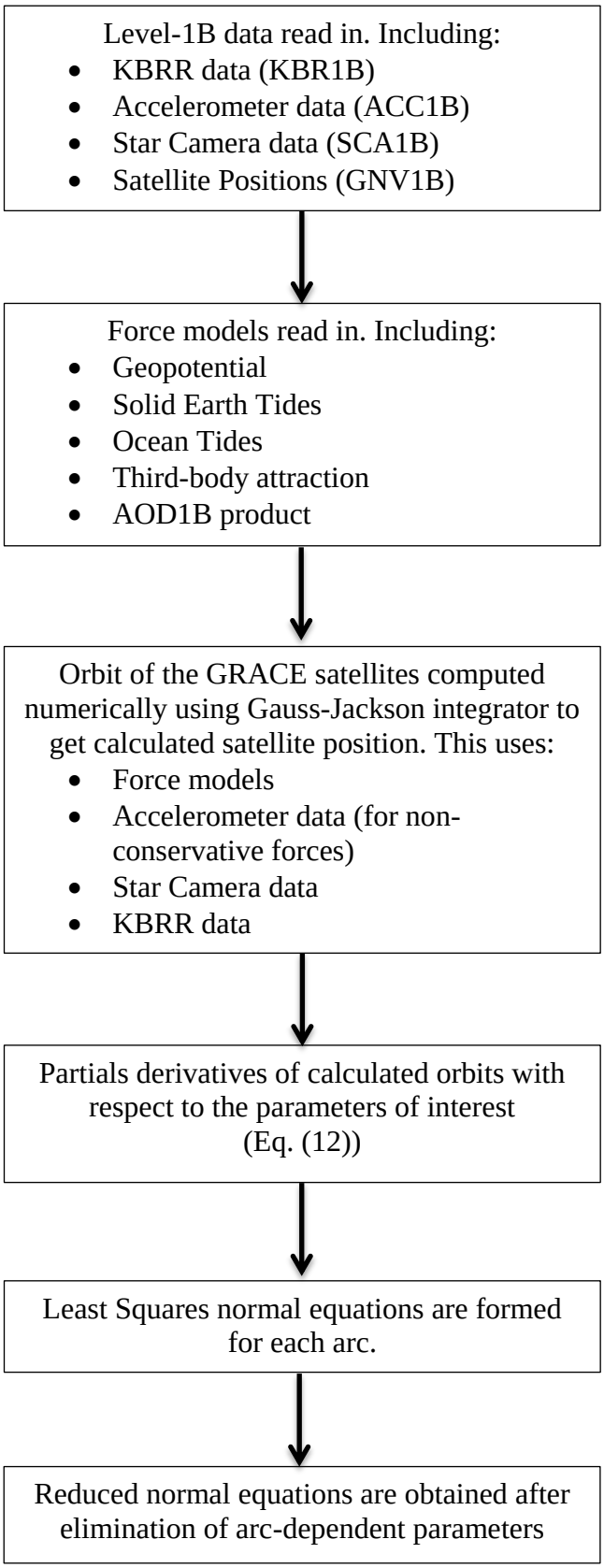

Outside *Faust*

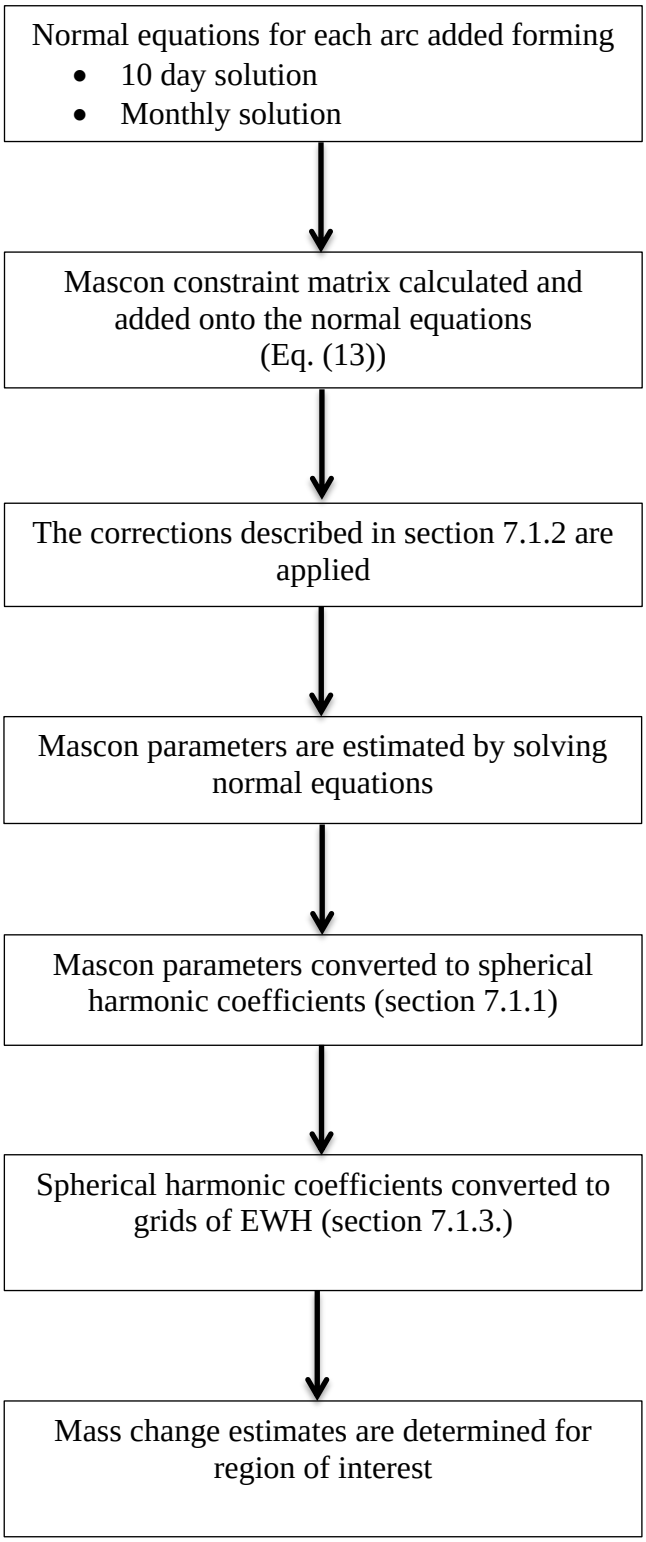

Appendix C

Plots of the number of days included (blue), rejected due to no accelerometer bias value (green) and rejected due to poor data (red) for each year from 2003 to 2013. The months where no information is available coincide with months when the satellite measuring equipment was turned off to preserve power. No solutions are available for those months from the official GRACE processing centres.

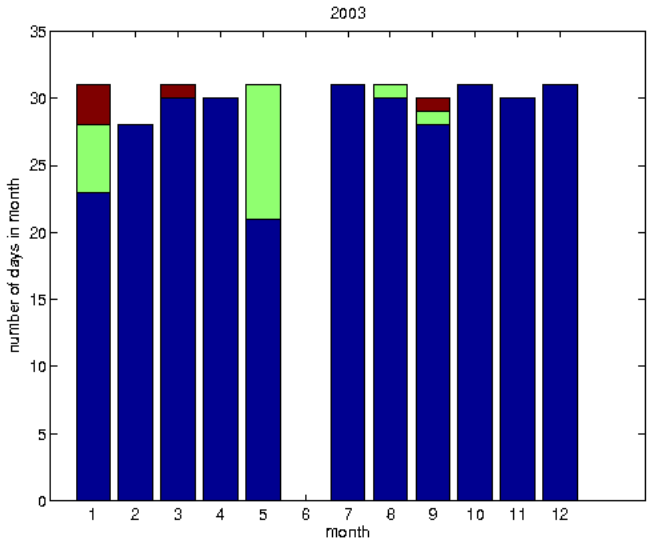

Figure C.1. Number of days included in the monthly solution (blue), rejected due to no accelerometer bias value (green) and rejected due to poor data (red) for 2003.

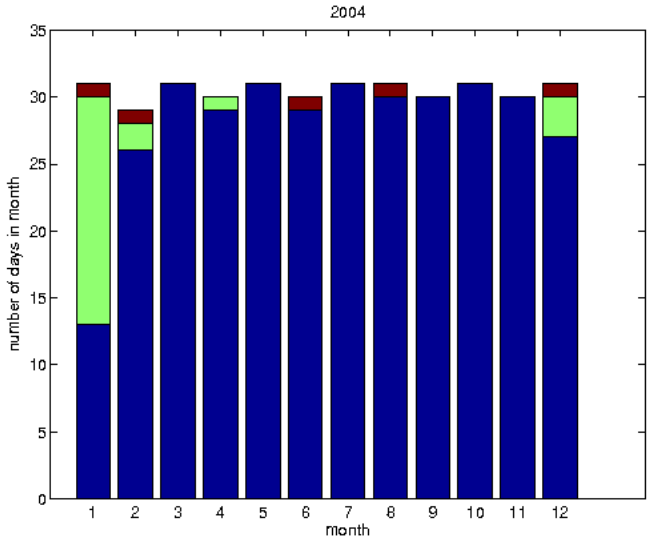

Figure C.2. Number of days included in the monthly solution (blue), rejected due to no accelerometer bias value (green) and rejected due to poor data (red) for 2004.

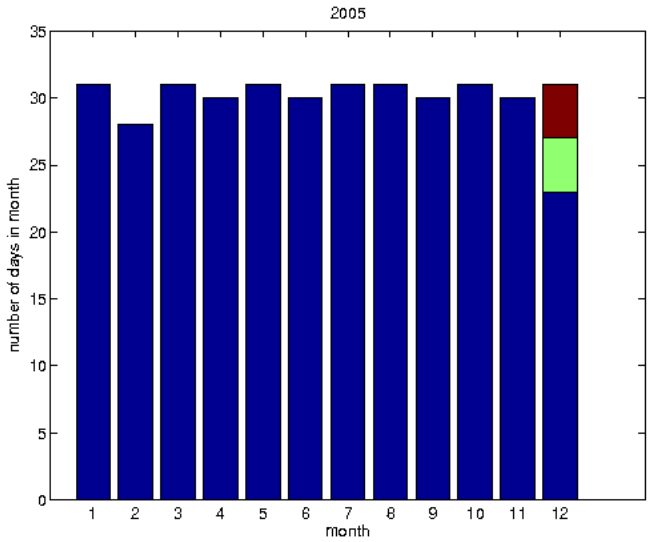

Figure C.3. Number of days included in the monthly solution (blue), rejected due to no accelerometer bias value (green) and rejected due to poor data (red) for 2005.

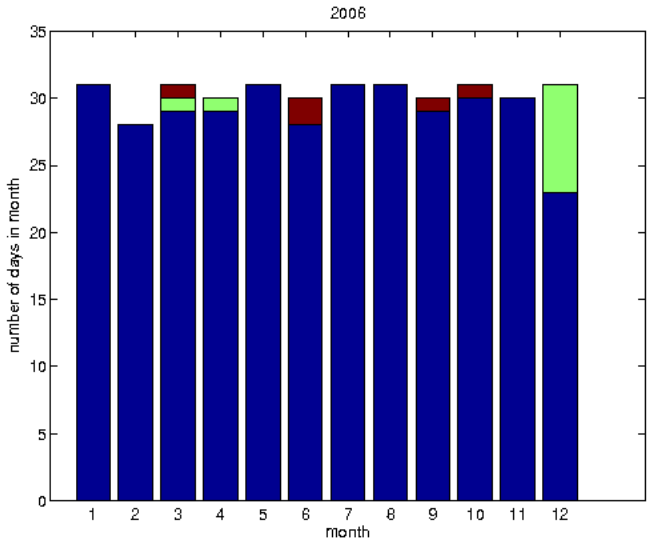

Figure C.4. Number of days included in the monthly solution (blue), rejected due to no accelerometer bias value (green) and rejected due to poor data (red) for 2006.

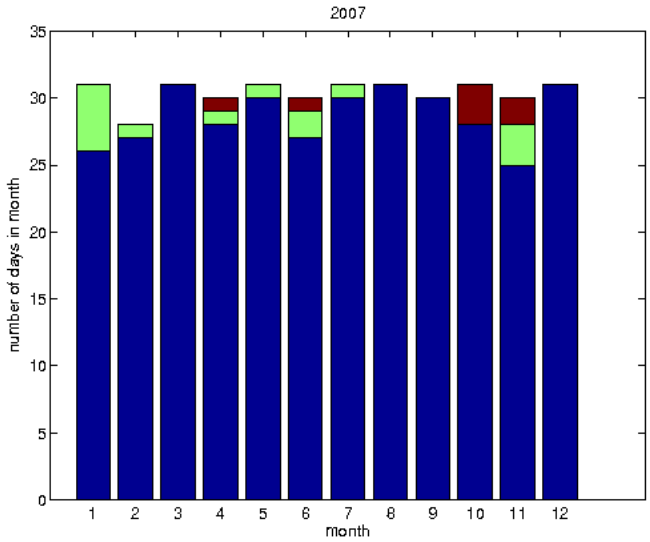

Figure C.5. Number of days included in the monthly solution (blue), rejected due to no accelerometer bias value (green) and rejected due to poor data (red) for 2007.

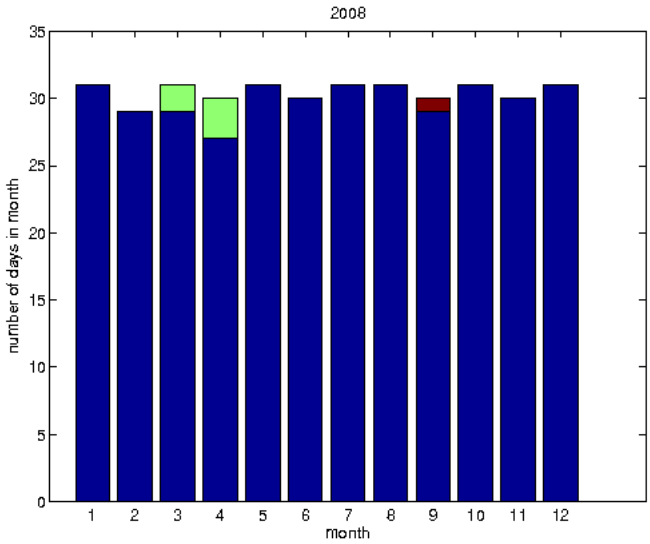

Figure C.6. Number of days included in the monthly solution (blue), rejected due to no accelerometer bias value (green) and rejected due to poor data (red) for 2008.

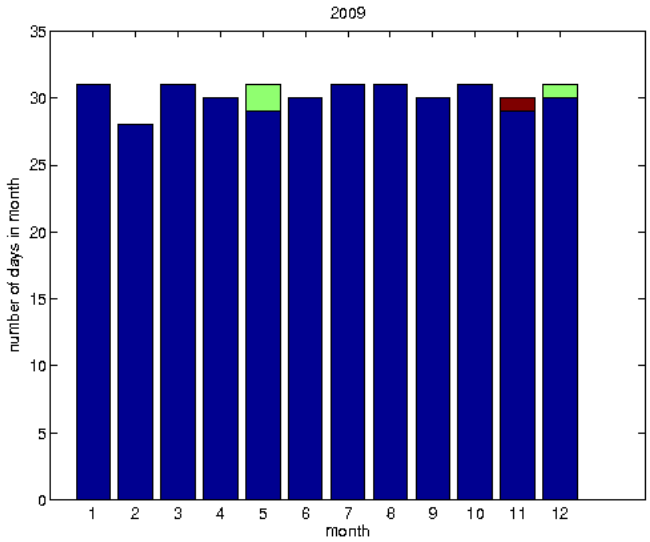

Figure C.7. Number of days included in the monthly solution (blue), rejected due to no accelerometer bias value (green) and rejected due to poor data (red) for 2009.

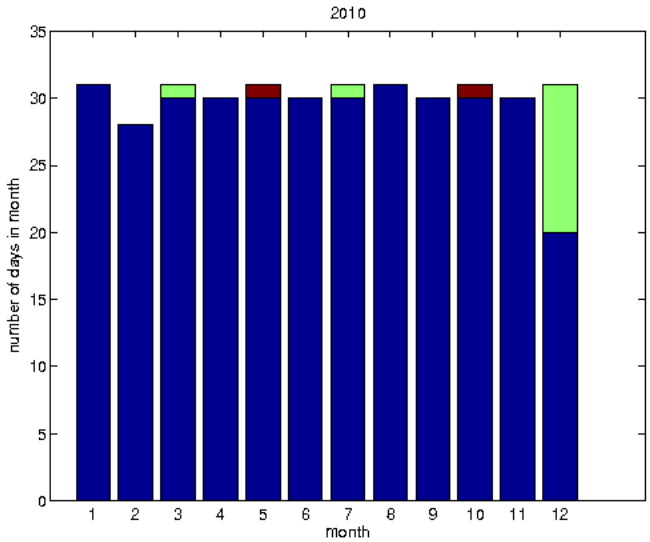

Figure C.8. Number of days included in the monthly solution (blue), rejected due to no accelerometer bias value (green) and rejected due to poor data (red) for 2010.

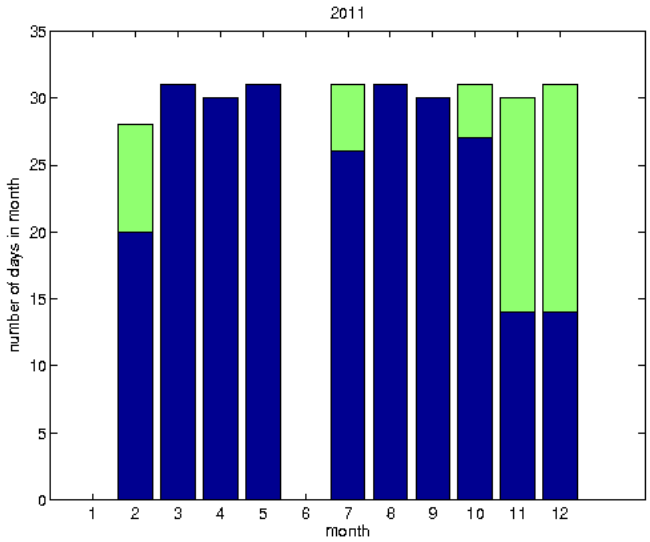

Figure C.9. Number of days included in the monthly solution (blue), rejected due to no accelerometer bias value (green) and rejected due to poor data (red) for 2011.

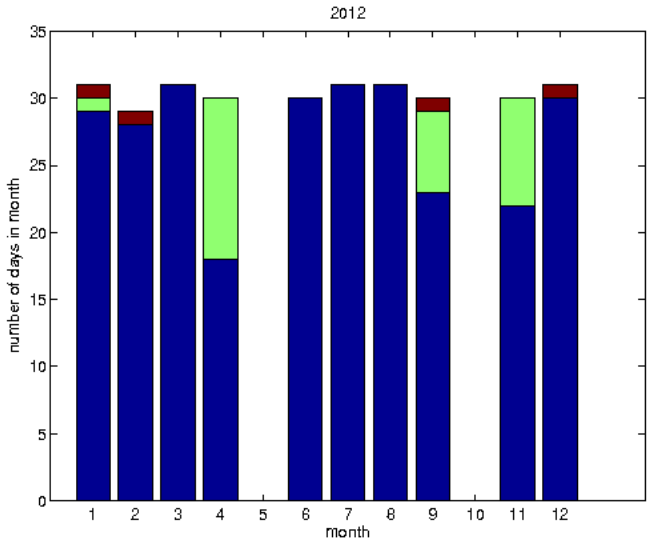

Figure C.10. Number of days included in the monthly solution (blue), rejected due to no accelerometer bias value (green) and rejected due to poor data (red) for 2012.

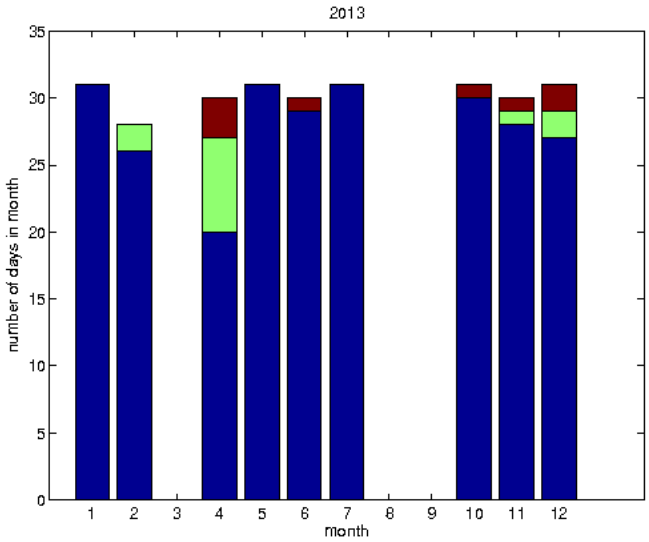

Figure C.11. Number of days included in the monthly solution (blue), rejected due to no accelerometer bias value (green) and rejected due to poor data (red) for 2013.

References

Andersen, O. B. (2010) *The DTU10 Gravity field and Mean sea surface: Second international symposium of the gravity field of the Earth (IGFS2), Fairbanks, Alaska.*

Andrews, S. B., Moore, P. and King, M. A. (2014) Mass change from GRACE: a simulated comparison of Level-1B analysis techniques *Geophysical Journal International,* **200,** 1 503-518.

Argus, D. F., Peltier, W. R., Drummond, R. and Moore, A. W. (2014) The Antarctica component of postglacial rebound model ICE-6G_C (VM5a) based on GPS positioning, exposure age dating of ice thicknesses, and relative sea level histories *Geophysical Journal International,* **198,** 1 537-563.

Awange, J. L., K M Fleming, M Kuhn, W E Featherstone, B Heck and I Anjasmara (2011) On the suitability of the 4 degree x 4 degree GRACE mascon solutions for remote sensing Australian hydrology *Remote Sensing of Environment,* **115,** 864 - 875.

Bandikova, T. and Flury, J. (2014) Improvement of the GRACE star camera data based on the revision of the combination method *Advances in Space Research,* **54,** 9 1818-1827.

Bandikova, T., Flury, J. and Ko, U.-D. (2012) Characteristics and accuracies of the GRACE inter-satellite pointing *Advances in Space Research,* **50,** 1 123-135.

Barletta, V. R., SÃ¸rensen, L. S. and Forsberg, R. (2013) Scatter of mass changes estimates at basin scale for Greenland and Antarctica *The Cryosphere***,** 7, 1411-1432, doi:10.5194/tc-7-1411-2013, 2013.

Barletta, V. R., Sabadini, R. and Bordoni, A. (2008) Isolating the PGR signal in the GRACE data: impact on mass balance estimates in Antarctica and Greenland *Geophysical Journal International,* **172,** 1 18-30.

Baur, O., Kuhn, M. and Featherstone, W. E. (2013) Continental mass change from GRACE over 2002–2011 and its impact on sea level *Journal of Geodesy,* **87,** 2 117-125.

Bettadpur, S. (2009) *GRACE TN-04-02 Recommendation for a-priori Bias & Scale Parameters for Level-1B ACC Data (Version 2).* Centre for Space Research ftp://podaac.jpl.nasa.gov/allData/grace/docs/TN-02_ACC_CalInfo.pdf:

Bettadpur, S. (2012a) *GRACE 327-720 Gravity Recovery and Climate Experiment Product Specification Document (Version 4.6).* Centre for Space Research ftp://podaac-ftp.jpl.nasa.gov/allData/grace/L1B/JPL/RL01/docs/ProdSpecDoc_v4.6.pdf:

Bettadpur, S. (2012b) *UTCSR Level-2 Processing Standards Document for Level-2 Product Release 0005*

Bezděk, A. (2010) Calibration of accelerometers aboard GRACE satellites by comparison with POD-based nongravitational accelerations *Journal of Geodynamics,* **50,** 5 410-423.

Bomford, G. (1980) *Geodesy* Oxford Univ. Press 1980. 90s.

Bonin, J., Bettadpur, S. and Tapley, B. (2012) High-frequency signal and noise estimates of CSR GRACE RL04 *Journal of Geodesy***,** 1-13.

Bonin, J. and Chambers, D. (2013) Uncertainty estimates of a GRACE inversion modelling technique over Greenland using a simulation *Geophysical Journal International*.

Bonin, J. A. and Chambers, D. P. (2011) Evaluation of high-frequency oceanographic signal in GRACE data: Implications for de-aliasing *Geophysical Research Letters,* **38,** 17 L17608.

Boomkamp, H. J. (1998) *Combination of altimetry data from different satellite missions.* PhD thesis, Aston University

Bouman, J., Fuchs, M., Ivins, E., van der Wal, W., Schrama, E., Visser, P. and Horwath, M. (2014a) Antarctic outlet glacier mass change resolved at basin scale from satellite gravity gradiometry *Geophysical Research Letters***,** 2014GL060637.

Bouman, J., Fuchs, M., Lieb, V., Bosch, W., Dettmering, D. and Schmidt, M. (2014b) 'GOCE Gravity Gradients: Combination with GRACE and Satellite Altimetry', in Flechtner, F., Sneeuw, N. and Schuh, W.-D.(Eds) *Observation of the System Earth from Space - CHAMP, GRACE, GOCE and future missions.* Springer Berlin Heidelberg, pp. 89-94.

Bruinsma, S., Forbes, J. M., Nerem, R. S. and Zhang, X. (2006) Thermosphere density response to the 20-21 November 2003 solar and geomagnetic storm from CHAMP and GRACE accelerometer data *J. Geophys. Res.*, **111,** A6 A06303.

Bruinsma, S., Lemoine, J.-M., Biancale, R. and Valès, N. (2010) CNES/GRGS 10-day gravity field models (release 2) and their evaluation *Advances in Space Research*, **45,** 4 587-601.

Bruinsma, S. L. and Forbes, J. M. (2010) Anomalous behavior of the thermosphere during solar minimum observed by CHAMP and GRACE *J. Geophys. Res.*, **115,** A11 A11323.

Case, K., Kruizinga, G. and Wu, S.-C. (2010) *GRACE Level-1B Data Product User Handbook.*

Castle, S. L., Thomas, B. F., Reager, J. T., Rodell, M., Swenson, S. C. and Famiglietti, J. S. (2014) Groundwater depletion during drought threatens future water security of the Colorado River Basin *Geophysical Research Letters*, **41,** 16 2014GL061055.

Chambers, D. P. (2006) Observing seasonal steric sea level variations with GRACE and satellite altimetry *Journal of Geophysical Research: Oceans*, **111,** C3 C03010.

Chambers, D. P. and Bonin, J. A. (2012) Evaluation of Release-05 GRACE time-variable gravity coefficients over the ocean *Ocean Sci.*, **8,** 5 859-868.

Chambers, D. P., Wahr, J. and Nerem, R. S. (2004) Preliminary observations of global ocean mass variations with GRACE *Geophysical Research Letters*, **31,** 13 L13310.

Chambers, D. P., Wahr, J., Tamisiea, M. E. and Nerem, R. S. (2010) Ocean mass from GRACE and glacial isostatic adjustment *J. Geophys. Res.*, **115,** B11 B11415.

Chen, J. L., Rodell, M., Wilson, C. R. and Famiglietti, J. S. (2005) Low degree spherical harmonic influences on Gravity Recovery and Climate Experiment (GRACE) water storage estimates *Geophys. Res. Lett.*, **32,** 14 L14405.

Chen, J. L., Wilson, C. R. and Seo, K. W. (2006a) Optimized smoothing of Gravity Recovery and Climate Experiment (GRACE) time-variable gravity observations *Journal of Geophysical Research: Solid Earth*, **111,** B6 B06408.

Chen, J. L., Wilson, C. R. and Tapley, B. D. (2006b) Satellite gravity measurements confirm accelerated melting of Greenland ice sheet *Science*, **313,** 5795 1958-1960.

Cheng, M., Ries, J. C. and Tapley, B. D. (2011) Variations of the Earth's figure axis from satellite laser ranging and GRACE *Journal of Geophysical Research: Solid Earth*, **116,** B1 B01409.

Cheng, M., Tapley, B. D. and Ries, J. C. (2013) Deceleration in the Earth's oblateness *Journal of Geophysical Research: Solid Earth*, **118,** 2 740-747.

CNES/GRGS (2015) *thegraceplotter*. Available at: http://www.thegraceplotter.com/ (Accessed: 21/4/2015).

Dahle, C., Flechtner, F., Gruber, C., König, D., König, R., Michalak, G. and Neumayer, K.-H. (2013) *GFZ RL05: An GFZ GRACE Level-2 Processing Standards Document for Level-2 Product Release 0005.*

Dahle, C., Flechtner, F., Gruber, C., König, D., König, R., Michalak, G. and Neumayer, K.-H. (2014) 'GFZ RL05: An Improved Time-Series of Monthly GRACE Gravity Field Solutions', in Flechtner, F., Sneeuw, N. and Schuh, W.-D.(Eds) *Observation of the System Earth from Space - CHAMP, GRACE, GOCE and future missions.* Springer Berlin Heidelberg, pp. 29-39.

Ditmar, P., Teixeira da Encarnação, J. and Hashemi Farahani, H. (2011) Understanding data noise in gravity field recovery on the basis of inter-satellite ranging measurements acquired by the satellite gravimetry mission GRACE *Journal of Geodesy***,** 1-25.

Dobslaw, H., Flechtner, F., Bergmann-Wolf, I., Dahle, C., Dill, R., Esselborn, S., Sasgen, I. and Thomas, M. (2013) Simulating high-frequency atmosphere-ocean mass variability for dealiasing of satellite gravity observations: AOD1B RL05 *Journal of Geophysical Research: Oceans,* **118,** 7 3704-3711.

Doornbos, E., Den Ijssel, J. V., Luehr, H., Foerster, M. and Koppenwallner, G. (2010) Neutral Density and Crosswind Determination from Arbitrarily Oriented Multiaxis Accelerometers on Satellites *Journal of Spacecraft and Rockets,* **47,** 4 580-589.

Dunn, C., Bertiger, W., Bar-Sever, Y., Desai, S., Haines, B., Kuang, D., Franklin, G., Harris, I., Kruizinga, G., Meehan, T., Nandi, S., Nguyen, D., Rogstad, T., Thomas, J. B., Tien, J., Romans, L., Watkins, M., Wu, S.-C., Bettadpur, S. and Kim, J. (2003) Instrument of GRACE: GPS augments gravity measurements *GPS World,* **14,** 16 - 28.

El Gammal, E. A., Salem, S. M. and El Gammal, A. E. A. (2010) Change detection studies on the world's biggest artificial lake (Lake Nasser, Egypt) *The Egyptian Journal of Remote Sensing and Space Science,* **13,** 2 89-99.

Farrell, W. E. (1972) DEFORMATION OF EARTH BY SURFACE LOADS *Reviews of Geophysics and Space Physics,* **10,** 3 761-&.

Flechtner, F. (2007) *GR-GFZ-STD-001 GFZ Level-2 Processing Standards Document For Level-2 Product Release 0004 (Rev. 1.0, February 19, 2007).* GFZ ftp://podaac.jpl.nasa.gov/allData/grace/docs/L2-GFZ_ProcStds_0004_v1.0.pdf:

Flechtner, F. (2014) *GR-GFZ-AOD-0001 AOD1B Product Description Document for Product Release 05 (Rev. 4.2, May 20, 2014).* GFZ ftp://podaac.jpl.nasa.gov/allData/grace/docs/AOD1B_20140520.pdf:

Flury, J., Bettadpur, S. and Tapley, B. D. (2008) Precise accelerometry onboard the GRACE gravity field satellite mission *Advances in Space Research,* **42,** 8 1414-1423.

Förste, C., Bruinsma, S., Shako, R., Marty, J. C., Flechtner, F., Abrikosov, O., Dahle, C., Lemoine, J. M., Neumayer, K. H., Biancale, R., Barthelmes, F., König, R. and Balmino, G. (2011) *EIGEN-6 - A new combined global gravity field model including GOCE data from the collaboration of GFZ-Potsdam and GRGS-Toulouse: Geophysical Research Abstracts Vol. 13, EGU2011-3242-2, EGU General Assembly, 2011.*

Förste, C., Schmidt, R., Stubenvoll, R., Flechtner, F., Meyer, U., König, R., Neumayer, H., Biancale, R., Lemoine, J.-M., Bruinsma, S., Loyer, S., Barthelmes, F. and Esselborn, S. (2008) The GeoForschungsZentrum Potsdam/Groupe de Recherche de Gèodésie Spatiale satellite-only and combined gravity field models: EIGEN-GL04S1 and EIGEN-GL04C *Journal of Geodesy,* **82,** 6 331-346.

Fretwell, P., Pritchard, H. D., Vaughan, D. G., Bamber, J. L., Barrand, N. E., Bell, R., Bianchi, C., Bingham, R. G., Blankenship, D. D., Casassa, G., Catania, G., Callens, D., Conway, H., Cook, A. J., Corr, H. F. J., Damaske, D., Damm, V., Ferraccioli, F., Forsberg, R., Fujita, S., Gim, Y., Gogineni, P., Griggs, J. A., Hindmarsh, R. C. A., Holmlund, P., Holt, J. W., Jacobel, R. W., Jenkins, A., Jokat, W., Jordan, T., King, E. C., Kohler, J., Krabill, W., Riger-Kusk, M., Langley, K. A., Leitchenkov, G., Leuschen, C., Luyendyk, B. P., Matsuoka, K., Mouginot, J., Nitsche, F. O., Nogi, Y., Nost, O. A., Popov, S. V., Rignot, E., Rippin, D. M., Rivera, A., Roberts, J., Ross, N., Siegert, M. J., Smith, A. M., Steinhage, D., Studinger, M., Sun, B., Tinto, B. K., Welch, B. C., Wilson, D., Young, D. A., Xiangbin, C. and Zirizzotti, A. (2013) Bedmap2: improved ice bed, surface and thickness datasets for Antarctica *The Cryosphere,* **7,** 1 375-393.

Frommknecht, B. and Schlicht, A. (2010) 'The GRACE Gravity Sensor System', in Flechtner, F. M., Gruber, T., Güntner, A., Mandea, M., Rothacher, M., Schöne, T. and Wickert, J.(Eds) *System Earth via Geodetic-Geophysical Space Techniques.* Springer Berlin Heidelberg, pp. 105-118.

Ghadi, Y. (2013) *Regional Gravity Field Modeling with Adjusted Spherical Cap Harmonics in an Integrated Approach.* thesis. TU Darmstadt.

Gunter, B., Urban, T., Riva, R., Helsen, M., Harpold, R., Poole, S., Nagel, P., Schutz, B. and Tapley, B. (2009) A comparison of coincident GRACE and ICESat data over Antarctica *Journal of Geodesy,* **83,** 11 1051-1060.

Gunter, B. C., Didova, O., Riva, R. E. M., Ligtenberg, S. R. M., Lenaerts, J. T. M., King, M. A., van den Broeke, M. R. and Urban, T. (2014) Empirical estimation of present-day Antarctic glacial isostatic adjustment and ice mass change *The Cryosphere,* **8, 743-760, doi:10.5194/tc-8-743-2014, 2014.**

Han, S.-C., Kim, H., Yeo, I.-Y., Yeh, P., Oki, T., Seo, K.-W., Alsdorf, D. and Luthcke, S. B. (2009) Dynamics of surface water storage in the Amazon inferred from measurements of inter-satellite distance change *Geophys. Res. Lett.,* **36,** 9 L09403.

Han, S.-C., Sauber, J., Luthcke, S. B., Ji, C. and Pollitz, F. F. (2008) Implications of postseismic gravity change following the great 2004 Sumatra-Andaman earthquake from the regional harmonic analysis of GRACE intersatellite tracking data *Journal of Geophysical Research: Solid Earth,* **113,** B11 B11413.

Han, S.-C., Shum, C. K., Bevis, M., Ji, C. and Kuo, C.-Y. (2006) Crustal Dilatation Observed by GRACE After the 2004 Sumatra-Andaman Earthquake *Science,* **313,** 5787 658-662.

Han, S.-C., Shum, C. K., Jekeli, C., Kuo, C.-Y., Wilson, C. and Seo, K.-W. (2005) Non-isotropic filtering of GRACE temporal gravity for geophysical signal enhancement *Geophysical Journal International,* **163,** 1 18-25.

Hanna, E., Huybrechts, P., Steffen, K., Cappelen, J., Huff, R., Shuman, C., Irvine-Fynn, T., Wise, S. and Griffiths, M. (2008) Increased Runoff from Melt from the Greenland Ice Sheet: A Response to Global Warming *Journal of Climate,* **21,** 2.

Helsen, M. M., van den Broeke, M. R., van de Wal, R. S. W., van de Berg, W. J., van Meijgaard, E., Davis, C. H., Li, Y. H. and Goodwin, I. (2008) Elevation changes in Antarctica mainly determined by accumulation variability *Science,* **320,** 5883 1626-1629.

Horwath, M. and Dietrich, R. (2009) Signal and error in mass change inferences from GRACE: the case of Antarctica *Geophysical Journal International,* **177,** 3 849-864.

Horwath, M., Lemoine, J.-M., Biancale, R. and Bourgogne, S. (2011) Improved GRACE science results after adjustment of geometric biases in the Level-1B K-band ranging data *Journal of Geodesy,* **85,** 1 23-38.

Ivins, E. R., James, T. S., Wahr, J., O. Schrama, E. J., Landerer, F. W. and Simon, K. M. (2013) Antarctic contribution to sea level rise observed by GRACE with improved GIA correction *Journal of Geophysical Research: Solid Earth,* **118,** 6 3126-3141.

Jacob, T., Wahr, J., Pfeffer, W. T. and Swenson, S. (2012) Recent contributions of glaciers and ice caps to sea level rise *Nature,* **482,** 7386 514-518.

Jekeli, C. (1981) *Alternative Methods to Smooth the Earth's Gravity Field* , Rep 327 Dep. of Geod. Sci. and Surv., Ohio State Univ., Columbus: (0923-2958).

Jekeli, C. (1999) The determination of gravitational potential differences from satellite-to-satellite tracking *Celestial Mechanics and Dynamical Astronomy,* **75,** 2 85-101.

Johannessen, O. M., Khvorostovsky, K., Miles, M. W. and Bobylev, L. P. (2005) Recent ice-sheet growth in the interior of Greenland *Science,* **310,** 5750 1013-1016.

Kang, Z., Nagel, P. and Pastor, R. (2003) Precise orbit determination for GRACE *Advances in Space Research,* **31,** 8 1875-1881.

Kang, Z., Tapley, B., Bettadpur, S., Ries, J. and Nagel, P. (2006a) Precise orbit determination for GRACE using accelerometer data *Advances in Space Research,* **38,** 9 2131-2136.

Kang, Z., Tapley, B., Bettadpur, S., Ries, J., Nagel, P. and Pastor, R. (2006b) Precise orbit determination for the GRACE mission using only GPS data *Journal of Geodesy,* **80,** 6 322-331.

Kelley, O. A. (2014) Where the Least Rainfall Occurs in the Sahara Desert, the TRMM Radar Reveals a Different Pattern of Rainfall Each Season *Journal of Climate,* **27,** 18 6919-6939.

Kim, J. and Lee, S. W. (2009) Flight performance analysis of GRACE K-band ranging instrument with simulation data *Acta Astronautica,* **65,** 11-12 1571-1581.

Kim, J. and Tapley, B. (2015) Estimation of non-gravitational acceleration difference between two co-orbiting satellites using single accelerometer data *Journal of Geodesy,* **89,** 6 537-550.

Kim, J. and Tapley, B. D. (2002) Error analysis of a low-low satellite-to-satellite tracking mission *Journal of Guidance, Control, and Dynamics,* **25,** 6 1100-1106.

Kim, J. R. (2000) *Simulation study of a low-low satellite-to-satellite tracking mission.* PhD thesis. University of Texas, Austin.

King, M., Moore, P., Clarke, P. and Lavallée, D. (2006) Choice of optimal averaging radii for temporal GRACE gravity solutions, a comparison with GPS and satellite altimetry *Geophysical Journal International,* **166,** 1 1-11.

King, M. A., Bingham, R. J., Moore, P., Whitehouse, P. L., Bentley, M. J. and Milne, G. A. (2012) Lower satellite-gravimetry estimates of Antarctic sea-level contribution *Nature,* **491,** 7425 586-589.

Klees, R., Revtova, E. A., Gunter, B. C., Ditmar, P., Oudman, E., Winsemius, H. C. and Savenije, H. H. G. (2008a) The design of an optimal filter for monthly GRACE gravity models *Geophysical Journal International,* **175,** 2 417-432.

Klees, R., Tenzer, R., Prutkin, I. and Wittwer, T. (2008b) A data-driven approach to local gravity field modelling using spherical radial basis functions *Journal of Geodesy,* **82,** 8 457-471.

Klokočník, J., Gooding, R. H., Wagner, C. A., Kostelecký, J. and Bezděk, A. (2013) The Use of Resonant Orbits in Satellite Geodesy: A Review *Surveys in Geophysics,* **34,** 1 43-72.

Klosko, S., Rowlands, D., Luthcke, S., Lemoine, F., Chinn, D. and Rodell, M. (2009) Evaluation and validation of mascon recovery using GRACE KBRR data with

independent mass flux estimates in the Mississippi Basin *Journal of Geodesy,* **83,** 9 817-827.

Kruizinga, G., Bertiger, W., Byun, S., Finch, C., Kuang, D., Watkins, M., Yuan, D.-N., Bettadpur, S. and Wang, F. (2012) *GRACE Level-1 Processing Status: GRACE Science Team Meeting* GFZ Potsdam, September 17-19, 2012.

Kurtenbach, E., Eicker, A., Mayer-Gürr, T., Holschneider, M., Hayn, M., Fuhrmann, M. and Kusche, J. (2012) Improved daily GRACE gravity field solutions using a Kalman smoother *Journal of Geodynamics,* **59–60,** 39-48.

Kusche, J. (2007) Approximate decorrelation and non-isotropic smoothing of time-variable GRACE-type gravity field models *Journal of Geodesy,* **81,** 11 733-749.

Kusche, J., Schmidt, R., Petrovic, S. and Rietbroek, R. (2009) Decorrelated GRACE time-variable gravity solutions by GFZ, and their validation using a hydrological model *Journal of Geodesy,* **83,** 10 903-913.

Larsen, C. F., Motyka, R. J., Freymueller, J. T., Echelmeyer, K. A. and Ivins, E. R. (2005) Rapid viscoelastic uplift in southeast Alaska caused by post-Little Ice Age glacial retreat *Earth and Planetary Science Letters,* **237,** 3–4 548-560.

Lay, T., Kanamori, H., Ammon, C. J., Nettles, M., Ward, S. N., Aster, R. C., Beck, S. L., Bilek, S. L., Brudzinski, M. R., Butler, R., DeShon, H. R., Ekström, G., Satake, K. and Sipkin, S. (2005) The Great Sumatra-Andaman Earthquake of 26 December 2004 *Science,* **308,** 5725 1127-1133.

Lemoine, F. G., Luthcke, S. B., Rowlands, D. D., Chinn, D. S., Klosko, S. M. and Cox, C. M. (2007) 'The use of mascons to resolve time-variable gravity from GRACE', in Tregoning, P. and Rizos, C.(Eds) *Dynamic Planet.* Vol. 130 Springer Berlin Heidelberg, pp. 231-236.

Lemoine, F. G., Smith, D. E., Kunz, L., Smith, R., Pavlis, E. C., Pavlis, N. K., Klosko, S. M., Chinn, D. S., Torrence, M. H., Williamson, R. G., Cox, C. M., Rachlin, K. E., Wang, Y. M., Kenyon, S. C., Salman, R., Trimmer, R., Rapp, R. H. and Nerem, R. S. (1998) 'The Development of the NASA GSFC and NIMA Joint Geopotential Model', in Segawa, J., Fujimoto, H. and Okubo, S.(Eds) *Gravity, Geoid and Marine Geodesy.* Vol. 117 Springer Berlin Heidelberg, pp. 461-469.

Lerch, F. J., Wagner, C. A., Smith, D. E., Sandson, M. L., Brownd, J. E. and Richardson, J. A. (1972) *Gravitational Field Models for the Earth (GEM1&2).* Report X55372146, Goddard Space Flight Center, Greenbelt/Maryland:

Liu, X., Ditmar, P., Siemes, C., Slobbe, D. C., Revtova, E., Klees, R., Riva, R. and Zhao, Q. (2010) DEOS Mass Transport model (DMT-1) based on GRACE satellite data: methodology and validation *Geophysical Journal International,* **181,** 2 769-788.

Llovel, W., Becker, M., Cazenave, A., Crétaux, J.-F. and Ramillien, G. (2010) Global land water storage change from GRACE over 2002–2009; Inference on sea level *Comptes Rendus Geoscience,* **342,** 3 179-188.

Longuevergne, L., Wilson, C. R., Scanlon, B. R. and Crétaux, J. F. (2013) GRACE water storage estimates for the Middle East and other regions with significant reservoir and lake storage *Hydrol. Earth Syst. Sci.,* **17,** 12 4817-4830.

Luthcke, S. B., Arendt, A. A., Rowlands, D. D., McCarthy, J. J. and Larsen, C. F. (2008) Recent glacier mass changes in the Gulf of Alaska region from GRACE mascon solutions *Journal of Glaciology,* **54,** 767-777.

Luthcke, S. B., Rowlands, D. D., Lemoine, F. G., Klosko, S. M., Chinn, D. and McCarthy, J. J. (2006a) Monthly spherical harmonic gravity field solutions determined from GRACE inter-satellite range-rate data alone *Geophys. Res. Lett.,* **33,** 2 L02402.

Luthcke, S. B., Sabaka, T. J., Loomis, B. D., Arendt, A. A., McCarthy, J. J. and Camp, J. (2013) Antarctica, Greenland and Gulf of Alaska land-ice evolution from an iterated GRACE global mascon solution *Journal of Glaciology,* **59,** 613-631.

Luthcke, S. B., Zwally, H. J., Abdalati, W., Rowlands, D. D., Ray, R. D., Nerem, R. S., Lemoine, F. G., McCarthy, J. J. and Chinn, D. S. (2006b) Recent Greenland ice mass loss by drainage system from satellite gravity observations *Science,* **314,** 5803 1286-1289.

Lyard, F., Lefevre, F., Letellier, T. and Francis, O. (2006) Modelling the global ocean tides: modern insights from FES2004 *Ocean Dynamics,* **56,** 5-6 394-415.

Mayer-Gürr, T., Eicker, A. and Ilk, K. (2006) 'Gravity Field Recovery from GRACE-SST Data of Short Arcs', in Flury, J., Rummel, R., Reigber, C., Rothacher, M., Boedecker, G. and Schreiber, U.(Eds) *Observation of the Earth System from Space.* Springer Berlin Heidelberg, pp. 131-148.

McAdoo, D. C. and Marks, K. M. (1992) Gravity fields of the Southern Ocean from Geosat data *Journal of Geophysical Research: Solid Earth (1978–2012),* **97,** B3 3247-3260.

Montenbruck, O. and Gill, E. (2005) *Satellite Orbits: Models, Methods and Applications.* Springer: Berlin, Heidelberg, New York.

Moore, P., Boomkamp, H. J., Carnochan, S. and Walmsley, R. J. (1999) FAUST: Multi-satellite orbital dynamics software *Advances in Space Research,* **23,** 4 785-795.

Moore, P. and King, M. A. (2008) Antarctic ice mass balance estimates from GRACE: Tidal aliasing effects *Journal of Geophysical Research: Earth Surface,* **113,** F2 F02005.

Moore, P. and Williams, S. D. P. (2014) Integration of altimetric lake levels and GRACE gravimetry over Africa: Inferences for terrestrial water storage change 2003–2011 *Water Resources Research,* **50,** 12 9696-9720.

Muala, E., Mohamed, Y. A., Duan, Z. and van der Zaag, P. (2014) Estimation of reservoir discharges from Lake Nasser and Roseires Reservoir in the Nile Basin using satellite altimetry and imagery data *Remote Sensing,* **6,** 8 7522-7545.

Muller, P. M. and Sjogren, W. L. (1968) Mascons: Lunar Mass Concentrations *Science,* **161,** 3842 680-684.

NASA/JPL (2002) *Artist's concept of Grace*. Available at: http://photojournal.jpl.nasa.gov/catalog/PIA04235 (Accessed: 25/6/2012).

Oki, T. and Sud, Y. C. (1998) Design of Total Runoff Integrating Pathways (TRIP)—A Global River Channel Network *Earth Interactions,* **2,** 1 1-37.

Pavlis, N. K., Holmes, S. A., Kenyon, S. C. and Factor, J. K. (2012) The development and evaluation of the Earth Gravitational Model 2008 (EGM2008) *Journal of Geophysical Research: Solid Earth,* **117,** B4 B04406.

Peltier, W. (2004) Global glacial isostasy and the surface of the ice-age Earth: the ICE-5G (VM2) model and GRACE *Annu. Rev. Earth Planet. Sci.,* **32,** 111-149.

Petit, G. and Luzum, B. (2010) *IERS Conventions (2010) (IERS Technical Note ; 36).* Frankfurt am Main: Verlag des Bundesamts für Kartographie und Geodäsie, 2010. 179 pp., ISBN 3-89888-989-6

Pritchard, H. D., Luthcke, S. B. and Fleming, A. H. (2010) Understanding ice-sheet mass balance; progress in satellite altimetry and gravimetry *Journal of Glaciology,* **56,** 200 1151-1161.

Ramillien, G., Biancale, R., Gratton, S., Vasseur, X. and Bourgogne, S. (2011) GRACE-derived surface water mass anomalies by energy integral approach: application to continental hydrology *Journal of Geodesy,* **85,** 6 313-328.

Ray, R. D. and Luthcke, S. B. (2006) Tide model errors and GRACE gravimetry: towards a more realistic assessment *Geophysical Journal International,* **167,** 3 1055-1059.

Ray, R. D., Luthcke, S. B. and Boy, J. P. (2009) Qualitative comparisons of global ocean tide models by analysis of intersatellite ranging data *J. Geophys. Res.*, **114,** C9 C09017.

Reigber, C., Balmino, G., Schwintzer, P., Biancale, R., Bode, A., Lemoine, J. M., König, R., Loyer, S., Neumayer, H., Marty, J. C., Barthelmes, F., Perosanz, F. and Zhu, S. Y. (2003) Global Gravity Field Recovery Using Solely GPS Tracking and Accelerometer Data from Champ *Space Science Reviews,* **108,** 1-2 55-66.

Reigber, C., Schmidt, R., Flechtner, F., König, R., Meyer, U., Neumayer, K.-H., Schwintzer, P. and Zhu, S. Y. (2005) An Earth gravity field model complete to degree and order 150 from GRACE: EIGEN-GRACE02S *Journal of Geodynamics,* **39,** 1 1-10.

Ries, J. C., Bettadpur, S., Poole, S. and Richter, T. (2011) *Mean Background Gravity Fields for GRACE Processing: GRACE Science Team Meeting.* Austin, TX, August 8-10, 2011.

Riva, R. E. M., Gunter, B. C., Urban, T. J., Vermeersen, B. L. A., Lindenbergh, R. C., Helsen, M. M., Bamber, J. L., de Wal, R., van den Broeke, M. R. and Schutz, B. E. (2009) Glacial Isostatic Adjustment over Antarctica from combined ICESat and GRACE satellite data *Earth and Planetary Science Letters,* **288,** 3-4 516-523.

Rodell, M., Houser, P. R., Jambor, U., Gottschalck, J., Mitchell, K., Meng, C.-J., Arsenault, K., Cosgrove, B., Radakovich, J., Bosilovich, M., Entin, J. K., Walker, J. P., Lohmann, D. and D. Toll (2004) The Global Land Data Assimilation System *Bull. Amer. Meteor. Soc., 85(3), 381-394.*

Rodell, M., Velicogna, I. and Famiglietti, J. S. (2009) Satellite-based estimates of groundwater depletion in India *Nature,* **460,** 7258 999-1002.

Rowlands, D. D., Luthcke, S. B., Klosko, S. M., Lemoine, F. G. R., Chinn, D. S., McCarthy, J. J., Cox, C. M. and Anderson, O. B. (2005) Resolving mass flux at high spatial and temporal resolution using GRACE intersatellite measurements *Geophys. Res. Lett.,* **32,** 4 L04310.

Rowlands, D. D., Luthcke, S. B., McCarthy, J. J., Klosko, S. M., Chinn, D. S., Lemoine, F. G., Boy, J. P. and Sabaka, T. J. (2010) Global mass flux solutions from GRACE: A comparison of parameter estimation strategies - Mass concentrations versus Stokes coefficients *J. Geophys. Res.*, **115,** B1 B01403.

Rowlands, D. D., Ray, R. D., Chinn, D. S. and Lemoine, F. G. (2002) Short-arc analysis of intersatellite tracking data in a gravity mapping mission *Journal of Geodesy,* **76,** 6-7 307-316.

Rummel, R., Balmino, G., Johannessen, J., Visser, P. and Woodworth, P. (2002) Dedicated gravity field missions—principles and aims *Journal of Geodynamics,* **33,** 1–2 3-20.

Sabaka, T. J., Rowlands, D. D., Luthcke, S. B. and Boy, J. P. (2010) Improving global mass flux solutions from Gravity Recovery and Climate Experiment (GRACE) through forward modeling and continuous time correlation *J. Geophys. Res.*, **115,** B11 B11403.

Sakumura, C., Bettadpur, S. and Bruinsma, S. (2014) Ensemble prediction and intercomparison analysis of GRACE time-variable gravity field models *Geophysical Research Letters,* **41,** 5 1389-1397.

Sasgen, I., Konrad, H., Ivins, E. R., Van den Broeke, M. R., Bamber, J. L., Martinec, Z. and Klemann, V. T. (2013) Antarctic ice-mass balance 2003 to 2012: regional reanalysis of GRACE satellite gravimetry measurements with improved estimate of glacial-isostatic adjustment based on GPS uplift rates *The Cryosphere,* **7, 1499-1512, doi:10.5194/tc-7-1499-2013, 2013.**

Sasgen, I., van den Broeke, M., Bamber, J. L., Rignot, E., Sørensen, L. S., Wouters, B., Martinec, Z., Velicogna, I. and Simonsen, S. B. (2012) Timing and origin of recent regional ice-mass loss in Greenland *Earth and Planetary Science Letters,* **333–334,** 0 293-303.

Save, H., Bettadpur, S. and Tapley, B. (2012) Reducing errors in the GRACE gravity solutions using regularization *Journal of Geodesy,* **86,** 9 695-711.

Schrama, E. J. O. and Visser, P. N. A. M. (2007) Accuracy assessment of the monthly GRACE geoids based upon a simulation *Journal of Geodesy,* **81,** 1 67-80.

Schrama, E. J. O. and Wouters, B. (2011) Revisiting Greenland ice sheet mass loss observed by GRACE *J. Geophys. Res.*, **116,** B2 B02407.

Schrama, E. J. O., Wouters, B. and Lavallee, D. A. (2007) Signal and noise in Gravity Recovery and Climate Experiment (GRACE) observed surface mass variations *Journal of Geophysical Research-Solid Earth,* **112,** B8.

Schrama, E. J. O., Wouters, B. and Rietbroek, R. (2014) A mascon approach to assess ice sheet and glacier mass balances and their uncertainties from GRACE data *Journal of Geophysical Research: Solid Earth,* **119,** 7 6048-6066.

Schwintzer, P., Kang, Z., Reigber, C. and Zhu, S. Y. (1995) GPS satellite-to-satellite tracking for TOPEX/Poseidon precise orbit determination and gravity field model improvement *Journal of Geodynamics,* **20,** 2 155-166.

Seeber, G. (2003) *Satellite Geodesy.* Walter de Gruyter: Berlin.

Seo, K.-W., Wilson, C. R., Chen, J. and Waliser, D. E. (2008a) GRACE's spatial aliasing error *Geophysical Journal International,* **172,** 1 41-48.

Seo, K. W., Wilson, C. R., Famiglietti, J. S., Chen, J. L. and Rodell, M. (2006) Terrestrial water mass load changes from Gravity Recovery and Climate Experiment (GRACE) *Water Resources Research,* **42,** 5 W05417.

Seo, K. W., Wilson, C. R., Han, S. C. and Waliser, D. E. (2008b) Gravity Recovery and Climate Experiment (GRACE) alias error from ocean *Journal of Geophysical Research-Solid Earth,* **113,** B3.

Shepherd, A., Ivins, E. R., A, G., Barletta, V. R., Bentley, M. J., Bettadpur, S., Briggs, K. H., Bromwich, D. H., Forsberg, R., Galin, N., Horwath, M., Jacobs, S., Joughin, I., King, M. A., Lenaerts, J. T. M., Li, J., Ligtenberg, S. R. M., Luckman, A., Luthcke, S. B., McMillan, M., Meister, R., Milne, G., Mouginot, J., Muir, A., Nicolas, J. P., Paden, J., Payne, A. J., Pritchard, H., Rignot, E., Rott, H., Sørensen, L. S., Scambos, T. A., Scheuchl, B., Schrama, E. J. O., Smith, B., Sundal, A. V., van Angelen, J. H., van de Berg, W. J., van den Broeke, M. R., Vaughan, D. G., Velicogna, I., Wahr, J., Whitehouse, P. L., Wingham, D. J., Yi, D., Young, D. and Zwally, H. J. (2012) A Reconciled Estimate of Ice-Sheet Mass Balance *Science,* **338,** 6111 1183-1189.

Simpson, M. J. R., Milne, G. A., Huybrechts, P. and Long, A. J. (2009) Calibrating a glaciological model of the Greenland ice sheet from the Last Glacial Maximum to present-day using field observations of relative sea level and ice extent *Quaternary Science Reviews,* **28,** 17–18 1631-1657.

Sinclair, A. T. and Appleby, G. M. (1986) *SATAN Programs for the determination and analysis of satellite orbits from SLR data. S.L.R. Technical Note 9, RGO*

Stammer, D., Ray, R. D., Andersen, O. B., Arbic, B. K., Bosch, W., Carrère, L., Cheng, Y., Chinn, D. S., Dushaw, B. D., Egbert, G. D., Erofeeva, S. Y., Fok, H. S., Green, J. A. M., Griffiths, S., King, M. A., Lapin, V., Lemoine, F. G., Luthcke, S. B., Lyard, F., Morison, J., Müller, M., Padman, L., Richman, J. G., Shriver, J. F., Shum, C. K., Taguchi, E. and Yi, Y. (2014) Accuracy assessment of global barotropic ocean tide models *Reviews of Geophysics,* **52,** 3 243-282.

Standish, E. M., Newhall, X. X., Williams, J. G. and Folkner, W. F. (1995) JPL Planetary and Lunar Ephemerides, DE403/LE403 *JPL IOM 314.10-127*.

Stockwell, D. (2006) *Niche modeling: predictions from statistical distributions.* CRC Press.
Strassberg, G., Scanlon, B. R. and Chambers, D. (2009) Evaluation of groundwater storage monitoring with the GRACE satellite: Case study of the High Plains aquifer, central United States *Water Resour. Res*, **45**.
Swenson, S., Chambers, D. and Wahr, J. (2008) Estimating geocenter variations from a combination of GRACE and ocean model output *Journal of Geophysical Research: Solid Earth*, **113,** B8 B08410.
Swenson, S. and Wahr, J. (2002) Methods for inferring regional surface-mass anomalies from Gravity Recovery and Climate Experiment (GRACE) measurements of time-variable gravity *J. Geophys. Res.*, **107,** B9 2193.
Swenson, S. and Wahr, J. (2006) Post-processing removal of correlated errors in GRACE data *Geophys. Res. Lett.*, **33,** 8 L08402.
Syed, T. H., Famiglietti, J. S., Rodell, M., Chen, J. and Wilson, C. R. (2008) Analysis of terrestrial water storage changes from GRACE and GLDAS *Water Resources Research*, **44,** 2 W02433.
Tapley, B., Ries, J., Bettadpur, S., Chambers, D., Cheng, M., Condi, F., Gunter, B., Kang, Z., Nagel, P., Pastor, R., Pekker, T., Poole, S. and Wang, F. (2005) GGM02 – An improved Earth gravity field model from GRACE *Journal of Geodesy*, **79,** 8 467-478.
Tapley, B. D., Bettadpur, S., Ries, J. C., Thompson, P. F. and Watkins, M. M. (2004a) GRACE Measurements of Mass Variability in the Earth System *Science*, **305,** 5683 503-505.
Tapley, B. D., Bettadpur, S., Watkins, M. and Reigber, C. (2004b) The gravity recovery and climate experiment: Mission overview and early results *Geophys. Res. Lett.*, **31,** 9 L09607.
Tapley, B. D., Chambers, D. P., Bettadpur, S. and Ries, J. C. (2003) Large scale ocean circulation from the GRACE GGM01 Geoid *Geophysical Research Letters*, **30,** 22.
Tregoning, P., Ramillien, G., McQueen, H. and Zwartz, D. (2009) Glacial isostatic adjustment and nonstationary signals observed by GRACE *Journal of Geophysical Research-Solid Earth*, **114**.
Van den IJssel, J. and Visser, P. (2010) Performance of GPS-based accelerometry: A simulation experiment *Advances in Space Research*, **45,** 2 225-238.
Van Helleputte, T., Doornbos, E. and Visser, P. (2009) CHAMP and GRACE accelerometer calibration by GPS-based orbit determination *Advances in Space Research*, **43,** 12 1890-1896.
Van Helleputte, T. and Visser, P. (2008) GPS based orbit determination using accelerometer data *Aerospace Science and Technology*, **12,** 6 478-484.
Velicogna, I. (2009) Increasing rates of ice mass loss from the Greenland and Antarctic ice sheets revealed by GRACE *Geophys. Res. Lett.*, **36,** 19 L19503.
Velicogna, I., Sutterley, T. C. and van den Broeke, M. R. (2014) Regional acceleration in ice mass loss from Greenland and Antarctica using GRACE time-variable gravity data *Geophysical Research Letters*, **41,** 22 8130-8137.
Velicogna, I. and Wahr, J. (2002) Postglacial rebound and Earth's viscosity structure from GRACE *J. Geophys. Res.*, **107,** B12 2376.
Velicogna, I. and Wahr, J. (2006a) Acceleration of Greenland ice mass loss in spring 2004 *Nature*, **443,** 7109 329-331.
Velicogna, I. and Wahr, J. (2006b) Measurements of Time-Variable Gravity Show Mass Loss in Antarctica *Science*, **311,** 5768 1754-1756.

Velicogna, I. and Wahr, J. (2013) Time-variable gravity observations of ice sheet mass balance: precision and limitations of the GRACE satellite data *Geophysical Research Letters***,** n/a-n/a.

Visser, P. N. A. M., Doornbos, E., Van den Ijssel, J. and da Encarnação, J. T. (2013) Thermospheric density and wind retrieval from Swarm observations *Earth, Planets, and Space*, **65,** 1319-1331.

Visser, P. N. A. M. and Schrama, E. J. O. (2005) 'Space-borne gravimetry: determination of the time variable gravity field Gravity, Geoid and Space Missions', in Jekeli, C., Bastos, L. and Fernandes, J.(Eds). Vol. 129 Springer Berlin Heidelberg, pp. 6-11.

Wahr, J., Molenaar, M. and Bryan, F. (1998) Time variability of the Earth's gravity field: Hydrological and oceanic effects and their possible detection using GRACE *J. Geophys. Res.*, **103,** B12 30205-30229.

Wahr, J., Swenson, S. and Velicogna, I. (2006) Accuracy of GRACE mass estimates *Geophysical Research Letters*, **33,** 6.

Wahr, J., Swenson, S., Zlotnicki, V. and Velicogna, I. (2004) Time-variable gravity from GRACE: First results *Geophys. Res. Lett.*, **31**.

Watkins, K. (2006) *Human Development Report 2006. Beyond scarcity: Power, poverty and the global water crisis.* United Nations Development Programme (UNDP)

Watkins, M. M. (2012) *JPL Level-2 Processing Standards Document for Level-2 Product Release 05*

Watkins, M. M., Gruber, T. and Bettadpur, S. V. (2000) *GRACE 327-710 Science Data System Development Plan - Revision C.* ftp://podaac.jpl.nasa.gov/allData/grace/docs/sds_dev_plan_c.pdf:

Watkins, M. M., Wiese, D. N., Yuan, D.-N., Boening, C. and Landerer, F. W. (2015) Improved methods for observing Earth's time variable mass distribution with GRACE using spherical cap mascons *Journal of Geophysical Research: Solid Earth*, **120,** 4 2648-2671.

Weigelt, M., van Dam, T., Jäggi, A., Prange, L., Tourian, M. J., Keller, W. and Sneeuw, N. (2013) Time-variable gravity signal in Greenland revealed by high-low satellite-to-satellite tracking *Journal of Geophysical Research: Solid Earth*, **118,** 7 3848-3859.

WGMS (1999) update 2012. World Glacier Inventory. [Alaskan/Yukon Basins]. Boulder, Colorado USA: National Snow and Ice Data Center. http://dx.doi.org/10.7265/N5/NSIDC-WGI-2012-02.

Whitehouse, P. L., Bentley, M. J., Milne, G. A., King, M. A. and Thomas, I. D. (2012) A new glacial isostatic adjustment model for Antarctica: calibrated and tested using observations of relative sea-level change and present-day uplift rates *Geophysical Journal International*, **190,** 3 1464-1482.

Wiese, D., Folkner, W. and Nerem, R. (2009) Alternative mission architectures for a gravity recovery satellite mission *Journal of Geodesy*, **83,** 6 569-581.

Williams, S. D. P., Moore, P., King, M. A. and Whitehouse, P. L. (2014) Revisiting GRACE Antarctic ice mass trends and accelerations considering autocorrelation *Earth and Planetary Science Letters*, **385,** 0 12-21.

Williams, S. P. (2008) CATS: GPS coordinate time series analysis software *GPS Solutions*, **12,** 2 147-153.

Wittwer, T. (2009) *Regional gravity field modelling with radial basis functions.* thesis. TU Delft.

Wolff, M. (1969) Direct measurements of the Earth's gravitational potential using a satellite pair *Journal of Geophysical Research*, **74,** 22 5295-5300.

Wouters, B., Bamber, J. L., van den Broeke, M. R., Lenaerts, J. T. M. and Sasgen, I. (2013) Limits in detecting acceleration of ice sheet mass loss due to climate variability *Nature Geosci,* **6,** 8 613-616.

Wouters, B., Chambers, D. and Schrama, E. J. O. (2008) GRACE observes small-scale mass loss in Greenland *Geophysical Research Letters,* **35,** 20.

Wouters, B. and Schrama, E. J. O. (2007) Improved accuracy of GRACE gravity solutions through empirical orthogonal function filtering of spherical harmonics *Geophys. Res. Lett.,* **34,** 23 L23711.

Zhao, Q., Guo, J., Hu, Z., Shi, C., Liu, J., Cai, H. and Liu, X. (2011) GRACE gravity field modeling with an investigation on correlation between nuisance parameters and gravity field coefficients *Advances in Space Research,* **47,** 10 1833-1850.

Zwally, H. J., Giovinetto, M. B., Beckley, M. A. and Sab, J. L. (2012) 'Antarctic and Greenland Drainage Systems, GSFC Cryospheric Sciences Laboratory,' in http://icesat4.gsfc.nasa.gov/cryo_data/ant_grn_drainage_systems.php. .

Zwally, H. J., Giovinetto, M. B., Li, J., Cornejo, H. G., Beckley, M. A., Brenner, A. C., Saba, J. L. and Yi, D. (2005) Mass changes of the Greenland and Antarctic ice sheets and shelves and contributions to sea-level rise: 1992-2002 *Journal of Glaciology,* **51,** 509-527.